Mechanical and hydraulic behaviour of compacting crushed salt backfill at low porosities

GRS - 450

Gesellschaft für Anlagen-
und Reaktorsicherheit
(GRS) gGmbH

Mechanical and hydraulic behaviour of compacting crushed salt backfill at low porosities

Project REPOPERM - Phase 2

(Appendix on CD)

Klaus-Peter Kröhn (GRS)
Dieter Stührenberg (BGR)
Michael Jobmann (DBE TEC)
Ulrich Heemann (BGR)
Oliver Czaikowski (GRS)
Klaus Wieczorek (GRS)
Christian Müller (DBE TEC)
Chun-Liang Zhang (GRS)
Helge Moog (GRS)
Sonja Schirmer (DBE TEC)
Larissa Friedenberg (GRS)

February 2017

Remark:
This report was prepared under contract no. 02 E 10740 with the Federal Ministry for Economic Affairs and Energy (BMWi).

This work was conducted by the Bundesanstalt für Geowissenschaften und Rohstoffe (BGR), the DBE Technology GmbH (DBE TEC) and the Gesellschaft für Anlagen- und Reaktorsicherheit (GRS) gGmbH.

GRS - 450
ISBN 978-3-946607-32-8

Keywords

high-level radioactive waste, repository, salt backfill, compaction, porosity, permeability, long-term safety, proof

Acknowledgement

This report summarizes the work performed in the joint project “Restporosität und –permeabilität von kompaktiertem Salzgrus-Versatz in einem HAW-Endlager (REPOPERM Phase 2)“. The project partners were the Bundesanstalt für Geowissenschaften und Rohstoffe (BGR), the DBE TECHNOLOGY GmbH (DBE TEC) and the Gesellschaft für Anlagen- und Reaktorsicherheit (GRS) gGmbH. The project was funded by the German Federal Ministry for Economic Affairs and Energy (BMWi) under the contract no. 02 E 10740.

We would like to express our thanks to all our colleagues who participated in this project without actually being an author of this report. These are in particular Christian Lerch and Liselotte von Borstel from DBE TEC and Jens Wolf and Rüdiger Miehe from GRS who contributed substantially to the success of the project by their extensive consulting work.

Abstract

The compaction behaviour of crushed salt has been extensively investigated by means of experimental as well as theoretical work. The readiness of numerical tools for the application to modelling the complex coupled thermo-hydro-mechanical processes in the crushed salt backfilled in a repository in salt rock has also been demonstrated.

Compaction tests were performed under repository-relevant conditions. These tests were supplemented by laboratory work aiming at specific aspects of compaction. The following list covers the topics of these investigations as well as the main results.

– *Revisiting the determination of the porosity in relevant, past experiments (BGR)*
  Uncertainty in determination of the grain density causes subsequently uncertainty of the derived porosity. Earlier laboratory tests were thus examined with a view to the accuracy of porosity values below 10 %. An uncertainty in void ratio was found in the range of 0.45 % to 0.65 % void ratio.

– *Influence of the grain size distribution on compaction (BGR)*
  As revealed in the framework of REPOPERM phase 1, the backfill resistance of reference material for drift backfilling (maximum grain size d = 31.5 mm) at 150 °C is quite similar to a material where grain size fractions larger than 8 mm have been removed (DEBORA material). The same result was found in a material comparison at 50 °C confirming the assumption that the compaction behaviour is largely controlled by the grain fractions of little grain diameters.

– *Triaxial compaction test with dry material at low porosities (BGR)*
  A triaxial compaction test with a pre-compacted sample was performed where the compaction stress was not raised above the expected formation pressure of about 20 MPa. The test was terminated at a porosity of 7.8 %. A comparison with an earlier oedometer test showed that the results appear to disagree increasingly towards small porosities.

– *Investigation of the influence of humidity on compaction covers several subtopics*
  • *Strain-rate controlled oedometer tests (BGR)*
    The backfill resistance for 1 % added brine at 33 °C compared well with the curve for 0.6 % added brine at 50 °C. Compaction under the influence of inject-

ed humid air of 85 % relative humidity at 33 °C was faster than with a comparable dry sample but not as fast as in tests with added brine. It has to be mentioned, though, that the moisture content of the sample had increased by more than 0.1 % by weight during the treatment with moistened air.

- *Stress-controlled uniaxial long-term compaction (GRS)*

  The test touches a number of aspects concerning the THM-behaviour of compacting crushed salt. It showed that an initial moisture content in the order of 0.1 % does not significantly influence compaction in comparison to initially oven-dry conditions. Compaction of the sample with initially 1 % moisture content was much faster under much less load than compaction of the initially dryer samples. A temperature increase of about 30 °C had a similar effect as a mechanical load increase in the range of 3 to 5 MPa. Temperature decrease at maintained mechanical load results in a “hardening” of the material as the subsequent strain rate dropped considerably. The effect of flooding under high stresses can result in a loss of porosity in the order of 8 to 13 % within a year. A qualitatively similar behaviour is expected for low stresses.
- *Triaxial compaction in an autoclave (GRS)*

  The test indicates that the transition from dry compaction to wet compaction occurs between 0.3 % and 0.6 % initial moisture content.
- *Compaction in a humid atmosphere (GRS)*

  In general the development of the porosity under increased humidity compares quite well with the measured porosity in the oven-dry sample of the long-term test. An influence of high relative humidity in the pore air can therefore not be confirmed by this test.
- *Adsorption of water to salt in a humid atmosphere (GRS)*

  The amount of water drawn by crushed salt from a moist atmosphere is very low. It can thus not be expected that sorption exerts a significant retardation to vapour flow in the pore space of a crushed salt backfill.

  At a relative humidity of 75 % the samples showed a remarkable increase in weight. This might indicate condensation of water on the salt grains due to little temperature variations. A subsequent capillary condensation can also not be excluded.

– *Permeability associated with low porosity includes two subtopics*
  - *A uniaxial permeameter test with brine (BGR)*

    The test supplements and confirms the permeability-porosity relation for wet crushed salt derived in /KRÖ 09/ particularly for low porosity values down to 2 % or a gas permeability of roughly 10^{-17} m².
  - *Permeability tests with gas (nitrogen) (BGR)*

    The gas permeability of highly-compacted crushed salt was measured under a considerable confining stress. In dry samples of 5 % and about 1 % porosity the gas flow could not be interrupted by repository-relevant stresses. Putting the samples over three weeks in an atmosphere of about 75 % relative humidity gave rise to a clear change in compaction and permeability behaviour that lay between completely dry conditions and wetting with brine. However, the findings must be verified by other tests and quantitatively expanded.

– *Constitutive equations for two-phase flow (GRS)*

  The measurements demonstrate that the constitutive relations for two-phase flow in crushed salt at a medium degree of compaction meaning a porosity of about 7 % and with a repository-relevant grain size distribution can be determined experimentally even if a lot of care and effort has to be spent. The material behaved qualitatively according to the expectation that capillary forces, the air entry pressure and the residual brine saturation increase with decreasing porosity.

  However, the well-known approaches for two-phase flow in common soils, for example the approaches of Brooks and Corey as well as those of van Genuchten, fail for compacting crushed salt. It is obviously not possible to derive the relative permeability-saturation relation for the gas phase from parameters for the capillary pressure-saturation relation as the work of Brooks and Corey and van Genuchten implies. This is particularly disturbing as the relative permeability-saturation relation for the liquid phase must therefore be determined directly which was not covered by the present measurements. Concrete model calculations based on the presented results are thus not advisable at the moment.

– *Microstructural Investigations (DBE TEC)*

  It was found that penetration of resin with very low viscosity into prepared compacted samples took place at grain boundaries as well as cracks that run through larger halite grains. The addition of 1.2 % brine during compaction had the effect that the

small grains in the fine grained section “bonded’’ leading to new crystalline structures so that the amount of fine pores in this section was reduced significantly. By contrast, the addition of moist air during compaction did not lead to such bonding. The microstructural analysis reveals furthermore that the pore space must be considered as isotropic in its connectivity and percolation threshold.

Parallel to the experimental work attention focussed on several aspects of the basics for modelling the compaction of crushed salt. This work covers checking the validity of the established numerical tools as well as exploring new methods. Topics and main results are listed below.

– *Development/definition and comparison of constitutive models (BGR)*
  Two established models (Hein /HEI 91/ and Olivella et al. /OLI 93/, OLI 02/) and one model advanced during the project (Heemann, Appendix A) were compared with a view to the mathematical process formulation. Overall, the three models yield similar results. The conditions under which the calculations gave rather big deviations practically are of little importance under in situ conditions, especially for a high porosity. The variant of Hein’s model proposed by Korthaus /KOR 96/, however, seems to lead to more plausible results than the original Hein model. The Korthaus variant is also in better agreement with the geometrically-physically based model of Heemann.
  Despite the advantages of an analytical derivation of the physical behaviour of crushed salt it cannot be ignored that the model of Heemann ultimately also is based on phenomenological fitting to experimental results, albeit to a lesser extent.

– *Benchmark calculations (BGR and GRS)*
  Different tests concerning dry compaction formed the basis for checking on the validity of the presently available material models. The idea behind this exercise was that a valid material model should correctly describe any of the compaction tests. However, this was not the case. None of the calibrated parameter sets could be transferred to another test with satisfying results. Using sets of intermediate parameter values led to the same result.
  The simulations have shown that the application of the available material models on the long-term compaction tests leads to plausible and coherent results. Compaction of crushed backfill can in principle be modelled, both for the dry case and for a brine inflow, at constant or variable temperature.

– *Capability of scaling-rules for capillary pressure from the oil industry (GRS)*
  Considering the fact that only few, very specific formations are of interest to the oil industry the derived formulations for the CPS-relations and scaling-rules are quite different and no method produced a prediction that was clearly superior to the others. It is interesting to note, though, that different authors from the oil industry returned in recent times to Leverett's J-function or certain variations of it.
  Scaling capillary pressure-saturation relations after Leverett yields satisfying results only for a permeability range of 2 to 3 orders of magnitude in case of the storage formations that are of interest for the oil industry. Crushed salt by comparison undergoes a permeability change over 8 to 9 orders of magnitude according to the permeability-porosity relation. The proposal from the literature to apply the J-function for cases of advanced degrees of compaction thus appears to be rather ambitious.
  All in all, scaling-rules derived from the extensively investigated storage formations for gas and oil are no alternative to determine retention curves and relative permeabilities for compacting crushed salt experimentally.

– *Application of discrete element codes to compacting crushed salt (DBE TEC)*
  Presented here are the first systematic studies that deal with the simulation of the compaction of granular rock salt at grain scale using the discrete element method (DEM). Several numerical problems and deficiencies in the knowledge about the required constitutive models were encountered, though, leading to the conclusion that the codes tested need significant improvements prior to practical applications.

Finally, repository-relevant scenarios are discussed as a basis for a realistic but generic numerical model of brine inflow into a converging backfilled drift under a thermal gradient (GRS). This exercise demonstrates the feasibility of modelling crushed salt compaction as a fully coupled thermo-hydraulic-mechanical process including two-phase flow effects.

Zusammenfassung

Der vorliegende Bericht präsentiert die Ergebnisse der umfangreichen experimentellen und theoretischen Untersuchungen zum Kompaktionsverhalten von Salzgrusversatz. Unter Einbeziehung der gewonnenen Erkenntnisse wurde außerdem die Einsatzbereitschaft numerischer Tools für die in komplexer Weise interagierenden thermischen, hydraulischen und mechanischen Prozesse während der Salzgruskompaktion demonstriert.

Kompaktionsversuche wurden unter endlagerrelevanten Bedingungen durchgeführt. Diese Versuche wurden durch weitere Labortests ergänzt, die auf spezielle Aspekte der Salzgruskompaktion abzielen. Die einzelnen Untersuchungen sowie die zugehörigen Ergebnisse sind nachfolgend zusammengestellt:

– *Wiederholung der Porositätsbestimmung für relevante vergangene Tests (BGR)*
  Unsicherheiten bei der Bestimmung der Korndichte haben Unsicherheiten bei der Bestimmung der Porosität zur Folge. Porositätsbestimmungen aus früheren Laboruntersuchungen wurden deshalb für Werte unter 10 % auf der Grundlage neuer Erkenntnisse aus dem Projekt REPOPERM Phase 1 wiederholt. Der sich ergebende Effekt für die Porenzahl ist nur für sehr kleine Werte von Bedeutung und liegt im Bereich einer Porenzahl von 0.45 % bis 0.65 %.

– *Bestimmung des Einflusses der Korngrößenverteilung auf das Kompaktionsverhalten (BGR)*
  Im Projekt REPOPERM Phase 1 war gezeigt worden, dass sich der Versatzwiderstand des Referenzmaterials (Größtkorndurchmesser 31,5 mm) bei 150 °C ähnlich verhält wie ein Material, bei dem die Kornfraktionen über 8 mm herausgesiebt wurden (DEBORA Material). Ein vergleichbares Ergebnis wurde nun für einen Vergleich bei 50 °C gefunden. Dieses Ergebnis bestätigt die Vermutung, dass das Kompaktionsverhalten wesentlich durch die Kornfraktionen mit kleinen Korndurchmessern bestimmt wird.

– *Triaxialer Kompaktionstest mit trockenem Material bei geringen Porositäten (BGR)*
  Eine trockene, vorkompaktierte Salzgrusprobe wurde in einem Triaxialversuch einer schrittweise steigenden Spannung von bis zu 20 MPa unterworfen, was der erwarteten Formationsspannung im Wirtsgestein im Bereich eines Endlagers entspricht. Der Test wurde bei einer Porosität von ca. 7,8 % abgebrochen. Der Vergleich mit einem

früher durchgeführten Oedometertest zeigt im Bereich kleinerer Porositäten zunehmende Unterschiede in den Versuchsergebnissen.

– *Untersuchung des Einflusses von Feuchtigkeit im Porenraum*
  - *Weggesteuerte Oedometertests (BGR)*
    Der Kompaktionswiderstand verhält sich bei Proben unter 33 °C, die mit 1 % Lösung angefeuchtet wurden, vergleichbar mit Proben unter 50 °C, die nur mit 0,6 % Lösung befeuchtet wurden. Kompaktion bei 33 °C unter dem Einfluss injizierter Luft von 85 % relativer Luftfeuchtigkeit erfolgte schneller als bei trockenen Proben aber nicht so schnell wie bei den mit Lösung befeuchteten Proben. Der Feuchtigkeitsgehalt der Probe nahm allerdings unter dem Einfluss der feuchten Luft um ca. 0,1 % zu.
  - *Spannungsgesteuerte Langzeitkompaktion im Oedometer (GRS)*
    Der Test berührt eine Reihe von Aspekten des THM-Verhaltens von kompaktierendem Salzgrus. Er zeigte, dass ein Anfangsfeuchtegehalt von 0,1 % das Kompaktionsverhalten nur unwesentlich gegenüber einem ofentrockenen Material beeinflusst. Die Kompaktion der Probe mit 1 % Anfangsfeuchtegehalt verlief bei geringerer mechanischer Last wesentlich schneller als die Kompaktion der trockeneren Proben. Ein Temperaturanstieg um 30 °C hatte in etwa denselben Effekt wie ein mechanischer Lastanstieg von 3 bis 5 MPa. Ein Temperaturrückgang bei gleichbleibender mechanischer Last ließ die Verzerrungsgeschwindigkeit nachfolgend erheblich sinken. Der Effekt einer vollständigen Auffüllung des Porenraums mit gesättigter Salzlösung unter hohen mechanischen Spannungen kann zu einer Porositätsabnahme von 8 % bis 13 % innerhalb eines Jahres führen. Ein ähnliches Verhlten wird auch bei geringeren Spannungen erwartet.
  - *Triaxiale Kompaktion in einem Autoklaven (GRS)*
    Der Test deutet an, dass das der Übergangsbereich zwischen dem für trockenes Material und dem für feuchtes Material typischen Kompaktionsverhalten zwischen 0.3 % und 0.6 % liegt.
  - *Kompaktion in feuchter Luft (GRS)*
    Im Großen und Ganzen ähnelt der Porositätsverlauf in diesem Kompaktionstest bei erhöhter Luftfeuchtigkeit dem Verlauf der ofen-trockenen Probe im Langzeitkompaktionsversuch. Ein Einfluss erhöhter Luftfeuchtigkeit auf das Kompaktionsverhalten kann hieraus nicht abgeleitet werden.

- *Adsorption von Wasser an Salzgrus bei zunehmender Luftfeuchtigkeit (GRS)*
  Die Wassermenge, die der feuchten Luft durch Salzgrus entzogen wird ist sehr gering. Daher ist keine signifikante Retardierung bei der Ausbreitung von Wasserdampf im Salzgrusversatz zu erwarten.
  Der Versuch zeigte bei einer Porenatmosphäre von 75 % Luftfeuchtigkeit eine auffallend starke Gewichtszunahme der Salzgrusproben. Kondensation auf den Salzkörnern infolge von kleinen Temperaturschwankungen und eventuell nachfolgende Kapillarkondensation können daher nicht ausgeschlossen werden.

– *Untersuchungen zur Permeabilität bei niedriger Porosität*
  - *Einaxialer Permeatertest mit gesättigter Salzlösung (BGR)*
    Die Testdaten bestätigen die Porositäts-Permeabilitäts-Beziehung nach /KRÖ 09/ und ergänzen sie im Bereich niedriger Porositäten bis hinab zu 2 %.
  - *Permeabilitätstests mit Gas (BGR)*
    Proben aus früheren Kompaktionsversuchen wurden einer erheblichen mechanischen Spannung unterworfen, um den Einfluss der Spannung auf die Gaspermeabilität zu untersuchen. In trockenen Proben von ca. 5 % und 1 % konnte der Gasfluss nicht durch endlagerrelevante Spannungen unterbrochen werden. Nachdem die Proben für drei Wochen in Luft mit 75 % relativer Luftfeuchtigkeit gelagert worden waren, lag das Kompaktionsverhalten zwischen demjenigen trockener Proben und Proben, die mit Lösung angefeuchtet worden waren. Zur näheren Untersuchung dieses Verhaltens sind weitere Tests erforderlich.

– *Messungen zur Bestimmung der konstitutiven Beziehungen für den Zweiphasenfluss (GRS)*
  Die Messungen zeigen, dass Zweiphasenfluss-Beziehungen für Salzgrus mit einer endlagerrelevanten Korngrößenverteilung und einem Kompaktionsgrad entsprechend einer Porosität van ca. 7 % experimentell bestimmbar sind. Dabei sind allerdings Sorgfalt und ein gewisser Aufwand erforderlich. Erwartungsgemäß stiegen die Kapillardrücke, der Gaseindringdruck und die residuale Lösungssättigung mit abnehmender Porosität an.
  Die Ansätze zur Beschreibung des Zweiphasenflusses insbesondere die gut bekannten Ansätze von Brooks und Corey sowie von van Genuchten lassen sich nicht auf kompaktierenden Salzgrus anwenden. Offensichtlich ist es nicht möglich, die Relative-Permeabilitäts-Sättigungs-Beziehung für die gasförmige Phase aus den Pa-

rametern für die Kapillardruck-Sättigungs-Beziehung abzuleiten, wie es das Ziel der genannten Ansätze ist. Dies ist besonders problematisch, weil die Relative-Permeabilitäts-Sättigungs-Beziehung für die flüssige Phase somit ebenfalls experimentell bestimmt werden muss, was mit den vorliegenden Messungen nicht möglich war. Konkrete Modellrechnungen auf der Basis des bisherigen Kenntnisstands zum Zweiphasenfluss erscheinen daher derzeit nicht ratsam.

– *Mikrostrukturuntersuchungen an kompaktiertem Salzgrusproben (DBE TEC)*
  Der Porenraum stark kompaktierter Salzgrusproben wurde mit Kunstharz mit sehr niedriger Viskosität angefüllt. Dieses Harz wurde danach sowohl auf den Korngrenzen als auch in Rissen durch große Salzgruskörner gefunden. Die Zugabe von Salzlösung in Höhe von 1,2 gew.% während der Kompaktion führte zu einer „Verklebung“ der feinkörnigen Kornfraktionen und nachfolgend zu neuen kristallinen Strukturen, so dass der Anteil kleiner Poren deutlich reduziert wurde. Bei Kompaktion mit feuchter Luft im Porenraum konnte dieser Effekt nicht beobachtet werden. Weiterhin wurde festgestellt, dass der Porenraum als isotrop bezüglich der Konnektivität zu betrachten ist.

Parallel zu den experimentellen Untersuchungen wurden verschiedene Aspekte der Grundlagen für die Modellierung der Salzgruskompaktion beleuchtet. Dabei ging es sowohl um die Anwendbarkeit bestehender numerischer Werkzeuge als auch um die Untersuchung neuer Methoden. Nachfolgend sind die dabei berührten Themen und (ggf.) die zugehörigen Ergebnisse aufgelistet:

– *Phänomene und physikalische Effekte bei der Salzgruskompaktion (BGR)*

– *Entwicklung und Vergleich der Materialmodelle (BGR)*
  Zwei etablierte Ansätze (Hein /HEI 91/ und Olivella et al. /OLI 93/, OLI 02/) und ein im Laufe des Projekts weiterentwickelter Ansatz (Heemann, Appendix A) wurden anhand der mathematischen Modelle für einzelne Prozesse verglichen. Im Großen und Ganzen zeigten die Modelle ähnliches Verhalten. Die Umstände, unter denen sich größere Abweichungen zeigten, sind für in-situ-Bedingungen von geringer Bedeutung.
  Eine von Korthaus vorgeschlagene Variante des Hein-Modells /KOR 96/ scheint plausiblere Ergebnisse zu liefern als das Originalmodell. Die Korthaus-Variante stimmt auch besser mit dem geometrisch-physikalisch motivierten Modell von Hee-

mann überein. Es bleibt festzuhalten, dass keins der drei Modelle vollständig ohne phänomenologische Anpassungen beim Materialmodell auskommt.

– *Benchmarkrechnungen (BGR und GRS)*
  Verschiedene Tests zur trockenen Kompaktion von Salzgrus wurden modellhaft nachgebildet, um die Übertragbarkeit kalibrierter Materialparameter zu überprüfen. Dahinter stand die Idee, dass ein belastbarer Satz an Materialparametern in allen Fällen zu einer zufriedenstellende Übereinstimmung von Messungen und Modellergebnissen führen muss. Dies war allerdings nicht der Fall. Mit keinem der Parametersätze konnte ein anderer Test als der, für den die Parameter kalibriert worden waren, auch nur annähernd nachgebildet werden. Dasselbe gilt auch für Materialparameter, die zwischen zwei kalibrierten Werten interpoliert wurden.
  Gezeigt werden konnte allerdings, dass die Anwendung bestehender Ansätze für Materialmodelle im Fall des Langzeitkompaktionsversuchs zu plausiblen und kohärenten Ergebnissen führt. Die Kompaktion von Salzgrusversatz kann im Prinzip für trockenes und für feuchtes Material auch unter veränderlicher Temperatur im Modell wiedergegeben werden.

– *Anwendbarkeit von Ähnlichkeitsbeziehungen aus der Ölindustrie (GRS)*
  In den letzten 70 Jahren wurde im Umfeld der Ölindustrie eine Reihe von Methoden entwickelt, um den Kapillardruck in Gesteinsformationen mit einem Minimum an Labormessungen vorhersagen zu können. Dabei erwies sich keine der Methoden als allen anderen Methoden überlegen. Es fällt allerdings auf, das in jüngerer Zeit wieder verstärkt auf Leveretts Ansatz mit der J-Funktion oder eine Variante davon zurückgegriffen wird.
  Skalierungen des Kapillardrucks mit Hilfe des Leverett-Ansatzes haben sich bei Speichergesteinen nur einem Bereich von 2 bis 3 Größenordnungen in der Permeabilität als erfolgreich erwiesen. Die Permeabilität im Salzgrusversatz erfährt dagegen bei der Kompaktion Änderungen von 8 bis 9 Größenordnungen. Der Vorschlag aus der Literatur, die J-Funktion auch für die Bedingungen einer fortgeschrittenen Kompaktion anzuwenden, erscheint daher außerordentlich ehrgeizig.
  Alles in allem bieten die Ähnlichkeitsgesetze, die für Speichergesteine für Gas und Öl entwickelt wurden, für kompaktierenden Salzgrus keine Alternative zur experimentellen Bestimmung der konstitutiven Beziehungen für den Zwei-Phasen-Fluss.

– *Anwendung der Diskrete Elemente Methode auf die Salzgruskompaktion (DBE TEC)*
  Im Rahmen des Projekts REPOPERM Phase 2 wurde die erste systematische Studie zur Simulation der Salzgruskompaktion auf Kornebene unter Verwendung der Diskrete-Elemente-Methode durchgeführt. Dabei traten verschiedene numerische Probleme und auch Lücken bei den erforderlichen Materialmodellen zu Tage, so dass die Anwendungsreife der Methode noch nicht erreicht werden konnte.

Auf der Grundlage einer Diskussion über endlagerrelevante Szenarien wurde schließlich ein generisches realitätsnahes Model für den Lösungszufluss in eine mit Salzgrus versetzte konvergierende Strecke erstellt (GRS). Damit wurde die Einsatzbereitschaft des Simulationscodes CODE_BRIGHT demonstriert, die bei der Kompaktion ablaufenden thermo-hydraulisch-mechanisch gekoppelten Prozesse einschließlich des Zweiphasenflusses nachzubilden.

Table of contents

1 Introduction

The German safety concept for disposal of high level radioactive waste (HLW) is based on the storage of the waste in a deep geological formation with a high containment capacity. According to the German Safety Requirements containment refers to a safety function of the repository system which is characterised by the fact that the radioactive waste is contained inside a defined rock zone in such a way that it essentially remains at the site of emplacement, and only minimal defined quantities of material are able to leave that rock zone (Federal Ministry for the Environment, Nature Conservation and Nuclear Safety 2010). According to this specification, the containment of the waste within the defined zone must be ensured by the host rock in conjunction with a system of technical measures and constructions, which have to seal the drifts and shafts connecting the repository with the geosphere outside the zone. As a further consequence, a modification of the concept for verifying compliance is necessary. Instead of assessing release scenarios, verification also has to be focused on the containment of the radioactive waste.

Salt rock is one type of host rock considered for the disposal of HLW because its significant visco-plastic deformation under effect of rock stresses and HLW-induced high temperatures is believed to seal the repository openings in the long term against water or brine intrusion. To avoid major stress redistributions in the rock that might compromise the integrity of rock, the remaining space between the canisters and the rock is to be filled up with crushed salt. This crushed salt backfill has an initial porosity of about 35 % which is reduced with time by convergent deformation of the surrounding salt rock responding to the formation stresses. The backfill material in turn builds up a mechanical resistance against further rock convergence slowing down the process. This resistance decreases with moisture that is adsorbed at the salt grains and with temperature. Hydraulically, a crushed salt backfill is of advantage since it expedites the sealing process, and thus the containment of the waste. This aspect has become more important due to the German Safety Requirements concerning a HLW repository.

Therefore, knowledge on physical and chemical properties, as well as on the thermo-hydro-mechanical (THM) behaviour of crushed salt during compaction, has become vital for the safety assessment. This includes changes in the mechanical and hydraulic behaviour if the pore space of the crushed salt is partly or completely filled with brine.

However, because the in-situ convergence rate is quite low (< 10^{-10} s^{-1}) and difficult to be reproduced in laboratory tests there still remains some uncertainty in the knowledge about long-term compaction behaviour of crushed salt, particularly in the range of porosities of less than 3 %. While the processes involved are qualitatively understood it remains rather unclear when the crushed salt compaction comes to a halt and which porosity is reached at that point. Most interesting would be, though, if there is a critical porosity in this process at which all flow channels between the salt grains are disconnected by compaction leading to a hydraulic tightness of the backfill that is comparable with the undisturbed salt rock.

While the final condition of the backfill is of obvious interest also the dynamics of compaction in combination with the concurrent changes in the hydraulics of the backfill play an important role in the design of the other technical barriers. Shaft and drift seals are necessary to prevent a possible brine flow towards the deposition holes until this task can be performed by the crushed salt backfill alone. The requirements concerning sealing capacity and lifetime for shaft and drift seals thus depend strongly on the transient flow resistance of the backfill.

On the way towards a reliable prediction of backfill compaction several theoretical models for the compaction behaviour[1] of dry crushed salt had been developed /SPI 89/, /HEI 91/, /HEE 91/, /ZHA 93/ and were checked and calibrated in the framework of the EU-project BAMBUS for a porosity range of 10 % < Φ < 35 % /BEH 03/. This work did not encompass wet salt, though. The present status concerning laboratory data and constitutive models for crushed salt with emphasis on porosities below 10 % was given in phase 1 of the project REPOPERM /KRÖ 09/. It turned out that

– many laboratory data for compacted crushed salt was compromised in the attempt to accelerate the compaction process. Often high deformation rates or high pressures had been applied to the samples that are strongly differing from the expected conditions in a real repository.
– comparatively little has been done to describe the compaction of wet crushed salt. While pressure solution has been identified as the additional relevant process only Spiers et al. /SPI 89/, /SPI 90/, /SPI 05/ and Olivella et al. /OLI 93/, /OLI 02/ have

[1] These will be called „material models“ further on.

formulated comprehensive material laws that in theory describe compaction under different moisture contents. The only implementation of such a constitutive model up to date can be found in CODE_BRIGHT but has not been applied to a full THM-problem yet.

– no data concerning constitutive relations (CR) existed for unsaturated flow or two-phase flow in compacted crushed salt with a realistic grain-size distribution curve. As the process of compaction deforms the grain shape the structure of the pore space is changed concurrently so that relative permeability and capillary pressure must be expected to change in an unpredictable way. This becomes relevant for modelling brine intrusion into to backfill.
– the determination of a porosity value of about 1 % from a compaction test was subject to uncertainties that add up to the same order as the measured value itself despite all efforts for accuracy. This casts doubt about the reliability of previously published data in this porosity range or below. The main contributor to these uncertainties is the exact value for the density of the salt grains. Since this density varies locally with the mineralogical composition it is also questionable whether porosity values in that range can be accurately determined at all.

Against this background two major deficits predicting the compaction behaviour of crushed salt become visible: firstly, the compaction of wet crushed salt – while understood qualitatively – can at the moment not be adequately modelled due to a lack of data. This concerns the moisture-dependent mechanical behaviour of the wet crushed salt as well as the hydraulic properties referring to unsaturated flow. Both effects not only occur simultaneously in case of a brine inflow into the backfill but obviously also interact with each other in a presently unforeseeable way. Further complexity might be added if evaporation of water from the brine and subsequent vapour diffusion in the pore space proved to be an additional water migration process in the backfill. Secondly, there is the problem of the huge uncertainties determining very low porosities that thwart the attempts to derive mechanical and hydraulic properties directly from measurements.

In REPOPERM phase 2 the question of the mechanical behaviour and the hydraulic properties of compacting crushed salt at low porosities (< 3 %) was therefore rephrased into the question: to what degree is it necessary to know these properties at all? The approach to answer this question consists of two parts:

– Provide a reliable set of parameters for the constitutive models in use for as low porosities as can be measured with reasonable accuracy.
    - Calibrate the model parameters against different compaction tests with dry crushed salt.
    - Provide a data base for compaction with wet material.
    - Calibrate the model parameters against compaction tests with wet crushed salt.
– Apply the constitutive models for the range of very low porosities, vary the parameters within reasonable boundaries and do a sensitivity analysis of the consequences for a brine intrusion scenario.

As this approach provides only a rough guideline several specific problems needed to be addressed calling for experimental as well as theoretical work and modelling. Experimentally, the following topics were investigated:

– Checking the validity of porosity values from earlier compaction tests,
– Permeability tests with brine and gas down to a porosity of about 2 %,
– Influence of the grain size distribution on the compaction behaviour of crushed salt,
– Anisotropy of the permeability in uni-directionally compacted crushed salt,
– Moisture- and temperature-dependent compaction behaviour,
– Microstructural analysis based on samples of compacted crushed salt, and
– Determination of CRs for unsaturated flow in the backfill at different levels of compaction.

This work is described in Chapter 2 of this report. The theoretical considerations – compiled in chapter 3 – were aimed at the

– Comparison of constitutive models for the simulation of compaction,
– Comparison and application of similarity relations to the CRs for unsaturated flow in compacting crushed salt, and
– Investigation of improved reproduction of compaction processes by discontinuum models.

The modelling part described in chapter 4 encompassed

– Relevant scenarios and boundary conditions and
– Orientating THM-modelling of crushed salt compaction including a first sensitivity analysis based on repository-relevant scenarios.

As in phase 1 of the REPOPERM-project all work was based on material as defined in /ROT 99/ with a maximum grain size of 8 mm [2].

A detailed description of all the work done in this project would have exceeded the size of a regular report. Therefore only the main results are compiled here. More detailed information to each section is provided in form of appendices on the enclosed CD where appropriate. The names of the text-files indicate the referenced section.

[2] informally called „DEBORA-material“

2 Experimental investigations

2.1 Examining the porosity in relevant, past experiments

Section 4 of the REPOPERM Phase 1 report /KRÖ 09/ revealed that a more precise determination of the void ratio e and/or porosity Φ according to equations (2.1) and (2.2) are necessary before conclusions and comparisons can be made of the barrier effectiveness of crushed salt in the residual porosity range. The accessible pore volume can be determined by pycnometer tests, but this can only be undertaken on small samples or parts of samples because of the limited space available in the apparatus. Porosities of laboratory samples with larger dimensions are therefore determined from the assumed solid density of the sample material (= rock salt density, e.g. ρ_S = 2.17 g/cm³) as a target parameter with the calculated value e = Φ = 0.

$$e = \frac{V - V_S}{V_S} = \frac{V_P}{V_S} = \frac{\rho_S}{\rho_{Sgr}} - 1 \qquad (2.1)$$

and/or

$$\Phi = \frac{V - V_S}{V} = \frac{V_P}{V} = 1 - \frac{\rho_{Sgr}}{\rho_S} \qquad (2.2)$$

where

$$\rho_{Sgr} = \frac{m}{V} \qquad (2.3)$$

and

V_0 = initial volume of sample,
V = actual volume of sample,
V_S = volume of sample after complete compaction (rock salt),
m = crushed salt mass (weight)
ρ_S = rock salt density
ρ_{Sgr} = density of crushed salt

with the conversion:

$$\Phi = \frac{e}{1+e}, \qquad e = \frac{\Phi}{1-\Phi} \tag{2.4}$$

The defined target density can vary depending on the properties of the material, with the exception of the permeability to be verified (/KRÖ 09/, Section 4.1). The quantitative effects were described in detail in this report using oedometer test 099 as an example. This means that the results of earlier laboratory tests need to be examined accordingly to verify their accuracy when the porosities were in the range of < 10 %. The size of the defined “backfill resistance” (see /KRÖ 09/, Section 4.2, Eq. 4.4 and Fig. 2.2) according to equation (2.5) remains unchanged:

$$\sigma_1 = \frac{F_1 - F_2}{A} \tag{2.5}$$

where

F_1 = main cylinder force (max. 3000 kN),

F_2 = measured frictional force between the specimen/pressure plate and oedometer ring,

A = sample cross-section (sample: 706.86 cm²).

The following solid densities were used for the dry (index tr) and/or (assumed) laboratory-moist (index f) condition of z2HS crushed salt material from the Asse salt mine in earlier investigations:

ρ_S^{tr} = 2.1600 g/cm³ ρ_S^{tr} ρ_S^{f} = 2.1708 g/cm³ (2.6)

The solid densities are replaced by the following on the basis of the values determined after /KRÖ 09/, Section 4.4.2, Table 4.1, and the actual moisture contents of less than 0.1 % measured by BGR on the used sample material:

ρ_S^{tr} = 2.1784 g/cm³ ρ_S^{f} = 2.1803 g/cm³ (2.7)

The following values are valid for the “table salt” z2HSSP facies used from the Asse underground workings:

ρ_S^{tr} = 2.1680 g/cm³ ρ_S^{f} = 2.1700 g/cm³ (2.8)

The conversion of the void ratio is undertaken using the formula:

$$e_2 = \frac{\rho_{S2}}{\rho_{S1}}(e_1 + 1) - 1 \qquad (2.9)$$

The effect on the void ratio of the oedometer tests used are in the range $\Delta e \approx 0.0045 - 0.0065$, and therefore lie within the material-related spread, in just the same way as the solid density. No special documentation of the older tests has been undertaken here. The changes will be taken into consideration accordingly when this data is used again.

2.2 Influence of the sieve line on compaction behaviour

As revealed by a compaction test undertaken as part of REPOPERM phase 1, the backfill resistance of material specified in Appendix G at 150 °C behaves in a similar way to the backfill resistance of reference material for drift backfilling, even though the latter has a much larger highest grain size (d = 31.5 mm) than the DEBORA material. The compaction test with designation Oedo-103 with z2HS2 material was repeated at a temperature of 50 °C to confirm the conclusion that this similarity would also apply to the temperatures typical for drift backfilling. For comparison purposes, oedometer test 049 from 1994 with the same z2HS2 material at T = 50 °C but with d_{max} = 31.5 mm was incorporated in the evaluation. The void ratio for this purpose was recalculated with the target density according to eq. (2.6) and eq. (2.8).

The test was carried out using BGR's well-known displacement controlled compaction configuration. Fig. 2.1 shows the change in time of the "backfill resistance" as a result of the applied compaction speeds and the void ratios achieved as a result. Fig. 2.2 shows the significant backfill resistance results of the various compaction speeds, and the interpolated values of test Oedo-103 as a function of the void ratio. Analogous to Fig. 4.13 in /KRÖ 09/, the results of the Oedo-049 test with the "reference backfill material" (drift backfill material, max d = 31.5 mm) are entered as dotted lines for the compaction speeds $\dot{\varepsilon} = 6.9 \cdot 10^{-7}$ and $6.9 \cdot 10^{-10}$ 1/s. The results of both tests are almost identical in the lower range of the backfill resistance.

The plots diverge slightly from approx. 15-20 MPa. The compaction rate $\dot{\varepsilon} = 6.9 \cdot 10^{-10}$ 1/s interesting for the in-situ behaviour, generates the backfill resistance of 26 MPa for the void ratio e = 0.10 in test Oedo-103, whilst the value in test Oedo-049 was 24.5 MPa. At values of around 35 and 33.5 MPa, the difference between the values is of a similar size at $\dot{\varepsilon} = 6.9 \cdot 10^{-7}$ 1/s. The result from project REPOPERM I was therefore also confirmed at T = 50 °C with respect to the comparison between borehole/drift backfill material with different grain sizes. The influence of the temperature remains significant. The backfill resistance level is much higher at T = 50 °C than at 150 °C. Analogous to the aforementioned values at e = 0.10, backfill resistances of only 9.5 and 16.5 MPa are reached in the Oedo-099 test (/KRÖ 09/, Fig. 4.13) at compaction rates of $\dot{\varepsilon} = 6.9 \cdot 10^{-10}$ and $6.9 \cdot 10^{-7}$ 1/s respectively.

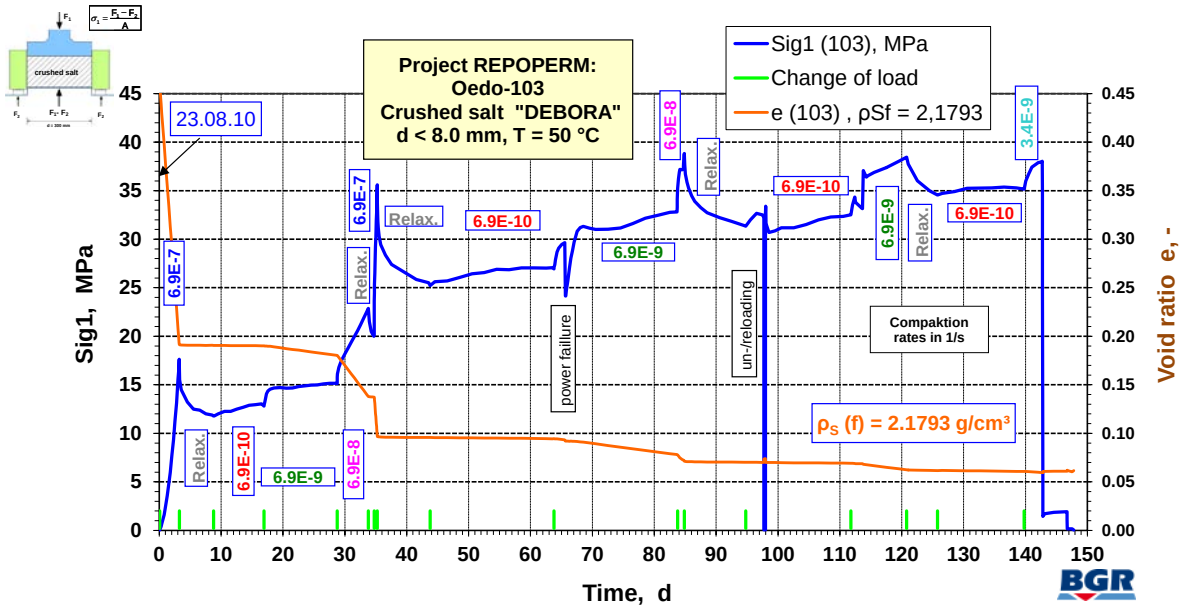

Fig. 2.1 Oedometer test 103: backfill resistance and void ratio

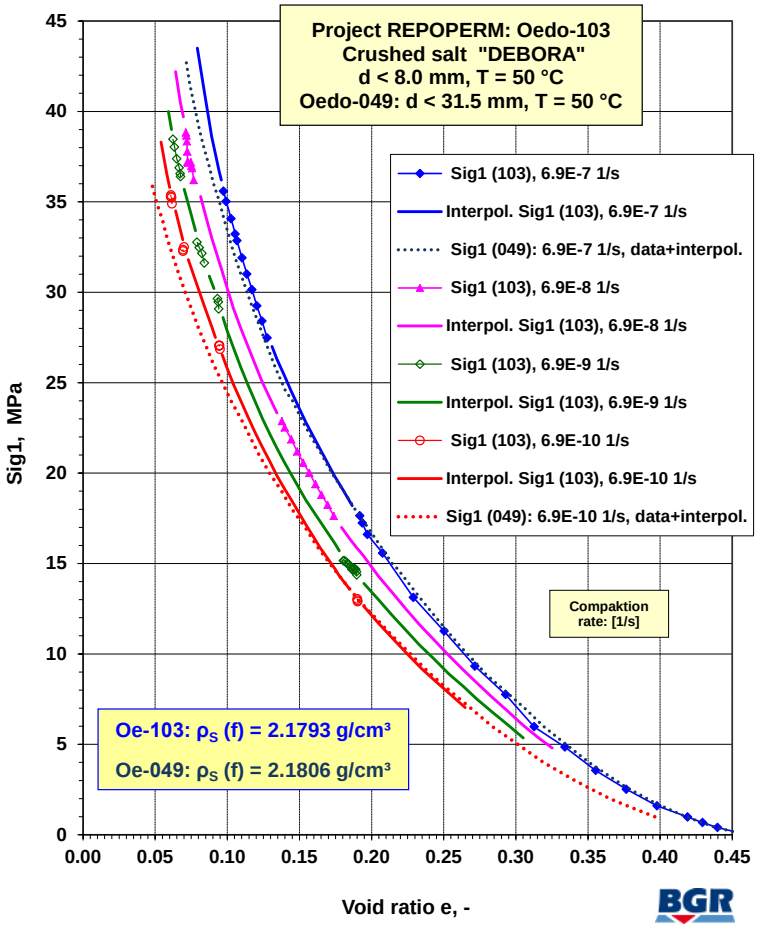

Fig. 2.2 Oedometer test 103: backfill resistance and interpolated values as a function of the void ratio with comparative values from Oedo-049

2.3 Triaxial compaction test with dry material at low porosities

The TK-031 triaxial compaction test was carried out with the aim of finding a more accurate quantitative determination of the stress state of the qualitatively identified compaction behaviour of laboratory-dry crushed salt revealed in the oedometer tests. The area of particular interest is the residual porosity range where compaction stress (formation pressure) is not expected to rise any further in situ, with the result that creep compaction dominates in the test specimen. The detailed course of the test (see Appendix C) documented in a separate report can also be used as the basis for verifying the numerical calculation models.

The uniaxially pre-compacted specimen with the dimensions d/h = 100/196.5 mm consisting of z2SP crushed salt of sieve line “DEBORA” (d ≤ 8.0 mm), was compacted under triaxial loads from e_0 = 0.1973 (Φ = 16.48 %) to e_E = 0.0840 (Φ = 7.76 %). In addition to the initial and final state in an unloaded condition, the measurement with a burette apparatus of the amount of air displaced by the compaction is a crucial metric for calculating the compaction.

Fig. 2.3 shows the volumetric strain ε_v, from the volume measurement as a function of time, the strain ε_1 derived from the axial deformation, and the radial strain ε_3 on the primary axis calculated from the previous values.

With respect to the secondary axis, the derivations of these parameters at specific times are shown as strain rates $\dot{\varepsilon}_v$. Pore ratios are shown which were calculated before the start of a new loading stage, as well as at some additional points during the test. For technical reasons, the test was unfortunately interrupted three times with short periods of depressurisation and reloading, which made the evaluation more difficult.

Five different, quasi-hydrostatic loading stages, σ_m = 10.3; 12.3; 15.3; 18.4 and 20.4 MPa, were run for a duration of 7, 19, 26, 27 and 202 days respectively. The loads and/or load increase rates were between 3 MPa/d and 1 MPa/d respectively. The transition to the next (higher) load stage was undertaken when the clear influence on the calculated compaction rate from the previous loading phase had obviously diminished. The values $\dot{\varepsilon}_v = 4.9 \cdot 10^{-9}$ and $2.1 \cdot 10^{-9}$ 1/s registered here are considered to be characteristic for the actual stress and compaction state. The last stage with σ_m = 20.4 MPa was car-

ried out as a long-term test on creep compaction. It not only provides the material parameters in the residual porosity range ($2.1 \cdot 10^{-9} > \dot{\varepsilon}_v > 1.5 \cdot 10^{-9}$ 1/s), but also forms the basis for a (manual) extrapolation of the volumetric strain rates over the whole test period, when this is shown as a function of the void ratio. Fig. 2.4 shows the results.

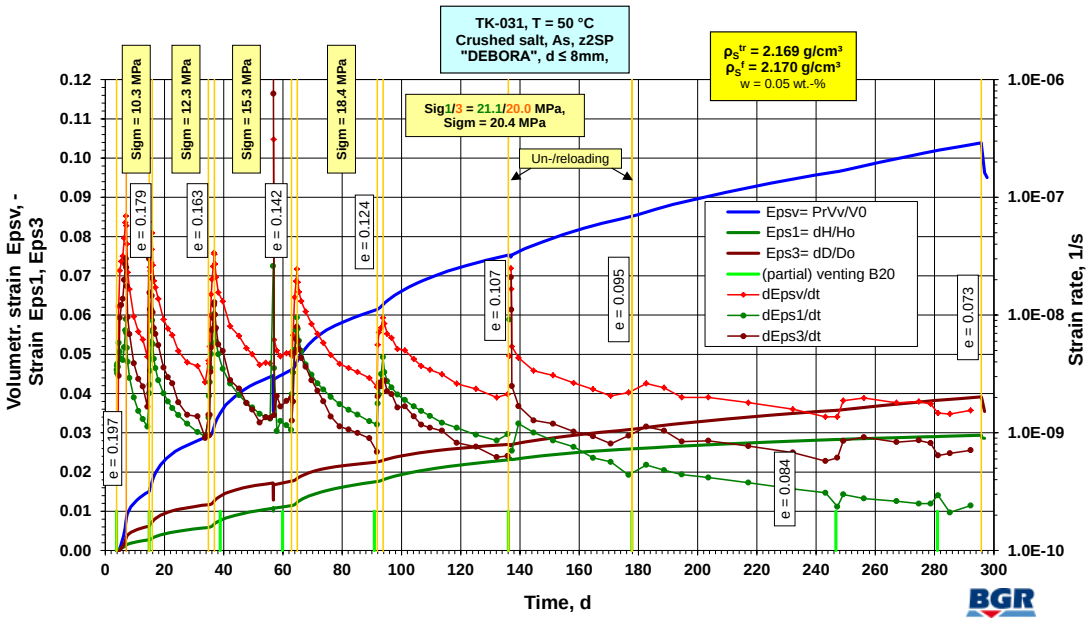

Fig. 2.3 Strain and strain rates of the triaxial compaction test TK-031

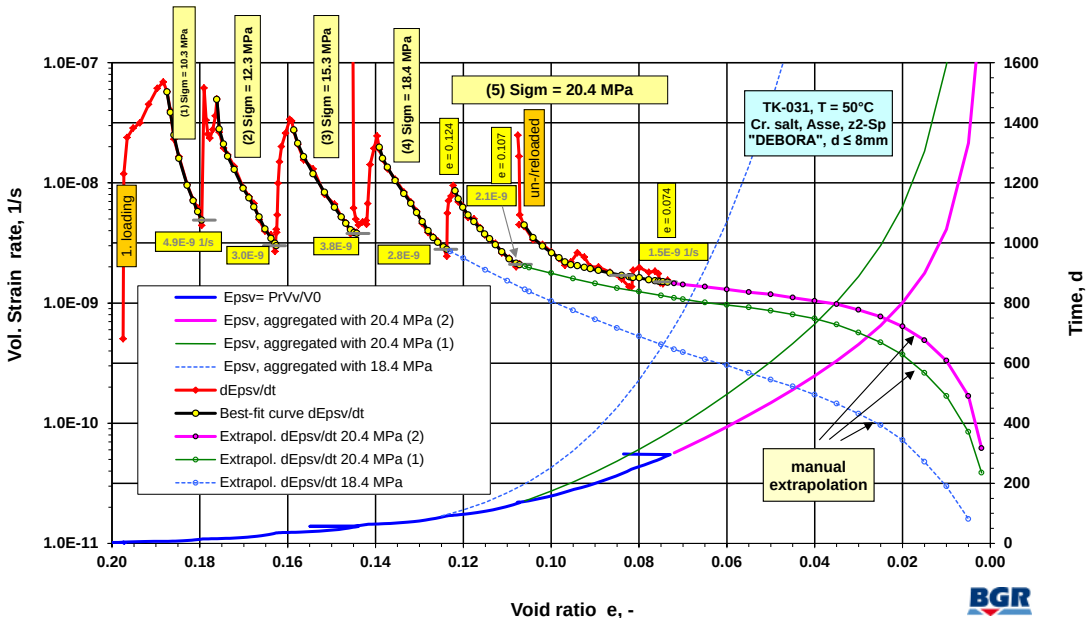

Fig. 2.4 Strain rates, extrapolations and void ratios of test TK-031

The results of oedometer test 049 (z2HS, d ≤ 31.5 mm) from 1994 were used as a comparative value in the stress-void ratio diagram. The “backfill resistance” values then de-

termined according to eq. (2.5), are converted to a ratio of axial to radial stress on the mean stress σ_m using the empirically determined calculation ansatz according to /BEH 99/ (Fig. 2.5, “FZK”). The compaction rates determined for the creep compaction phases 1 to 4 in test TK-031 lie in the σ-e diagram with a growing trend above the corresponding comparative value from the oedometer test, i.e. more unfavourable in the sense of the fastest possible compaction rates. Values for the more than 200 day 5th loading stage lying on the horizontal line σ_m = 20.4 MPa, are also more unfavourable initially, but do not demonstrate the marked slowing down in compaction rate with increasing compaction as extrapolated from the displacement controlled oedometer tests. The compaction rate in test TK-031 within the relevant void ratio range of 0.095 to 0.074 at $\dot{\varepsilon}_v$ = 2.1·10^{-9} to 1.5·10^{-9} s^{-1} has dropped by less than 15 % of an order of magnitude. The converted oedometer results in this range vary by 3 orders of magnitude from $\dot{\varepsilon}_v$ ≈ 1·10^{-8} to 1·10^{-11} s^{-1}. This does not therefore confirm the significant decline in compaction rates extrapolated in general from oedometer test results in the residual porosity range at low temperatures under no longer intensifiable formation pressure levels.

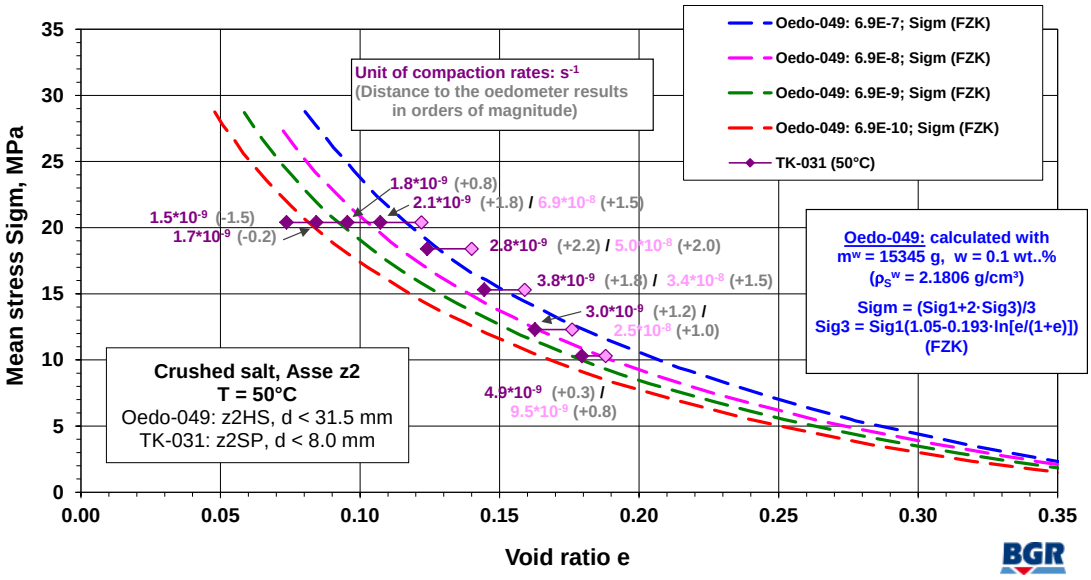

Fig. 2.5 Comparison of the results of TK-031 with Oedo-049

Because of the two counteractive trends of the differences between the triaxial and oedometric test results, and their spread of up to 3 orders of magnitude, measuring inaccuracies and simple spreading of the results are likely to be the primary cause. It would be prudent to check the validity of the estimate of the oedometer results according to /BEH 99/.

A comparison of the results of triaxial and oedometric compaction assumes that clear material behaviour exists at every compaction state, in other words, that the combination of “displacement controlled loading – backfill resistance” and “stress controlled loading – compaction rate” produce the same results. However, despite the relatively large dimensions of the samples, it is not possible to exclude the possibility that different compaction mechanisms dominate in the different tests because of the differences in geometry, the boundary conditions, and the possible anisotropic material behaviour of crushed salt (grain shape and position of non-round grains). It is feasible that horizontal grain relocation caused by confining pressure under triaxial loading requires a smaller amount of energy than the vertical compaction required in the laterally restricted oedometer cell. This aspect cannot be clarified within the framework of this test.

With the help of the analysis of the way the trends change, a qualitative basis has been created for the original objective of quantifying the results of the less complicated oedometer tests with the results of the triaxial compaction tests.

To estimate the material behaviour beyond the change in compaction occurring during the course of the experiment, the compaction rate trend derived from the loading phase with σ_m = 20.4 MPa for a period of 200 days, was extrapolated as a function of the void ratio (Fig. 2.4). The entered equalisation curve was extended in line with the trend until the progressive asymptotic decline in the compaction rate expected with increasing compaction reaches e = 0. The compaction increments calculated and added together for small time intervals produce a plausible compaction curve trend which reaches a void ratio of e = 0.02 after 2.2 years (Fig. 2.4: approx. 800 d). This takes 3 years for a slightly less favourable version under the same load. The curve for the extrapolation oriented to a constant load of σ_m = 18.4 MPa takes 11 years to reach a void ratio of e = 0.02.

These estimates can be used in numerical calculations as a preliminary basis for determining the creep compaction rates expected in situ in a developing barrier consisting of crushed salt. However, because of the current uncertainties in the extrapolation, tests under relevant in situ conditions in the residual porosity range are still required to confirm that a barrier effect is achieved in this compaction range. These tests need to be carried out despite the expected large amount of time involved.

2.4 Influence of humidity on compaction

2.4.1 Strain-rate controlled oedometer tests

The compaction process involving crushed salt backfill material in situ can be accelerated by moisture. Laboratory experiments looking at this were already carried out by BGR in the 1990s at room temperature conditions (T = 30 – 33 °C) (/KRÖ 09/, Section 2.4.5). To quantify the influence of levels of moisture on the material behaviour in the ultimately critical residual porosity range, tests are necessary on crushed salt with different amounts of added brine. For this purpose, two displacement controlled oedometer tests according to the BGR standard programme were carried out with crushed salt material z2SP of the DEBORA sieve line (borehole backfill material, d_{max} = 8.0 mm), and the addition of brine ranging between 1.0 and 0.6 wt.-%. The solid density was calculated with the relevant moisture levels according to equation (8). The material moisture between 0.02 % and 0.09 % already present in the laboratory-dry condition, was ignored because of the small amount, the determination inaccuracy, and the imprecise distribution throughout the whole mass of the sample.

Although the oedometer cell is equipped with sealing rings, brine is squeezed out at rising pressures via the annulus crack between the cell wall and the pressure plates, where it primarily enters the channels for the flow tests. For technical reasons, it is only possible to roughly estimate the quantities involved. However, the expulsion of brine in the tests begins much earlier than the time when the continuously reducing (calculated) pore volume of the sample drops below the volume of the added brine. This important finding must be taken into consideration when defining a recipe for the backfill material.

Oedometer test 105: crushed salt + 1.0 % brine, T = 33 °C

The crushed salt mass of test Oedo-105 weighing 15 034.6 g, was sprayed with 1.0 wt.% brine (163.8 g = 136.5 cm³), and stored in the compaction cell with an initial void ratio of e_0 = 0, = 0.539 (Φ = 35.0 %), and compacted for 280 days until the void ratio reached e_E = 0.0197 (Φ = 1.93 %). Fig. 2.6 shows the change in time of the backfill resistance according to eq. (2.5), and the void ratio according to eq. (2.1) at the different compaction rates applied, and other significant events. The sample had already entered the residual porosity range by around the 30th test day. The expulsion of brine was ob-

served on the lower side of the sample (O-ring and outflow pipe of the flow apparatus) on the 100th test day with a void ratio of around 0.05.

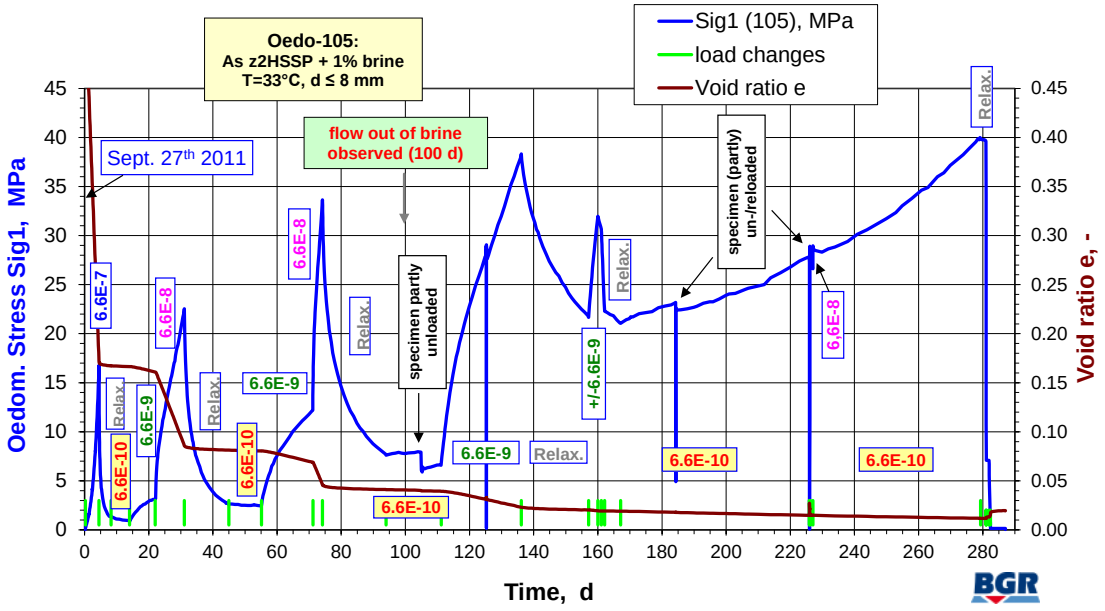

Fig. 2.6 Oedometer test 105, change in backfill resistance and void ratio over time

Fig. 2.7 shows the calculated backfill resistance for the whole oedometer test 105 (aquamarine), and the characteristic curves for the four different compaction rates derived by interpolation and extrapolation: $\dot{\varepsilon} = 6.6 \cdot 10^{-7}$ to $6.6 \cdot 10^{-10}$ 1/s in blue, magenta, green and red. They show the dominant dependence of the backfill resistance on the compaction rate of the crushed salt wetted with brine, which is important for extrapolating laboratory results to in-situ conditions.

Selected test values for the critical smallest speed $\dot{\varepsilon} = 6.6 \cdot 10^{-10}$ 1/s are shown as yellow dots with a red ring. The trend of this curve is crucial for assessing the material behaviour and/or a recipe in the residual porosity range. The maximum formation pressure of around 20 MPa expected in situ is achieved with the backfill resistance of sample 105 at e = 0.02. For comparison, the (interpolation/extrapolation) curves of test Oedo-056 and Oedo-057 (z2HS) for $\dot{\varepsilon} = 6.5 \cdot 10^{-10}$ 1/s are shown from years 1995/96 with an added brine proportion of 1.2 and 0.6 % respectively: these are shown as dashed red curves. The (fictive) solid densities in the wet conditions are calculated using equation (7), Section 2.1. The backfill resistance of all 3 recipes remains below 2 MPa all the way down into the residual porosity range (e ≤ 0.10) under the smallest compaction speed. The

backfill resistance only differs from this point on because of the different moisture contents.

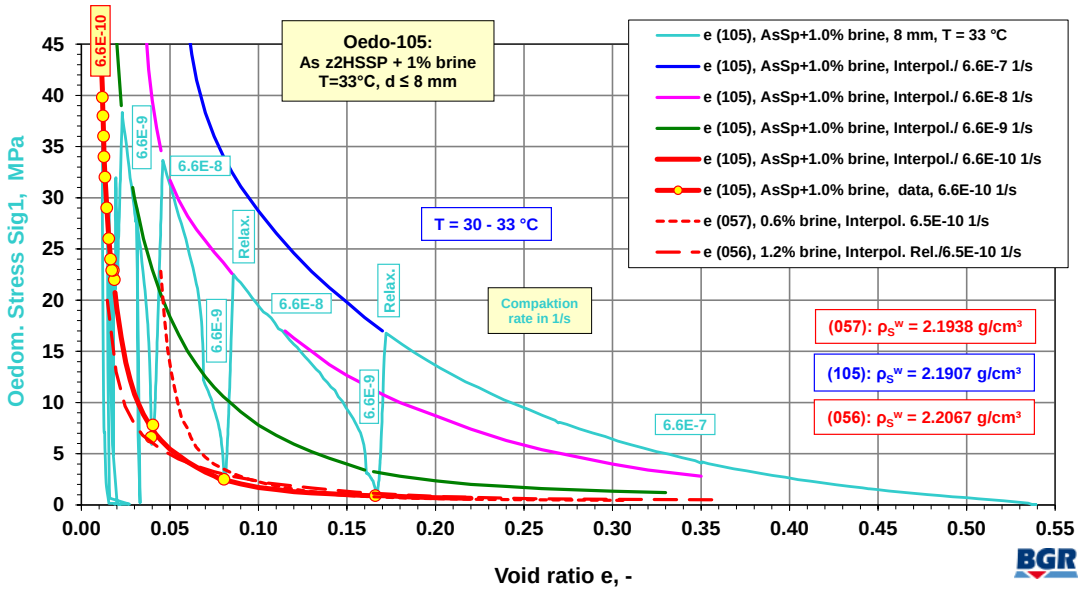

Fig. 2.7 Oedometer test 105, backfill resistance as a function of void ratio

No direct effect of the loss of brine on the compaction behaviour was identified. At time t = 100 d, the remaining pore volume in the crushed salt sample was calculated as more than 280 cm³. This is much larger than the volume of the added brine of 136.5 cm³. The sample was therefore not saturated. Fig. 2.8 shows the assumed ratios of solid, brine and pore volumes for selected void ratios in the stacked column diagram. The right-hand diagram shows a magnification of the residual porosity range. Without the expulsion of brine, the free pore volume is calculated to have been exhausted at e = 0.0188.

The volume and weight balance at the end of the test revealed that around 106 cm³, in other words 77 %, of the added brine, must have been squeezed out. It therefore makes sense to add less moisture when used under real conditions.

Note that because of the nature of the material, the expected accuracy of the void ratio calculation according to /KRÖ 09/, Section 4.9, is Δe = 0.01. In test Oedo-105, this corresponds to a volume of approx. 70 cm³.

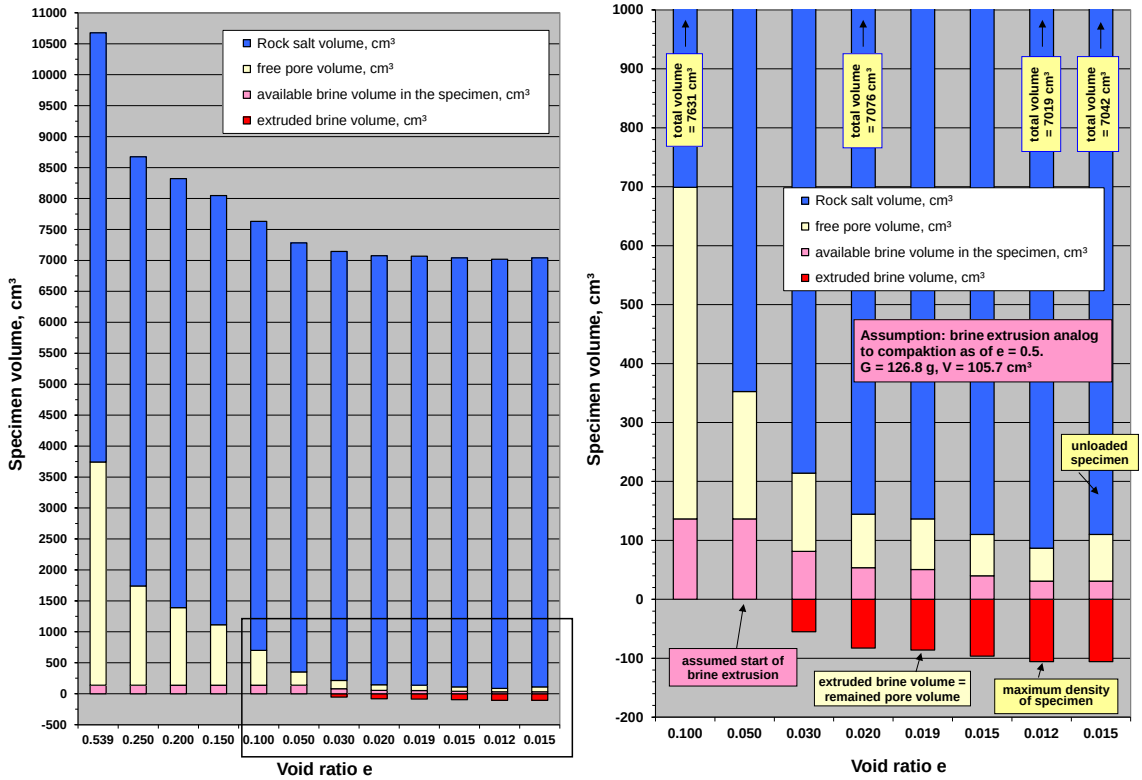

Oedo-105, crushed salt +1.0 wt.% saturated brine volume balance owing to compaction

Oedo-105, crushed salt +1,0 wt.% saturated brine volume balance owing to compaction

Fig. 2.8 Oedo-105: Volume balance in selected test stages

Oedometer test 106: crushed salt + 0.6 % brine, T = 50 °C

The Oedo-106 test was carried out using the same z2HSSP crushed salt material as test 105, but only with the addition of 0.6 wt.-% of brine in this case. The test temperature of 50 °C approximates that of real repository conditions. Minor deviations from the set value cannot be excluded because of evaporation or the inhomogeneous distribution of the brine when setting up the test. The minor natural moisture content of the crushed salt, which is one order of magnitude lower, is not taken separately into account in the calculation. This means that the solid density for the wet state is ρ_S^f = 2.169 * 1.006 = 2.182 g/cm³. The initial void ratio is e_0 = 0.5038 (porosity Φ = 33.5 %) when adding the space required by the brine to the pore volume.

Analogous to test 105, the sample was compacted using the displacement controlled method during 266 days to reach a void ratio of e = 0.0145. It was then subjected to 29 days of constant loading at the axial force of around 2710 kN reached at that point. Because of the declining frictional force, the backfill resistances of 33.3 to 33.6 MPa

were reached, causing the sample to compact further by Δe = 0.008 to e = 0.013 respectively. The compaction rate was in the $1 \cdot 10^{-10}$ - $2 \cdot 10^{-10}$ s^{-1} range.

A small amount of expelled and crystallised brine was observed in the upper inlet pipe at the end of the test. The expected outflow from the lower inlet pipe was prevented by the formation of plugs. As revealed when removing the sample, the whole area around the upper and lower perforated pressure plates, and the associated distribution channels, were coated with brine. This thus confirmed the finding from test Oedo-057 (1995) that even when only a small amount of brine is added amounting to 0.6 %, this is squeezed out at high levels of compaction. The configuration of the apparatus does not allow determination of the start of the squeezing out, nor the build-up of pore water pressure which probably takes place as a result.

Fig. 2.9 shows the results of the Oedo-106 test in a backfill resistance-void ratio diagram for the residual porosity range (e < 0.10, Φ < 9.1 %). The grey line shows the backfill resistance of the sample, whilst the curves coloured magenta, green and red are the characteristic curves derived from interpolation and/or extrapolation for the three different compaction speeds $\dot{\varepsilon}$ = $6.6 \cdot 10^{-8}$, $6.6 \cdot 10^{-9}$ and $6.6 \cdot 10^{-10}$ 1/s respectively. The significant influence of the compaction speed is confirmed again, and highlights the need to carry out laboratory tests on compaction rates relevant for in-situ conditions. The results of the smallest speeds in tests 105, 057 and 056 are shown for comparison.

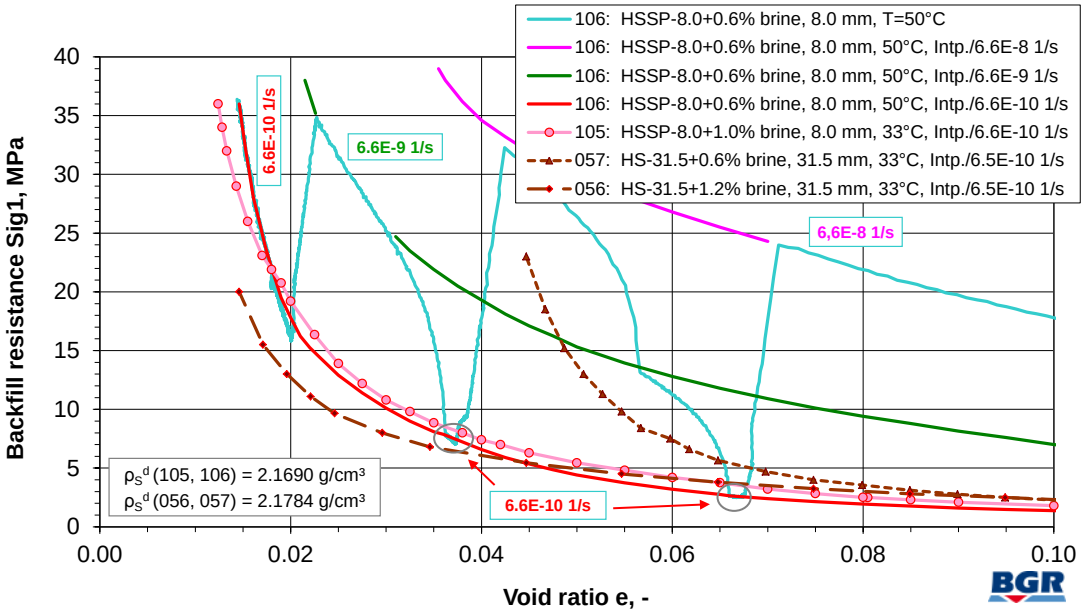

Fig. 2.9 Oedometer test 105: backfill resistance in the residual porosity range

The backfill resistance of sample Oedo-106 is similar to the adequate curve from sample 105 (z2HSSP, 1.0 % brine, T = 33 °C) with a slightly higher amount of added brine, but a lower temperature. The backfill resistance of the earlier Oedo-056 test with drift backfill material z2HS and 1.2 wt.-% brine at T = 31 °C is slightly lower. The oedometer stress at e > 0.02 in all 3 tests remains below the formation pressure stress of 20 MPa. In contrast, the backfill resistance of test Oedo-057 (z2HS) with only 0.6 wt.-% brine at T = 31 °C, is already much higher, even at around e = 0.05, than the values in the other tests. The difference between the curves with respect to the void ratio is around $\Delta e = 0.02 - 0.03$.

The database for the 4 tests shows plausible differences overall in the backfill resistance building up in the residual porosity range. Because of the squeezing out of the brine, testing is required to reveal whether crushed salt with even lower amounts of added brine also produces acceptable results. A test with 0.3 % added brine is currently being carried out.

Oedometer test 102: flow with moist air, T = 33 °C

When using brine to speed up the compaction of crushed salt, verification as part of the long-term analysis is required to determine whether the brine maintains its ascribed properties until the backfill achieves its barrier effect, and to determine the effect it has on other construction components in a multi-barrier system, e.g. on freshly excavated crushed salt backfill installed in the area. This need is highlighted by the findings on the influence of moisture on the creep behaviour of rock salt in a dilatant or unconsolidated state /SCH 07/, /SCH 14/. Oedometer test 102 therefore used the flow apparatus in the BGR oedometer cell, together with a vacuum pump, to allow moist air to flow through a crushed salt sample undergoing displacement controlled compaction. The air sucked through, which was moistened first in a special chamber with a water bath, had a humidity of around 85 %. The aim of the test was to identify the influence of moist air on the compaction behaviour of crushed salt, and to compare this with the material behaviour of dry and wet samples.

The laboratory-dry z2HS crushed salt with d_{max} = 31.5 mm (“drift backfill material”), and an average moisture content of less than 0.1 wt.-%, was placed in the oedometer cell with an initial void ratio of $e_0 = 0.452$ ($\Phi_0 = 31.1$ %, $\rho_S^f = 2.1803$ g/cm³ according to

eq. (2.7). A sinter plate was placed on both sides of the oedometer sample to achieve an optimal distribution of the air across the whole cross-section of the sample. Fig. 2.10 shows the backfill resistance as a function of void ratio for the whole time period of the test, together with interpolated and extrapolated curves. The dotted lines show the results of oedometer sample 097 with the same lab-dry material and the same temperature.

The laboratory-dry crushed salt sample was compacted over a period of 19 days with a compaction speed of $\dot{\varepsilon} = 6.9 \cdot 10^{-7}$ and $6.9 \cdot 10^{-10}$ 1/s, and an intermediate relaxation phase, until it reached a void ratio of e = 0.21 (Φ = 17.4 %). The vacuum pump was switched on at the same time as maintaining the low compaction rates, and moistened air was continually sucked through the sample. The backfill resistance of 10 MPa reached at that point immediately began to drop after moist air began to flow through the sample. It continued to fall over a period of 12 days to reach only 5 MPa. Because of time constraints, the test was then run at different speeds according to the BGR procedure before the sample was depressurised and removed after 164 days at e = 0.045 (Φ = 4.3 %).

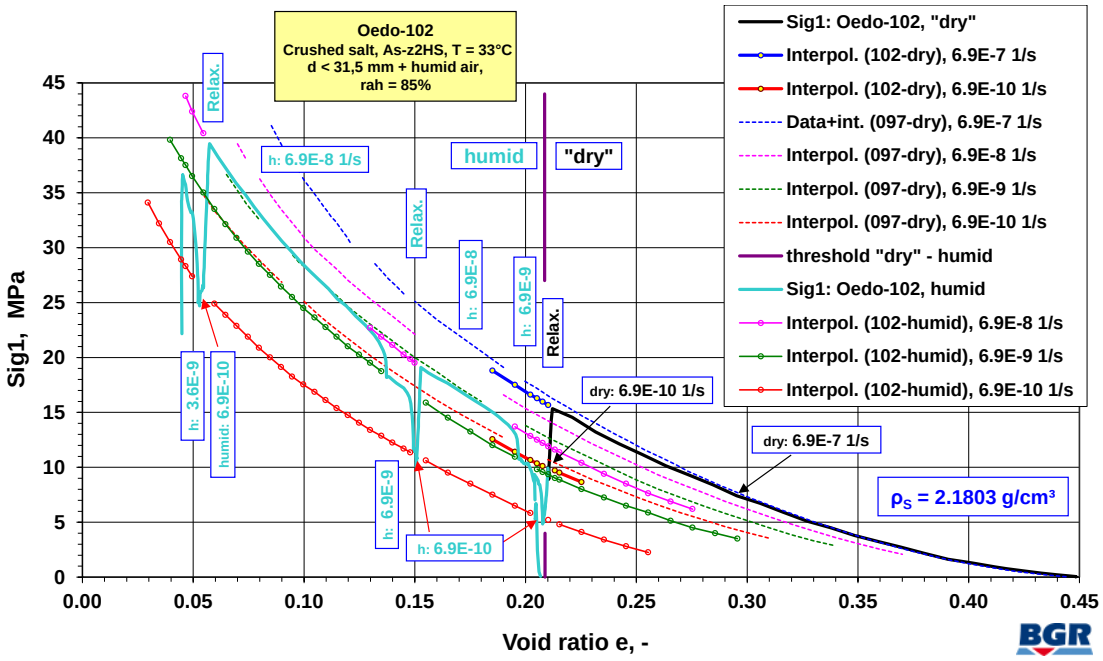

Fig. 2.10 Oedometer test 102, backfill resistance as a function of the void ratio

The backfill resistance of sample 102 in a laboratory-dry condition is slightly less than the value of test 097. To aid orientation, Fig. 2.10 for Oedo-102 includes the interpolated curve sections $\dot{\varepsilon} = 6.9 \cdot 10^{-7}$ and $6.9 \cdot 10^{-10}$ 1/s in the $0.225 < e < 0.185$ range.

The backfill resistance is much lower when moist air is added, but still follows the same course as the results of test 097. The backfill resistance curves developing under compaction rates $\dot{\varepsilon} = 6.9 \cdot 10^{-9}$ and $6.9 \cdot 10^{-8}$ 1/s are already exceeded by the laboratory-dry material at $\dot{\varepsilon} = 6.9 \cdot 10^{-10}$ and $6.9 \cdot 10^{-9}$ 1/s (difference ≈ 1 order of magnitude). The values determined in the wet state are even lower at $\dot{\varepsilon} = 6.9 \cdot 10^{-10}$ 1/s. For instance, at e = 0.10 (Φ = 9.1 %) the laboratory-dry crushed salt can expect to have a backfill resistance of approx. 25 MPa, the values under the moist through-flow conditions are only 17.5 MPa. Nevertheless, these results are still much higher than the results for crushed salt with added brine. The backfill resistance here in the e = 0.10 range in all of the tests is smaller than 3 MPa (cf. Fig. 2.7 and Fig. 2.9).

The mass balance after removing the sample with the still adhering sinter plates was 20.4 g heavier compared to the weight at installation. If one assumes that this is all attributable to the entry of moisture into the originally laboratory-dry amount of crushed salt weighing 15,345 g, this corresponds to an additional moisture content of 0.13 wt.-%. For technical reasons, the air flow could only be measured approximately: it was between 30 and 14 l/h. At 14 l/h, the permeability is around $5 \cdot 10^{-15}$ m² according to Darcy's Law and taking into consideration the geometrical and hydraulic parameters.

2.4.2 Stress-controlled uniaxial long-term compaction

2.4.2.1 Test principle

The experiment comprised three oedometer compaction tests with crushed salt that were intended to be identical except for the initial moisture content *w* of the material. The adopted moisture contents for the experiment were 0 % (assumed for the state after heating over 24 hours at 105 °C), 0.1 weight percent (moisture content at delivery) and 1 % by artificial wetting.

In principle, all three tests followed the same procedure:

– installation by hand to an initial porosity of about 30 %

– measurement of the initial gas permeability[3]
– step-wise mechanical loading
    • spontaneous increase of mechanical load
    • observing the axial deformation at constant load
    • measurement of gas permeability at the end of each load step[1]
– step-wise temperature changes where applicable[4]
    • increase or decrease of temperature at constant load
– flooding with brine where applicable[5]
    • monitoring response in terms of deformation
– gas testing
    • measurement of gas breakthrough pressure of the flooded samples
– dismantling and measuring of the end porosity

2.4.2.2 Test equipment and test set-up

Titanium test cells were developed that allowed for a permanent data acquisition during compaction including load, temperature and displacement as well as for permeability measurements during the test. The hook-ups for the permeability measurements allowed also for a later flooding of the samples.

Each cell was then installed in a test chamber that could be heated from inside. The three chambers were then in turn installed in two frames of a universal testing machine providing the controlled mechanical load.

Each frame could take only two chambers at the time but a second frame was available for the third chamber. As a result, two samples experienced the same loading history while the third one could be mechanically loaded independently. Anticipating less differences in the compaction behaviour of the dryer samples, these samples were installed in the same frame Sample preparations

---

[3] only for the oven-dry sample

[4] not performed for the sample with 1 % initial moisture content

[5] not performed for the sample with 1 % initial moisture content as it was already at an advanced state of compaction

Crushed salt “table salt” z2HSSP facies from the Asse mine was used for the tests. The grain size distribution of the material was set to the specifications given in Appendix G.

Preparation of the specimen was slightly different for each sample:

– sample 1
  - heating at 105 °C for 24 hours before installation
– sample 2
  - no special preparation
– sample 3
  - heating at 105 °C for 24 hours before installation
  - saturating water with salt from the sample material
  - adding red dye to the brine for later microstructural investigations[6]
  - adding brine equivalent to 1 weight percent to the sample by spraying

The crushed salt material was poured into the respective test cell in three layers. Each layer was compacted by hand. Some characteristic data of the samples are compiled in Tab. 2.1. Then the sinter plates as well as the load piston were inserted in the cell. Finally sample 1 was flushed with nitrogen until relative humidity in the outflow became constant.

Tab. 2.1 Initial geometry and mass of the samples

Sample	Initial moisture content [%]	Diameter [mm]	Length [mm]	Mass [kg]
1	0	120	113	1,95770
2	0.1	120	107	1,8173
3	1.0	120	104	1,80215

2.4.2.3 Execution

Each of the three samples had its individual loading history due to different mechanical and thermal loads. The events are listed in tabular form in Appendix E and visualised in Fig. 2.11 and Fig. 2.12.

[6] During the project it was decided that letting the compaction test run as long as possible had priority over post-test microstructural investigations which were thus dropped

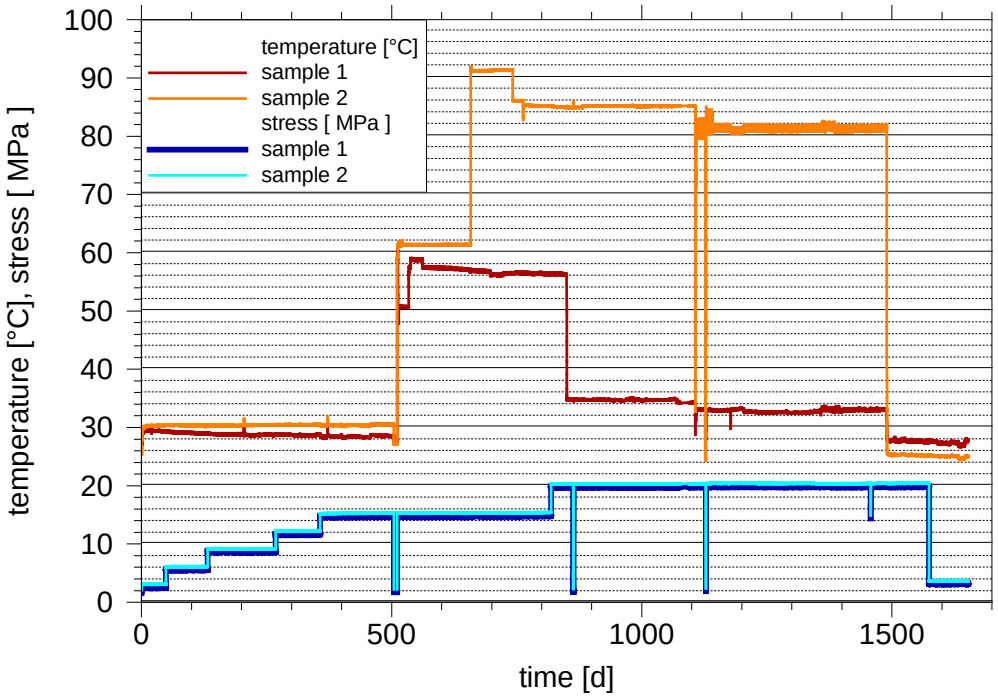

Fig. 2.11 Mechanical and thermal loading for samples 1 and 2

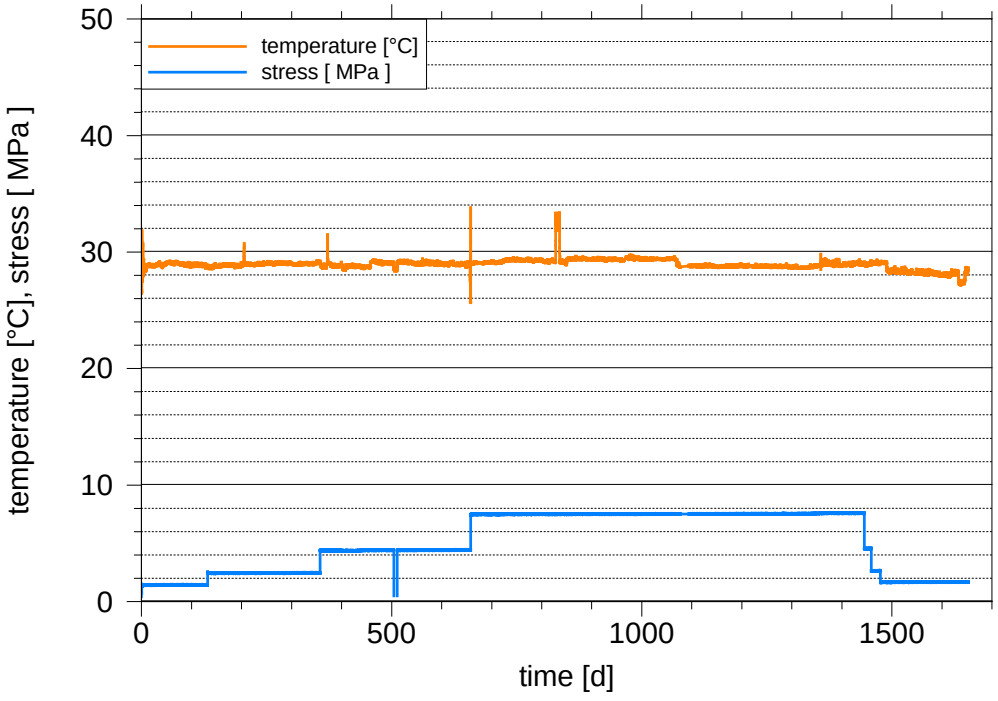

Fig. 2.12 Mechanical and thermal loading for sample 3

Heating of samples 1 and 2 commenced during the load step of 13 MPa. A failure of heating in cell 1 was repaired provisionally lowering the upper temperature limit to about

60 °C. At a stress level of 18 MPa this provisional heating was switched-off again. Approaching the end of the test heating was also stopped in cell 2. The two heated samples were flooded with brine when the compaction rate had become very small during the final load step of 18 MPa.

Data were initially recorded once a minute. Because of the excessive amount of accumulated data it was later thinned out on a heuristic basis. Taking and processing samples of the extracted brine are described in detail in Appendix D. At the end of the test it was tried to determine the gas breakthrough pressure of the fully saturated samples.

2.4.2.4 Post-test investigation

Dissolution by brine injection

Flooding of samples 1 and 2 had been prepared with considerable care to avoid solution or precipitation of solutes in the pore space of the samples. Brine was prepared from the same salt that had been used for the crushed salt samples themselves. And in case of the heated sample, the temperature of the injected brine had been raised to about the same heat level. However, to be on the safe side, samples of the injected brine as well as of the brine that was squeezed out later on were taken and analysed (see Appendix D). A comparison of the different brine samples showed, though, that the pore space was not seriously affected by the brine injection.

Terminal porosity

The porosity calculated from the displacement data for sample 3 had become negative in terms of figures during the final phase of the test. It was therefore suspected that the salt might have crept into the pores of the sinter plates at the bottom and at the top. As it turned out after dismantling, this had indeed happened to a certain extent. Between 10 and 25 g of salt were found to be lost to the sinter plates.

The transient porosity data derived from displacement measurements thus needed to be corrected. For this purpose the terminal porosity of the samples was determined. This was achieved straight forward by measuring the amount of salt that had crept into the sinter plates. From this follows the remaining mass of compacted crushed salt between

the sinter plates. By measuring the volume of the compacted sample, the bulk density was determined. After drying at 105 °C for 24 hours, the moisture content was obtained. Based on the measured data and the grain density, the terminal porosity was determined. Following this procedure it was found that the terminal porosity of all three samples was indeed positive, amounting to 1.11 %, 0.88 %, and 2.00 % for samples 1, 2, and 3, respectively.

2.4.2.5 Results

Creep compaction

Generally speaking, the strain rates reflect clearly changes in the loading by increasing very fast over several orders of magnitude. Some additional sample-specific features can also be observed

Sample 1

- The temperature increase to 60 °C causes a similar reaction in sample 1 as each stress increase.
- The creep accelerating effect of the load increase to 18 MPa is cancelled at 850 days by reducing the temperature from 60 °C to 34 °C.
- Flooding accelerated compaction in terms of the initial drop of porosity more than any other load change.
- The two events of thermal and mechanical unloading that occurred in quick succession at day 1107 and 1127 had very little influence on further compaction.

Sample 2

- The temperature increase to 60 °C causes a similar reaction as the next temperature increase to 90 °C as well as each mechanical load increment as shown in Fig. 2.14.
- While thermal and mechanical unloading at day 1107 and 1127 had very little influence on compaction of the oven-dry sample (cf. Fig. 2.13) the impact on sample 2, by contrast, was were rather dramatic as the strain rate decreased afterwards by about one order of magnitude. Interestingly, the strain rates after day 1127 were very similar in both cells despite the rather different prevailing temperature.

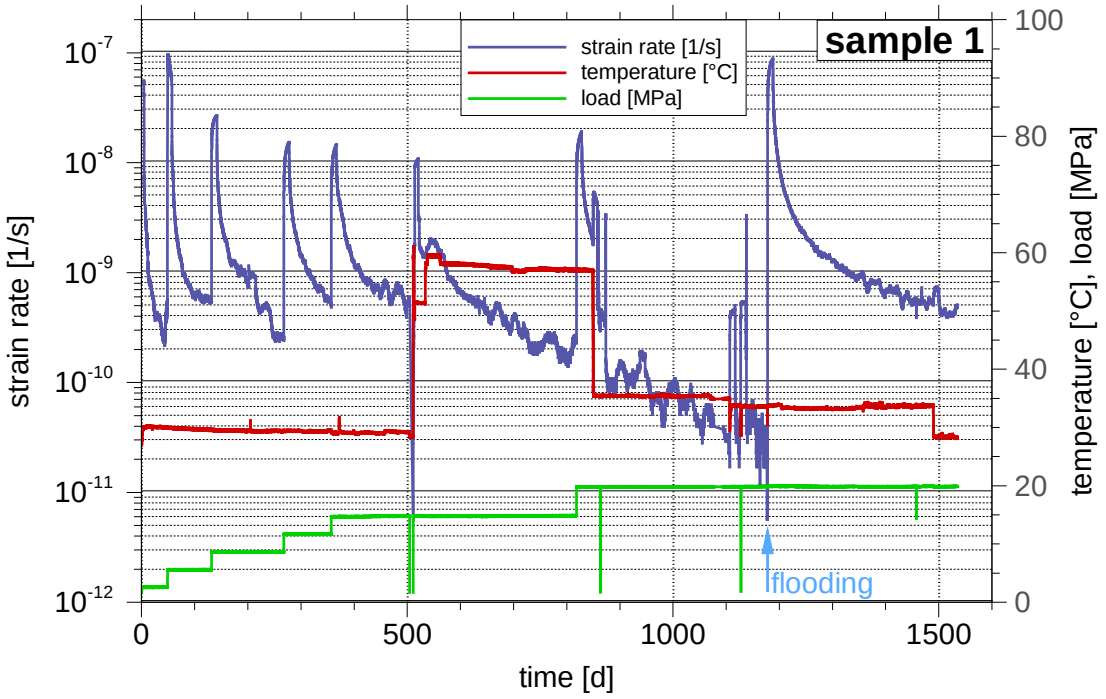

Fig. 2.13 Strain rates and loading for the oven-dry sample (sample 1)

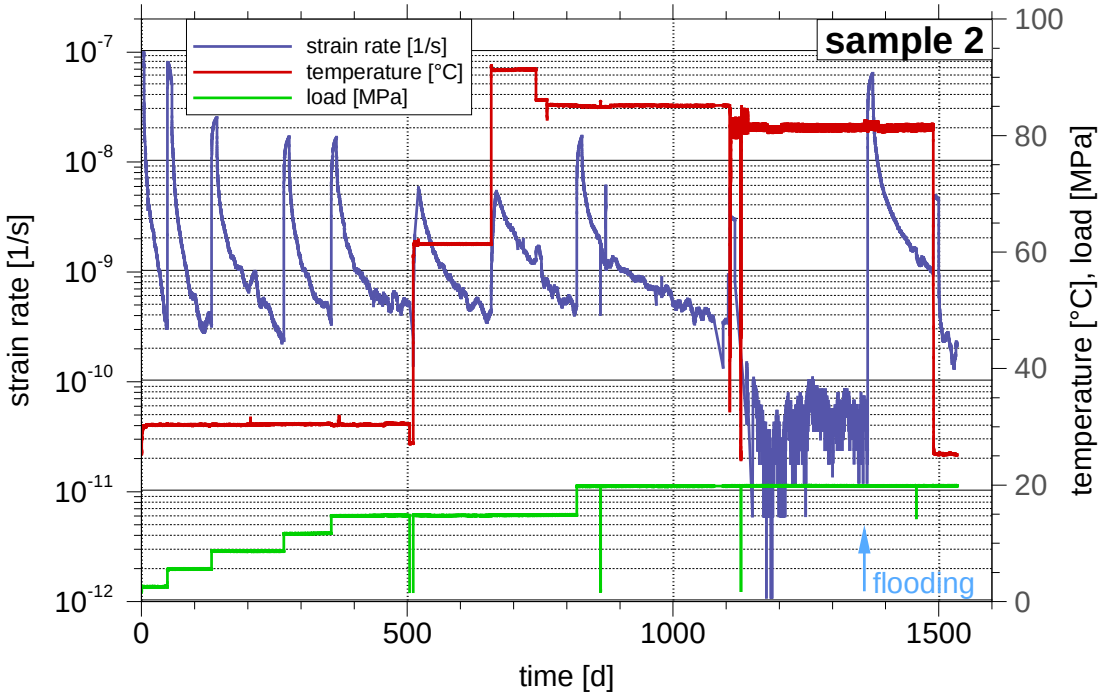

Fig. 2.14 Strain rates and loading for sample with initially 0.1 % brine (sample 2)

– Flooding accelerated compaction also in sample 2 more than any other load change.
– The temperature drop from 88 °C to 25 °C on day 1490 caused also a drop in the strain rate by almost an order of magnitude. Note that the temperature drop of about 10 °C in sample 1 (cf. Fig. 2.13) had by contrast no visible effect on the creep.

Sample 3

– The strain rate in the wetted sample depicted in Fig. 2.15 decreases during the first load step much slower than in the two dryer samples. This behaviour can also be observed further on.
– At the end of the experiment all samples had reached a porosity between 0.88 % and 2.0 % and were highly saturated with brine. The gradient of the strain rate indicating the further evolution of the respective porosity appears to be quite different, though. Sample 2 had experienced a serious temperature drop during the flooded phase and can thus hardly be compared with the other two tests. However, at about day 1420 when the porosity in sample 1 passed the value of 2 % (see dashed horizontal line in Fig. 2.17) the gradient of the strain rate was much higher than the gradient for sample 3 at the end of test.

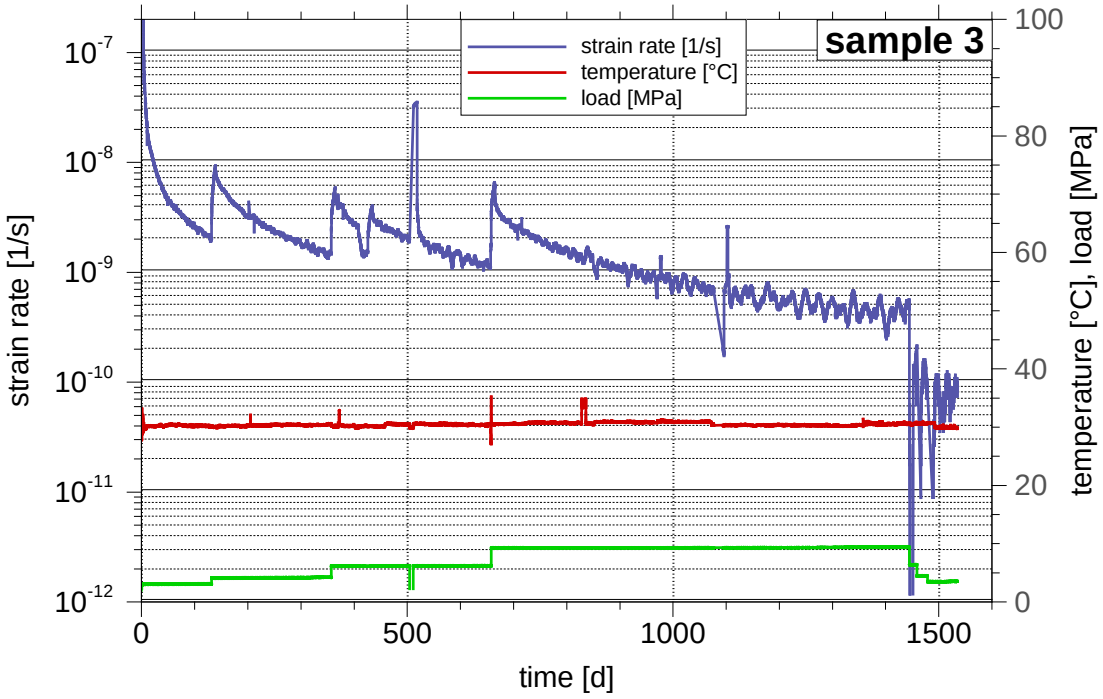

Fig. 2.15 Strain rates and loading for sample with initially 1.0 % brine (sample 3)

Porosity

Bounding curves

The exact course of the porosity evolution over time cannot be reconstructed. While it is clear that the process that leads to creep into the sinter plates is influenced by temperature and the mechanical load, it is presently not possible to quantify the referring dynamics. However, bounding curves for the true course can be found. The lower bound is given by the curve that was derived from the displacement measurements beginning with the correct initial porosity. This curve becomes increasingly too low because of the unaccounted mass loss to the sinter plates. The upper bound can thus be found by shifting the lower bounding curve upward until the correct terminal value is met. The resulting bandwidth between the bounding curves amounts to 1.11 %, 1.36 %, and 0.53 % for samples 1, 2, and 3, respectively, and is thereby satisfyingly small. The bounding curves for all three samples are compiled in Fig. 2.16. Bounding curves in the context of the loading history are depicted separately for each sample in Fig. 2.17 to Fig. 2.19.

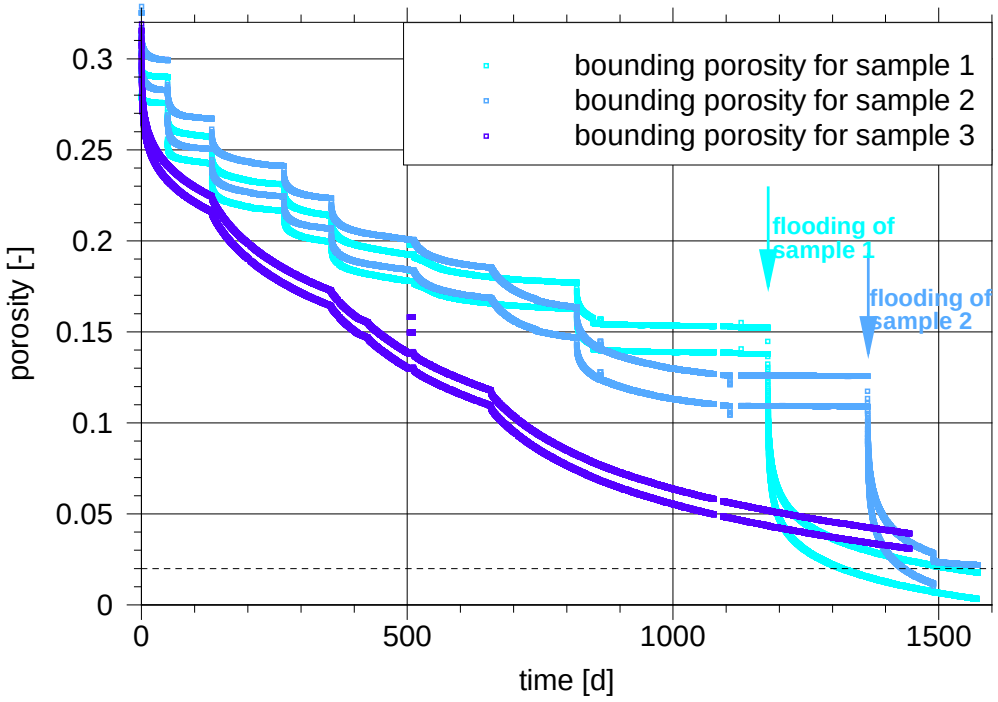

Fig. 2.16 Bounding data for the porosity evolution for all three samples

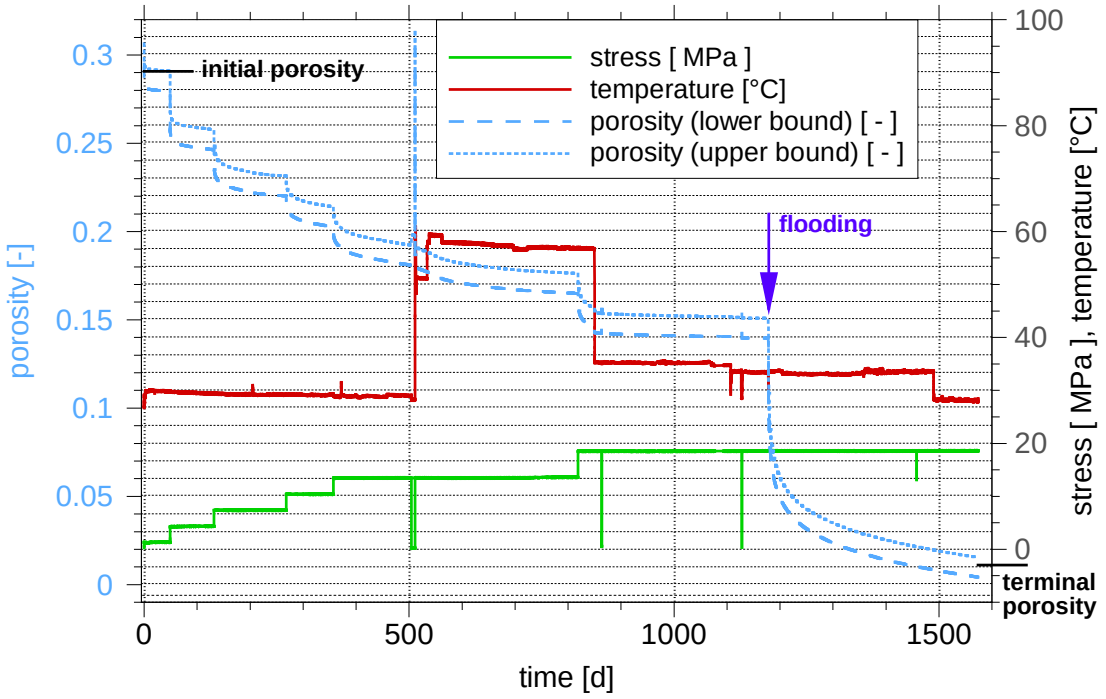

Fig. 2.17 Mechanical load, temperature and bounding porosity of the oven-dry sample

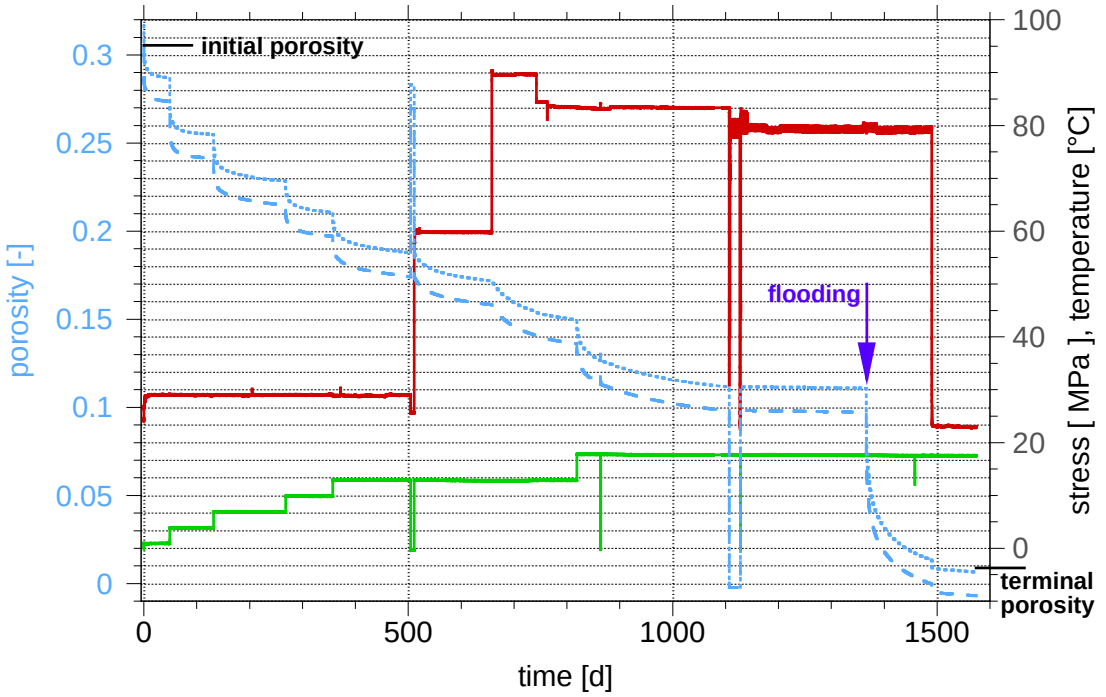

Fig. 2.18 Stress, temperature and bounding porosity of the sample with 0.1 % brine; for legend see Fig. 2.19

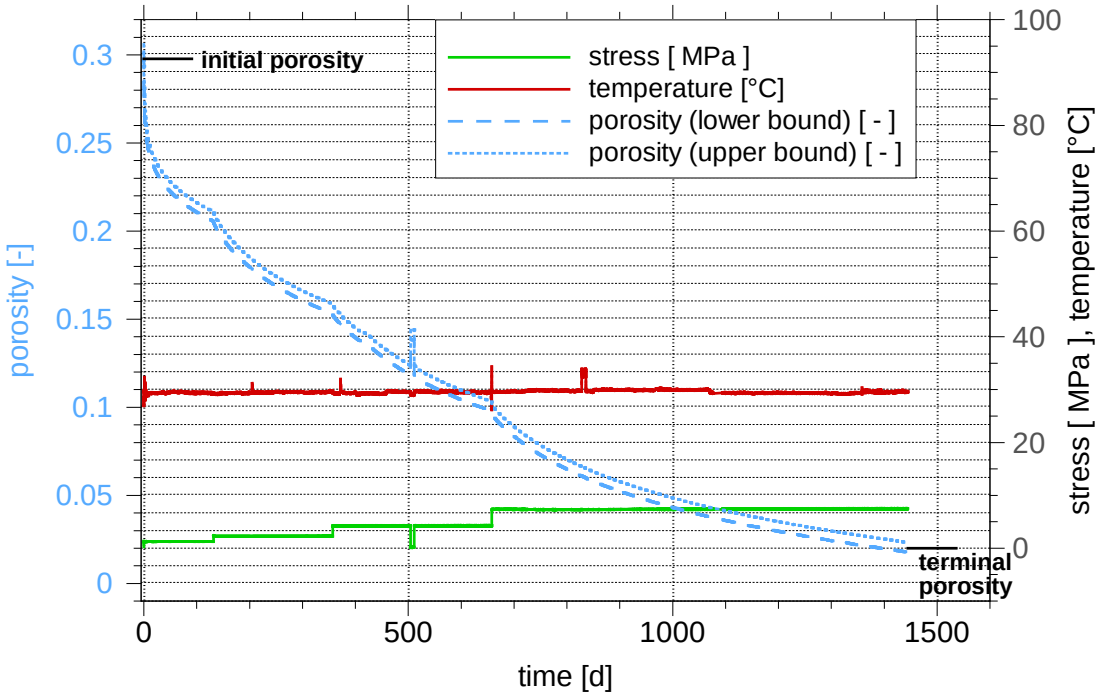

Fig. 2.19 Stress, temperature and bounding porosity of the sample with 1.0 % brine

Response to loading

Samples 1 and 2 experienced exclusively mechanical loading during the first 500 days which was exactly the same for technical reasons (cf. section 2.4.2.2). The porosity evolution was quite similar during this period (cp. Fig. 2.16). The different initial moisture contents of 0 % and 0.1 % did thus not exert a significant difference.

The initial moisture content of 1 % in sample 3 caused a rather different evolution by comparison. Despite the fact that the first load step of 1 MPa was maintained much longer than for the dryer samples 1 and 2, the strain rate of sample 3 had not yet reached nearly the low level of samples 1 and 2 when the load was eventually increased. It was thus that in case of sample 3 the following load level amounted only to 2 MPa compared to the 4 MPa in case of samples 1 and 2.

The response of the samples to loading in general (stress, heat, flooding) can be divided into two phases of different dynamics. The first phase is characterised by a very fast reduction of porosity which cannot be identified in the strain rate plots but in close-ups of the porosity evolution as shown exemplarily for sample 1 in Fig. 2.20. Data from these close-ups concerning the compaction rate during this first phase were taken and com-

piled in Tab. 2.2. This could be done only in an ad-hoc manner, though, because the temporal resolution of the data acquisition did not allow for deciding conclusively when this fast phase ended. The values for the compaction rate given in Tab. 2.2 can thus be much higher. In general, the resulting data indicate a decreasing porosity reduction at also decreasing compaction rates.

For the same shortcomings of temporal resolution in the data it was also not possible to decide whether the first phase fades to the second one or if there is a sharp transition. It appears, though, that the transition is most pronounced in case of mechanical load changes and only hardly visible in case of flooding.

The second phase comprises a seemingly convergent reduction of the strain rate later on. A constant strain rate was not reached, however, in the experiment at any time. Only sample 3 came near to such a state at the end of the test. The strain rate plots suggest that a constant strain rate could have been reached in the long run. Due to the consolidation effect, though, the strain rate decreases continuously and cannot become constant. Consolidation is higher in case of wetted salt than in case of the rather dry material.

Subsequent dynamics of porosity reduction in the second phase appear to be similar for all three types of loading. However, the strain rate seems to decrease less in case of temperature load than in case of mechanical load. Most dramatic and smoothest decrease occurs in case of flooding.

Samples 1 and 2 were flooded at 32 °C and 80 °C, respectively, and thus give some insight into the dependency of compaction after flooding on temperature. A rigorous comparison of the compaction dynamics is not possible, though, because the porosity was quite different at the beginning of flooding. But visual comparison of the porosity curves for samples 1 and 2 suggests that temperature seems to have secondary influence on the compaction after flooding.

Response to temperature decrease

Only samples 1 and 2 experienced elevated temperatures. Reducing the thermal load resulted in a significant decrease in the progress of compaction indicating hardening of

the material. This applies to the dry sample (cf. Fig. 2.17 and also Fig. 2.13) as well as to the fully flooded sample (cf. Fig. 2.18 and also and Fig. 2.14).

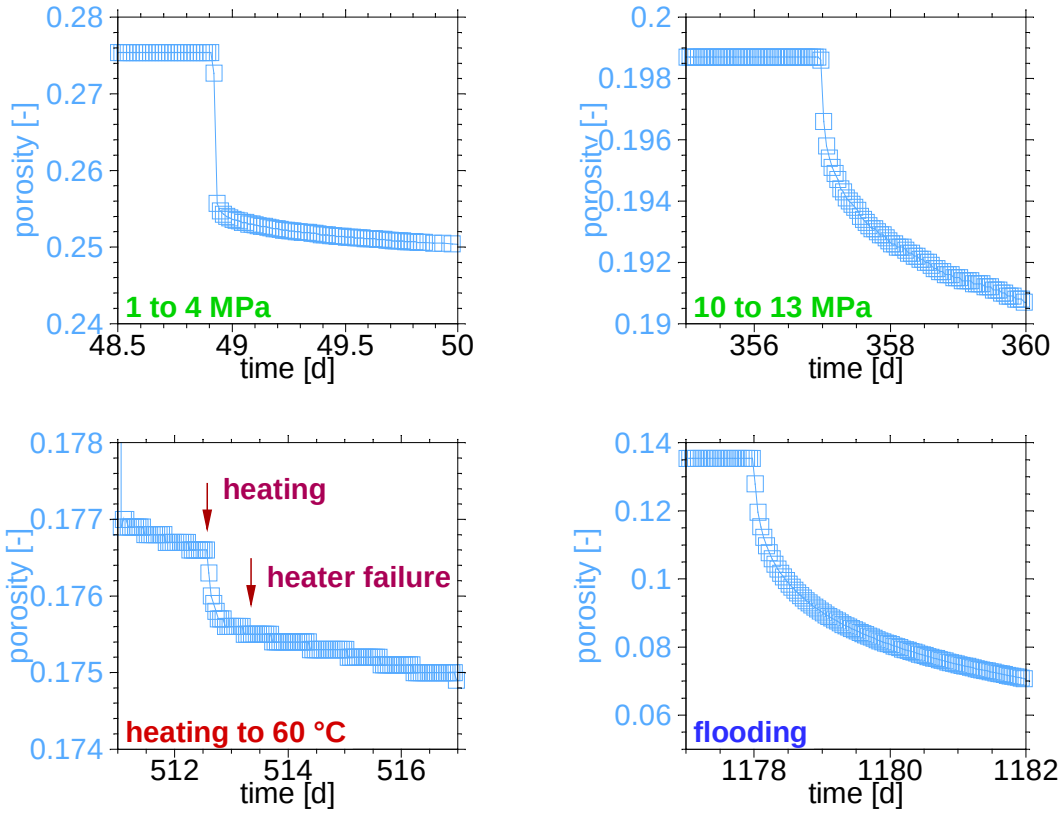

Fig. 2.20 Close-ups of the porosity evolution in the oven-dry sample (sample 1)

Tab. 2.2 Characteristic data at load changes for sample 1

Time [days]	Event	ΔΦ [%]	Δt [d]	ΔΦ/Δt [%/d]
0	Stress increase to 1 MPa	0.93	0.0015	620
48	Stress increase to 4 MPa	1.95	0.0017	1147
131	Stress increase to 7 MPa	0.71	0.041	17.3
267	Stress increase to 10 MPa	0.20	0.040	5.00
357	Stress increase to 13 MPa	0.21	0.049	4.29
512	Temperature increase to 60 °C	0.06	0.189	0.317
818	Stress increase to 18 MPa	0.29	0.043	6.74
1178	Flooding	1.55	0.09	17.2

Permeability

Data for the transient gas permeability of the oven-dry sample (sample 1) generally decreased from 2.9·10-12 m² at the beginning of the test to 1.3·10-12 m² at 14.2 % porosity on day 1107 shortly before flooding the sample (see table in Appendix E). The permeability values fit well into the bandwidth determined in the framework of phase 1 of the Repoperm-project.

At the end of the tests, a low gas injection pressure was applied to samples 1 and 2 and slowly increased up to 7 MPa. Neither gas nor brine outflow could be detected even at 7 MPa. Without further testing it is doubtful, though, if this value actually represents a lower bound for the air entry pressure as the salt in the sinter plates might have spoiled an accurate measurement.

2.4.2.6 Conclusions

The experiment presented here is done in such a way that a number of aspects concerning the THM-behaviour of crushed salt during compaction are touched. Progress of stress-controlled compaction was observed on three samples. Recorded was the impact on compaction by

– different initial moisture contents
– incrementally increased mechanical load from 1 MPa up to 18 MPa[7]
– incrementally increased temperature at a mechanical load of 13 MPa
  • up to 60 °C in one step in case of sample 1
  • up to 60 °C, then to 90 °C in case of sample 2
– decrease of temperature down to 34 °C in case of sample 1
– flooding of samples 1 and 2
  • at 18 MPa, 14 % porosity and 32 °C (sample 1)
  • at 18 MPa, 10 % porosity and 80 °C (sample 2)

Additional permeability measurements were performed:

[7] 7 MPa in case of sample 3

– The gas permeability of the oven-dry sample (sample 1) was measured at the end of each mechanical load step.
– At the end of the experiment it was tried to determine the air entry pressure but not achieving gas flow does not necessarily indicate a lower bound for this quantity.

Interpretation of the porosity evolution

– An initial moisture content in the order of 0.1 % does not significantly influence compaction in comparison to initially oven-dry conditions.
– Compaction of the sample with initially 1 % moisture content was much faster under much less load than compaction of the initially dryer samples.
– A temperature increase of about 30 °C had a similar effect as a mechanical load increase in the range of 3 to 5 MPa.
– Temperature decrease at maintained mechanical load results in a “hardening” of the material as the subsequent strain rate dropped considerably.
– The effect of flooding under high stresses can result in a loss of porosity in the order of 8 to 13 % within a year. A qualitatively similar behaviour is expected for low stresses (cp. section 2.4.4).

Procedural conclusions

– Uncontrolled solution or precipitation in the pore space of the samples can be avoided by careful preparation of the injected brine.
– The tests were not significantly disturbed by short interruptions in applying the mechanical load like during adjustments of the displacement transducers.

All in all, the gained data thus give valuable insight into the THM-behaviour of compacting crushed salt and forms a comprehensive basis for testing related constitutive models.

2.4.3 Triaxial compaction in an autoclave

2.4.3.1 Test principle and set-up

The test described in the following was intended to investigate the influence of the initial moisture content on compaction under a triaxial load. An autoclave was used for the test that could contain up to 5 samples. Four samples of crushed salt prepared to have different initial moisture contents. The cylindrical samples had an axial length of 200 mm

and a diameter of 100 mm. They were installed in rubber jackets and capped off with sinter plates and metallic cylindrical head ends with a gas outlet as depicted in the left sketch in Fig. 2.21.

Flexible tubes connected the gas outlets of the samples with water-filled burettes at the outside of the autoclave to measure the amount of expelled pore air during compaction. To account for changes in temperature and atmospheric pressure an incompressible cylinder was emplaced besides the four samples for reference. The samples and the incompressible cylinder were then emplaced in the autoclave, which was afterwards filled with oil whose pressure controlled with the help of an oil pump. The principle is shown in the right sketch in Fig. 2.21.

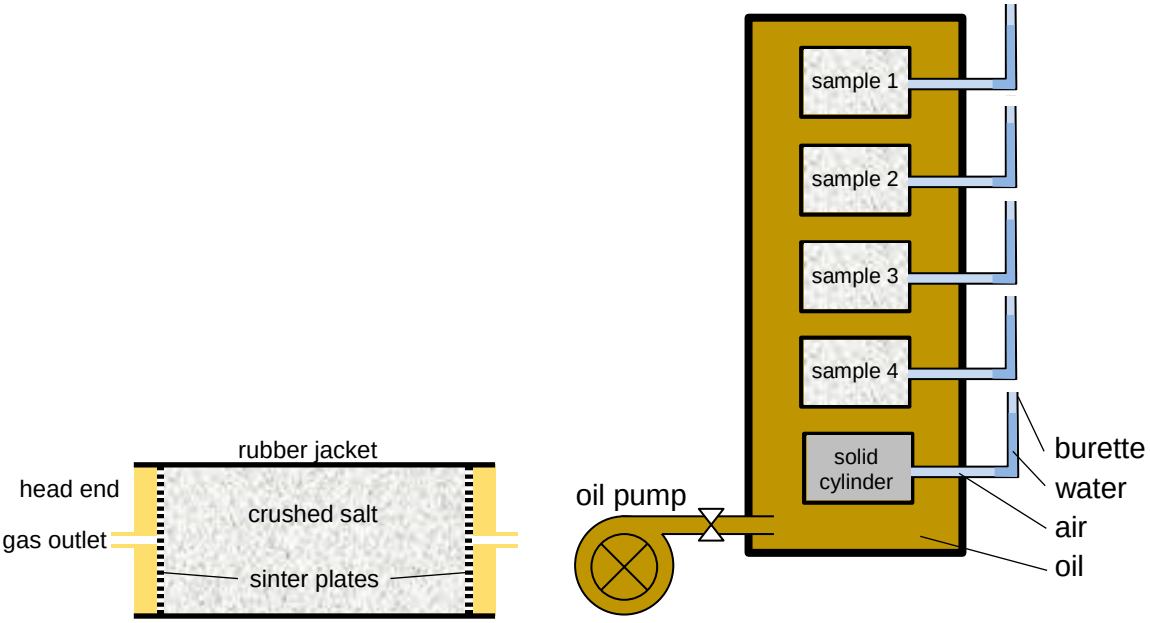

Fig. 2.21 Single “cell” and test set-up

When serious difficulties arose with this method a different procedure for monitoring the porosity was devised. First the samples were equilibrated with the atmospheric pressure. The burettes were then sequentially replaced by a box of known volume that was temporarily shut off from the sample by a valve. The box was pressurized and the pressure noted. The valve was opened and the subsequently equalizing pressure was noted as well. From these data the gas accessible volume beyond the valve could be calculated. Subtracting the volume of the tubing and the sinter plates led eventually to the pore volume of the samples.

Note that only the gas accessible volume is measured by both of these methods. Deriving the porosity by measuring mass and bulk volume in the post-test investigations provides by contrast the total pore volume.

2.4.3.2 Preparation

First, a crushed salt mixture with salt from the Gorleben mine with a grain size distribution according to Appendix G in the main report was prepared. Afterwards, the material was dried for 24 hours at 105 °C. The dry crushed salt was then divided into four batches of pre-determined mass. An appropriate amount of brine was added by spraying and subsequent mechanical mixing before it was pre-compacted for test 1 and simply filled into the rubber jackets in case of test 2.

2.4.3.3 Test 1

In the first test and initial moisture content of the samples was set to 0,3 % 0,6 %, 1,0 %, and 1,3 %, respectively. The four samples were quickly pre-compacted to a target porosity of 18.6 % to achieve comparability with the long-term compaction test. Actually reached were 18.3 %, 18.3 %, 18.5 % and 18.6 %.

Monitoring the porosity during the test showed a rather slow reduction of the porosity in comparison to the long-term compaction test described in section 2.4.2 of the main report. This was interpreted as hardening of the material caused by a rather high compaction pressure during pre-compaction. Later, however, an increase of porosity instead of a decrease was observed. The test was thus considered to be a failure and prematurely terminated after 159 days. After dismantling the reason for this failure was found in a constructional fault of the test cells. In order to minimize the gas volume outside the samples no sinter plates had been foreseen. This resulted in a considerable creep of salt into the gas outlet and thus distorted the results.

Post-test investigation of the acquired final total porosity showed considerably lower values than the spoiled results from the transient monitoring of the gas accessible porosity. No noticeable difference was found in the total end porosity for the samples with an ini-

tial moisture content of 0,6 %, 1,0 % und 1,3 %, respectively. Distinctly higher was the porosity in the fourth and least moist sample.

Tab. 2.3 Total end porosity of the samples of the second test

target moisture content	0,3	0,6	1,0	1,3
end porosity from mass and volume	11,42	8,68	8,69	8,72

2.4.3.4 Test 2

Repeating the test opened up the chance to optimize the measurements by

– introduction of sinter plates at the gas outlet of the head pieces to avoid the test compromising creep of compacting crushed salt into these outlets,
– dropping pre-compaction to avoid possible hardening,
– a softer increase of the mechanical load, again to avoid hardening of the material. The first 4 MPa were therefore applied in steps of about 0.2 MPa over 5 days, and
– changing the set of initial moisture contents to 0 %, 0,3 %, 0,6 % und 2,0 % for better comparability with the long-term compaction test and to gain more insight into the impact of an initial moisture content being significantly higher than 1 %.

At day 106 the rubber jacket of the oven-dry sample became apparently punctured. Oil from the autoclave could enter the sample rendering further testing of this sample useless.

Measurements of the porosity by means of monitoring the amount of expelled pore air in the burettes produced after about 40 days suspiciously little progress if any at all. It took some time to realize that the measurements had become useless and to devise the alternative method with the pressurized box. The results from both methods together with the loading history are depicted in Fig. 2.22. A conclusive reason for the failure of the direct measurement of the expelled pore air was not found. It was speculated, however, that the variations of atmospheric pressure and temperature dominated after the initial loading phase over the little quantities of air being extruded by compaction and thus rendered the measurement useless.

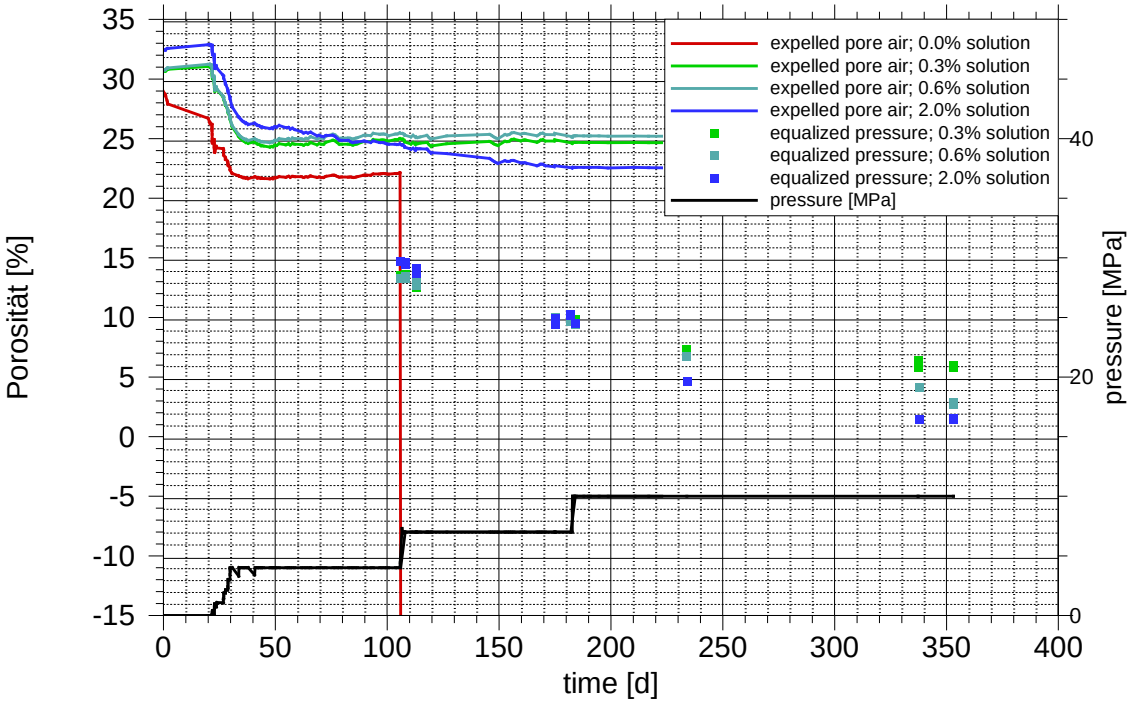

Fig. 2.22 Data from the two porosity determining methods

Just before the last porosity measurement it was discovered that brine had been expelled from the sample with 2 % initial moisture content and had entered the tubing. 7.1 g of salt had left the sample representing a volume of 19.8 cm³ of brine.

The porosity data derived from the direct measurement of the expelled pore air appear to be partly consistent with the data from the equalized gas pressure of sample and attached box. A suggestive shape emerges if the curves from the first 30 days of the direct measurements are connected to the point data of the gas pressure measurements as indicated in Fig. 2.23.

Post-test determination of the total porosity required first expelling the remaining water in the samples by heating. Doing this at 105 °C not only over 1 day but also over 4 days revealed an interesting fact concerning the drying dynamics. No significant difference in sample weight was observed on the sample with 0.3 % initial moisture content. By contrast, a much higher and almost identical difference was found for the samples of 0.6 % and 2.0 % initial moisture content (cp. Tab. 2.4). This might indicate a principle difference in the microstructure of the pore system at the end of the test. It can further be

speculated that this observation narrows the transition from dry to wet compaction to the range of a moisture content between 0.3 % and 0.6 %.

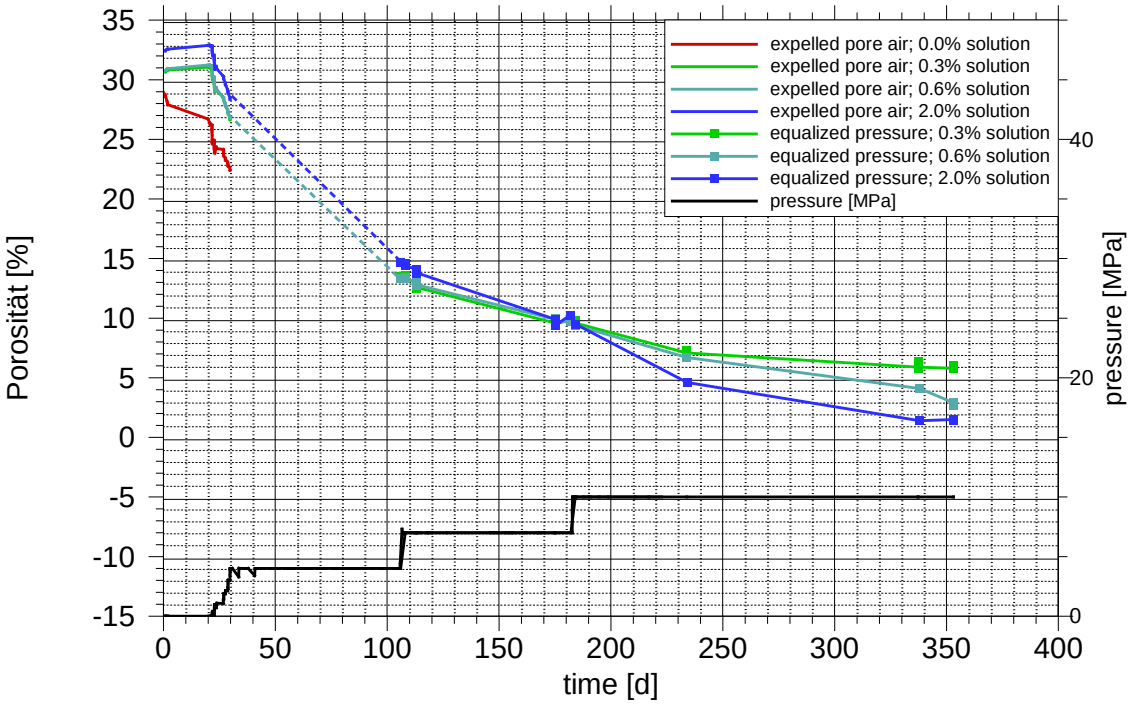

Fig. 2.23 Combination of the two transient porosity determining methods

Tab. 2.4 Weight loss of the wet samples after 1 and 4 days

target moisture content [-]	0.3	0.6	2.0
weight loss after 1 day [g]	4,0	6,2	11,5
weight loss after 4 days [g]	4,1	8,3	13,8
difference [g]	0.1	2.1	2.3

The next step in determining of the total porosity was to weigh the dried sample and to measure its volume. As compaction of the samples was impeded by the head pieces the resulting shape was not cylindrical anymore (see Fig. 2.24). The volume was thus calculated from the mean of nine equidistantly located perimeter measurements.

Fig. 2.24 Sample with 0.6 % initial moisture content after dismantling

In the end the determined total porosity values were rather confusing than enlightening. While the last measurement of the gas accessible porosity provided the expected trend of decreasing porosity with increasing moisture content as shown in Fig. 2.23, the post-test investigations revealed exactly the opposite (cp. Tab. 2.5). If this can also be considered to indicate consequences of the transition from dry to wet compaction remains to be unclear.

Tab. 2.5 End porosity of the samples of the second test

target moisture content	0	0.3	0.6	2.0
gas accessible porosity (pressure method)	-	6.00	2.90	1.40
total end porosity	19.58	5.60	6.30	9.52

2.4.4 Compaction in a humid atmosphere

2.4.4.1 Test set-up and procedure

To investigate the influence of increased air humidity on compaction of crushed salt two test cells were constructed according to the sketch in Fig. 2.25. Photos of the cell components as well as an assembled cell are shown in Fig. 2.26. The conceptual idea behind the test was that the cells would be completely surrounded by humid air. Water vapour subsequently enters the pore space of the sample and migrates within the sample by vapour diffusion in air. This process can be described with Fick's second law. Based on the diffusion coefficient for binary diffusion of vapour in air /VAR 96/, an assumed tortuosity of 0.1 and an analytical solution for vapour diffusion based on a formulation

from /CAJ 59/ it was estimated that equilibrium of humidity inside and outside the sample would be reached inside half an hour for all practical purposes.

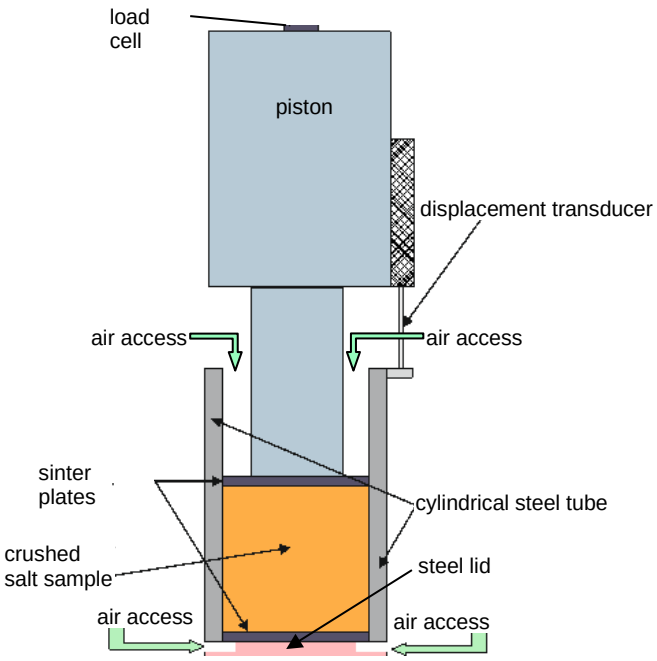

Fig. 2.25 Test cell for compaction under increased air humidity

The cells were thus emplaced in an air tight box. Together with a pump, a desikkkator and some fexible tubes a closed air circuit was constructed. A salt solution in the desikkator provided a controlled humidity in the air that was circulated by the pump through the desikkator as well as the air tight box.

The mechanical load was applied with the help of levers and weights as indicated by the sketch in Fig. 2.27. The levers consisted of solid steel rods with a diameter of 50 mm that were fixed to a wall by a joint. With this set-up it was possible to apply a compaction pressure of close to 1 MPa as in the first loading stage in the long-term compaction test (cp. section 2.4.2).

The full mechanical load was applied right at the beginning and maintained for the whole time. The relative humidity was intended to be set initially to a rather low value to be increased later to a high level. Room temperature as well as the temperature in the airtight box were checked during the whole test. A humidity sensor measured the relative humidity in the box.

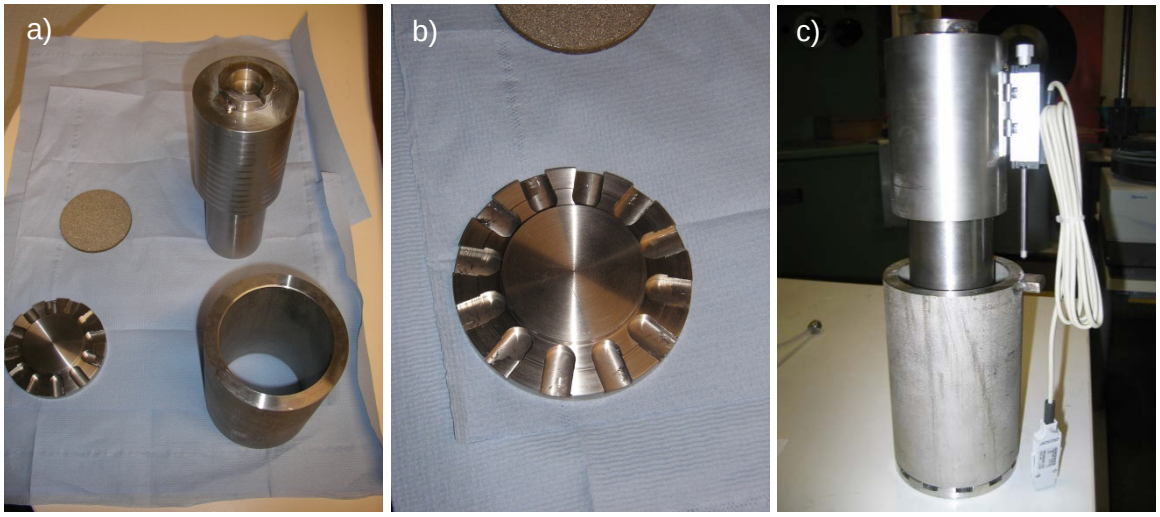

Fig. 2.26 Test cell for compaction under increased air humidity;
a) cell components, b) bottom lid, c) assembled test cell

Initially, a different control system for the humidity in the airtight box had been devised that proved to produce intolerable variations in the humidity. When it became clear that the test had to be repeated with an improved system also the application of force at the top of the piston as well as the attachment of the levers at the wall were optimized. The samples could not be used in the rerun of the test. It was realized, though, that they would not suffer from a badly working humidity control if they were flooded with brine. This was subsequently done to provide some qualitative insight into the compaction behavior of wet crushed salt. Everything reported in the following refers to the improved test if not expressively stated otherwise.

Control of the humidity in the air tight box remained to be difficult even in the improved set-up. Humidity inside the box increased slowly during the first 90 days and remained only then to be somewhat constant, oscillating around a mean of about 55 %. On day 155 the planned increase raised the humidity to a value of about 70 % which prevailed comparatively nicely until the end of the test. The evolution of the relative humidity is included in Fig. 2.28 in the next section.

Crushed salt from the z2HSSP facies at the Asse mine (“table salt”) according to the specifications in Appendix G was used for the test. Size and mass of the cylindrical samples are compiled in Tab. 2.6. Derived from these data is the initial bulk density of the samples and based on a grain density of 2.17 g/cm³ also the initial porosity.

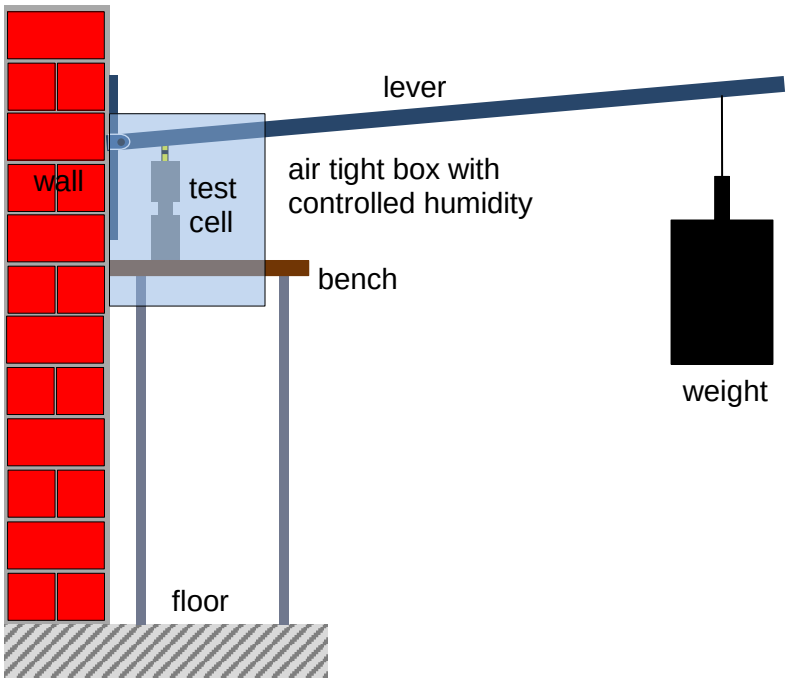

Fig. 2.27 Side view of complete test set-up

Tab. 2.6 Initial properties of the samples

radius [cm]	height [cm]	volume [cm³]	mass [g]	density [g/cm³]	porosity [-]	remark
4.00	7.10	356.885	567.65	1.590	0.3396	cell 1
4.00	7.80	392.071	572.47	1.460	0.3357	cell 2

2.4.4.2 Results

The measured temperature showed clear daily fluctuations which lie typically in the range between 2 °C and 4 °C. The difference between temperatures in the room and in the box amounts with few exceptions to less than 1 °C

Depicted in Fig. 2.28 is the evolution of the porosity in cells 1 and 2 as well as the relative humidity. The relative humidity varies seemingly on a daily basis but does so also sometimes at a higher frequency. Fluctuations are typically lower than 10 %. An additional low-frequency fluctuation with a period of about 10 days and a bandwidth of 20 % can furthermore be noticed.

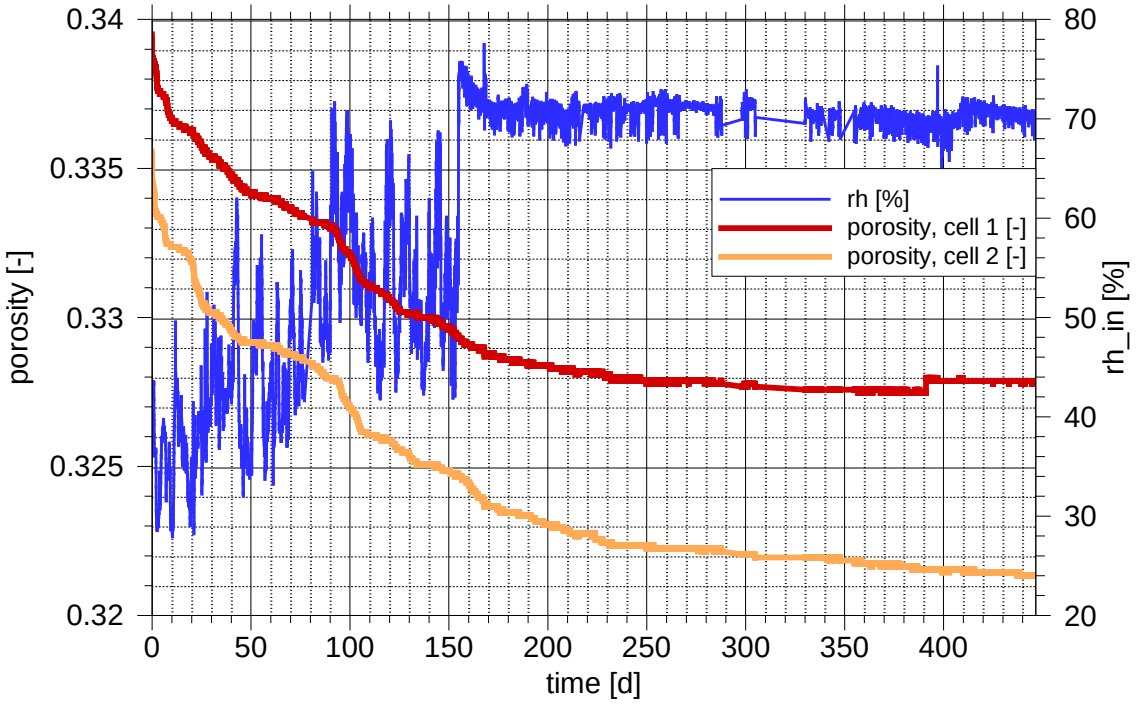

Fig. 2.28 Evolution of relative humidity in the box and porosity in cells 1 and 2

The evolution of the porosity which is calculated from the displacement of the piston, shows that compaction is visibly affected by the humidity at two times: first when the humidity exceeded 65 % for the first time on day 90 and second when the humidity of the vaporous air in the box increased to 70 % on day 155. On the whole, these events had apparently only a minor impact on compaction, though.

The first loading stage of the long-term compaction test with the oven-dry sample where a compaction pressure of 1 MPa was applied, lasted for a little more than 45 days. This timeframe can thus be used for a comparison of the porosity evolution between

– cells 1 and 2 of the test with increased humidity,
– the oven-dry sample of the long-term compaction test, and
– the sample with 1 % initial moisture content in the long-term compaction test.

Compared in Fig. 2.29 are days 0 to 45 in the long-term compaction test and days 155 to 200 in the test with increased humidity. The latter period has been chosen because it represents the compaction behavior after increasing to the highest humidity of 70 %. The same curves for the period between 90 and 135 days when the other visible acceleration of compaction occurred have essentially the same shape at a slightly higher level.

In general the development of the porosity under increased humidity compares quite well in terms of shape with the measured porosity in the oven-dry sample of the long-term test. It is thus completely different from the porosity development of the sample with 1 % initial moisture content in the long-term compaction test. An influence of high relative humidity in the pore air can therefore not be confirmed.

The results from flooding of the samples in the spoiled test as well as from flooding in the long-term compaction test are shown in Fig. 2.30. For an intelligible qualitative comparison, the time point of flooding was chosen to coincide for all curves close to the left vertical axis. Additionally, the depicted time interval amounts to 120 days in all cases. The resulting curves look qualitatively rather similar considering that the porosity as well as the mechanical load were quite different at the time of flooding (36 %, 33 %, 15 %, and 11 %, together with 1 MPa and 18 MPa).

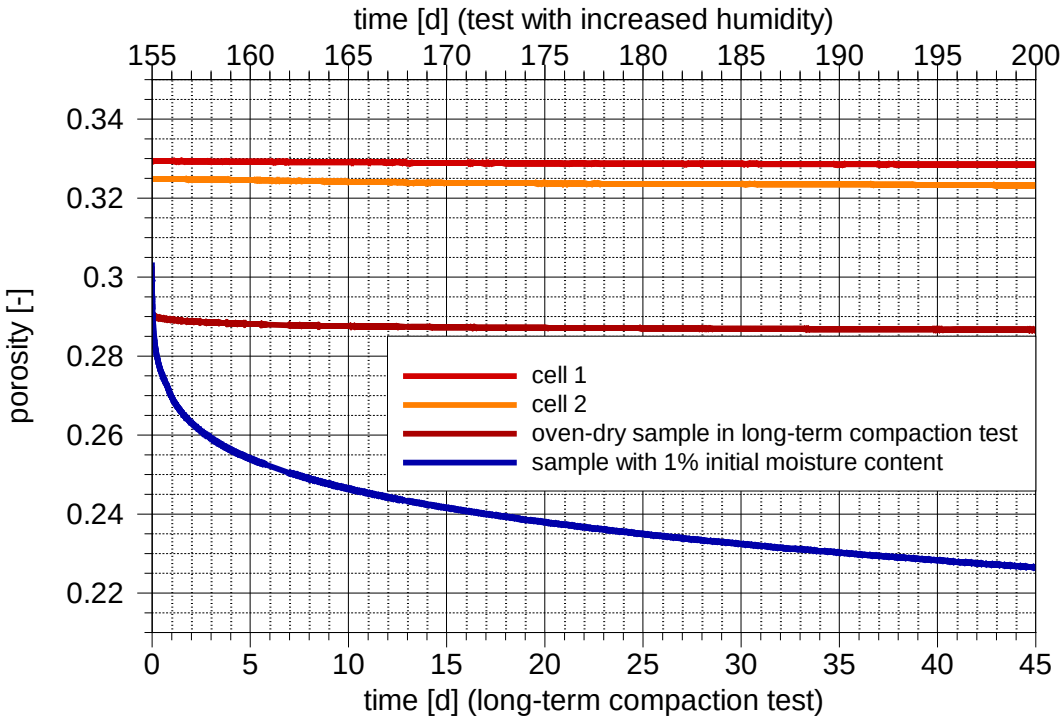

Fig. 2.29 Porosity in samples of the present and the long-term compaction test

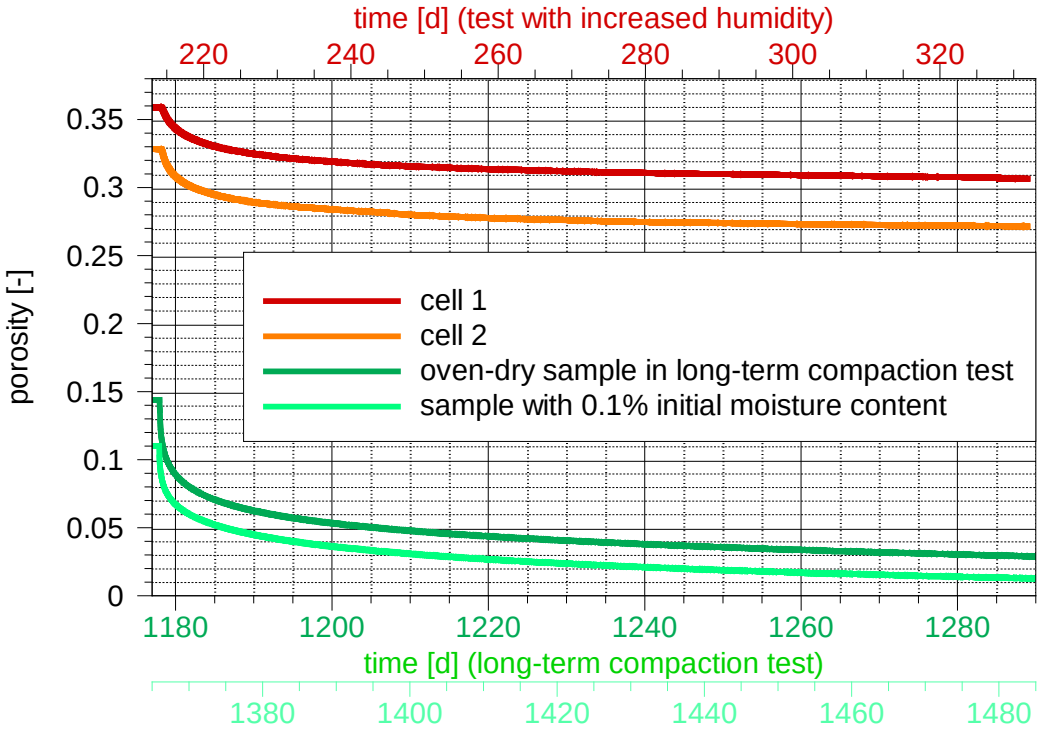

Fig. 2.30 Porosity in samples of the present and the long-term compaction test

2.4.5 Adsorption of water to salt in a humid atmosphere

2.4.5.1 Test description

The crushed salt used in the experiment was prepared from the z2HSSP facies (table salt) from the Asse mine. It contained more than 99 % halite and was mixed according to the grain size distribution described in Appendix G.

Six samples with a weight between 85 to 139 g were dried at 105 °C over 24 hours. Another batch of six samples was prepared but left at the moisture content of 0.02 % that represents the equilibrium content at storage conditions. The samples were allocated to two desiccators in such a way that each desiccator contained three moist and three dried samples. The set-up is shown in Fig. 2.31.

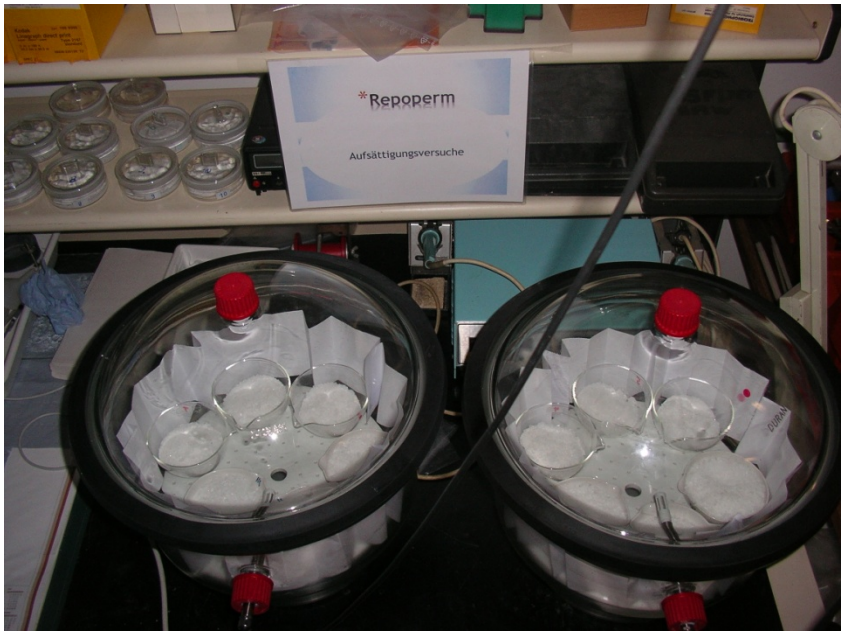

Fig. 2.31 Test set-up

The desiccators were located in a climate controlled room with nearly constant temperature. The humidity in the desiccators was controlled by salt solutions at the bottom. The first solution used at the beginning of the test had an equilibrium humidity of 12 % above the surface. The mass of the samples was measured frequently. After periods of 2 to 4 weeks, depending on the data, the salt solution was exchanged, thereby increasing the relative humidity. The final test period was performed under 75 % humidity which is the equilibrium humidity over a fully NaCl-saturated solution. The target humidity and the period of time over which each humidity level prevailed are listed in Tab. 2.7.

Tab. 2.7 Humidity levels and related test durations

Humidity level [%]	Test duration [d]	Time [d]
12	27	0 - 26
22	16	27 - 43
31	31	44 – 75
43	14	76 – 90
62	37	91 – 128
75	288	129 - 417

2.4.5.2 Results

The evolution of humidity and temperature in the desiccators is depicted in Fig. 2.32. It shows that the temperature had been kept indeed nicely between 22 °C and 24 °C for

most of the time. A temporary increase to about 27 °C between day 85 and day 100 had apparently rather little influence on the humidity anyway (cp. Fig. 2.33).

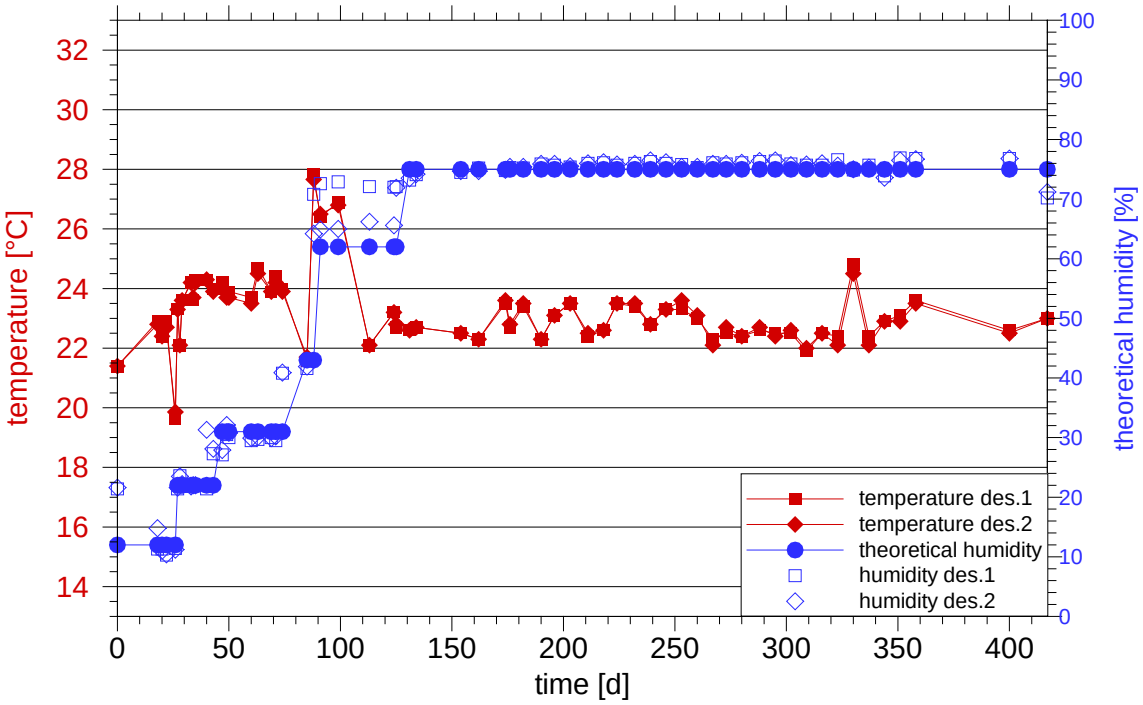

Fig. 2.32 Evolution of humidity and temperature in the desiccators

The measured relative humidity corresponded well to the theoretical values for the respective salt solution which are also indicated in Fig. 2.32. An exception is the 62 %-level, though, where the measured humidity exceeded the theoretical value in both desiccators considerably. No explanation for this behaviour could be found.

The evolution of the total weight of the samples is shown in Fig. 2.33. It appears that very little happens until full humidity is reached. There are, however, several jumps in the otherwise exceptionally smooth course of the curves in this range. These jumps can partly be related to irregularities such as mass losses during the weighing procedure. In case of the moist sample 5 the jar containing the sample was broken and had to be replaced.

The development of only minimal weight changes continues for the first 40 – 50 days at 75 % humidity. But then a significant increase in weight could be observed that exceeded all previously water uptake and did not seem to come to an end over time. In hind-

sight it was suspected that this was not an effect of sorption but rather an effect of condensation (see section 2.4.5.3). The data for the period after 120 days are therefore considered to be spoiled.

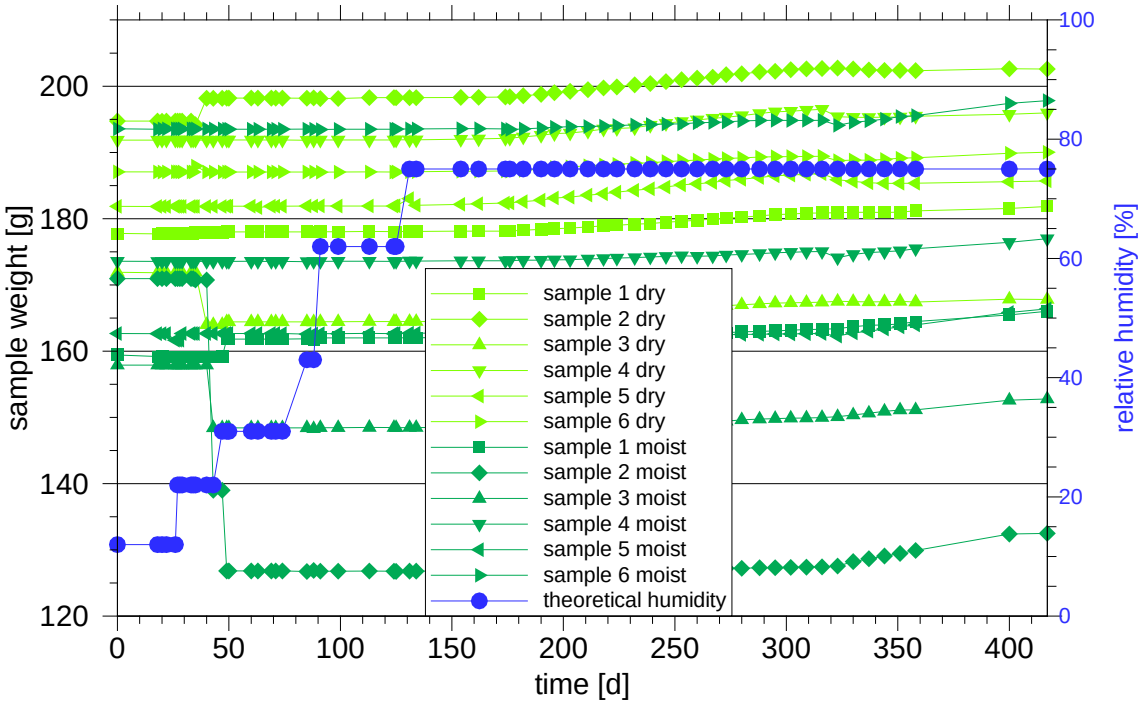

Fig. 2.33 Evolution of the total mass of the samples

2.4.5.3 Interpretation

Weight changes of the samples during the experiment and in particular before reaching maximum humidity were apparently minimal. The irregularities mentioned above had a much bigger impact on the sample weight than the sorption process itself thus making it difficult to recognise the effect of sorption in the weight data. To gain a clearer picture of the evolution of the moisture content the weight data was therefore corrected to show no higher difference in weight from measurement to measurement than 0.1 g. The resulting curves are depicted in Fig. 2.34.

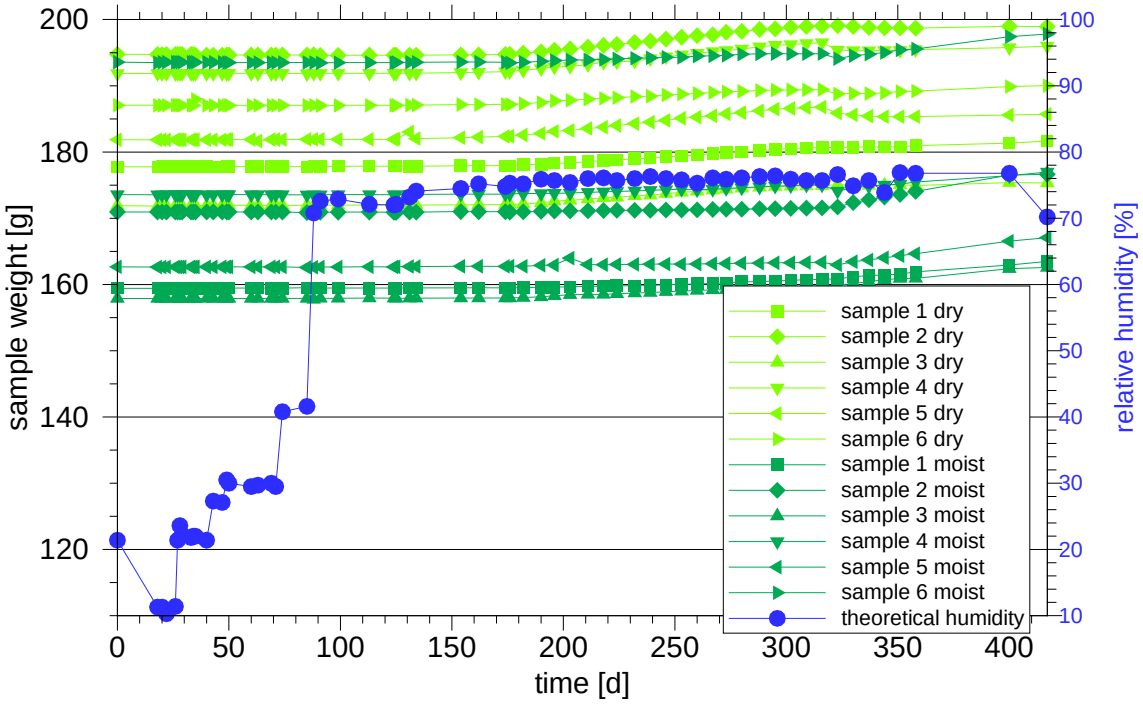

Fig. 2.34 Evolution of the total mass of the samples – corrected data

From the weight data the amount of the water sorbed during the experiment could be derived by calculating the difference of the moist salt mass and the dry mass. The result for the whole experiment is shown in Fig. 2.35. The plot confirms the observation that much more water was gained by the samples during maximum humidity than at the previous humidity levels. While the initially dry samples seem to take up water more readily at first than the initially moist samples these trends go into reverse for the last 100 days.

The somewhat delayed begin of the comparatively strong water uptake after raising the humidity to 75 % is not easily explained. It might be that the vapour saturation pressure in the samples could have been temporarily exceeded because of temperature variations. This would have caused condensation of water which would have retreated to the contact zones of the salt grains due to capillary forces. Lowering of the vapour saturation pressure at the meniscus of the water air interface leads then to further condensation. This effect, known as “capillary condensation”, would thus be self-sustaining even if loosing strength over time as the amount of accumulated water would increase thereby decreasing the curvature of the menisci. However, this effect has nothing to do with sorption so that the period after 120 days can be considered to be spoiled rendering further discussions concerning this phase pointless.

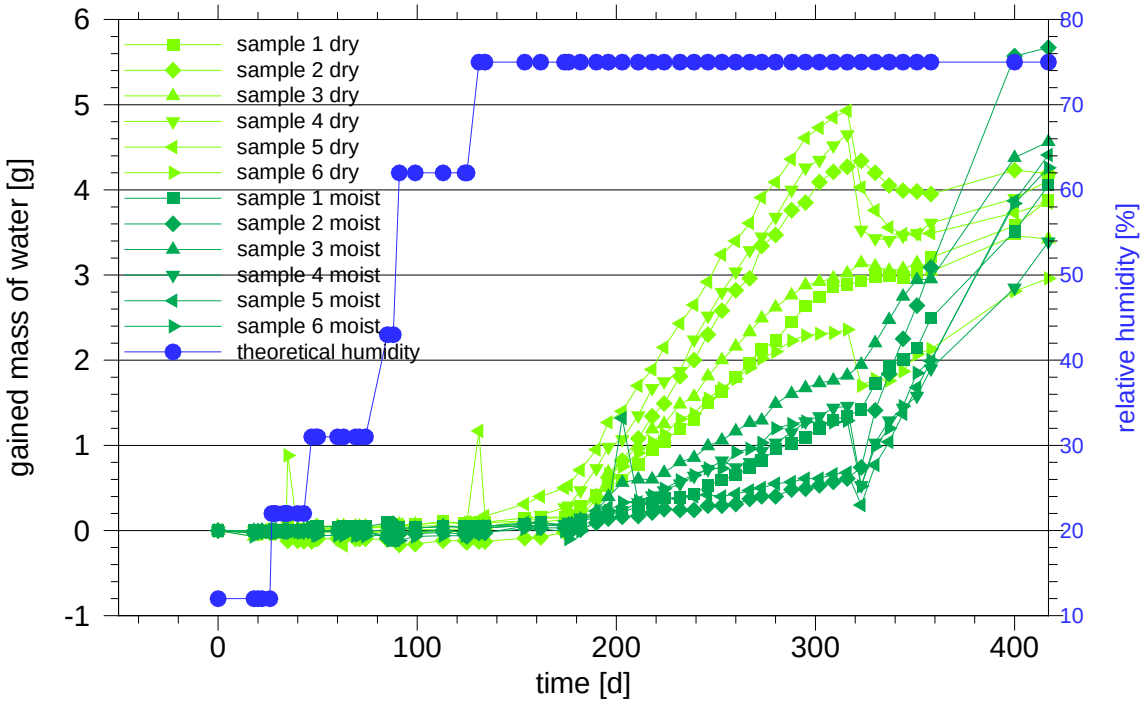

Fig. 2.35 Mass of water gained by the samples during the experiment

The following discussion thus concentrates on the first 120 days. From the mass of gained water the evolution of the moisture content can be calculated. The resulting plots are shown in Fig. 2.36 and Fig. 2.37. The cluster of individual curves seems to indicate a certain increase of adsorbed water which is confirmed by the curve for the mean values. The curve for the mean values even allows quantifying the gain to amount to roughly 0.04 % moisture content before maximum humidity was reached.

A still open question is if an equilibrium between relative humidity and moisture content has actually been reached at each humidity level. This cannot conclusively deduced from the data. What can be stated, though, is that if adsorption was still ongoing at the times of humidity increase, the kinetics involved must very slow.

In contrast to the initially dry samples, the mean for the initially moist samples – depicted in Fig. 2.37 – indicates an increase of adsorbed water only after increasing the humidity to the maximum. Again, it cannot entirely be excluded that the sorption process is just extremely slow.

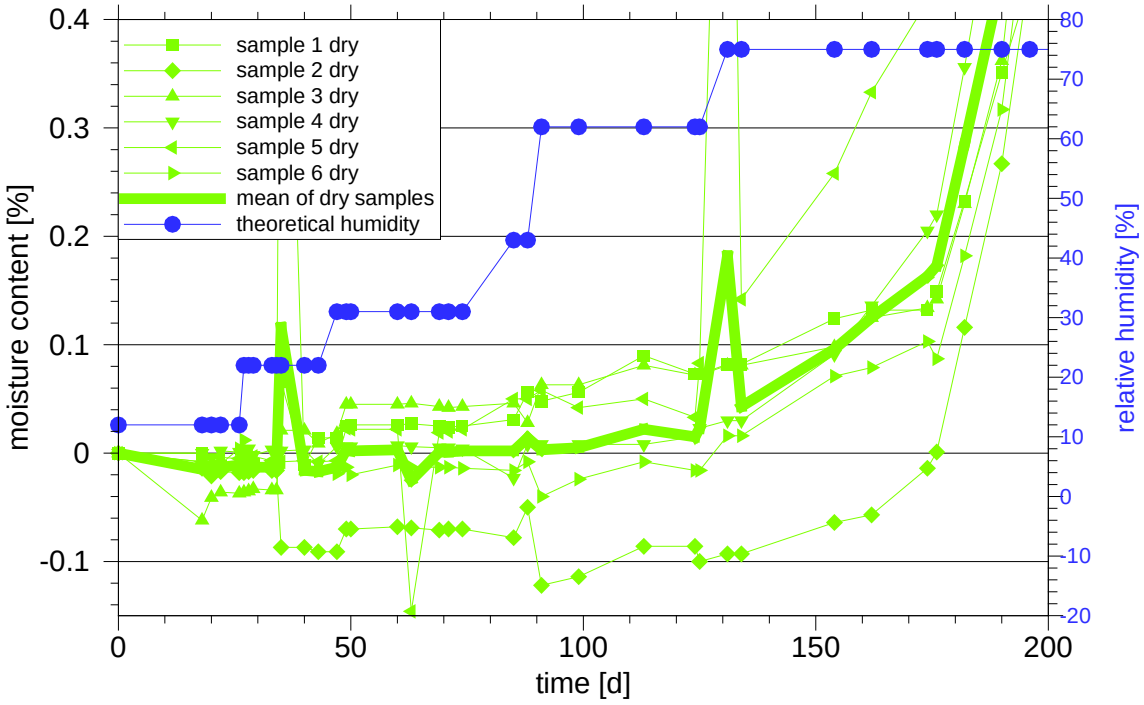

Fig. 2.36 Evolution of the moisture content of the initially dry samples

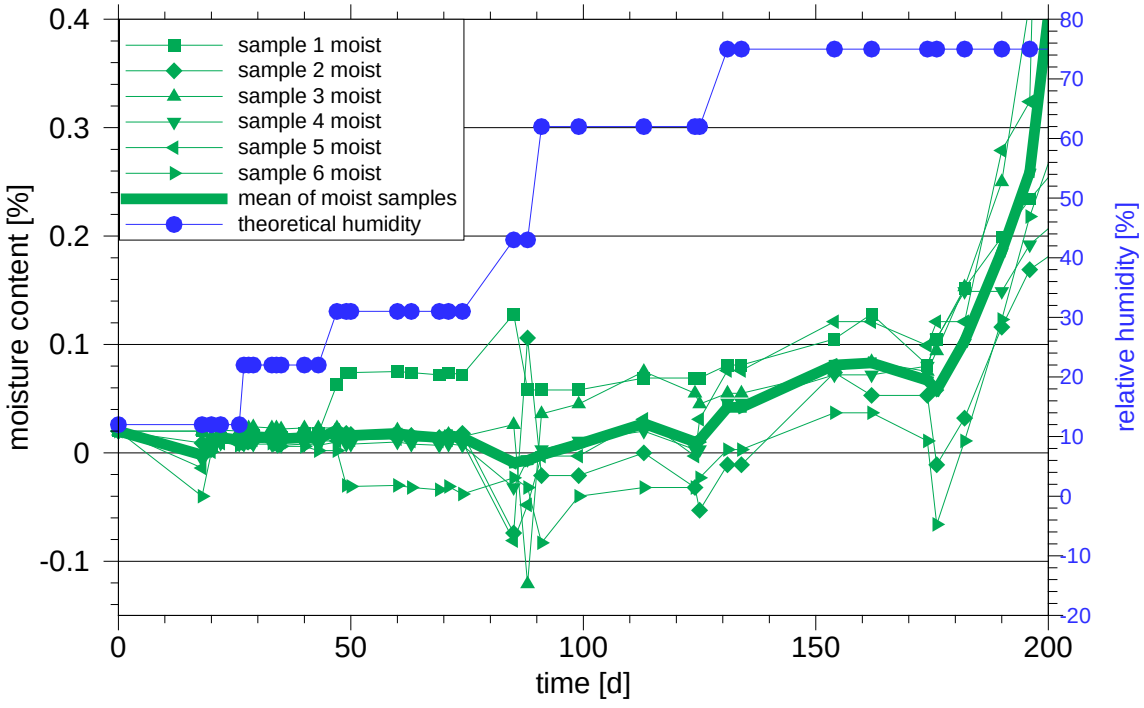

Fig. 2.37 Evolution of the moisture content of the initially moist samples

2.4.5.4 Conclusions

The deficiencies in the presented experiment to determine isotherms for the sorption of water vapour on crushed salt from the z2HSSP facies of the Asse mine (table salt) prevent a quantitative evaluation of the data. Some conclusions can nevertheless be drawn, though.

In the investigated crushed salt the amount of water drawn from a moist atmosphere is either rather low or it takes time in the order of years to reach a significant mass of adsorbed water. Low sorption capability in combination with a high diffusivity of water vapour in air thus strongly suggests that vaporous water can reach deeply into a crushed salt backfill. It might even reach the waste canister and be doing harm to them by corrosion.

The little amount of sorbed water indicates furthermore that a reduction of the resistance of the backfill to compaction will remain minimal. This deduction is consistent with the results of the compaction tests in a humid atmosphere of different relative humidities (see section 2.4.3.1).

It has to be pointed out, though, that these results refer to an almost pure halite. Different observations and conclusions cannot be excluded for other types of salt with a different mineralogical composition as the discussion of a similar experiment /FRÖ 95/ in Appendix H shows.

In general, the experiment shows the extreme difficulties arising from test conditions with relatively high air humidity. It had been expected that the relative humidity of 75 % created over the surface of a NaCl-solution would not interact with the crushed salt sample beyond water adsorption on the surface of the salt grains as in the previous test step at 62 % humidity. A considerable uptake of water in the samples has been observed, though, that continued over the remaining almost 300 days until termination of the experiment. While it is suspected that little temperature variations might have led to condensation triggering further capillary condensation this assumption needs to be confirmed yet.

2.5 Permeability associated with low porosity

2.5.1 D-A-025 uniaxial permeameter test with brine

The D-A-025 permeability test was carried out at room temperature in BGR's uniaxial permeameter (d = 10 cm) with the grain distribution of the borehole backfill material (d_{max} = 8.0 mm). The crushed salt backfill material is compacted in steps according to the oedometer principle, and brine is allowed to flow through several times at adapted fluid pressure in the relaxation phases. The outflow values which rose almost linearly during each flow phase are evidence for an almost constant flow which can be used to calculate the permeability according to Darcy's Law.

The permeabilities determined in this way were compared with the results of the earlier D-A-016 and D-A-017 tests with (d_{max} = 16.0 mm) which were already incorporated in /KRÖ 09/, Section 2.5. The test apparatus and the procedure are described in /STÜ 95a/, Section 5.

Fig. 2.38 shows the calculated permeabilities of the D-A-025 test as a function of the void ratio in a double-logarithmic diagram. 11 flow campaigns were undertaken, i.e. 3, 4 or 2 flow phases (total 34) were carried out in the 11 different compaction statuses of the samples. The flow pressure differences were in the range of 0.12 to 19.7 bar. Each individual result is shown as a yellow point in Fig. 2.38. The red points show the geometrical mean values of a campaign.

The spread of the calculated permeabilities up to e > 0.03 is very low with the exception of the first flow campaign with low fluid differential pressures of 0.12 and 0.14 bar undertaken immediately after the saturation phase at e = 0.32. There is a significant increase in the spread of the individual values with an increase in density and lower flow. The accuracy of the void ratio also has an increasing influence in the higher compaction ranges. The configuration of the apparatus means that salt particles can penetrate the rough surface of the arranged sinter plates – this makes determination of the length of the sample increasingly imprecise as the test progresses. The control measurement of the sample undertaken after the test with the calliper is influenced by the squeezing out of the test cylinder and the elastic relaxation of the material. Consideration also needs to

be given to the fact that the accuracy of the void ratio can already be 1 % ($\Delta e = 0.01$) due to the nature of the material alone.

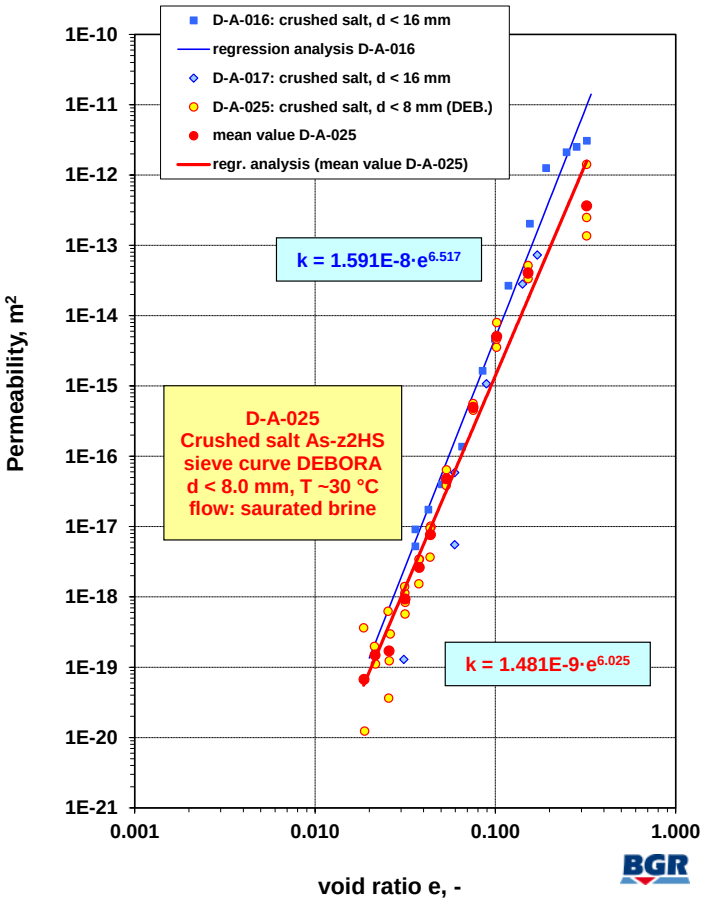

Fig. 2.38 Permeability of crushed salt, comparison of results with max d = 16 and 8 mm

The final height of the sample without any loading can be given as 131.54 mm (e = 0.025; Φ = 2.5 %). The highest compaction during the last compaction phase was determined as e = 0.019 (Φ = 1.9 %).

The porosity-permeability relation can be well approximated by a power function because of the distribution of the results. The red line shown in Fig. 2.38 is derived from a double-logarithmic depiction of the average values of D-A-025. The results of permeability test D-A-016 with the relevant regression, and the values of experiment D-A-017, are also shown (blue) for the purposes of comparison. No serious differences are revealed by this diagram due to the selected grain distribution. The slightly lower permeability in the upper part of the diagram shown along the red line is attributable to the value from

the first flow campaign at e = 0.32 when the sample was still in a relatively loose condition.

The aforementioned imprecision of the measured flow values, and the determination of the void ratio in the residual porosity range, are exaggerated even more by the double-logarithmic depiction. The extrapolation of the power function referred to is therefore inadequate to determine a porosity limit after which there is no longer any significant brine flow.

2.5.2 Permeability tests with gas (nitrogen)

2.5.2.1 Background, test apparatus and specimens

Permeability tests with liquids reach their limits with porosities in the range < 3 % when the amounts of liquid involved become too small, and in addition, when the porosity in the selected uniaxial permeameter can no longer be determined accurately enough. Innovative tests are therefore undertaken in BGR's Z3 testing machine which uses gas as the flow fluid. Rock samples with diameters of 100 mm and heights of max 250 mm undergo triaxial testing in the Z3 apparatus at the same time as being axially perfused with a gas pressure of up to 40 bar (max confining pressure = 40 MPa, max axial force = 1000 kN, max T = 60 °C). In addition to flow measured under constant differential pressure (gas volume per time unit), the tests are also usually carried out as pulse tests. This involves exposing the base of the sample to a pressure of a known size followed by evaluation of the pressure equalisation attributable to the sample. The apparatus is designed so that the volume of the sample accessible to the gas can also be determined pycnometrically at specific points by applying the gas law ("calibration"). However, for technical reasons, the measuring system currently reaches the limits of its accuracy with sample porosities of less than 2 to 3 %. The porosities of the sample were therefore derived from density measurements using scales and measurements with the slide gauge in an unpressurised condition.

Clear pore structures are still identifiable even after advanced compaction when compacting "dry" crushed salt (/BEH 04/, Section 2.5). Plastic deformation initially occurs primarily in the form of crystal fractures, and not in the sense of healing and recrystallisation. There is also no (partial) reaction between the sample and the flow medium when

allowing inert media to flow through the specimen, unlike the situation when using brines. No capillary seal pressures are expected. As a result, relatively high permeabilities are still determined in flow experiments with gas in the residual porosity range (/KRÖ 09/, Section 2.5). A not insignificant influence on the permeability is expected from the external mechanical loading.

The major influence of even low quantities of moisture on the material behaviour is known from investigations looking at the dilatance, damage, fracture and healing (reconsolidation) of mechanically stressed compact rock salt in the excavation disturbance zone (EDZ) – and particularly the way the permeability develops in the low porosity range, cf. /STÜ 12/, /SCH 14/. In the same way, compaction can be accelerated by moisture. Relevant investigations would therefore also be prudent in the residual compaction range of crushed salt used as a backfill material. The ultimate aim of the investigations is to verify the framework conditions under which the still existing gas permeability can be minimised after extensive compaction of “dry” crushed salt.

The pre-compacted cylindrical specimens were taken from BGR oedometer samples Oedo-051 and Oedo-099. Fig. 2.39 shows the already partially sectioned and lathed samples. In the Oedo-051 test carried out in 1994, crushed salt material z2HS from the Asse salt mine (d_{max} = 31.5 mm) were compacted up to a density of ρ = 2.0507 g/cm³ in 5 days at T = 100 °C under “fast” compaction speeds $\dot{\varepsilon}$ = $6.9 \cdot 10^{-6}$ and $6.9 \cdot 10^{-7}$ s^{-1}, with intermediate relaxation phases.

Fig. 2.39 Oedometer specimens 051 and 099 and products created from them

The maximum stress reached in this way was 34.2 MPa according to eq. (2.5) without taking into consideration the frictional forces, i.e. with $\sigma = F_1/A$, gives 43.8 MPa. The specimen was stored in the air-conditioned warehouse at BGR at approx. 22 °C and a

relative humidity of 45 ± 5 %rh. The specimen was sectioned into pieces in 2008 from which several precisely dimensioned cylindrical cores or disks were cut using a lathe. The piece D-OE-051/4 intended for use in the first permeability test under mechanical loading (Fig. 2.39 left; in the middle of the photo at the top), has the following dimensions: d/h = 99.86/103.80 mm. The density and void ratio from eq. (3) and (1) with a rock salt density according to eq. (7) are as follows:

ρ = 2.0590 g/cm³ and e = 0.0589 (porosity Φ = 5.1 %).

Cylindrical test specimens D-OE-099/01 and D-OE-099/02 were cored from the core of oedometer test 099 (Fig. 2.39 right). These specimens, also from z2HS material, but with a sieve line for borehole backfill material (d_{max} = 8.0 mm), was compacted well into the residual porosity range in the REPOPERM project in 2007/08 during a compaction phase exceeding more than four months at T = 150 °C. It is described in detail in /KRÖ 09/ and /KRÖ 12/, and was used in a special accuracy analysis /STÜ 09/. The final density and void ratio of the whole Oedo-099 sample in an unstressed state were calculated from eq. (7) as ρ^f = 2.1548 g/cm³ and e = 0.0109 (Φ = 1.08 %) respectively. Core D-OE-099/01 with dimensions d = 99.98 mm and h = 98.77 mm was cut from a vertical position. The calculated density and void ratio are:

ρ = 2.1578 g/cm³ and e = 0.0104 (Φ = 1.03 %).

Core D-OE-099/02 cut from a horizontal position and twice as long, measures d = 96.98 mm and h = 219.93, mm. Its density and void ratio are:

ρ = 2.1558 g/cm³ and e = 0.0114 (Φ = 1.13 %).

According to /STÜ 09/, the determination of the void ratio was associated with an inaccuracy of Δe = 0.005 – 0.01 (0.5 – 1.0 %) primarily because of the nature of the material.

The tests were carried out between 2009 and 2014. The permeability of all of the samples was investigated triaxially under various pressure stages (hydrostatic up to an axial overload of 1 MPa), and with adapted gas pressures (nitrogen) at a test temperature of 30 °C. The complex test runs were shown graphically using core D-OE-099/02 as an example. The precise analysis of the figures is necessary because of the residual porosity range involved.

2.5.2.2 Results of tests on “dry” material (test phase 1)

The first test of this kind was carried out on sample **D-OE-051/4**. The test configuration and the results were also published in /STÜ 12/. The core was loaded in steps of 1 – 3 days apart with loads of $\Delta\sigma$ = 5 MPa up to σ_3 = 38 MPa, and then kept at 15 days under a load of σ_3/σ_1 = 30/31 MPa. The pycnometric volume measurements carried out at the end of each loading stage revealed continuous compaction which was qualitatively confirmed by the axial compaction of the sample measured during the test with inductive sensors. During the subsequent step-wise pressure reductions to 20, 10 and 2 MPa, the measured porosities rose again, but still clearly remained below the level of the loading phases. The figures were not used further because of the aforementioned measurement limits. The volume reduction of 11 cm³ was calculated from the remaining mass measured after the test (Δe = 0.0014). The metrics after the “dry” compaction are as follows:

ρ = 2.0870 g/cm³ and e = 0.0447 (Φ = 4.3 %).

The pulse tests carried out before calibration at the end of the loading and depressurisation stages, determined the permeabilities to be in the $k = 1.4 \cdot 10^{-14}$ m² range. The value of only $k = 2.2 \cdot 10^{-14}$ m² was reached even under the highest load of 38 MPa. Independent of the uncertain void ratio existing under load, it was not possible to prove that a “dry” compacted crushed salt specimen (D-OE-051/4) has adequate barrier properties in the residual porosity range even under high loads.

The crushed salt specimen **D-OE-099/1** which had already undergone higher compaction, underwent a similar programme of varying pressures and pulse tests during test phase 1.

After obvious leakages under low load, the applied axial pressure differential of 1.9 bar was equalised for after approx. 1 hour ($k = 9.5 \cdot 10^{-17}$ m²) under an external load of σ_3/σ_1 = 2.0/3.0 MPa in pulse test no. 2. Four days after raising the load to σ_3/σ_1 = 20/21 MPa, the applied pressure differential of 2.0 bar dropped to 0.6 bar during a measurement period of approx. 5 hours. The calculated permeability $k = 7.3 \cdot 10^{-18}$ m² is more than one order of magnitude lower than in pulse test 2, and was maintained even after lowering the external confining load to 2.0/3.0 MPa. This trend was largely verified during the subsequent test stages under load increases to σ_3 = 20 and 35 MPa. After the load in-

creases, the permeabilities were lower than before (factor 0.4 and 0.3), but did not rise to the same extent after reducing the loads (factor 1.6 and 1.3). The last pulse test gave a permeability of $k = 1.1 \cdot 10^{-18}$ m².

The permeability behaviour is very likely attributable to the compaction of the sample caused by the external load. The measurement after the test revealed that the volume had reduced by 1.1 cm³ ($\Delta e = 0.0015$). The associated density and void ratio of the almost unchanged mass of the sample are therefore $\rho = 2.1611$ g/cm³ and $e = 0.0089$ ($\Phi = 0.88$ %) respectively. Fig. 2.40 shows the core after the “dry” compaction/permeability test. The optically clear zones recognizable at the lower edge of the sample indicate the start of recrystallisation under “dry” conditions.

Fig. 2.40 Crushed salt core D-OE-099/1 after the “dry” compaction/permeability test

With the test using the **D-OE-099/02** crushed salt specimen, which was more than double the length, the around 3 mm large difference between the diameter of the sample and the pressure plates had to be equalised, which led to leakages under low loads. Fig. 2.41 and Fig. 2.42 show the changes in time of the test metrics p_in, p_out and the 10-times exaggerated average axial deformation (path) on the primary axis, as well as the measured flow and the mechanical confining stress (confining pressure) on the secondary axis.

A total of 15 pulse tests were carried out under external confining stress $\sigma_3 = 5$ or 20 MPa, and 7 long-term flow tests with different differential pressures between 5 and 15 bar under 5 MPa confining pressure. The permeabilities which were determined are shown in the diagram. The axial displacement measurements show elastic-plastic deformation related to the external change in loading. The measured, non-reversible sam-

ple compression in the constant loading phases, particularly with σ_3/σ_1 = 20/21 MPa, are a qualitative measure of the creep compaction which has taken place. Although the mass remains the same, the measurement of the sample after the “dry” test revealed a decrease in volume of almost 3 cm³ (Δe = 0.0019) with the following metrics:

ρ = 2.1598 g/cm³ and e = 0.0095 = 0.95 % (Φ = 0.94 %).

In pulse test P2, a permeability of $9.9 \cdot 10^{-16}$ m² was calculated under a confining stress of σ_3/σ_1 = 5/6 MPa, at 2 bar initial flow pressure. Tests P3 to P5 under confining pressures of σ_3/σ_1 = 20/21 MPa, and initial flow pressures between 2 and 10 bar, produced much lower values between $6.7 \cdot 10^{-18}$ and $4.8 \cdot 10^{-18}$ m² with a declining trend. When the load was reduced to 5/6 MPa, the calculated permeabilities rose again to $1.4 \cdot 10^{-17}$ and $1.6 \cdot 10^{-17}$ m² (P6, P7), but were still almost 2 orders of magnitude below the value determined in P2. After again raising the confining pressure to 20/21 MPa, tests P8 to P11 produced permeabilities between $3.6 \cdot 10^{-18}$ and $2.4 \cdot 10^{-18}$ m². These figures also have a declining trend and their absolute sizes tie in directly to the previous results determined under similar loads (P3 to P5). Overall, permeability under a confining pressure of σ_3/σ_1 = 20/21 MPa characterised by creep compaction, increases by almost half an order of magnitude (P3, P11 = $6.7 \cdot 10^{-18}$ m² and $2.4 \cdot 10^{-18}$ m², factor 0.36). The values for tests P12 to P14, again under σ_3/σ_1 = 5/6 MPa, lay between $7.9 \cdot 10^{-18}$ and $9.8 \cdot 10^{-18}$ m² so that they were again slightly higher than during the preceding loading stage. The rising trend is an indication of relaxation processes still taking place in the sample as a result of the reduction in load. The seven flow tests carried out in the following 3 days under a constant pressure gradient between 5 and 15 bar, produced an average permeability of $1.1 \cdot 10^{-17}$ m² (spread approx. 13 %). This figure was confirmed in the subsequent pulse test (P15).

Even with the already highly compacted cores from oedometer test 099 in the range e = 1 %, it has not been possible to verify complete barrier effectivity under natural (“dry”) moisture conditions.

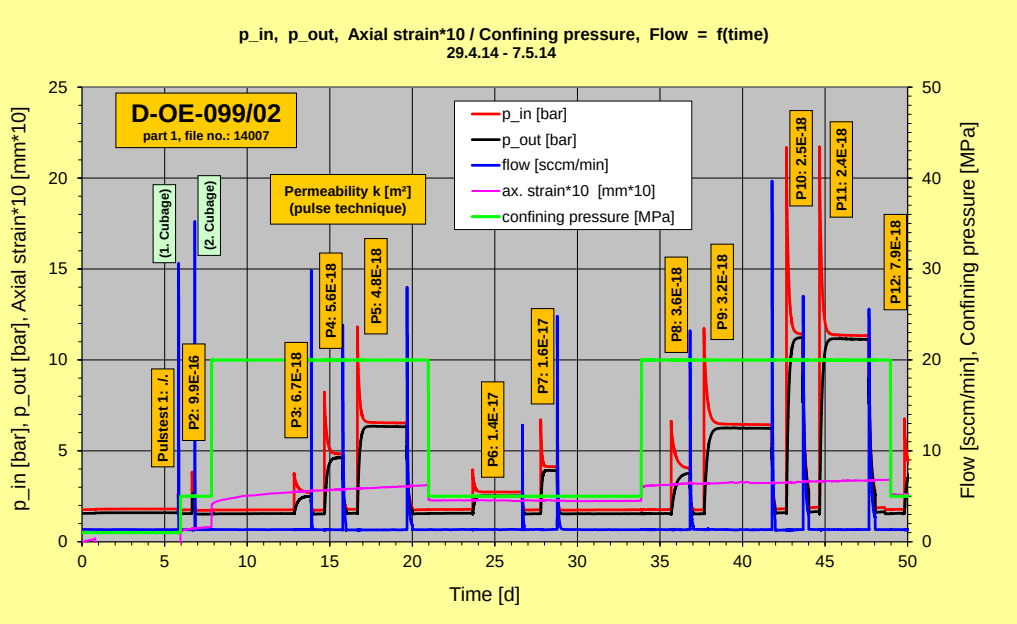

Fig. 2.41 Test run (part 1) on crushed salt core D-OE-099/02 ("dry" compaction/permeability test)

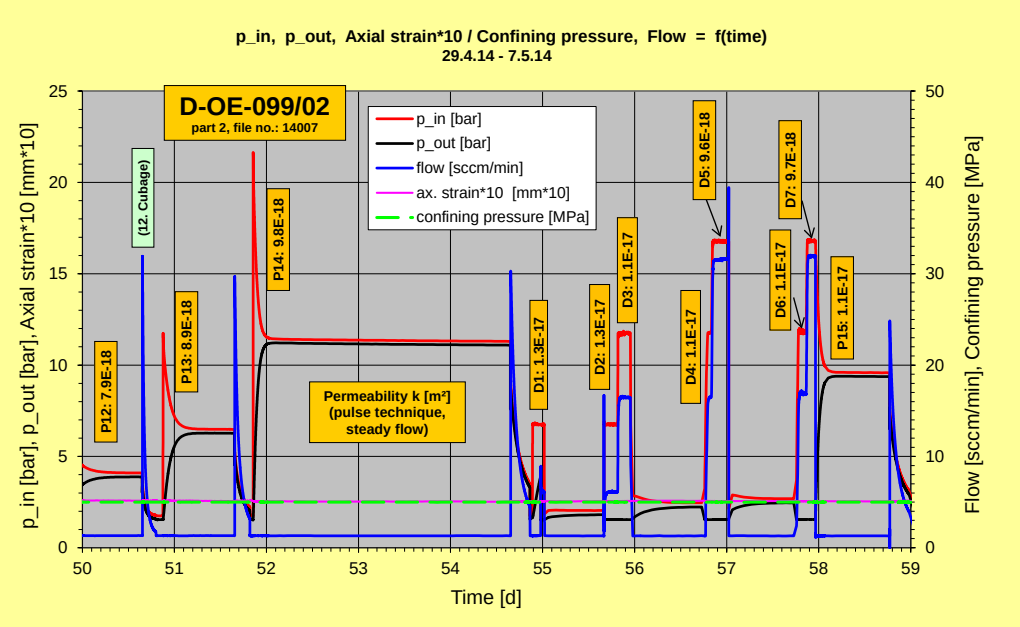

Fig. 2.42 Test run (part 2) on crushed salt core D-OE-099/02 ("dry" compaction/permeability test)

2.5.2.3 Results from “wet” material (test phase 2)

Test phase 1 carried out on “dry” material, was followed by placement of the samples for up to three weeks at a room temperature of approx. 22 °C in an exsiccator overlying a saturated NaCl-solution, but without any direct contact. The relative humidity under these conditions is approx. 75 %rh. The masses of cores 051/4, 099/01 and 099/02 increased as a result by 2.0 g, 1.9 g and 1.3 g respectively, and therefore proportionally by Δm = 0.12 %, 0.11 % and 0.04 % respectively. The measured volumes only increased marginally because of the relaxation of the samples. The samples were then placed back into the Z3 test apparatus in test phase 2 (“wet”), and again tested to determine their permeabilities.

Core D-OE-051/4 was tested in test **D-OE-051/4A** by being put under load for 30 days with a confining pressure of 10 MPa prior to carrying out the pulse test. To avoid drying out as a result of flow, the gas was passed through a washing bottle with a brine before entering the sample. Pressure equalisation via the sample took 4 – 5 hours during a pulse test with a differential pressure of 1.6 bar. The permeability calculated from this result was $k = 1.0 \cdot 10^{-16}$ m², and therefore two orders of magnitude smaller than in test phase 1. No flow was registered after increasing the confining pressure of the sample to 20 MPa for 14 days under the same differential pressure. The sample was then depressurised in steps of 2 MPa with 6 – 7 days between each reduction step until the confining pressure reached 4 MPa. No significant reduction in pressure was registered during the whole test procedure lasting more than 70 days. The permeability calculated from this was $k = 1.2 \cdot 10^{-21}$ m².

The inductively measured axial deformation, and the measurement of the sample after the test confirmed that sample D-OE-051/4 had been further compacted (creep compaction) during the phase 2 test lasting 118 days. A loss in volume of 20 cm³ (Δe = 0.0260), was determined, as well as a loss in weight of 1.1 g compared to the initial state when installed in the test apparatus. The density and void ratio calculated from this for the unloaded state where ρ_S = 2.1803 g/cm³ are ρ = 2.140 g/cm³ and e = 0.0187 (Φ = 1.84 %) respectively. Assuming that the changes in mass which were measured were exclusively attributable to the moisture, and had no influence on the proportion of pores, there was then a slightly higher void ratio with e = 0.0192 (Φ = 1.88 %).

Prior to the test, the density and void ratio of core D-OE-099/1 were ρ = 2.1622 g/cm³ and e = 0.0095 (Φ = 0.94 %) respectively, when the moisture input was taken into consideration according to /KRÖ 09/, Section 4.4.2, eq. (4.13). In experiment **D-OE-099/1A**, it was loaded for 10 days with σ_3/σ_1 = 20/21 MPa after a four-day compression phase to achieve consolidation. Several pulse tests (without a washing bottle), with gas pressure differentials up to 10 bar, gave rise to permeabilities in the 10^{-21} m² range or smaller. The results stayed at the edge of the verifiable limit even after reducing the load to 5/6 MPa (7 d). Higher permeabilities were determined in some cases under minor loading σ_3/σ_1 = 2/3 MPa (14 d), but were probably attributable to artefacts. No reduction in pressure was registered over a period of 5 days under a confining pressure of σ_3/σ_1 = 3/4 MPa, and a gas pressure differential of 10 bar. With a calculated value of $k = 3.3 \cdot 10^{-22}$ m², the sample can be considered impermeable.

After removal from the apparatus, the sample weighed 1.6 g less than prior to the last test. The reason for this is unclear. The removal of moisture to this extent by the nitrogen during the flow phases is unlikely because of the low decline in pressure. No damage to the sample was observed. However, the test specimen was further compacted during the “wet” test phase. The calculated volume had declined by 6.9 cm³ (Δe ≈ 0.008). The corresponding density and void ratio were ρ = 2.1796 g/cm³ and e ≈ 0.001 respectively.

Test specimen D-OE-099/02 which took up relatively minor amounts of moisture in the exsiccator, was tested to determine the permeability in test number **D-OE-099/02A** with nitrogen, which was not passed through a washing bottle in this case as well. Fig. 2.43 shows the load path (σ_3), the p_in and p_out, and the axial compression (10-times exaggeration) during the test lasting 59 days.

Just as in the test on the “dry” sample D-OE-099/02, the axial displacement measurement indicated elastic-viscous deformation analogous to the external loading. The digressive rise in compression as an indicator of the compaction taking place, is again much higher under “wet” conditions. The calculated volume loss was 14.2 cm³ (Δe = 0.0087 = 0.87 %). This is more than four times as high as in the “dry” sample, (Δe = 0.19 %), even though the high 20 MPa loading stage during the “dry” test was maintained for almost twice as long.

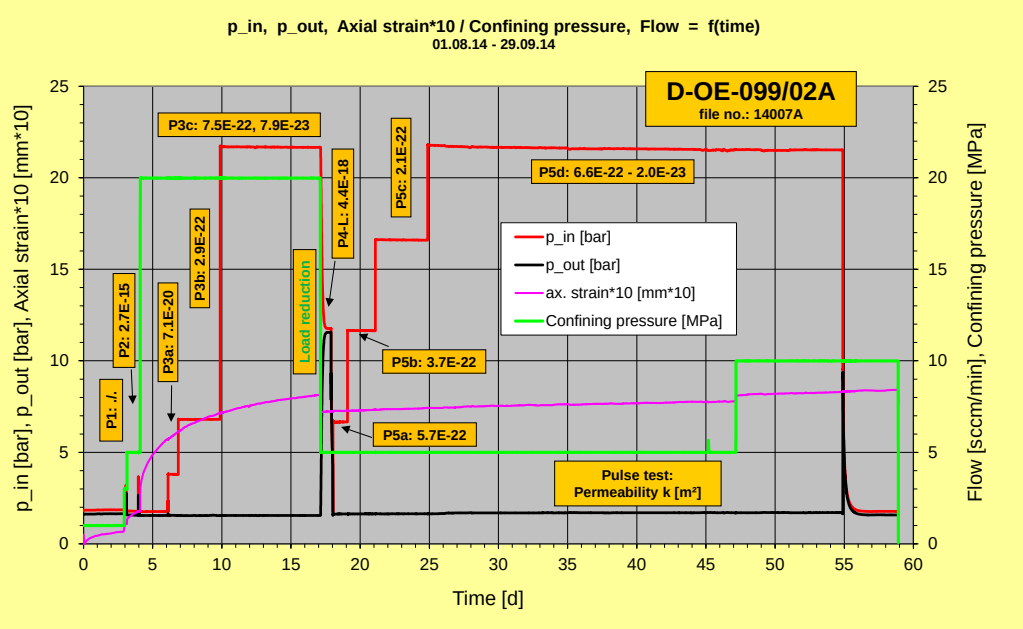

Fig. 2.43 Test run on crushed salt core D-OE-099/02A ("wet" compaction/permeability test)

Significant flow (pressure equalisation via the sample in the pulse test) is only observed in test sections P1 (completely permeable), P2, and in P4-L after reducing the load at t = 17.1 d. This may be due to the influence of artefacts. Transmissivity along the butt joint of the equalisation confining sleeve is highly likely during test P1, at least under low confining pressure conditions σ_3/σ_1 = 3/4 MPa. After raising the load to σ_3/σ_1 = 5/6 MPa, the permeability in test P2 under Δp =1.6 bar, was still at a level of k = $2.7 \cdot 10^{-15}$ m². This is 2 to 3 orders of magnitude higher than in the previous test from the "dry" sample under the same conditions.

A low permeability of $7.1 \cdot 10^{-20}$ m² was calculated under a confining pressure of σ_3/σ_1 = 20/21 MPa, but only at the immediate start (P3a). During the remaining tests, there was usually a very minor but continuous decrease in the applied flow pressure ("Z3 p_out"), but without any corresponding increase in the component at the other end of the specimen ("Z3 p_in"). This finding means that the sample can be considered impermeable even though the cause of the declining pressure on the input side remains unclarified. The calculated permeabilities are in the range of 10^{-22} m² and lower.

The start of pressure equalisation was registered from a pressure of approx. 7 MPa after dropping the confining pressure from 20 to 5 MPa (adjusted by hand, duration approx.

40 minutes). The differential pressure under σ_3/σ_1 = 5/6.2 MPa was still 0.5 bar after approx. 6.5 hours, and complete equilibrium had been established after approx. 11 hours. The calculated permeability value from this result of $k = 4.4 \cdot 10^{-18}$ m² (P4-L) must also be considered under the aforementioned reservation, because no permeability was measurable any more under the same confining pressure with differential pressures of up to 20 bar in the subsequent pulse tests (P5a – P5d) ($k < 7 \cdot 10^{-22}$ m²).

Fig. 2.44 is a typical example to show the sensitive evaluation of the measuring results: it shows a high resolution plot of the pressure components with an offset scale for pulse test 5d (25 d < t < 55 d) under confining pressures of 5 and 10 MPa. The registered "Z3 p_out" and the "p_out_sc" scale value used to calculate the pressure difference, drop by around 0.2 bar between t = 26 d and 45 d. By contrast, the rise in pressure on the upper face of the sample ("Z3 p_in") after a consolidation phase at t = 26 d is only around one tenth of this value. The pressure difference Δp is critical for the evaluation. The permeability is calculated from the rise (-α) of the term $\ln(\Delta p/\Delta p_0)$. The oscillation of the pressure curve is primarily attributable to the fluctuations in room temperature which have an influence on the measuring instruments. For quality assurance, test sections with relatively constant values were selected and separately evaluated. The results spread by less than one order of magnitude 10^{-22} m².

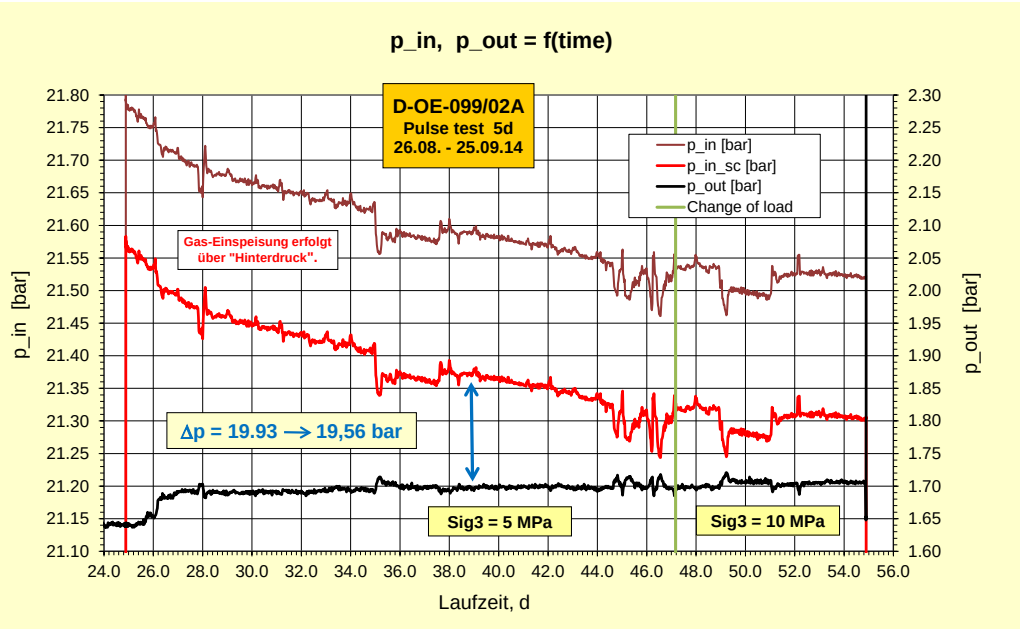

Fig. 2.44 Crushed salt core D-OE-099/02A: pressure measurements in pulse test 5d ("wet" compaction/permeability test)

After raising the confining pressure from 5 to 10 MPa at the end of the test, the calculated permeabilities drop by around one order of magnitude in part to the range of 10^{-23} m².

2.5.2.4 Results with "dried" material (test phase 3)

To test whether a fluid film developed in the pore space as a result of its absorption of moisture, and whether this gives rise to a capillary seal pressure, two of the three samples were placed in a warming cabinet at 40 °C to dry them out.

After 7 days in the warming cabinet, the mass of core D-OE-051/4 (e ≈ 1.9 %, see above) dropped by around 1.3 g. Renewed measurement with the slide gauge also gave a slight decrease in the calculated sample volume of almost 2 cm³ (V = 780.5 cm³). The density only changed to a minor degree at ρ = 2.144 g/cm³. Based on a solid density of ρ_S = 2.1803 g/cm³, this gives a void ratio of e = 0.0171 (e = 1.71 %, Φ = 1.68 %).

After being placed back into the Z3 triaxial test apparatus, the sample in test phase 3 (**D-OE-051/4B**) again had an easily measurable permeability of k = $2.0 \cdot 10^{-16}$ m² under an initial pressure of 4 MPa. This renewed transmissivity is attributed to the deconsolidation of previously "healed" or only blocked migration paths, because possible leakages are considered unlikely with a confining pressure of 4 and 5 MPa. However, after increasing the loading to 20 MPa, there was again almost no pressure equalisation in the pulse test. This situation remained unchanged even during the repeated step-wise depressurisation down to 4 MPa. The calculated permeability in this case is less than $5 \cdot 10^{-21}$ m². Measuring the dimensions of the sample after removal from the apparatus revealed a volume loss of ΔV = 2.9 cm³ (= 0.37 %). The density of the obviously further compacted sample, with an otherwise unchanged mass was calculated as ρ = 2.1517 g/cm³. The calculated void ratio was e = 0.0133 (e = 1.33 %, Φ = 1.31 %).

The mass loss of the "wet" core D-OE-099/1 after 35 days in the warming cabinet at T = 40 °C was 0.3 g. In the subsequent permeability test in the Z3 apparatus (test phase 3: **D-OE-099/1B**), no measurable permeability could be registered (permeabilities in the 10^{-22} m² range) under loading of σ_3/σ_1 = 5/6 MPa and 10/11 MPa, and gas pressure differentials of up to 40 bar. A minor loss in mass of 0.3 g was again determined with a "dry" specimen after the end of this test lasting over 80 days. The calculated geometrical loss in volume (compaction) was, however, less than 0.5 cm³. This gives a density of

ρ = 2.1794 g/cm³. The void ratio calculated assuming a solid density of ρ_S = 2.1803 g/cm³ is therefore less than e < 0.001 (e < 0.1 %). Bearing in mind the achievable measuring accuracy when determining the volume, and an assumed solid density, the sample can be considered to be completely compacted, and therefore an effective barrier. Drying with a renewed permeability test on core 099/2 has so far not been carried out.

2.5.2.5 Permeability test on "wet" compacted material

In oedometer test 105, crushed salt moistened with the addition of 1 wt-% brine was compacted (cf. Section 2.4.1). Two horizontal cracks arose when squeezing it out of the oedometer cell. This was not detrimental to further use because the parts could be exactly put together again. According to the weight balance, around 106 cm³ of the 137 cm³ added brine was squeezed out during the oedometer test, even though the available pore space in the sample was not yet saturated. Mass, volume, (dry) density and void ratio were determined after the test when the specimen was in an unloaded condition: m = 15071.6 g, V_E = 7068.0 cm³, ρ_E = 2.127 g/cm³ and e_E = 0.0197 (Φ = 1.93 %). The compacted sample was then stored in a warming cabinet at T = 40 °C for 87 days. The sample weight diminished constantly at around 0.133 g/d after relatively fast weight loss during the first 3 days (2.5 g in 69 hours). At the end of the period in the warming cabinet, it weighed 15058 g. If it is assumed that the evaporated mass of 13.6 g consisted exclusively of water, then this involves a brine mass of 13.6/0.8784 = 15.5 cm³ containing a salt mass of 15.5·0.3216 = 5.0 g or 5.0/2.169 = 2.3 cm³ volume. If one then adds the amount of crystallised salt remaining in the sample to the existing mass of the crushed salt, this gives an actual dry crushed salt density of ρ_{E*} = 2.1278 g/cm³ and a void ratio of e_{E*} = 0.0193 (Φ = 1.90 %), which is slightly less than prior to the drying. The percentage of brine still remaining in the sample is calculated as 0.12 wt.-%. After the warming cabinet phase, the sample was stored in BGR's (air-conditioned) core store. Renewed weighing and measuring after 40 days revealed no significant changes.

The test specimen for test D-OE-105/01 with d = 100 mm, was cut with a lathe from a vertical position out of the (ruptured) core of the oedo-105 test. Fig. 2.45 shows the new test specimen (middle of the left-hand photograph) with the remaining parts immediately after production. The picture on the right shows the sample after the permeability test

under triaxial load described in the following. The fractures have healed and are hardly recognisable any more.

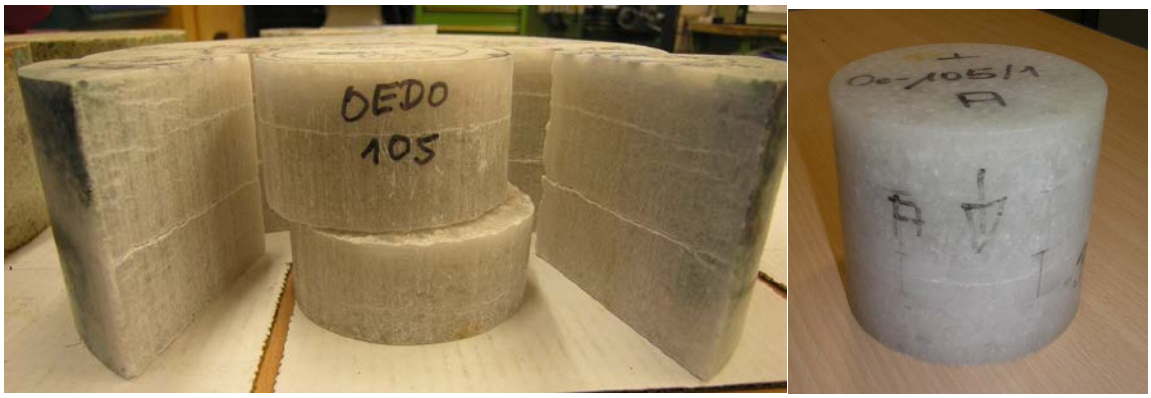

Fig. 2.45 Crushed salt core D-OE-105/01 with sample remains, and the core after the triaxial compaction/permeability test

Before the test started, the core weighing 1577.2 g (m^f) had the dimensions d/h = 100.02/93.67 mm, and therefore a volume of V_0 = 736.0 cm³. Assuming the last calculated proportion of brine of 0.12 %, the remaining mass of brine is 1.9 g (1.6 cm³), and the solid salt mass m^{tr} = 1575.3 g. The solid volume is 1575.3/2.169 = 726.3 cm³, the dry density of the core ρ^{tr}_0 = 1575.3/736.0 = 2.1404 g/cm³, and the void ratio e_0 = (2.169/2.1404)-1 = 0.0133 (Φ = 1.31 %). The void ratio behind the third decimal point is therefore smaller than in the complete sample (e = 0.0193, see above), which lies within the range of the achievable compaction and measuring accuracy. The following values were measured after the test: V_E = 731.1 cm³ (ΔV = 4.9 cm³), m^f = 1576.8 g. Assuming that the minor loss in weight of 0.4 g was exclusively due to squeezed out brine (0.3 cm³), there was no change in the dry mass of the sample. The calculated density is ρ^{tr}_E = 1575.3/731.1 = 2.1404 g/cm³. The void ratio has almost halved with e_E = (2.169/2.1548)-1 = 0.0066 (Φ = 0.66 %).

Fig. 2.46 shows the plot of the loading and reactions during the triaxial compaction and permeability test D-OE-105/01. The graph shows the p_out on the lower face of the sample, the developing p_in (upper face) and the resulting difference. The confining pressure shows the outer confining pressure of the core during the test. The axial sample compression (path) shown with an exaggeration of ten times, can be taken as a qualitative measure of the compaction occurring during the test. Under an initial pressure of 1 MPa during the first 36 days, the sample already showed clear creep deformation, alt-

hough this could also have been influenced by the cracks which were present at the start. A clear jump in compaction with a large elastic-plastic share and subsequent creep compaction then took place after raising the load to 20 MPa. The subsequent axial deformation under slight creep compaction then qualitatively matched the external changes in load.

After a standstill of 36 days caused for technical reasons, under an external load of σ_3 = 1 and σ_1 = 2 MPa, a pulse test with Δp = 2 bar differential pressure which was carried out indicated a permeability of k = $2.7 \cdot 10^{-17}$ m² (P1). Artefacts (leakages) could not be excluded, however, because of the low confining pressure.

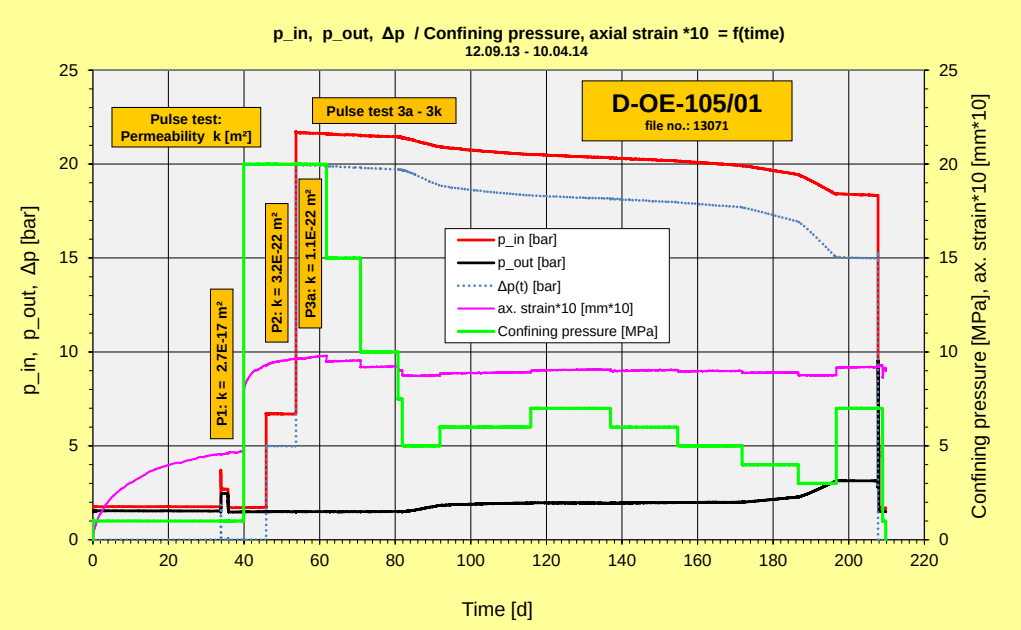

Fig. 2.46 Plots of the test on crushed salt core D-OE-105/01

On the 40th day of the test, the external load was raised to σ_3/σ_1 = 20/21 MPa. The P2 pulse test with Δp = 5 bar produced a calculated permeability of k = 3.2E-22 m²; when the differential pressure was raised fourfold to almost 20 bar, almost the same result was achieved (P3a: Δp = 19.9 bar, k = $1.1 \cdot 10^{-22}$ m²). This test arrangement with closed front and rear pressure chambers was maintained up until the end of the test after 207 days. The only thing that changed was the external loading. The result is shown in Fig. 2.47 with a higher resolution from t = 50 d. The applied p_out decreases over the course of the whole of pulse test phase 3, but a rise in pressure is only registered on the opposite face of the sample in phases 3d, 3e, 3i and 3j. In phases 3a to 3c at confining pressures

of 20, 15 and 10 MPa, the p_out (absolute pressure) for instance, as well as the calculated pressure differential declines by 0.26 bar in 27 days, whilst the p_in remained unchanged. The continuing loss can be approximately estimated at around 0.01 bar/d. This is probably attributable to an unidentified leak in the measuring system which has nothing to do with the permeability of the sample. Independent of this fact, the values are conservatively taken into consideration in the permeability calculation. As shown in Fig. 2.47, the calculated permeability values in most of the test phases lie in the range of 10^{-22} to 10^{-23} m². The calculated values only rise by one order of magnitude to $1.2 \cdot 10^{-21}$ m² or $3.6 \cdot 10^{-21}$ m² after lowering the confining pressure from σ_3/σ_1 = 10/11 MPa to σ_3/σ_1 = 5/6 MPa in phase 3d, and from σ_3/σ_1 = 4/5 MPa to σ_3/σ_1 = 3/4 MPa in phase 3j. The values returned to the previous level after increasing the external load again.

The consolidation of the core from e = 1.33 % to e = 0.66 % revealed by the void ratio determination on the unloaded sample before and after the test, is reflected in the trend in the calculated permeabilities. In the first half of the test, the limited influence of the external confining pressure on the permeability lies in the 5 to 7 MPa range, but in the 3 to 5 MPa range in the second half. Overall though the calculated permeabilities with $k < 4 \cdot 10^{-21}$ m² throughout the test – also with external loads below the confining pressures expected in situ – are so low that no significant permeability could be detected.

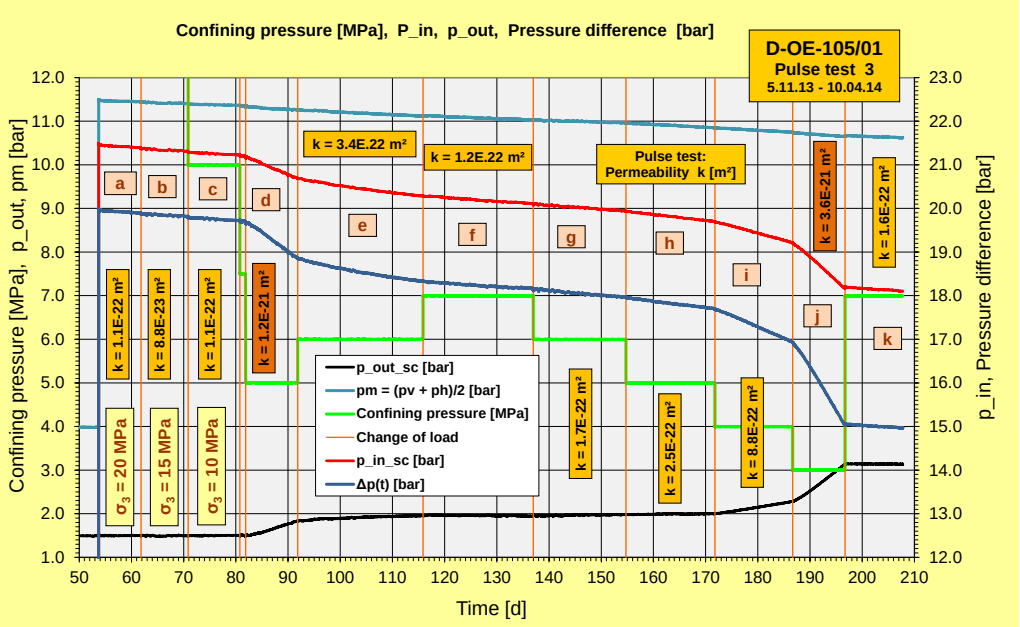

Fig. 2.47 Flow pressure measured on crushed salt core D-OE-105/01 from t = 50 d

2.5.2.6 Evaluation of the permeability tests with moisture

With the results of the tests described here carried out on specimens pre-compacted in an oedometer and consisting of laboratory-wet (“dry”) crushed salt, the influences of the existing porosity, the external load (triaxial confinement), and the spontaneous influence of moisture on the barrier behaviour of the already highly compacted crushed salt is identified and delimited. The results are confirmed by the findings in a crushed salt core which was slightly moistened prior to the start of the compaction process. There is therefore still no evidence to indicate that the time at which the moisture enters the sample has any fundamental influence on the compaction and permeability behaviour of crushed salt. Although the figures quoted here with respect to their absolute sizes are subject to provisions regarding measurement accuracy, they show a clear trend when compared with one another.

In sample 051/4 with a void ratio of $0.05 > e > 0.04$ (4 – 5 %), no barrier effectiveness could be determined in a “dry” state even under high confining pressures ($k = 2 \cdot 10^{-14}$ – $1 \cdot 10^{-14}$ m²). Permeabilities in the range $10^{-17} > k > 10^{-18}$ m² were measured in samples 099/01 and 099/02 with $e \approx 0.01$ (1 %).

The externally applied load (confining pressure with 2-5 MPa < σ < 20 or 35 MPa) influences the measured permeability up to around one order of magnitude, whereby the load case “high compaction – low confining pressure” is not relevant in situ under continuous compaction and the associated growing formation pressure. The compaction effect is also limited in the case of “dry” crushed salt samples even under high loads during the relatively short laboratory test periods. In the case of the less compacted sample 051/4 $\Delta e = 0.0142$ (1.42 %), and in the case of sample 099/01 and 099/02, it was $\Delta e = 0.0015$ (0.15 %) and 0.0019 (0.19 %) respectively.

The mass of the sample rose by 2.0, 1.9 and 1.3 g, and therefore proportionally by 0.12 %, 0.11 % and 0.04 % respectively after storing samples 051/4, 099/01 and 099/02 for one to three weeks above a brine but with no direct contact. This spontaneous treatment of the highly compacted crushed salt samples with moist air gave rise to a clear change in compaction and permeability behaviour. The reduced backfill resistance in the “wet“ state gives rise to a much higher compaction under triaxial load than in the “dry“ state. The moisture within the samples can influence the healing of the migration paths

(recrystallisation), as well as temporarily or permanently closing the migration paths by way of the bottleneck effect.

In test phase 2 on sample 051/4, the permeability measured after being confined under a pressure of σ = 10 MPa for 30 days was $k = 10^{-16}$ m², in other words, two orders of magnitude lower than when measured in the dry state. After raising the loading to 20 MPa, and also after subsequent stepwise depressurising down to 4 MPa, no additional decline in pressure was registered across the sample (standstill for a total of 70 days). A void ratio of e = 0.0192 (Φ = 1.88 %) was determined after the test, which indicates a further compaction of around Δe = 0.026.

After drying at 40 °C for 7 days (mass loss of 1.3 g), sample 051/4 again had an easily measurable permeability of $k = 2.0 \cdot 10^{-16}$ m² in test phase 3 under an initial pressure of 4 MPa. If artefacts can be excluded, the fluid film formed in the pore space during test phase 2 had obviously lost its effect after drying and deconsolidation. However, after raising the load to 20 MPa, followed by another period of depressurisation down to 4 MPa, the pulse test failed again to measure any kind of pressure equalisation. Here again, the compaction of around Δe = 0.013 which also took place in phase 3 is thought to be the main cause. A void ratio of e = 0.0133 (e = 1.33 %, Φ = 1.31 %) was calculated from the final measurement of the dimensions. This therefore reached the porosities of the two other samples in test phase 1.

In test phase 2 on sample 099/01 after moistening, and after the various confining pressures, no pressure equalisation was registered across the sample in the pulse test. K-values of maximum $7 \cdot 10^{-21}$ m² were calculated under the confining pressure of 20.5 and 3 MPa. Artefacts are considered the likely cause of the two measurement results in the 10^{-19} m² range. Compaction was Δe = 0.008, so that the void ratio had declined to around 0.001 (e = 0.1 %). The barrier effect was maintained even after drying the sample (40 °C) for 7 days with a mass loss of 0.3 g.

In core 099/02 which was tested as well, but had absorbed a much lower amount of moisture (0.04 %), no transmissivity could be measured in most of the approx. 20 evaluations ($k < 10^{-21}$ m²). Two measurements under slight confining pressure produced permeabilities in a range of 10^{-15} and 10^{-18} m², but are very likely to be caused by artefacts.

A void ratio of e < 0.1 % was determined after the test on the unloaded core. Special drying of the sample with renewed permeability testing was not carried out afterwards.

The results are confirmed by test 105/01. The cylindrical sample is part of a specimen consisting of crushed salt with added brine compacted in an oedometer. Of the initial amount of brine absorbed by the specimen amounting to 1 wt-%, a significant proportion was squeezed out during compaction, or extracted from the sample again during the subsequent drying in a warming cabinet at 40 °C. The remaining volume at the start of the flow test under triaxial load was estimated to be 0.12 wt-%. At porosities of between 1.3 % and 0.7 %, very minor pressure equalisation was registered in only a few pulse test phases dependent on the external loading. The permeabilities calculated from this are maximum $4 \cdot 10^{-21}$ m². The influence here of the external loading on the permeability is also in the range of one order of magnitude. This finding can be considered for the time being as the reference for extrapolating the results from unloaded samples to in situ conditions.

The investigations revealed that “laboratory-dry” crushed salt is still permeable to gases even after a high level of compaction, and develops no barrier effect. The significant transition zone lies at porosities of e < 0.01 – 0.02 (1 - 2 %). However, because of the nature of the material, this value already lies within the range of determination accuracy according to /STÜ 09/. Nevertheless, actually still present or spontaneously influencing levels of moisture do have a crucial influence, which can generate a barrier effect in connection with the accelerated compaction, under pressures which are relevant in situ.

The findings discussed here must be verified by other tests and quantitatively expanded. This requires more precise determination of the porosity and/or the void ratio even during the test on loaded samples.

Microscopic or other investigations to analyse the pores have not been undertaken so far on the crushed salt samples still available. They are considered to be a prudent addition to the macroscopically derived findings.

2.6 Constitutive relations for two-phase flow

2.6.1 Introduction

Because of the extremely low permeability of undisturbed rock salt it is expected that fluids will only enter the repository via shafts and drift seals. Eventually, the brine will also come into contact with the backfill. This implies that an initially dry section of the backfill will be wetted. Two distinct phases, air and brine, can subsequently be found in the pore space. The dynamics of the related wetting depend not only on porosity and permeability but also strongly on two constitutive relations (CRs): the capillary pressure-saturation relation (CPS) and the relative permeability-saturation relation (RPS) (e.g. /HEL 97/).

The porosity-permeability relation that is required to describe single-phase flow in such an environment has been subject to numerous experimental investigations, and is rather well known (e.g. /KRÖ 09/). Despite the obvious necessity to consider unsaturated or two-phase flow in a repository, data on the CRs for crushed salt are still quite scarce. They are restricted to a certain degree of compaction, and are either providing only CPS /MAL 15/ or referring to a material of single grain size /CIN 06/. The data presently available therefore lacks information on relative permeability of crushed salt with a repository-relevant grain size distribution as well as on the dependency of the CRs on the degree of compaction i.e. porosity.

The idea of applying Leverett's J-function to extrapolate the CPS must be dismissed as this scaling rule is based on the assumption of similarity of the pore space topography /LEV 41/. Furthermore this rule is known to fail for sand- and limestone if applied to permeability variations of more than two orders of magnitude /HAR 01/.

2.6.2 Scope

Presented here are therefore test results to derive CRs for crushed salt with a repository-relevant grain size distribution. The material is tested at different degrees of compaction and thus allows already for a first insight into the nature of CRs for repository-relevant backfill material as well as into the impact of compaction on the CRs.

In advanced stages a comparatively little porosity decrease can lead to permeability changes over orders of magnitude. For the investigations presented here, different degrees of compactions were chosen based on the following target brine permeabilities: 10^{-14} m², 10^{-15} m², and 10^{-16} m². Testing covered two pre-tests (P) with samples called “P1” and “P2a” and “P2b”, respectively, to demonstrate the feasibility of the test in general and to examine the test procedure. Due to a technical error during preparation, the unsaturated part of the actual first main test (M) was spoiled. The single-phase flow parameters of the two referring samples “M0a” and “M0b”, however, were determined. This was followed by two main tests with samples “M1a” and “M1b” as well as samples “M2a” and “M2b”.

2.6.3 Preparations

Samples

Crushed salt from the Gorleben mine was used for the experiment. The grain density of the crushed salt material was measured to amount to 2,183 g/cm³. The grain size distribution was chosen to fit in with the possible backfill material that had been investigated in several earlier projects on crushed salt (e.g. /ROT 99/, /KRÖ 15/, see Appendix G of the main report). Maximum grain size of the material was 8 mm.

Samples were prepared in a hollow steel cylinder by axial compaction from both sides. Tentatively prepared samples under compaction from just one cylinder end had shown in ultra-sonic control measurements a considerable inhomogeneity along the sample axis (for details see Appendix F).

The cylindrical samples had a designed length of 100 mm and a diameter of 50 mm. The amount of crushed salt material required for the samples thus depended on the respective target porosity, 10 %, 7.5 %, and 5.5 % which was derived from a data compilation for the porosity-permeability relation of crushed salt /KRÖ 09/ to meet the previously defined target brine permeability values.

Fluids

The brine used in the test had to be saturated with the same salt with which the samples had been prepared to avoid solution of sample material in the presence of brine. Determined in the laboratory were a density of 1.20157 g/cm³ and a viscosity of 2.303 mPa*s.

Nitrogen was used where gas was involved in the test. Since all measurements were performed under room temperature the related gas viscosity was 0.0174 mPa*s.

2.6.4 Test procedure

For each test several cylindrical samples were prepared to match a target permeability which was checked by gas permeability tests of the air-dry samples. Well-suited samples were flooded with the pressurized brine applying additionally a vacuum at the other end of the sample to minimize the remaining air saturation. Subsequently, the brine permeability was measured. The single-phase flow parameters for all samples are compiled in Tab. 2.8 (see section 0).

Unsaturated conditions were initiated by applying gas pressure at one side of the sample while monitoring the opposite side for gas and brine outflow. The gas pressure was carefully increased in steps to identify the gas entry pressure as it can only be narrowed down to the range between two consecutive gas pressure levels.

When outflow occurred and came close to steady-state the amount of expelled brine allowed calculating the actual brine saturation of the sample. This saturation together with the related injection pressure constituted the first point in the CPS-curve. The gas outflow rate, observed in parallel, lead to an effective gas permeability providing eventually the first point of the RPS-relation.

Further points constituting these curves were gained by the same procedure: increase the gas pressure, measure brine outflow until reaching equilibrium and measure the related gas permeability.

The test was terminated when the increase of injection pressure did not result in further brine outflow. Air entry pressure and residual brine saturation are compiled in Tab. 2.9.

After dismantling the sample the remaining amount of brine was measured for a consistency check of initial brine content and outflow against the final brine content.

Note: The test set-up is not entirely consistent with an inflow scenario. It is rather applicable to a situation where the backfill is already fully brine saturated and gas production starts to de-saturate the backfill again.

2.6.5 Tests

Pre-test 1

The pre-test was performed in a Hassler-type cell. To prevent the testing fluids from circumventing the sample during hydraulic testing the sample was placed in a rubber jacket which was then loaded by a circumferential pressure exceeding the injection pressure by 2 bar.

The results of the pre-test (for details see Appendix F) have been published in /KRÖ 15/. While the determined CPS and RPS curve show a shape characteristic for two-phase flow, relative permeability at residual brine saturation was conspicuously low. It was thus suspected that the brine in the pore space had reduced the mechanical resistance to compaction to the point where the overpressure on the rubber jacket would result in a significant reduction of the pore volume and thus of the single-phase gas permeability. To check this effect a second pre-test was performed.

Pre-test 2

After measuring the gas permeability the samples were saturated under vacuum and installed in the Hassler cell. Saturated brine was then injected as in pre-test 1. After breakthrough it was additionally circulated to minimise possible solution or precipitation effects in the pore space. Fig. 2.48 shows the evolution of the brine permeability for samples P2a and P2b.

The data shows a more or less linear decline of the permeability for both samples from $2.0 \cdot 10^{-14}$ m² to $2.0 \cdot 10^{-15}$ m² and from $1.1 \cdot 10^{-14}$ m² to $2.0 \cdot 10^{-15}$ m², respectively, over a period of about 10 days. After these 10 days, the permeability value does not change sig-

nificantly for some time (38 and 14 days, respectively) before the permeability decreases quickly. The curves end when no outflow could be measured within the accuracy of the test method.

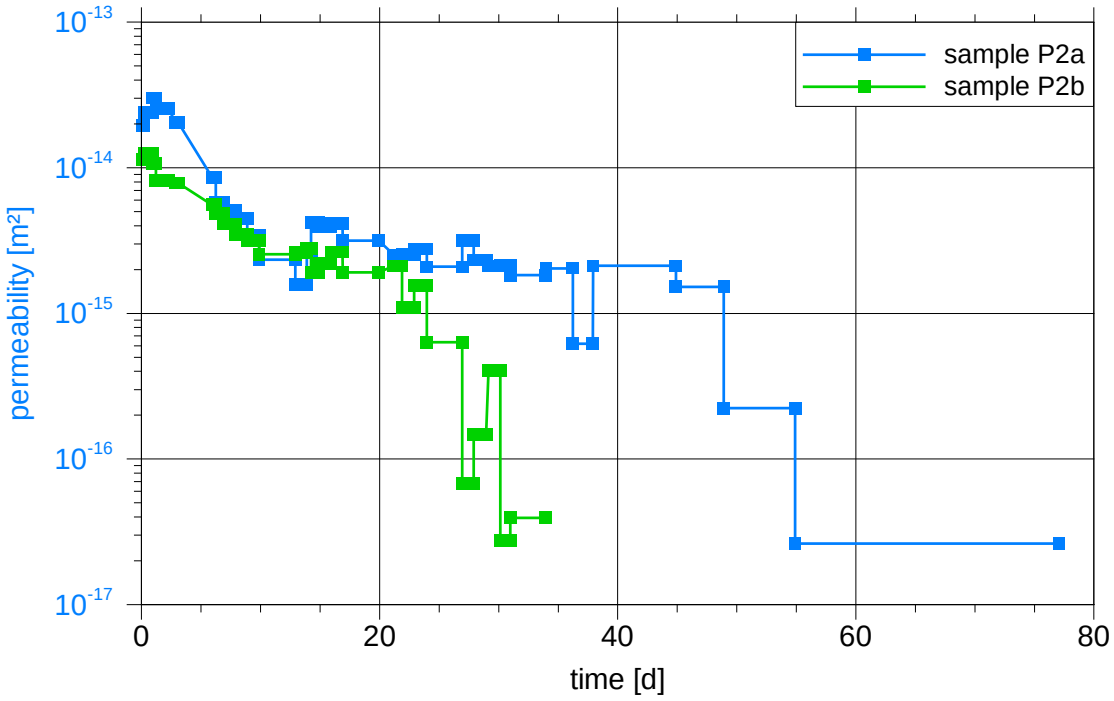

Fig. 2.48 Brine permeability in tests with samples P2a and P2b

The first decline of permeability was interpreted as the result of the overpressure from the rubber jacket while no conclusive explanation could be found for the second and final decrease. To avoid this effect the test design was changed for the main tests. As it turned out later, though, this did not help to prevent a considerable decrease of the permeability.

Main test 1

While sample preparation was performed for the main test as in the pre-test, the samples for the main tests were afterwards inserted in steel tubes instead of a Hassler cell to avoid the suspected compaction from the excess pressure on the rubber jacket. The remaining annulus between sample and tube was filled with a low-viscosity epoxy resin. To ensure that only the annulus was filled but not the pores of the sample, a tentatively prepared sample was opened up with a saw. Very little of the epoxy resin, indeed, had

entered the pore space thus leaving the sample basically free of alterations (see Fig. F.6 in Appendix F). The whole improved test set-up is sketched in Fig. 2.49.

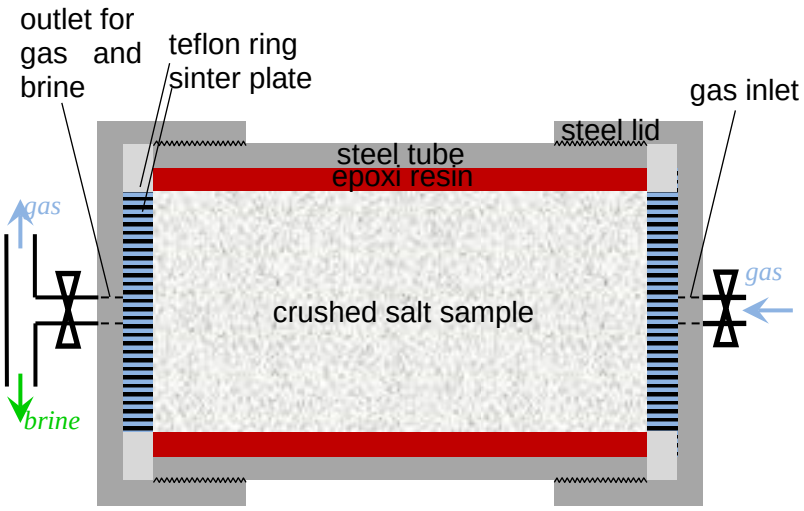

Fig. 2.49 Improved test set-up (sketch true to scale).

The test procedure was essentially the same as in the pre-test. However, more emphasis had unintentionally been placed on reaching steady-state in the outflow and to ensure full collection of brine during each pressure level as close as possible. The resulting evolution of injection pressure, cumulative mass of brine and gas permeability is discussed in detail in Appendix F. Exemplarily, the data for sample M1b are visualised in Fig. 2.50.

Outflow of brine from sample M1b at the initially very low injection pressure was not accompanied by gas flow and is thus interpreted as brine flow through the sample draining the design-inherent unavoidable additional brine-filled volume at both ends of the cell. Air entry pressure was reached only when gas was flowing through the whole sample.

The decrease of gas permeability during each load step is interpreted to be a consequence of a complex interplay of several effects and processes. The first consideration here is that the local gas pressure in a sample is conveyed via the capillary pressure also to the liquid phase thereby introducing a pressure gradient in the liquid phase as well. As a consequence, a certain brine displacement towards the outlet is suspected to occur. In the presence of open flow channels for the gas, however, this does not necessarily result in an outflow of brine from the sample. A fraction of the brine mass might as well simply have been redistributed along the sample axis, more precisely from the inlet

towards the outlet because in this case the local brine saturation increases with a decreasing gas pressure. As a result the flow channels for the gas become widened at the inlet and at the same time constricted at the outlet forming a bottleneck for gas flow at the outlet.

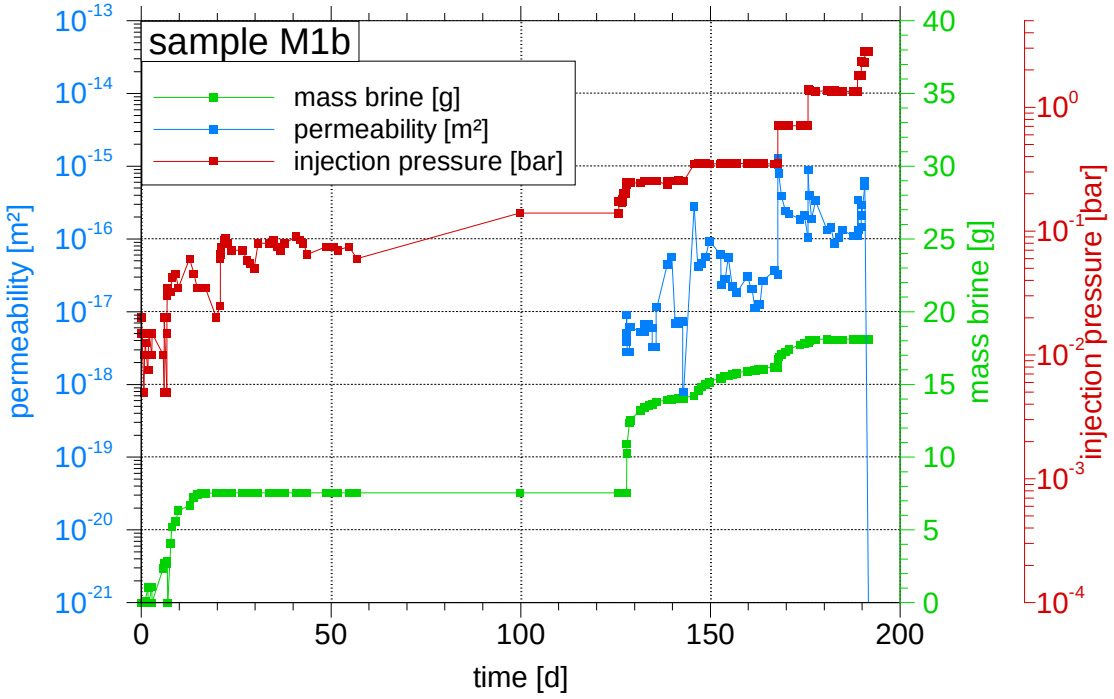

Fig. 2.50 Measured data for sample M1b.

Generally, brine displacement by gas in the pore space of the sample comes to an end when the gas pressure reaches equilibrium with the antagonizing capillary pressure. Due to the complexity of this process the conditions at steady-state are hard to predict. It is thus that two characteristic properties of the gas permeability evolution – the strong decrease after increase of the injection rate and the rapidness of this process increasing with the injection pressure – could only be explained in hindsight. Qualitatively, the effect itself appears to be a consequence of redistribution while the process velocity is controlled by the pressure gradient in the liquid phase. Against this background the acquired data were processed (for details see Appendix F).

Main test 2

Generally, during main test 2 some limits in the applicability of the chosen measuring method became apparent. The first such indication came up during the measurement of

the brine permeability of sample M2a. Permeability was more or less stable slightly above 10^{-15} m² until the injection pressure was increased to 3 bar. All of the sudden, outflow increased to the extent that the injection pressure broke down and the apparent permeability increased by three orders of magnitude as shown in (see Fig. F.11 in Appendix F). This event compromised sample M2a and no meaningful data for unsaturated conditions could be collected further on.

Later, at the end of the experiment, the samples had to be removed from the test cells. This was begun by repeatedly dropping cell and sample into a pot of boiling water in order to dissolve the salt. After the first such dissolution of salt the outer sections of compacted salt had vanished. Inspection showed that sample M2a had indeed been structurally compromised. A big hole could be observed at both ends of the tests cell which appear to have been connected by a considerable hole (see Fig. 2.51). This underpins the notion of a forced channel through the sample as this could not be seen in sample M2b.

Fig. 2.51 Sample M2a after some dissolution in boiling water.

By contrast, sample M2b showed rather little outflow in the course of testing, even at 4.5 bar. The amount of expelled brine, however, was quite small, meaning that a more advanced compaction would probably have resulted in even less outflow rendering recognition of changes in the brine saturation virtually impossible.

2.6.6 Check of single-phase permeabilities

The relevant single-phase flow parameters for all samples are compiled in Tab. 2.8. To check the consistency with earlier data, the single-phase permeabilities are compared to a compilation of data on the porosity-permeability relation of crushed salt /KRÖ 09/ as depicted in Fig. 2.52. Also included in the graph are the data from the new test D-A-025 presented in section 2.5.1. Note that tests with spindle oil provided the same results as the tests with nitrogen. The permeability values determined in this project are denoted by coloured symbols. They fit well into the ranges of uncertainty that come with the earlier data.

In case of pre-test 2 with brine, the range between the first measured permeability value as well as the temporary constant value are indicated in Fig. 2.52. It appears that the lower permeability value generally fits much better into the previously derived range of values than the initial one.

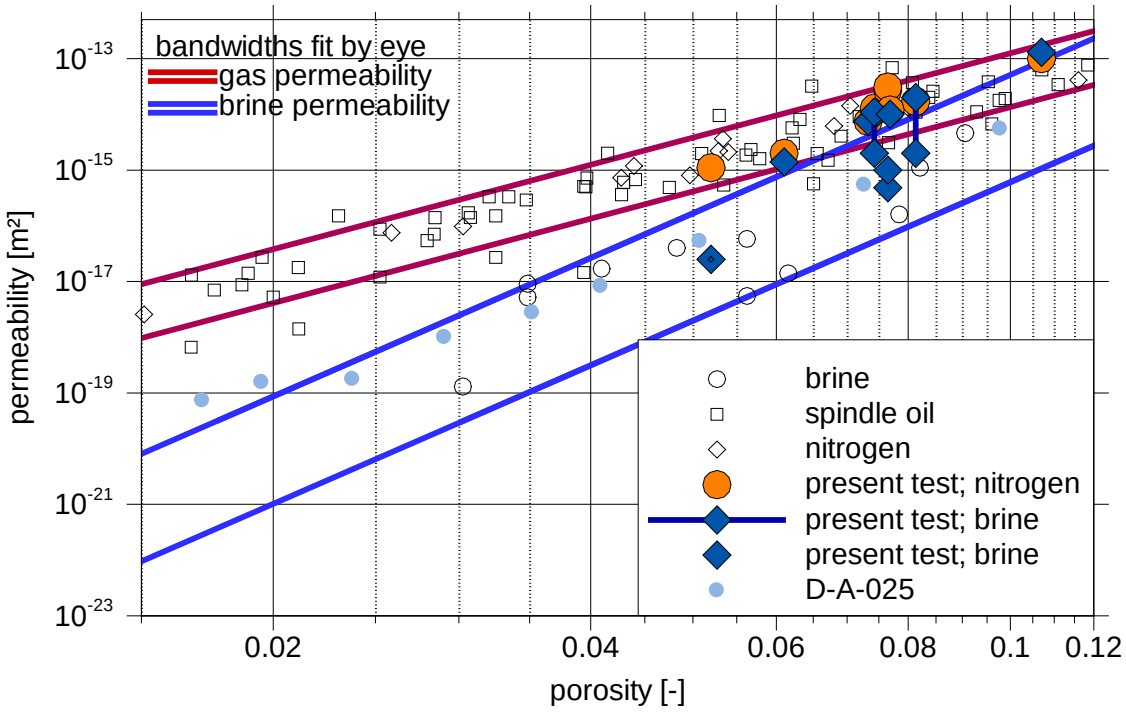

Fig. 2.52 Consistency of measured permeabilities; modified from /KRÖ 09/.

Tab. 2.8 Compilation of single-phase flow parameters

Sample	Porosity [%]	Gas permeability [m²]	Brine permeability [m²]
P1	7.33	$7.5 \cdot 10^{-15}$	$7.5 \cdot 10^{-15}$
P2a	8.13	$1.7 \cdot 10^{-14}$	$2.0 \cdot 10^{-15}$ - $2.0 \cdot 10^{-14}$
P2b	7.43	$1.3 \cdot 10^{-14}$	$2.0 \cdot 10^{-15}$ - $1.1 \cdot 10^{-14}$
M1a	10.70	$1.0 \cdot 10^{-13}$	$1.3 \cdot 10^{-13}$
M1b	7.69	$1.2 \cdot 10^{-14}$	$1.0 \cdot 10^{-14}$
M2a	6.10	$2.0 \cdot 10^{-15}$	$1.4 \cdot 10^{-15}$
M2b	5.20	$1.1 \cdot 10^{-15}$	$2.5 \cdot 10^{-17}$

2.6.7 Compilation of CRs for all tests

Supplementary sample data for two-phase flow concern the bounding values for the air entry pressure and the residual brine saturation. They are compiled in Tab. 2.9.

Tab. 2.9 Supplementary two-phase flow data

Parameter\ Sample	P1	M1a	M1b	M2b
$p_{e,}$ lower bound [MPa]	0.0050	0.0040	0.0140	0.14
$p_{e,}$ upper bound [MPa]	0.0100	0.0075	0.0250	0.20
S_{rb} [-]	0.38	0.115	0.35	0.43
S_{rg} [-]	0.25	0.03	0.13	0.44

The compiled data on the CRs that have been derived from the tests are presented in Fig. 2.53. Besides the trustworthy data, marked with full symbols and lines, two other categories of data are distinguished here: (a) data with some sort of uncertainty because of a continuous decrease of gas permeability during the overly long equilibration period are called “unreliable” and are marked with open symbols and lines; (b) data that were obviously spoiled by the too long equilibration periods showing lower instead of higher gas permeability are marked with open symbols only.

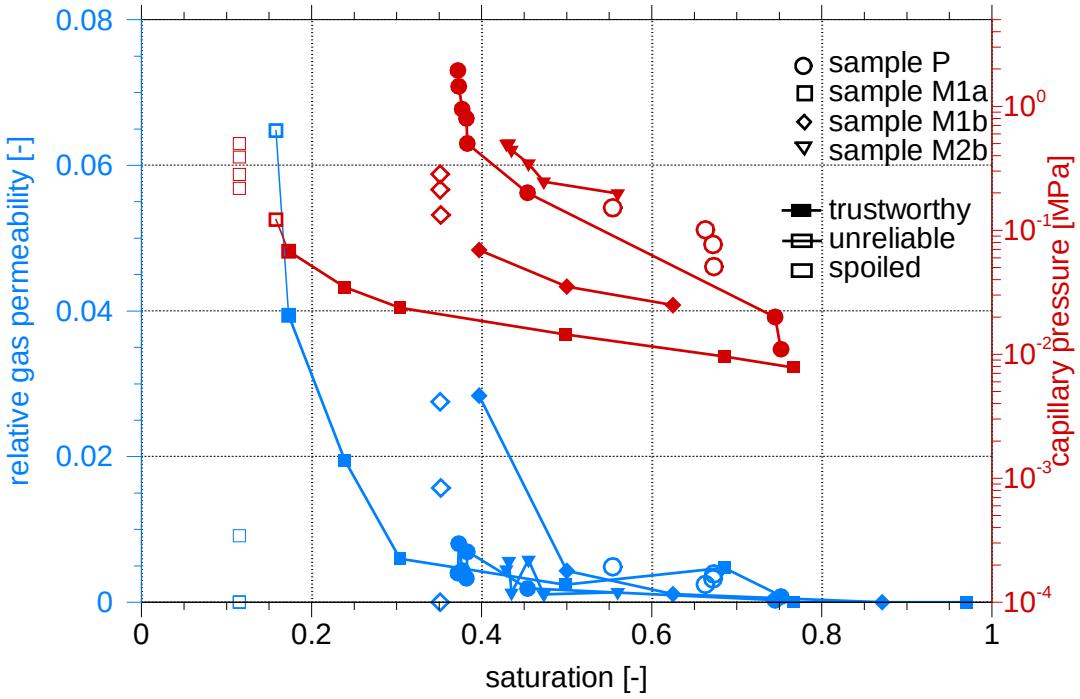

Fig. 2.53 RPS and CPS for all samples.

The CPS curves seem to follow the classical two-phase flow theory. This applies also to sample P1 despite the different set-ups for the pre-test and for the main tests. As expected, the capillary pressure increases inverse proportionally to the porosity.

It had also been expected that the residual brine saturation as well as the air entry pressure increase with decreasing porosity. This has been confirmed by the measurements even if it has to be conceded that in case of the residual saturation the derived values for samples M1a and M1b might be erroneous due to the long equilibration periods during the first main test.

2.6.8 Fitting a Brook-Corey approach to the data

Each of the measured CPS curves can reasonably well be reproduced by a Brooks-Corey approach as shown in Fig. 2.54. The resulting fitting parameters are compiled in Tab. 2.10. Differences between the pre-test and the first main test can clearly be seen in Fig. 2.54 as the shape of the curve for the pre-test does not fit in with the shape of the other two.

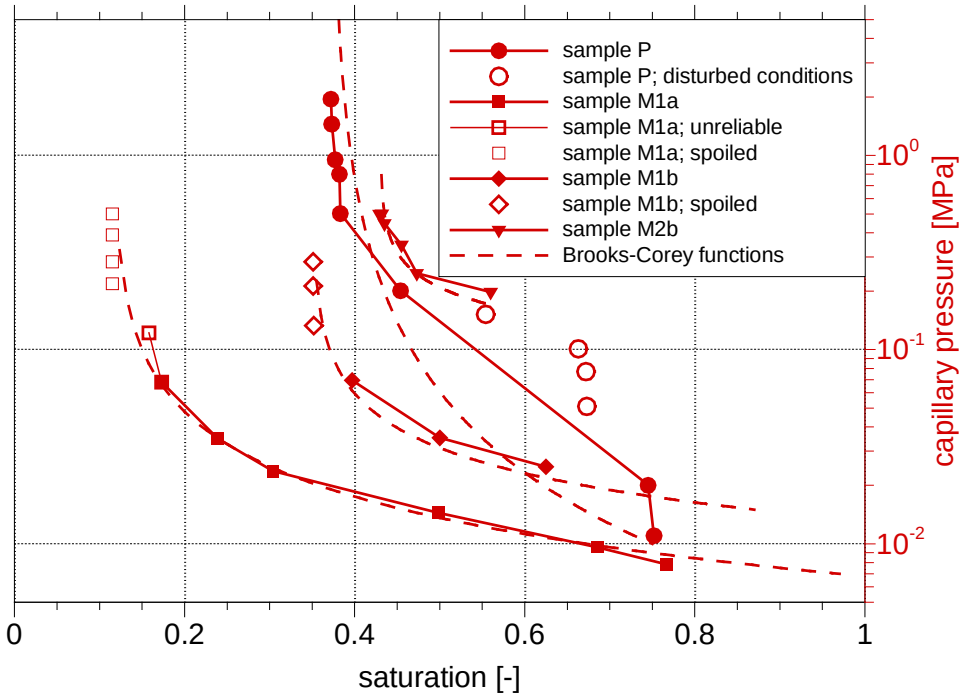

Fig. 2.54 Measured and tentatively fitted CPS'.

Tab. 2.10 Compilation of parameters for the Brooks-Corey approach fitting the CPS

Parameter	Sample P1	Sample M1a	Sample M1b	Sample M2b
porosity	7.33 %	10.7 %	7.69 %	5.2 %
λ	0.6	1.2	1.7	3
air entry pressure	0.01 MPa	0.007 MPa	0.015 MPa	0.170 MPa
residual brine saturation	0.372	0.115	0.35	0.43
brine sat. at resid. gas sat.	0.75	0.97	0.87	0.56

Depicted in Fig. 2.55 are the RPS curves that were also calculated with the parameters from Tab. 2.10. A comparison of the calculated with the measured curves indicates no relation at all. This did not change when using even extreme λ-values. Relative gas permeability is very low over a wide range of saturations and appears to increase strongly only in the vicinity of the residual brine saturation. The data does not show conclusively whether a dependency on the porosity exists in the low value range at all. This observation remains the same if the results of the pre-test fit are included. The RPS curves thus deviate considerably from the classical two-phase flow theory.

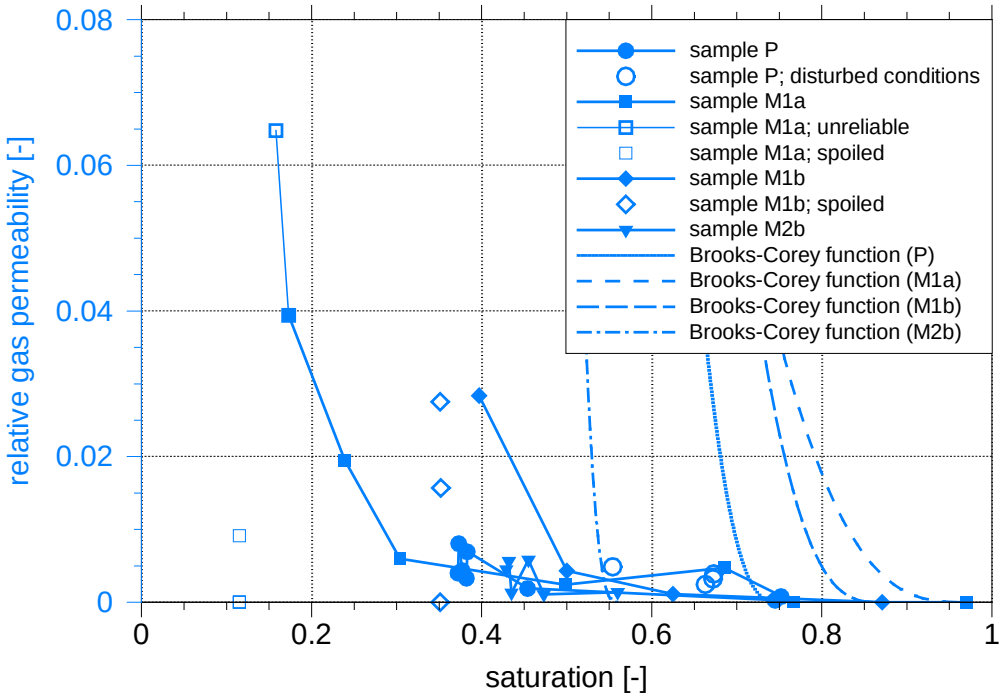

Fig. 2.55 Measured and tentatively fitted RPS'.

2.6.9 Summary and discussion

Two pre-tests and one main test were performed providing a total of 3 data sets to derive constitutive equations for the capillary pressure and the relative permeability of compacting crushed salt. The single-phase flow data for gas and brine permeability follow previously derived porosity-permeability relations within the observed uncertainties. Air entry pressure and residual brine saturation develop according to the expectation that both values increase with decreasing porosity.

Each of the measured CPS curves is also consistent with the two-phase flow theory for common soils and could thus be fitted reasonably well with the approach of Brooks and Corey. The curves show the expected general increase of capillary pressure with decreasing porosity. However, with presently only two comparable CPS curves available, it does not make sense, yet, to formulate a dependency on porosity.

The RPS curves for gas showed by contrast such a big difference to the classical two-phase flow theory that reproducing the individual RPS curves even with extreme parameter values failed. This is a considerable drawback because it means that the theory of

Brooks and Corey fails for compacting crushed salt. It is apparently not possible to derive the RPS from parameters for the CPS as the work of Brooks and Corey implies. While new formulations for the RPS can certainly be found, the RPS for brine can thus not be predicted on a purely theoretical basis. Consequently, this calls for different tests that provide data for brine permeability under unsaturated conditions.

A second conclusion from the measured RPS curves concerns the relation to the degree of compaction. In principle, the RPS curves for gas look the same for all samples. They are remarkably gently inclined resulting in very low values except for the immediate range of the residual brine saturation. Here, the relative permeability increases strongly. The only difference between the RPS curves thus seems to be the saturation range limiting residual saturation. Note that it is presently not clear if the single-phase gas permeability had remained unchanged and a relative permeability of “1” could have actually been reached in the experiment.

The results from the second main test indicate the limits of the test procedure when it comes to low permeabilities. An advanced degree of compaction beyond a brine permeability of 10^{-17} m² or a porosity of less than 5 % could not have been tested with the procedure followed in this experiment.

Two-phase flow in general is a highly non-linear process /HEL 97/. Erroneous CRs can have a much bigger impact on the results than merely badly chosen single-phase parameters as they may change the flow dynamics not only quantitatively but also qualitatively. Minimisation of uncertainties in the CRs must therefore have high priority for reliable two-phase flow simulations. Considering the limited amount of tests, the present experiment can thus provide not more than a first impression of the CRs for compacting crushed salt. Concrete predictions based on these results are therefore not advisable. Against this background further testing is recommended to quantify the range of uncertainties.

Additionally, it has to be pointed out that the crushed salt material investigated here was well-defined and of a comparatively high degree of homogeneity. A much higher range of data scatter is to be expected from the uncertainties caused by the backfill preparation under in-situ conditions in an operational repository. This effect has to be taken into ac-

count because otherwise, it will eventually compromise the validity of predictions concerning two-phase flow.

Further testing of the CRs for crushed salt should also focus conceptually on a realistic representation of the two-phase flow process in question. One concern should relate to the wetting dynamics in the test. In the experiment presented here the samples were stepwise desaturated beginning at full brine saturation. Inflow into a real repository, by contrast, would begin at a comparatively dry state of the backfill and lead to an increasing brine saturation. This process can later be reversed, though, if gas production kicks in and desaturates the backfill again.

An additional argument pointing in the same direction can be derived from the surprisingly low relative gas permeabilities in both of the experimental set-ups. The fact that they were observed independently of a circumferential pressure indicates another pore volume changing process like re-distribution of salt on the pore scale. The CRs and thereby the flow dynamics in general might thus be strongly influenced by the underlying wetting scenario and in particular by the initial conditions for which the test is conceived.

Another concern arises then from the idea of salt re-distribution. The phenomenon of pressure solution at the contact between two salt grains that are mechanically squeezed together is a well-established fact. Further hydraulic tests under compacting conditions might therefore be advisable.

It thus appears that the robustness of the safety case regarding the compaction of crushed salt must be strengthened. As long as it is relying on quantitative two-phase flow calculations for the backfill it is unavoidable to perform an extensive laboratory program with the following agenda:

– determine the RPS for brine directly,
– determine the uncertainties related to inhomogeneities in the grainy backfill material under laboratory and under operational conditions
– quantify the uncertainty in the dependency of the CRs on different degrees of compaction,
– determine the impact of a mechanical load on the CRs, and
– determine the impact of different wetting conditions on the CRs.

The decision about which alternative should be followed in the future should be carefully considered as it is foreseeable that modifying the safety case as well as investigating two-phase flow properties of crushed salt will require substantial effort.

2.7 Microstructural Investigations

2.7.1 Thin Section Analyses

BGR provided samples from compaction studies for initial investigations on microstructures (Tab. 2.11). The samples have different compaction degrees and, thus, different porosities and were compacted both in dry and in moist condition. The individual samples were evacuated in a desiccator and then soaked with a blue resin with very low viscosity. This is to make visual remaining pore spaces at different compaction degrees and after different compaction methods have been used, as these pore spaces could transport fluids. After adequate time had passed and the resin had hardened, thin sections of each sample were prepared. Subsequently, the thin sections were photographed under a microscope.

Tab. 2.11 List of samples provided by BGR

Identifier	Material	Size [cm]	Compaction rate [mm/h]	T [°C]	Test duration [d]	Void ratio
Oedo-047/5	z2Hs	7.0x3.7x1.4	0.36 – 0.00036	200	78	0.006
Oedo-051/8	z2Hs	7.8x5.2x1.6	3.6 – 0.36	100	6	0.063
Oedo-051/9	z2Hs	7.8x5.2x1.6	3.6 – 0.36	100	6	0.063
Oedo-056/5	z2Hs+ 1.2 % brine	7.0x3.7x1.4	0.36 – 0.00036	~30	112	0.031
Oedo-102/1	z2Hs+ air moisture	6.0x5.0x1.8	0.36 – 0.00036	~33	134	0.046
Oedo-102/2	z2Hs+ air moisture	6.0x5.0x1.8	0.36 – 0.00036	~33	134	0.046
D-A-025/2	Z2Hs seeped)	6.0x2.0x3.0	n. s.	~30	n. s.	n. s.

Photographic logging was carried out in two steps. After the complete thin section had been recorded, selected areas were photographed with a significantly higher resolution in order to be able to carry out detailed analyses. In a second step, the samples soaked with resin were cut open and the cut surfaces were coated with a red resin and polished. This makes pore spaces visible that have been opened by the cut and have not been penetrated by the blue resin. It cannot be excluded that these pores maybe penetrated by gas, but it is assumed that these pores are mainly dead pores that – although they contribute to the total porosity – are not involved in water or brine migration. The images have been analysed and described.

The thin section cut close to the surface (thin section 1) shows that the blue resin has penetrated the crushed salt body across the entire surface of the cut (Fig. 2.56). This shows a completely interconnected pore system. Open pores with sizes of 2-3 mm can be identified, especially where larger salt grains adjoin each other. Only a few isolated, open areas (dyed red) can be made out.

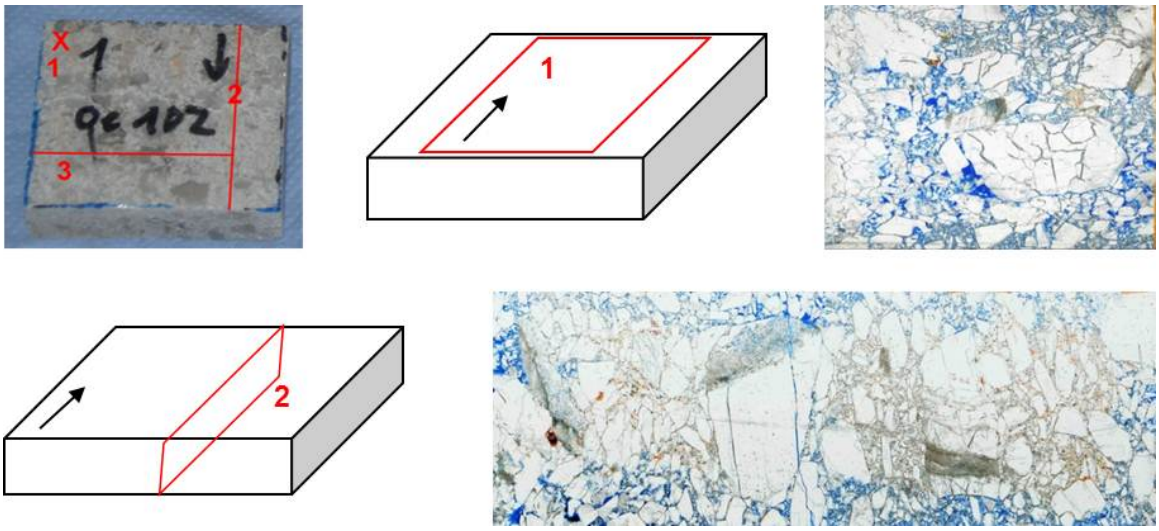

Fig. 2.56 Image of the crushed salt sample used by BGR in oedometer test 102/1 and thin section images of an area close to the surface (thin section 1) of the sample and of a perpendicular cut (thin section 2)

The thin section cut perpendicular to the sample (thin section 2) shows a different situation with a central area that is mostly free of the blue resin but shows a number of red areas, i.e. dead pores. Only a few spots in this central area have been penetrated by the blue resin. These are mostly cracks that run through larger halite grains. Such an area is shown in Fig. 2.57 with a higher resolution. The open pathways along cracks and larger pore spaces are clearly visible. This indicates that the resin was able to penetrate to the core of the sample via grain boundaries and cracks. This may indicate a need to filter out the coarsest grains when defining the grain-size distribution curve or when fabricating the crushed salt in order to reduce fluid paths along grain boundaries. The black spots visible within these pathways are probably small air bubbles that have not been completely removed during evacuation and were enclosed by the blue resin during soaking.

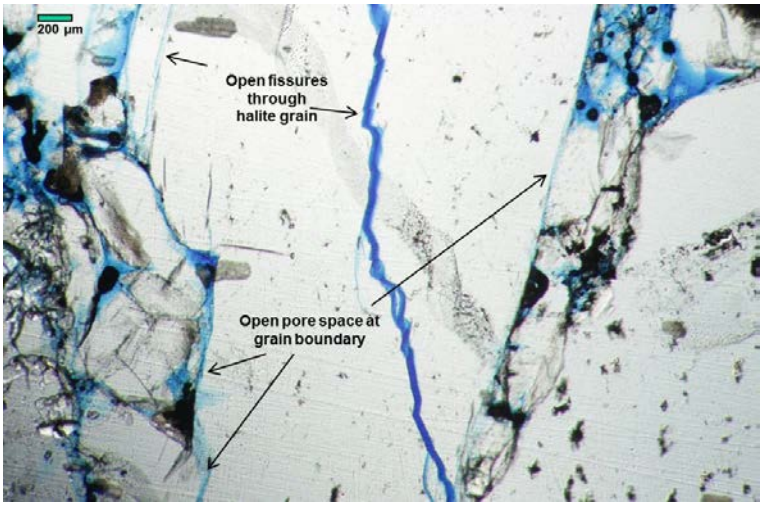

Fig. 2.57 Enlarged view from the thin section of sample 102/1 (~4.6 % porosity) showing main fluid pathways through cracked halite grains and at its boundaries

Fig. 2.58 shows an enlarged section of the central area that has not been penetrated by the blue resin. This area shows a number of brine inclusions within the halite grains, especially along dead pores. In addition to this, dead pores dyed red can be identified as well.

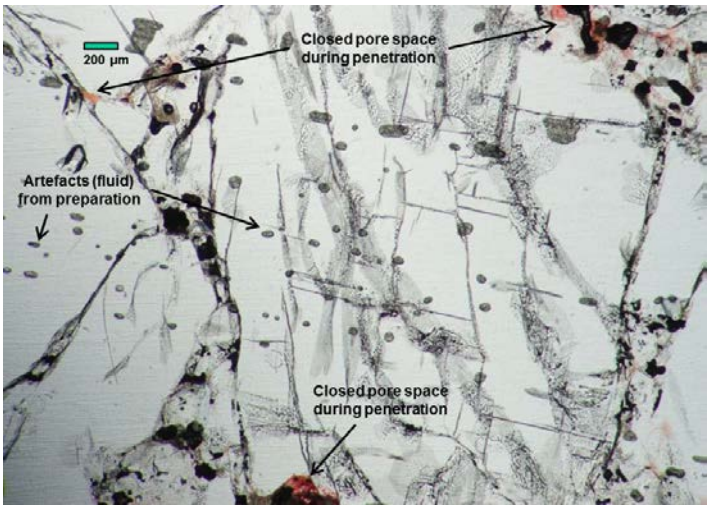

Fig. 2.58 Enlarged view from the thin section of sample 102/1 (~4.6 % porosity) showing dead pores and artefacts from preparation

Fig. 2.59 shows thin section images of three crushed salt samples that were compacted using different methods. Sample 047/5 was compacted in dry condition at 200 °C for 78 days and has a void ratio of 0.006. Sample 051/8 was compacted at 100 °C for 6 days and has a void ratio of 0.063. Sample 056/5 was also compacted at 100 °C for 6 days

with the addition of 1.2 % brine. The images of the thin sections show different characteristics. The structures of the first two samples shown in Fig. 2.59 are similar, while the third sample looks quite different. It is obvious that hardly any resin penetrated into sample 047/5 (compacted at 200 °C), although the thin section was taken close

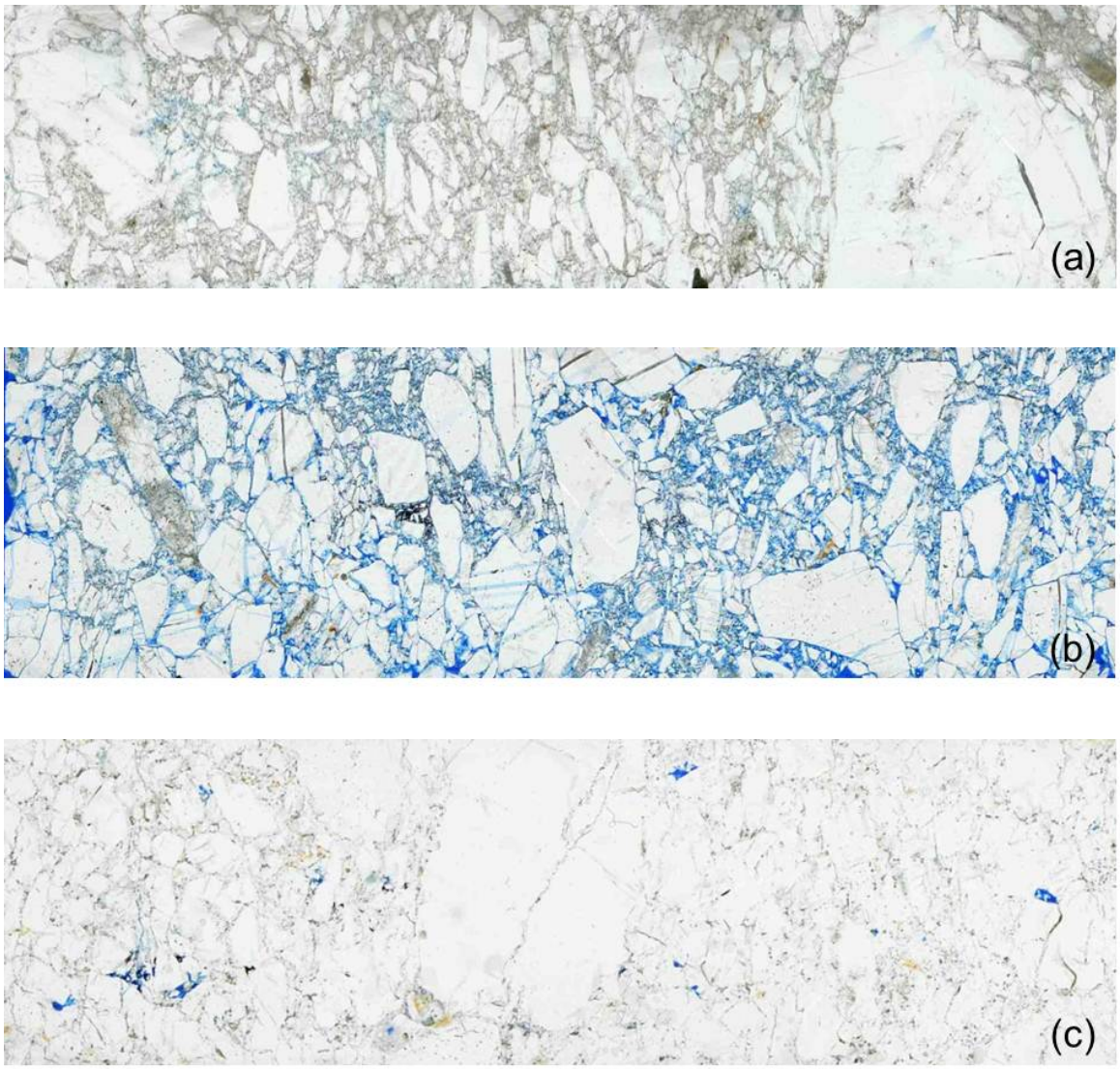

Fig. 2.59 Thin section images (120x40 mm) of three differently compacted crushed salt samples

(a) Sample 047/5, compacted at 200 °C, porosity ~0.6 %;
(b) Sample 051/8, compacted at 100 °C, porosity ~6.3 %;
(c) Sample 056/5, compacted at 100 °C, porosity ~3.1 % and1.2 % brine added

to the sample surface. Contrary to this, the resin is completely distributed in the pore net of the fine grained section of sample 051/8. The third image; i.e. the thin section of sample 056/5, shows a completely different structure. Although the large grains can be seen as well, the fine grained section is not as recognizable as in the two other samples. The addition of 1.2 % brine during compaction obviously had the effect that the small grains in the fine grained section “bonded’’ so that the amount of fine pores in this section was reduced significantly.

While the first two images show more or less clearly that the resin permeates the samples like a network, such a network cannot be identified in the third image. However, this sample is interspersed with local “hot spots” that seem to be not linked in the plane of the thin-section. (cf. enlarged section). If and to what extent these “hot spots” are linked via a three-dimensional pore system (perpendicular to the thin-section plane) cannot be assessed this way. Fig. 2.60 and Fig. 2.61 show enlarged areas of the images (a) and (c) in Fig. 2.59. Although sample 47/5 is highly compacted down to a porosity of less than 1 % (see Fig. 2.59), it is easy to distinguish between individual grains and the fine salt (grey areas). Larger grains are even “embedded” in the fine salt mass as can be seen in the left image of Fig. 2.60. In these highly compacted areas it seems that remaining pathways for a moving fluid through the sample are mainly along the boundaries of larger grains indicated in the right image.

Looking at the enlarged areas of sample 56/5 (Fig. 2.61) the picture is completely different. Compared to Fig. 2.60, individual grains can hardly be identified which indicates that additional microstructural processes must have taken place during deformation. Especially when the sample has small but significant amounts of water, recrystallization processes (e.g. fluid assisted grain boundary migration) and solution-precipitation creep (pressure solution) move into focus (e.g. /URA07/. As can be seen in Fig. 2.61 the microstructure of the fine salt mass has been altered due to processes specified. An example has been marked by a red circle in the left image of Fig. 2.61.

With regard to remaining pathways it can be observed that instead of a fine network local “hot spots” appeared as indicated in the right image of Fig. 2.61. In addition to this, two other samples were investigated. The sample (102/1) was prepared by adding moist air during compaction (Fig. 2.62) and sample D-A-025/2 which was initially compacted in a dry state and subsequently permeated with brine in order to determine its permeability to

brine (Fig. 2.63). A comparison of sample 102/1, which had been prepared by adding moist air, with sample 056/5, which had been prepared by adding 1.2 % brine, shows that the structure of sample 102/1 is similar to those of the samples that were prepared in dry condition but is completely different from sample 056/5 (added brine). This means that the addition of moist air is not sufficient to modify the pore system on the fine grain level in such a way that “bonding” or cementation takes plays as does when brine is added.

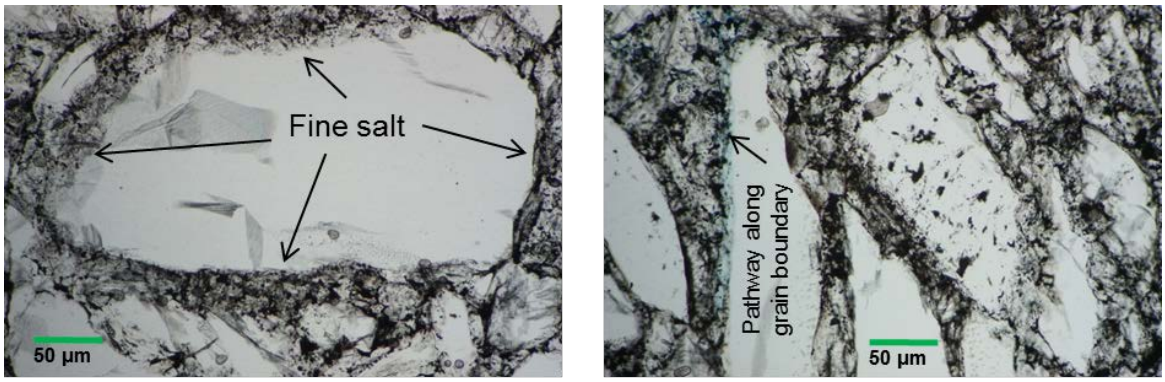

Fig. 2.60 Enlarged thin section areas of the highly compacted sample 47/5

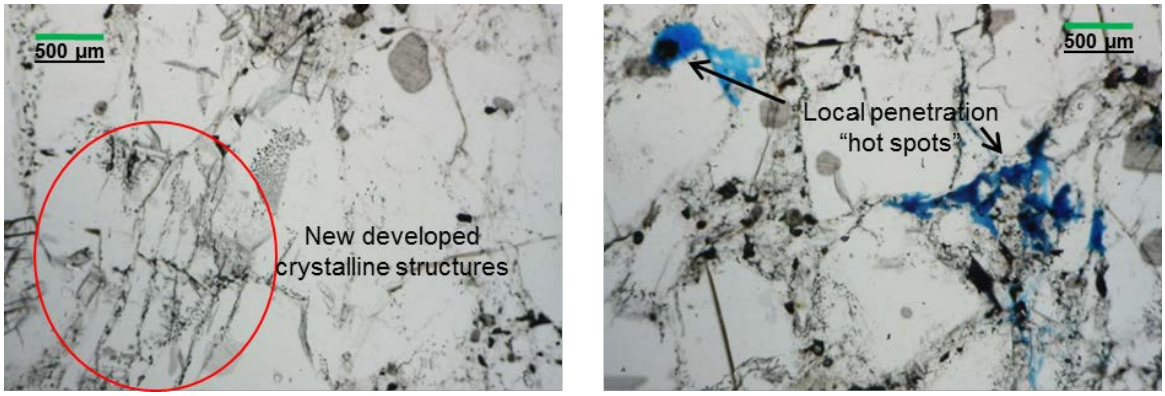

Fig. 2.61 Enlarged areas of sample 56/5 compacted with 1.2 % brine

Compared with sample 056/5, the sample that had been permeated with brine after dry compaction (D-A-025/2) shows a lot more “hot spots”. This indicates that leaching took place during permeation, which led to the formation of a “vessel system” that could be permeated by the resin. This vessel system seems to be permanent. With regard to the real situation in a repository where crushed salt is used as backfill material in the drifts, this could indicate that the occurrence of an early brine inflow and pressure build up in the crushed salt; i.e. when it has not yet completely compacted, could lead to the for-

mation of an unwanted system of larger pores which might remain for a certain period of time until it is compacted and closed by the convergence.

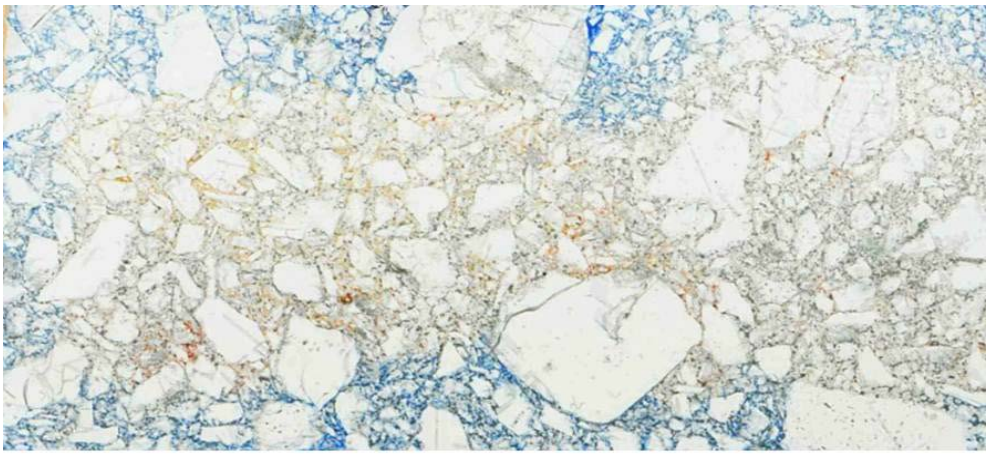

Fig. 2.62 Thin section images (120x55 mm) of the crushed salt sample 102/2 compacted at ~33 °C with moist air added during compaction, porosity ~4.6 %

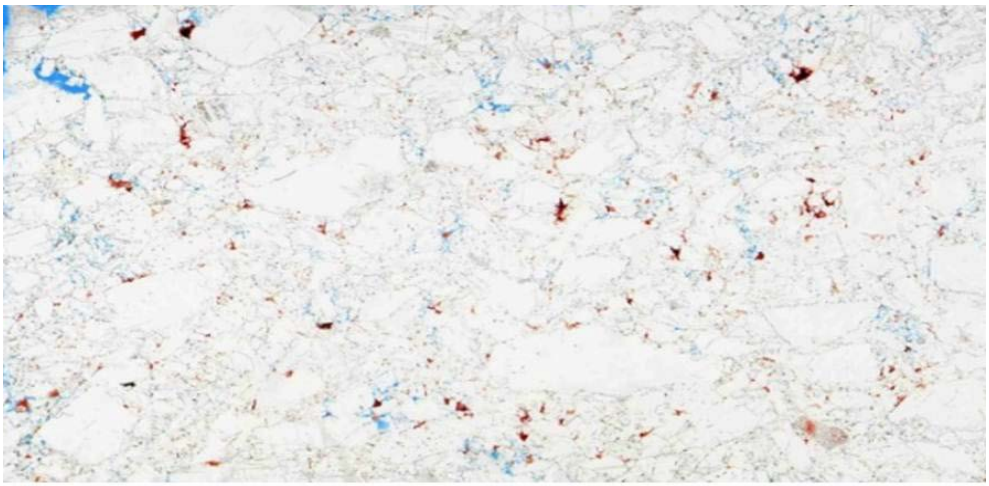

Fig. 2.63 Thin section images (120x55 mm) of the crushed salt sample D-A-25/2 initially compacted in a dry state and subsequently permeated with brine

2.7.2 Computer tomographic analyses

The aim of the XCT (X-ray Computer Tomographic) measurement was to investigate whether tomographic methods together with percolation theory can give indications about a critical porosity of crushed rock salt that, once reached, doesn't allow any more permeation. To assess these sealing properties of crushed rock salt XCT and FIB-nT (Focussed Ion Beam nano Tomography) was used to obtain 3D reconstructions of the

macroporosity (radii > 4 µm) and microporosity (radii < 1 µm). Some details of resolution effects of XCT can be found in /PEN 12/. The reconstructed pore microstructures were then analysed with respect to homogeneity, percolation properties and representativity using the same procedure that was recently applied to Opalinus Clay /KEL 13/. The two samples 47/5 and 51/8 (Tab. 2.11) with different degrees of compaction were examined.

2.7.2.1 Results

Micro- to macro-scale pore structures based on BIB and SEM imaging

SEM images on the hundreds of micron scale and SEM images at higher magnifications of the prepared samples are shown in Fig. 2.64 and Fig. 2.65. The SEM images reveal that the examined samples contain nano-scale (micropores) and micron-scale pores (macropores).

The geometry of the macropores is defined by geometric incompatibilities between angular salt grains. Geometric compatibility between grains is higher in sample 47/5 when compared to sample 51/8, which results in a lower porosity and connectivity in sample 47/5. Micropores are located in compact grain aggregates, mainly along grain boundaries but also in the interior of grains. In 2D these pores have a circular shape and can be seen as fluid inclusions.

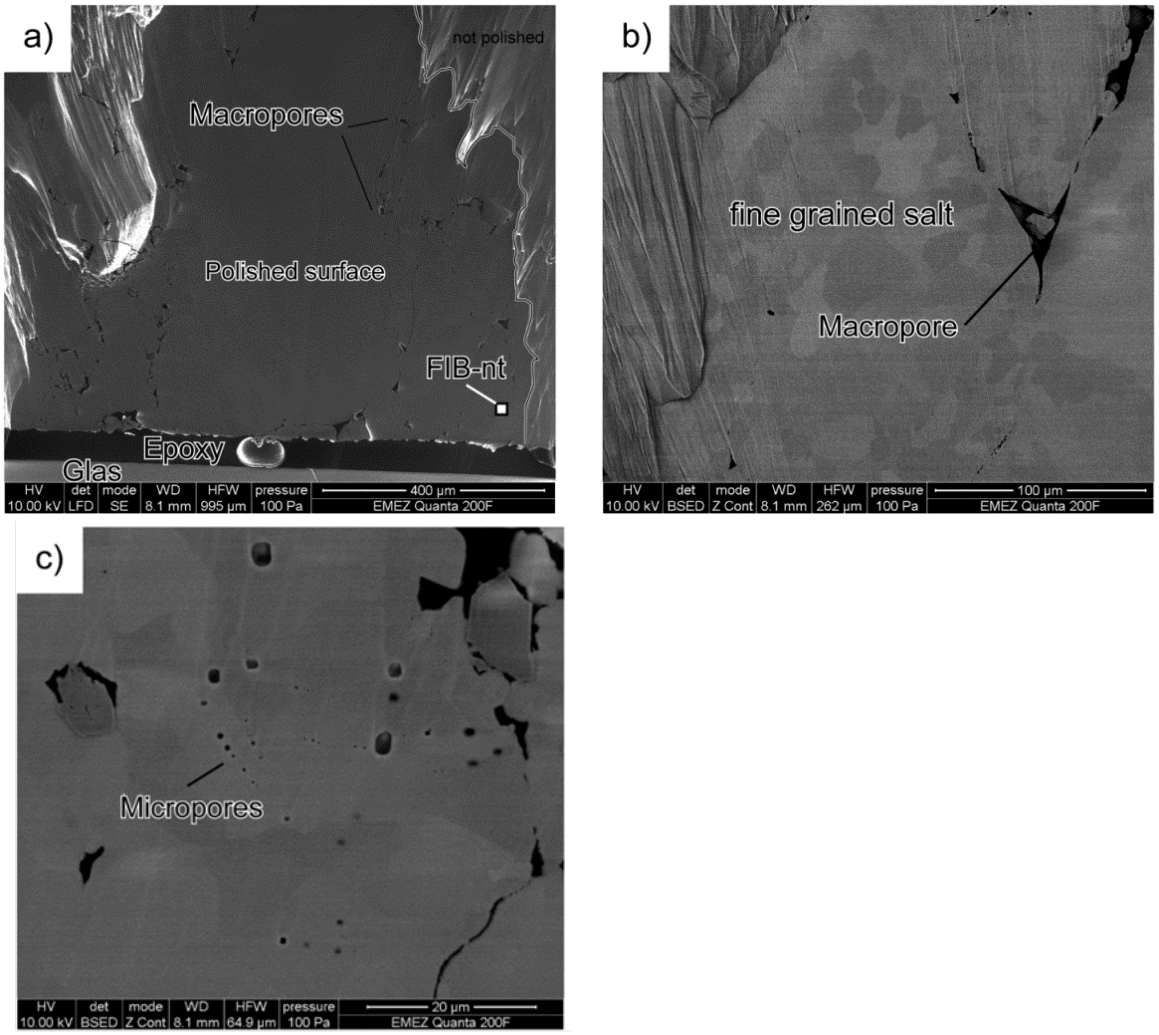

Fig. 2.64 SEM images at different magnifications of sample 47/5

a) Overview of the area polished with the help of a BIB instrument

b) Orientation contrast between individual salt grains. The image shows that the compact areas are in fact grain aggregates and no single crystals

c) Image at higher magnification shows micropores in otherwise compact grain aggregates

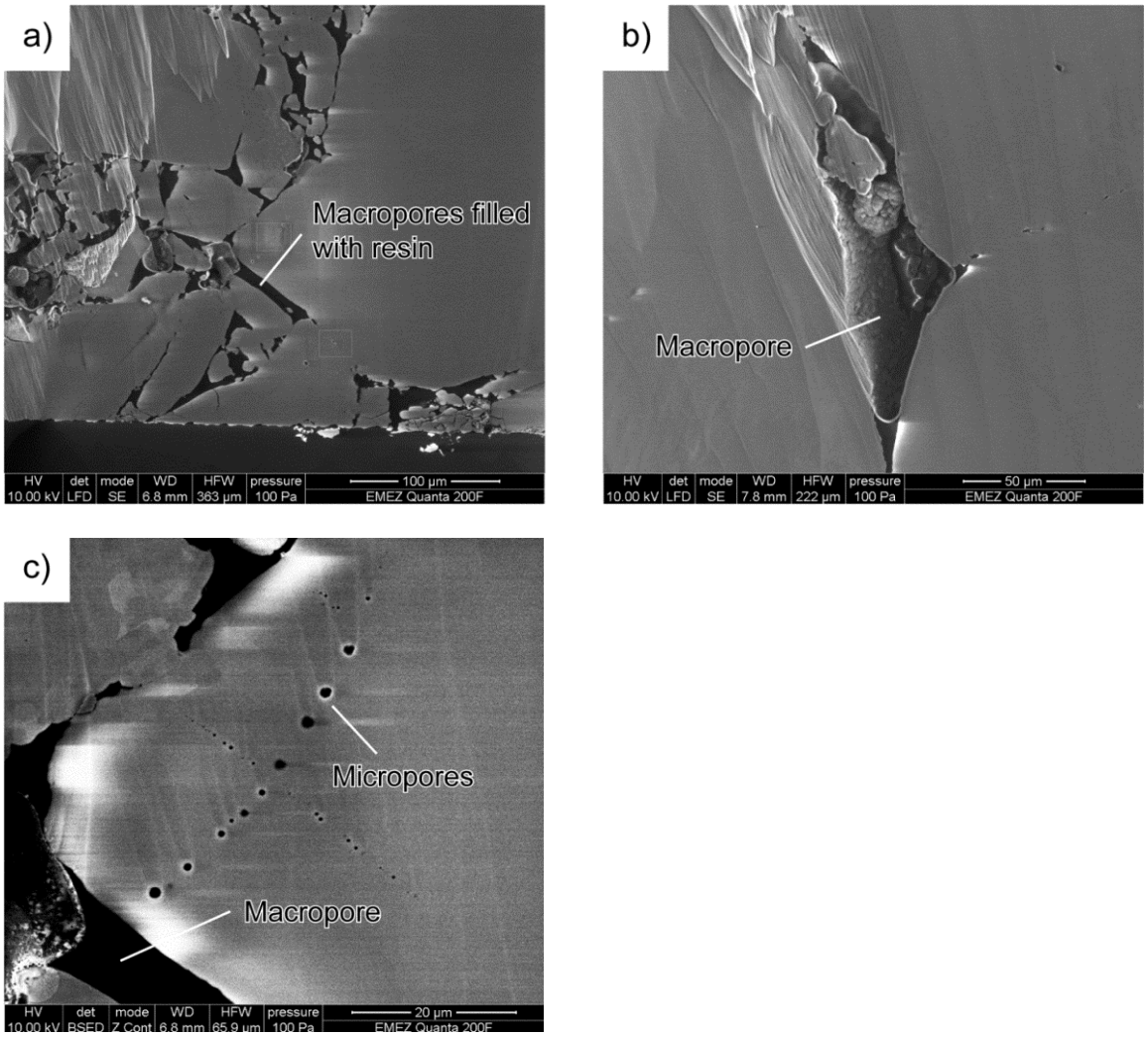

Fig. 2.65 SEM images at different magnifications of sample 051/8

a) Overview of the area, which was polished with help of a BIB instrument
b) Image at higher magnifications shows micropores in grain aggregates
c) Image at higher magnification shows micropores in grains

Macro-scale pore structure based on XCT

3D reconstructions of the analyzed samples (051/8 and 047/5) and pore space reconstructions are shown in Fig. 2.66 and Fig. 2.67.

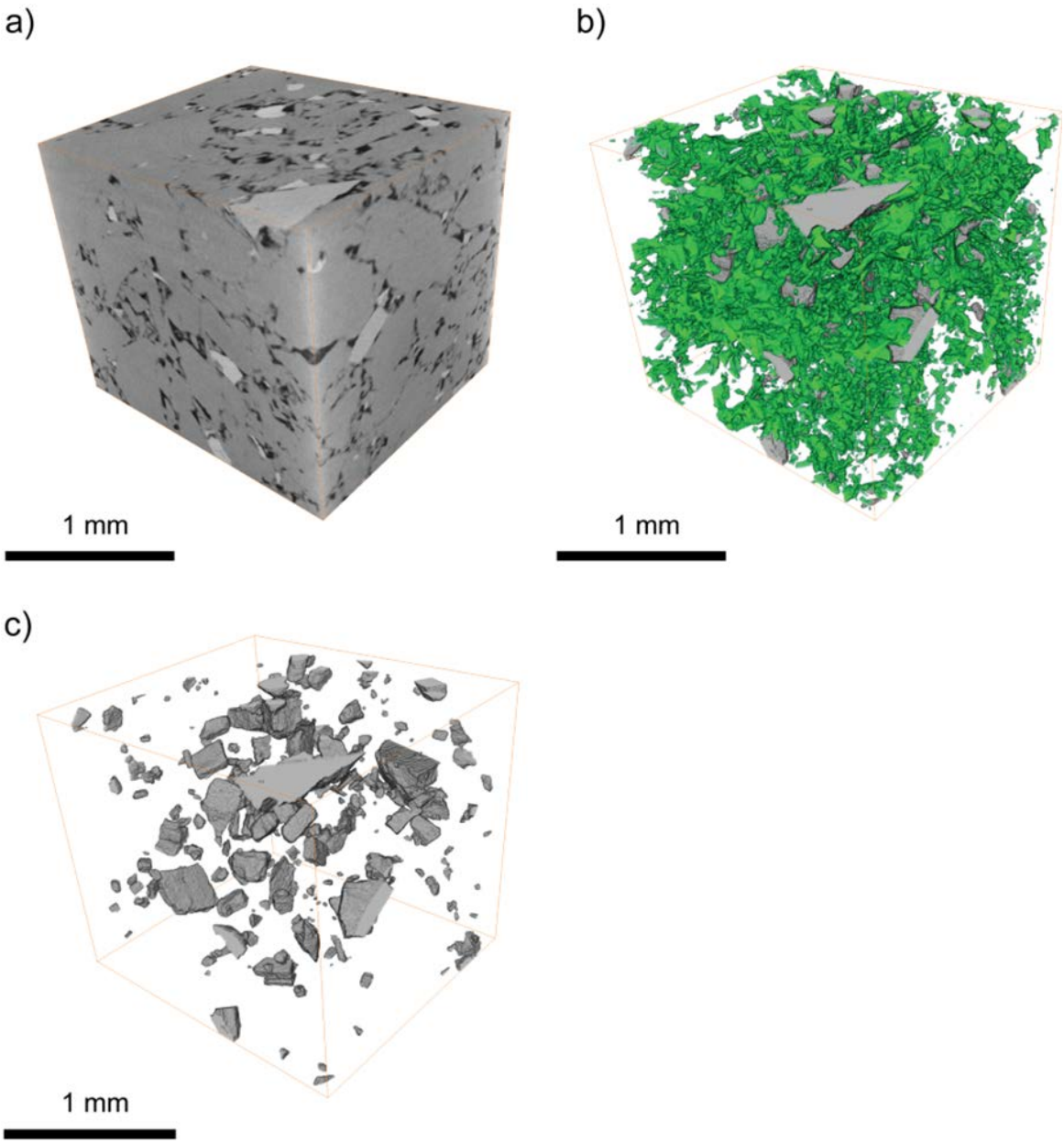

Fig. 2.66 Visualization of two XCT data sets of sample 051/8

a) 3D reconstruction of the analyzed volume.

b) 3D reconstruction of pore space (green) and the anhydrite mineral with bright image contrast (grey).

c) Reconstruction of anhydrite distribution.

The reconstructed samples are on the left image (a) and the reconstructed pore spaces are on the right images (b). The light grey objects in the reconstructed samples have

been identified as anhydrite and its distribution is exemplarily shown in image (Fig. 2.66 c).

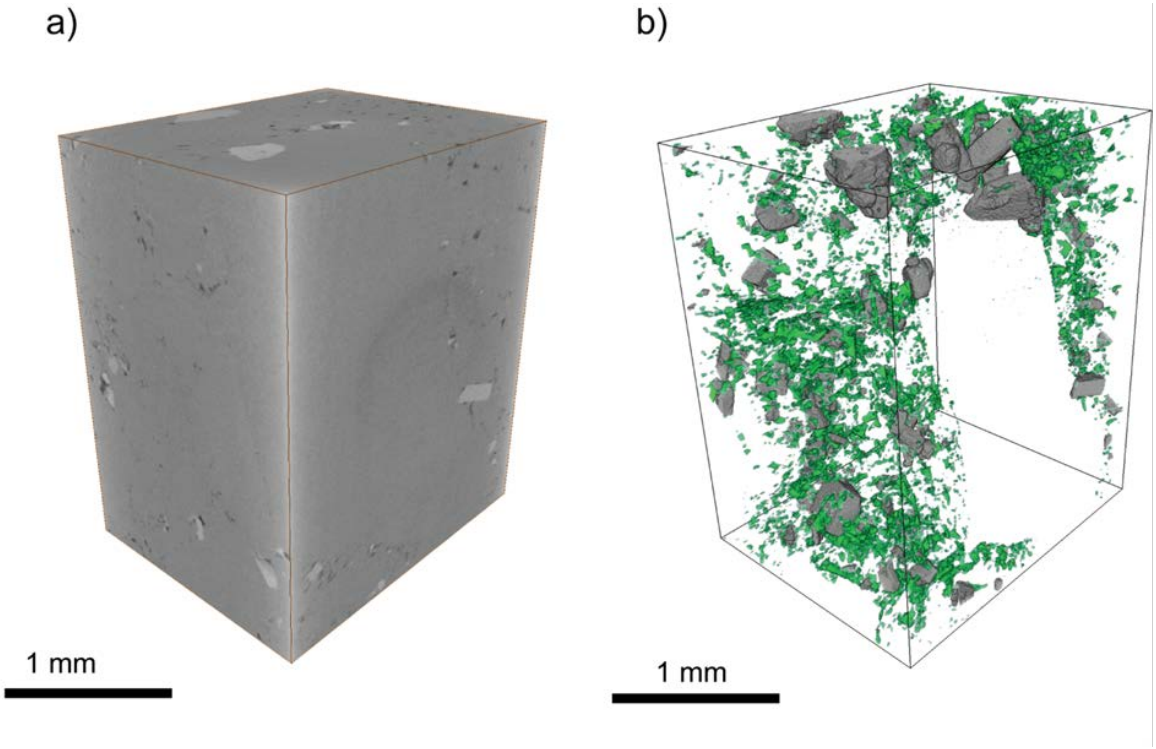

Fig. 2.67 Visualization of two XCT data sets of sample 47/5

a) 3D reconstruction of the analyzed volume.

b) 3D reconstruction of pore space (green) and anhydrite minerals (grey).

Regarding sample 47/5 (Fig. 2.67), the porosity related to pores with radii > 4 µm is around 1 vol. % and the pore space consist of numerous isolated pore objects. Substantially higher macro porosity (~10 vol. %) was found in sample 051/8 (Fig. 2.66).

The samples differ also with respect to pores size distribution. Continuous pore size distributions calculated on the base segmented image stacks /MÜN 08/ are shown in Fig. 2.68. The majority of pores in sample 47/5 have radii < 20 µm and the most frequent pore radii is around 10 µm. Sample 051/8 contains larger pores with radii < 40 µm and the most frequent pore radii is around 15 µm and is thus, similar to the one of sample 47/5.

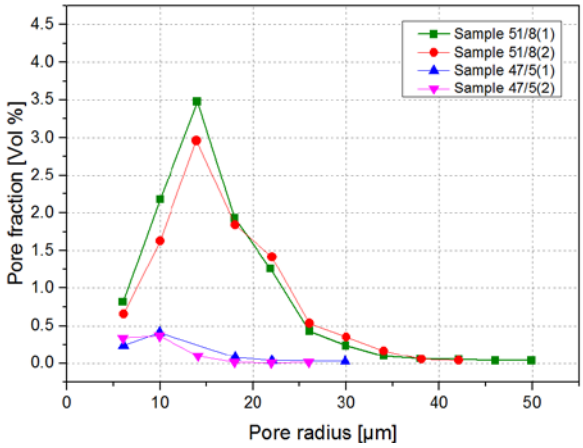

Fig. 2.68 Pore size distributions for two different compacted crushed salt samples, which are based on 3D data from XCT

Micro-scale pore structure based on FIB-nt

3D reconstructions of the analyzed volume and 3D reconstructions of the pore space are shown in Fig. 2.69 and Fig. 2.70. Often crystal planes define the pore shape, which in the case of salt results in a cubic or circular pore geometry (Fig. 2.69). On the scale of observation, these pore objects are spatially isolated (fluid inclusions) and do not touch each other (Fig. 2.69, Fig. 2.70). Such micropores occur in-plane along grain boundaries or within the grain as fluid inclusions (Fig. 2.70) and at grain triple points. The orientation contrast between salt grains visible in SEM images gives an idea of the sub-grain size of such aggregates (Fig. 2.69). Within the analyzed volume the sub-grain size ranges between a few microns to tens of microns.

The analyzed volumes contain a small number of pores with radii < 1 µm (Fig. 2.71). On the size of the analyzed volumes, micropores are inhomogenously distributed and the pore size distributions of the two samples are therefore difficult to compare. The pore size distributions indicate that sample 51 only contains a limited amount of pores on the nanometer scale (no pores of a size between 500 nm and 1 µm were found) whereas sample 47/5 contains pores distributed among the whole nanometer scale.

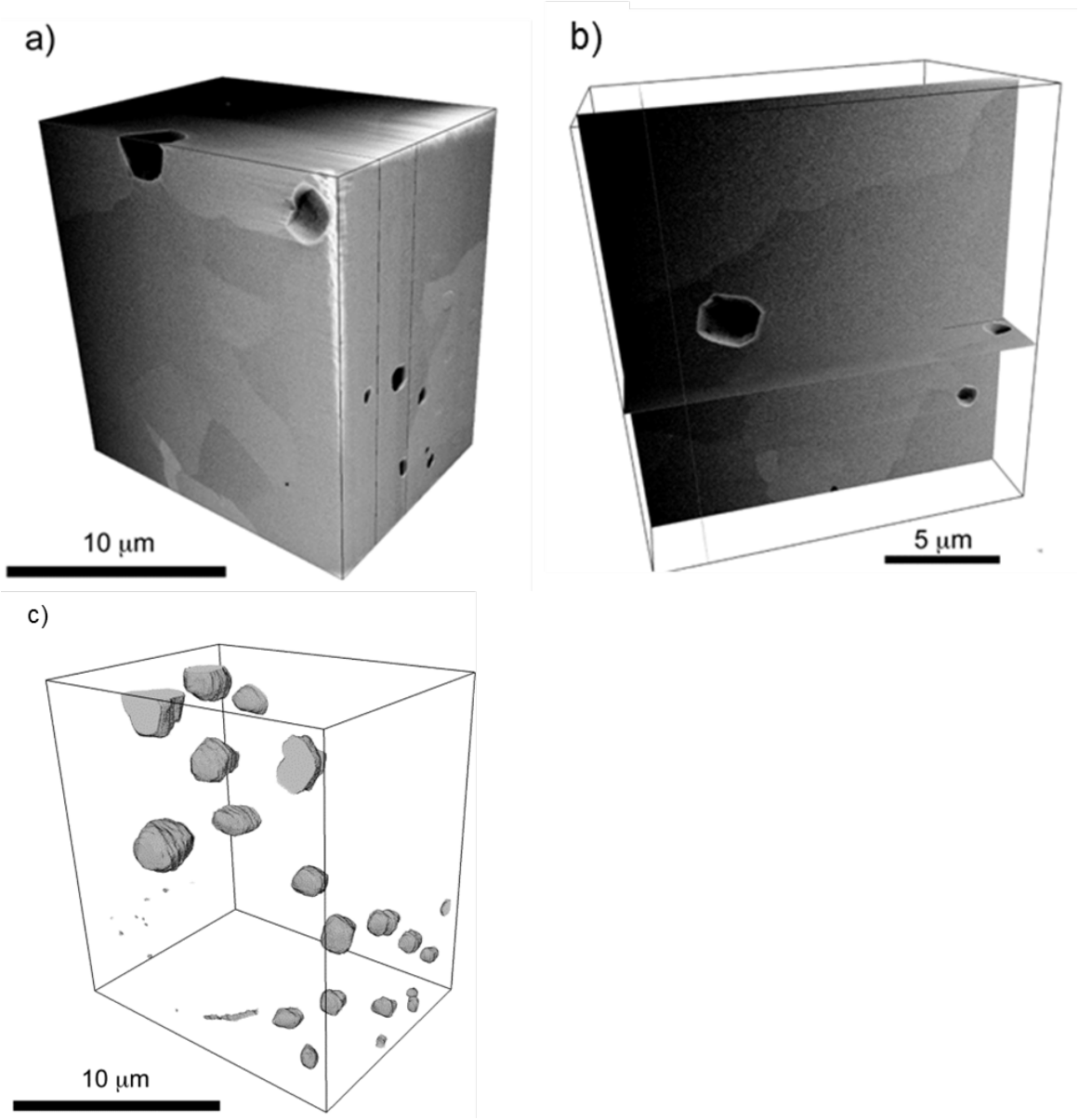

Fig. 2.69 Visualization of the FIB data set of sample 47/5

a), b) 3D reconstructions of the analyzed volume documenting the granular pore geometry.

c) 3D reconstruction of pore space.

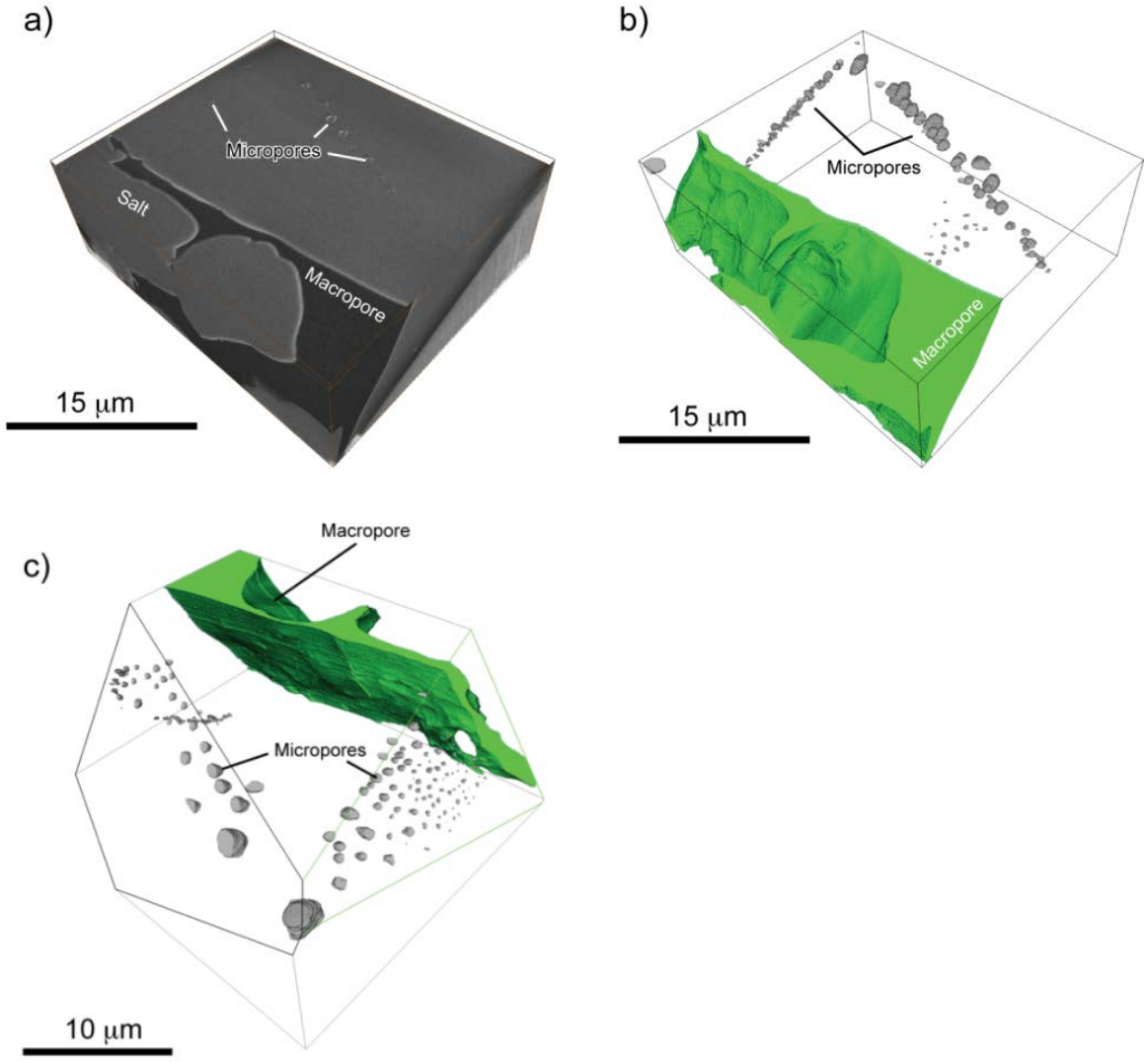

Fig. 2.70 Visualization of the FIB data set of sample 51/8

a) 3D reconstructions of the analyzed volume

b) 3D reconstruction of pore space showing a macropore and numerous in plane fluid inclusions

c) 3D reconstruction of pore space showing that the micropores or fluid inclusions are aligned in planes (i.e. sub-grain boundaries).

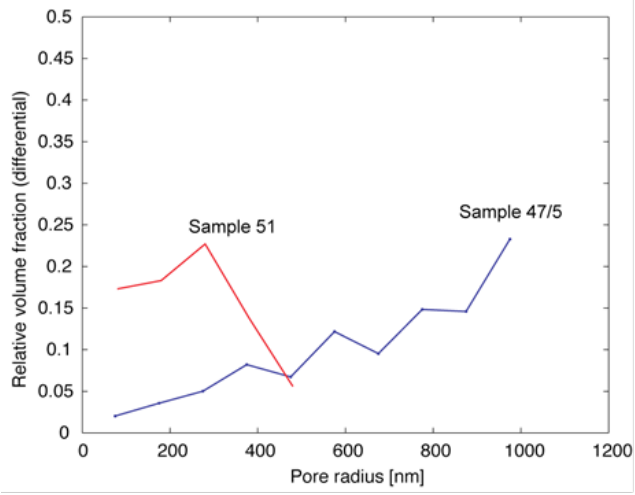

Fig. 2.71 Pore size distributions of microporosity in samples 47/5 and 051/8 based on 3D data from FIB

2.7.2.2 Critical porosity

The critical porosity at which one can expect a percolating pore network is a crucial parameter. Using finite-size scaling schemes in combination with local percolation analysis (/PRI 09/; /KEL 13/) the critical porosity can be estimated. Details about the critical porosity estimation can be found in /JOB 15/. Concerning the macroporosity of sample 47/5, the calculations yielded values for the percolation threshold in the 0.08 – 0.14 porosity range. Values along axes in different directions and calculated with a specific scaling scheme do not differ much (i.e. ~ 0.02) indicating an isotropic space geometry (Fig. 2.72). The calculated values are substantially higher than the bulk porosity, which documents the poor connectivity of the pore space.

Regarding sample 051 the calculations yielded values in the 0.05 – 0.11 porosity range but values related to a specific scaling scheme do not differ much (i.e. ~ 0.03) which indicates a near isotropic space geometry (Fig. 2.72). Critical porosities are much lower than the bulk porosity, which indicates good connectivity of macropores in sample 051. Regarding the porosity of sample 47/5 the critical porosity is > 0.06 and is much higher than the bulk porosity determined on the base of FIB-nt. This documents the poor connectivity of the pore microstructure.

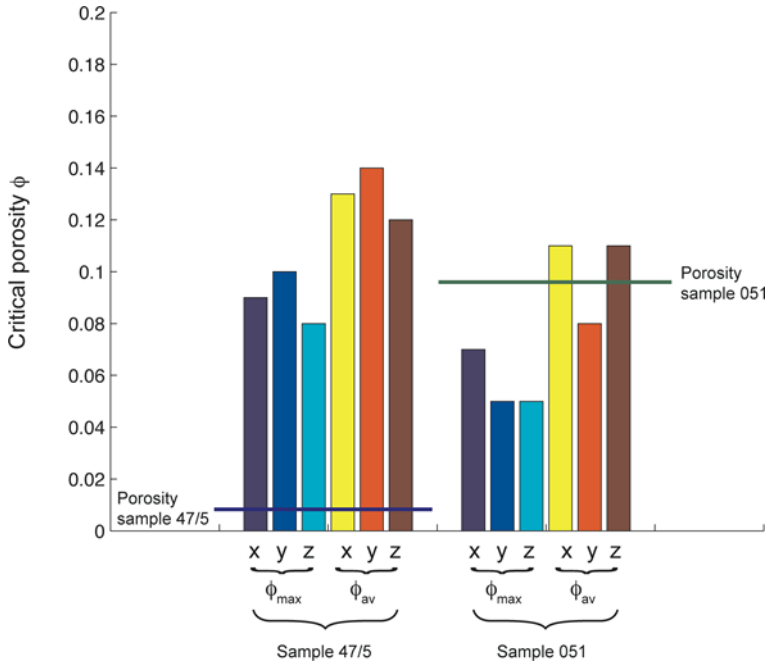

Fig. 2.72 Bar plot shows a compilation of the calculated percolation thresholds related to macroporosity for all samples. The values related to different percolation directions (x,y,z) are grouped according to the applied scaling scheme (i.e. Φ_{max} and Φ_{av})

2.7.2.3 Discussion

The porosity related to pores with radii > 4 µm was investigated in millimeter size compacted crushed rock salt samples by using XCT. The two analyzed samples differ substantially in porosity and pore connectivity. The pore space of sample 051 is fully connected. On the contrary, sample 47/5 has a porosity of around 1 % and the pore space is very poorly connected or maybe even not connected. By applying an approach, which combines local porosity theory and percolation theory, to reconstructed pore microstructures gives an idea of the porosity at the onset of percolation (i.e. percolation threshold or critical porosity). From the investigation of these two samples it can be stated that for porosities exceeding 5 % a percolating pore network must be taken into consideration. In addition, the analysis reveals that the pore space must be considered as isotropic in its connectivity and percolation threshold.

Micropores with radii < 1 µm can often be observed along grain boundaries of otherwise compact salt grain aggregates. A porosity that is related to these small pores is 1 % or

less and the pore space can be seen as very poorly or even not connected. Often the pore geometry is defined by crystallographic planes, which suggest that these pores are related to the formation of fluid inclusions which are per se not connected. These observations are in line with investigations described in /POP 12/. They found that added moisture was coating individual grains at the grain boundaries or located as droplet between grains or as intra-crystalline fluid inclusions. Increasing compaction leads to a microstructural redistribution of the brine from extended fluid films to isolated fluid inclusions as it is schematically shown in Fig. 2.73.

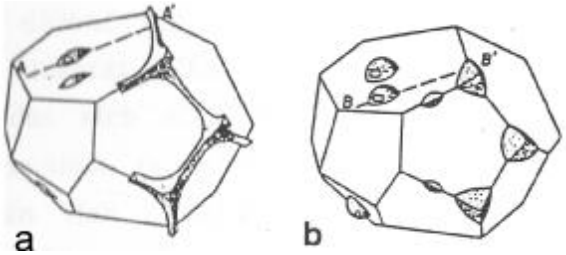

Fig. 2.73 3D-distribution of fluid phases in a pore space during compaction

(a) uncompacted sample – planar fluid films of fluid channels between grains,

(b) after compaction – discontinuation of the fluid films and development of isolated fluid inclusions /WAT87/

Taking small samples from large rock bodies raises the question about the representativeness of the reconstructed pore microstructures. Regarding porosity calculations based on local porosity theory and RVE calculations /JOB 15/ reveal that the pore space on the millimeter scale possess a certain degree of homogeneity. Thus, the samples size that can be analyzed by XCT is large enough to provide representative geometric information on the pores structure, of which radii exceed 4 µm. On the contrary the sample size that can be analyzed by FIB-nt is too small to provide representative geometric information on microporosity. Nevertheless, FIB based pore microstructures gives at least an idea of the 3D geometry of these smaller pores.

3 Basics for numerical modelling of compacting crushed salt

3.1 Scope

Chapter 3 covers a wide range of topics related to the modelling of compacting crushed salt. The first three subsections focus on the phenomena that are relevant for the compaction behaviour (section 3.2), the mathematical description of these phenomena (section 3.3) and the performance of the related models at simulating laboratory experiments (section 3.4).

Three approaches that are already in use are compared in section 3.3 on the basis of the mathematical formulations representing single physical effects:

– an extensively updated and advanced version of the model of Heemann, fully described in Appendix A,
– the model of Hein /HEI 91/ which was later modified by Korthaus /KOR 96/, and
– the model of Olivella et al., originally described in /OLI 93/ and later extended for humidity enhanced compaction in /OLI 02/.

The approach of Heemann is realised in the code JIFE /HEE 04/ while the approach of Olivella et al. was implemented in the code CODE_BRIGHT /COD 10/. In section 3.4 the performance of those two models is compared by means of benchmark calculations based on three laboratory tests.

Afterwards possibilities are explored to minimise the effort of determining constitutive relations for two-phase flow in compacting crushed salt (section 3.5) and to use the Discrete Element Method for numerically describing compaction (section 3.6).

3.2 Phenomenology and physics related to crushed salt compaction

At least three separate compaction regimes exist for crushed salt. Where humidity is involved, a fourth deformation mechanism may dominate deformation behaviour throughout all states of compaction.

– In the case of highly porous material, compaction may be dominated by grain slipping and rolling as well as by fracturing due to very high local stresses at the initially very small contact zones between the grains.
– In the case of moderately porous material, compaction is characterised by enlargement of the contact zones between the grains.
– In highly compacted material the ongoing compaction will be characterised by pore closure, similar to the convergence of caverns and mine drifts in rock salt.
– Where humidity is involved, pressure solution in the junction between two grains will enhance the global compaction rate drastically, especially in the case of small contact zones.

It appears plausible that the material response of dry crushed salt is defined by the creep behaviour of rock salt as well as the geometry of the compacting grains.

3.2.1 Compaction by creep of salt

Even in the case of a cursory visual inspection of usual crushed salt it can be seen that large grains are emplaced into a bed of small grains. The big grains predominantly are in rare contacts to other large pieces. The large grains thus swim within the finer material and are therefore only superficially deformed. The deformation on both sides of the contact area is defined by the same stress concentration due to the small contact areas at corners or edges of the fine grains. So the deformation and thus closure of pores by far most is ruled by the deformation of the fine grains. The big grains mainly do not deform except for a certain very small deformation at their surface where they are in contact with neighbouring fine grains. Under the microscope the finely crushed salt grain proves to be in the order of some 10 µm and predominantly is rectangular in shape.

The density of loose non-compacted crushed salt varies between about 1200 kg/m³ and 1800 kg/m³. That is equivalent to an initial void ratio of $\sim 0.2 \leq e_0 \leq 0.8$. In addition to the effect of grain size distribution, this variation results from different grain arrangement

(see Fig. 3.1). It also can be seen from Fig. 3.1 that in the case of such inelastic deformation the diameter of the contact zone will grow linearly with compaction due to the angular shape if there is no grain rearrangement. Furthermore, in the case of creep compaction, the contact zone between the crystals in densely packed material will grow faster than in the case of larger initial porosity. This is also true in the case of compacting 3-dimensional bodies. Thus the stress concentration initially will be very high due to the initially very small (by theory: infinitely small) contact area. With growing contact area this concentration of stress will be inversely reduced till there is no enhancement left for full compaction.

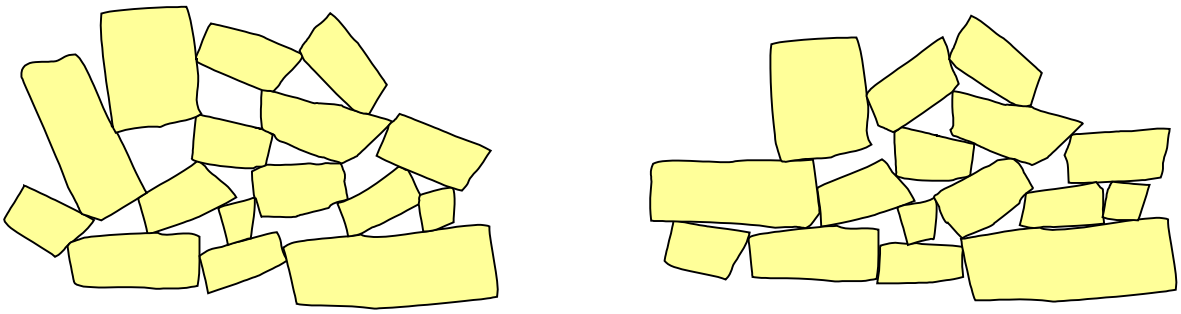

Fig. 3.1 Sketch of loose and dense crushed salt. The two piles only differ in the arrangement of the crystals. In case of the right pile the rearrangement of the grains may have been achieved by just shaking the pile. But it principally also can happen during compaction.

Of course, creep will occur due to local stresses following the mechanical laws of creep. In case of high stress concentration rather big stresses will appear in the contact zone even for moderate global stresses. Due to the very non-linear response of creep rate to stress the contact zone will be the dominating creep zone ruling the compaction behaviour of crushed salt. Within the bulk of the grain the stress will be about the same as that of global strain – at least its mean value.

While for loose or medium compacted crushed salt creep is ruled by the small but steadily increasing contact areas at corners and edges of the fine grains for highly compacted crushed salt the voids must decrease by a process similar to the convergence of caverns and drifts. If so, the creep rate of the voids must be proportional to the void ratio itself. That is different to the behaviour before where it is bound to the development of the con-

tact zones. Deviatoric strain rates must converge to the creep behaviour of ordinary (may be hardened, see below) creep of salt.

Despite any consideration on the major influence of the fine grains on compaction rate there is some reason that the coarse grains also play a certain active role in the deformation of crushed salt. Theoretical modelling of permeability as a function of changing porosity strongly suggests a relation governed by the third power of void ratio about (/KOZ 27/, /CAR 48/, unpublished work of Heemann on crushed salt). This does not completely match the experimental finding of a power of 3.84 on porosity (/MLY 99/) for dry crushed salt and even shows big differences in case of BGR-data (fifth power on porosity for “natural dry” crushed salt, /STÜ 95a/) or data of the DEBORA-Project (/ROT 99/). The reason for that may be found in a possible shielding of fine grain material by some coarse grains more or less in direct contact different to the assumption above. This would lead to a porosity that is kept open in some parts of the specimen while it is closing in most parts where it determines the global permeability. This way the “natural relation” between porosity and permeability will be distorted. The data of BGR also suggest a strong influence of grain size distribution on permeability. Among other effects that influence permeability via deformation mechanisms these effects will have to be investigated.

The stationary creep rate of salt can be captured by means of a Norton type stress dependency as well as – physically better founded – by means of a hyperbolic relation on deviatoric stress (e.g. /CAD 88/). But it has to be taken into account that creep of salt is strongly affected by a hardening (and softening) effect. This will be of important influence in case of sudden stress increase or reduction which seems to suggest a much higher power of stress for creep rate as it given physically. Without consideration of this effect the results of different laboratory strategies and technics (e.g. /STÜ 95a/, /STÜ 95b/, /KOR 96/) cannot be compared and evaluated in a joint way. Under common conditions in laboratory and in situ the local stresses at the broadening contact zones will be reduced with compaction. Thus generally the salt locally will be strongly hardened so that for constant or gradually increasing global stress the crushed salt will always provide quasi-stationary creep behaviour. So without sudden stress changes compaction of dry crushed salt probably can be modelled without taking regard of hardening effects.

3.2.2 Effect of grain rearrangement

But there is some evidence that usual creep is not the only effect of compaction in case of dry crushed salt. It is obvious that in case of shaking a rather loose pile will rearrange its grains with the consequence of a decreasing pore volume without any deformation of the grains (see Fig. 3.1).

Rearrangement can be defined as a sudden displacement of neighbouring grains, probably connected with a certain amount of rotation, leading to a higher coordination number (number of neighbouring grains in contact) and a smaller volume per grain. So compaction by usual creep deformation will not be considered here as grain rearrangement.

Nevertheless, in principle rearrangement can happen during compaction as well – without any shaking. But slip of grains is inseparably connected with friction which is ruled by the ratio of shear stress to vertical stress on the potential slip plane. It has to be assumed that the ratio of vertical stress to shear stress usually will grow so that, beyond a very short moment during emplacement, the relative positions of the grains should be fixed, mostly preventing any slip and rearrangement.

So, if there is any relevant amount of rearrangement it has to be associated with another deformation mechanism. The only mechanism left is fracturing due to high local stress at the contact zone that exceeds the fracture stiffness of salt (see Fig. 3.2). It has to be taken into account that fracturing is well known to be dependent on the square root of the grain diameter in case of solid multi grain bodies. It is to be expected that this effect will also apply in case of single grains in small contact areas with neighbouring grains.

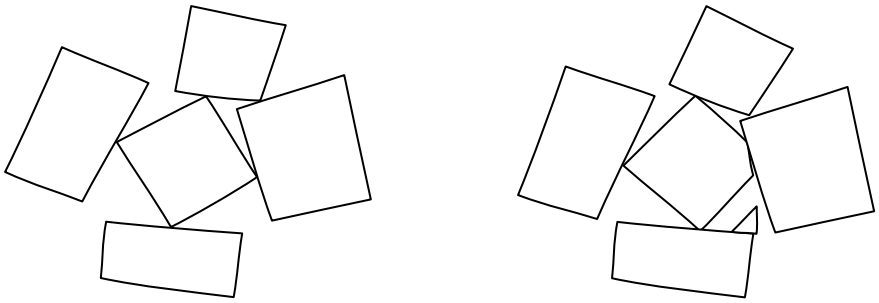

Fig. 3.2 Grain displacement (rearrangement) due to local fracture.

It has to be regarded that without any rearrangement the initial void ratio would be a very good phenomenological and physical parameter to describe the inner geometry of the pile. So, if shaking can influence the initial porosity and thus geometrical response of the material the rearrangement due to fracturing must have the same effect. Rearrangement can have a volumetric as well as a deviatoric component. But only the volumetric component changes the parameter “initial void ratio”.

3.2.3 Humidity enhanced compaction

Water has a big influence on the mechanical behaviour of crushed salt. Due to strong dipole forces the water molecules are bound to the surface of the salt ions. So, despite any high pressure at the contact areas between the grains water molecules still are located there thus enabling an easy exchange of places with salt ions. This way the high local pressure between the two grains promotes the diffusion of salt ions outside of the contact area where they reach a lower energetic place. This process is called pressure solution. It is usually described by means of a linear stress dependency. But there is some theoretical evidence that it gets a non-linearity for high stresses. The experimental results of Spiers /SPI 90/, /SPI 93/ support this assumption but the reason for this might also be found in the fact that the creep of the crystals due to intra-crystalline deformation is getting dominant for higher stresses. This has not been clarified yet. It also is not known how much the humidity influences the general shape of the grains and pores by promoting rounded geometries.

The diameter of the contact area determines the rate of compaction. In case of a diffusional process the rate of mass removal at the contact area must be given inversely proportional to the square of its diameter. This area is furthermore predefined by the diameter of the grains. Thus the small grains again bear the prominent part of compaction.

3.2.4 Permeability

Steady-state single-phase groundwater flow in common soils i.e. porous media with a rigid matrix can mathematically be described exclusively by the permeability. Only in case of transient flow the porosity is required as well. In case of compacting crushed salt, however, the porosity and thus also the permeability decreases. For modelling flow

over long periods of time a continuous permeability-porosity relation is therefore required.

In case of gas and liquid coexisting in the pore space the effective permeability of one of the two phases is reduced because a part of the pore space is occupied by the other phase. Additionally, capillary forces act on the interface between the liquid and the gas phase. These two-phase flow effects depend among other things on the heterogeneity of the pore space on the micro-scale which is caused by the specific grain size distribution of the porous material. It is thus apparent that these effects also change quantitatively in a compacting porous matrix. Note that the heterogeneities mentioned above occur on the micro-scale of a homogeneous, well-mixed material. It must be acknowledged that macroscopic inhomogeneities that are caused by a varying local grain size distribution result in related changes of all geohydraulic properties.

It has been mentioned already that the permeability found in laboratory does not fit to simple models of permeability as a function of decreasing void ratio (see section 3.2.1). It seems to be due to inhomogeneous development of porosity and permeability. Already a rather small fraction of non-compacting voids would explain the difference. These small portions themselves do not have a chance to connect to build a net of pathways with higher permeability that might dominate the global permeability. But there has not been gained a convincing model to describe that.

In case of grain size separation horizontal layers develop and the layers with coarse grains should keep a higher porosity than the layers with fine grains thus evoking an anisotropy in permeability. This effect is assumed to be much stronger in case of wet crushed salt than in case of dry material because – due to the dependency of humidity creep on the inverse of the third power of grain size – the layers with fine grains will develop much faster than those with coarse grains. The permeability in line with the layers should mostly be defined by the porosity of the coarse grains while the vertical permeability component mainly is ruled by the remaining pores of the fine grains.

There is experimental and theoretical support that pressure solution supports the closure of pores thus converging towards zero permeability. Nevertheless, an experimental proof is still missing due to problems in precise measurement of porosity. Furthermore, up to now it is not clear how much two-phase flow effects or other laboratory effects are pro-

voking these results. On the other hand, it cannot be excluded that surface stresses also in case of low or even zero humidity might have a similar effect.

Qualitatively, two-phase flow applies to the backfill material considered here as well as to common soils. However, quantitative differences caused by the specifics of the crushed salt material were to be expected and are actually found in the experimental work on the constitutive equations for two-phase flow described in section 2.6. Note that the impact of inhomogeneities in the crushed material that has been discussed above with respect to single-phase flow is much stronger in case of two-phase flow because of the strong non-linearity of the processes involved. It must therefore be of particular interest to assess the uncertainties in the backfill composition introduced by the preparation and emplacement procedure under operational conditions.

3.2.5 Dissolution and precipitation of salt

The solubility of salt in water is a function of temperature. Flow of brine in a domain of variable temperature can therefore lead either to dissolution of the crushed salt constituting the matrix or to precipitation of dissolved salt in the brine. Both effects change the pore channel diameter and thus the local porosity and permeability. On a larger scale they can result in a redistribution of salt in the backfill especially under large temperature gradients. A variety of possible effects that can occur depending on absolute temperature, temperature gradient, initial permeability etc. are indicated in /BEC 00/.

3.3 Development/definition and comparison of material models

3.3.1 Elastic behaviour

It generally can be stated that the elastic properties of crushed salt are of minor importance for numerical calculations because elastic strains mostly can be taken as much less than creep strains. Yet, their definition is essential for the calculation of stresses and should be as near to physical finding as possible. For full compaction the elastic moduli should reach the values of intact salt. For numerical reasons the stiffness has to be bigger than zero also for the loose initial state.

Model Heemann

Heemann has developed a rather complex expression giving, dependent on the grain size distribution, a mostly linear or slightly curved run with void ration e. Within the FEM-program JIFE this relation has been defined by definition points which have to be interpolated linearly.

Model Hein

Hein supposes a slightly concave run of stiffness with porosity η or void ratio e given by an exponential expression.

$$K = K_f \exp\left(-c_K \eta \frac{1-\eta_0}{1-\eta}\right) = K_f \exp\left(-c_K \eta \frac{1+e}{1+e_0}\right) \qquad (3.1)$$

$$G = G_f \exp\left(-c_G \eta \frac{1-\eta_0}{1-\eta}\right) = G_f \exp\left(-c_G \eta \frac{1+e}{1+e_0}\right) \qquad (3.2)$$

The transformation is given by $\eta = e/(1+e)$. For equal parametrisation with $c_K = c_G$ the Poisson ratio results as constant. The following parameters are given

$$\left.\begin{aligned} E &= 25\,GPa \\ \nu &= 0.27 \end{aligned}\right\} \Leftrightarrow \begin{cases} K_f = 18.12\,GPa \\ G_f = 9.84\,GPa \end{cases}$$

$$c_K = c_G = 9.2 \Leftrightarrow E = 1-25\,GPa \;\text{ für }\; \eta = 0.35-0.0 \qquad (3.3)$$

Model CODE_BRIGHT

CODE_BRIGHT makes use of a linear variation with porosity.

$$E = E_0 + (\eta - \eta_0)\frac{dE}{d\eta} \qquad (3.4)$$

The parameters are given by

$$E_0 = 1\,MPa \qquad \frac{dE}{d\eta} = -4500\,MPa$$

$$\eta_0 = 0.35 \qquad (3.5)$$

The elastic modulus $E(0) = 1576\,MPa$ for full compaction is clearly beyond that of rock salt. The Poisson ration is constant.

$$\nu = 0.27 \qquad (3.6)$$

3.3.2 Creep

Model Heemann

For volumetric creep the model of Heemann provides a creep rate

$$\dot{\varepsilon}_{\mathrm{vol}} = -2\,\mathrm{A}\exp\left(\frac{-\mathrm{Q}}{\mathrm{R}^{\mathrm{gas}}\,\mathrm{T}}\right)\left(\frac{\sigma_{\mathrm{local}} - \sigma_{\mathrm{RV}}}{1-\mathrm{z}}\right)^{\mathrm{n}-1}\cot(\alpha)\sqrt{\mathrm{U}}\left(\frac{\mathrm{p}}{\mathrm{U}'}\right)\mathrm{e}\frac{\mathrm{k}^{-1}+\mathrm{e}}{1+\mathrm{e}} \qquad (3.7)$$

with the local stress

$$\sigma_{local} = \sqrt{\left(\frac{p}{U'}\right)^2 + b\left(\frac{q}{U'^{\beta}}\right)^2} \qquad (3.8)$$

at the contact zones as a function of the hydrostatic pressure p and the deviatoric stress q (parameters $b = 2.53$ and $\beta = 0.82$). The parameter k has to be taken as a measure for the width of the grain size distribution. $k = 6$ has been determined for the standard crushed salt while for a unit grain size the correct value would be $k = 1$. The relative area U of the contact zone resulting from the geometrical model ($U = 0$ for virgin uncompacted crushed salt and $U \simeq 1$ for complete compaction)

$$U = \left(\frac{3}{2}\tan(\alpha)\right)^2 \left(\left(\frac{1+k\,e_o}{1+k\,e}\right)^{1/3} - 1\right)^2 \qquad (3.9)$$

has been extended to overcome slight insufficiencies of the geometric modelling

$$U' = (\kappa\, U)^{\gamma} \qquad (3.10)$$

with the two parameters $\kappa = 1.41$ and $\gamma = 0.84$.

In eq. (3.7) the Norton-approach is easily to be identified for the creep of rock salt with the parameters

$$A = 0.18\, d^{-1}$$
$$Q = -54\, kJ / mol$$
$$n = 5 \qquad (3.11)$$

and the universal gas constant $R^{gas} = 8.3143E-3\, kJ/(mol\, K)$. σ_{RV} is a dynamically developing resistive stress due to hardening which in a stationary state tends to

$$\sigma_{RV} \rightarrow z\, \sigma_{local} \qquad (3.12)$$

with $z \simeq 0.65$. The angle α (see Fig. A.1 and eq. (3.7)) is a function of initial void ratio.

$$\cot(\alpha) = \sqrt{1 + k\, e_0} - 1 \qquad (3.13)$$

For small void ratios volumetric creep is decreasing linearly with void ratio thus fulfilling theoretical expectation and avoiding negative porosity. Deviatoric creep is divided up into the creep due to the effect of the voids (analogous to volumetric creep, eq. (3.7)) as well as creep of the inner bulk of the grains not seeing any relevant enhancement but also is connected with a hardening stress σ_R.

$$\dot{\varepsilon}_{dev} = 2\,A\exp\left(\frac{-Q}{R^{gas}\,T}\right)\left(\frac{\sigma_{local}-\sigma_{RV}}{1-z}\right)^{n-1}\cot(\alpha)\sqrt{U}\,c\left(\frac{q}{U'^{\beta}}\right)e\frac{k^{-1}+e}{1+e} + A\exp\left(\frac{-Q}{R^{gas}\,T}\right)\left(\frac{q-\sigma_R}{1-z}\right)^{n} \qquad (3.14)$$

The new constant c is given by $c = 0.85$. Combining the approaches of volumetric and deviatoric creep the tensorial expression for creep of crushed salt results in

$$\dot{\varepsilon}_{ij} = 2\,A\exp\left(\frac{-Q}{R^{gas}\,T}\right)\left(\frac{\sigma_{local}-\sigma_{RV}}{1-z}\right)^{n-1}\cot(\alpha)\sqrt{U}\,e\frac{k^{-1}+e}{1+e}\left(\frac{p}{U'}\frac{\delta_{ij}}{3}+\frac{3}{2}c\left(\frac{q_{ij}}{U'^{\beta}}\right)\right) + \frac{3}{2}A\exp\left(\frac{-Q}{R^{gas}\,T}\right)\left(\frac{q-\sigma_R}{1-z}\right)^{n-1}q_{ij} \qquad (3.15)$$

For a complete derivation of the creep model see Appendix A.

Model Hein

The Hein-model is given in a way common for continuum-mechanics-approaches.

$$\dot{\varepsilon}_{ij}^{DC} = \Gamma\left\langle\varphi\left(F-F_0\right)\right\rangle\frac{\partial G}{\partial\sigma_{ij}} \qquad (3.16)$$

Here an associated flow rule is chosen using identical functions F and G. The functions are given by

$$\Gamma = \frac{1}{2} A e^{-\frac{Q}{RT}}$$
$$\varphi\left(F - F_0\right) = F^n$$
$$F = G = \left(h_1\, p^2 + h_2\, q^2\right) \qquad (3.17)$$

The flow yield F_0 is assumed to be zero. Thus crushed salt principally is deforming even for slightest stresses. For reasons of comparison with the model of Heemann the quadratic stress expression in eq. (3.17) can be transformed to

$$_{Hein}\sigma_{local} = \sqrt{h_1\, p^2 + h_2\, q^2} \qquad (3.18)$$

which can be interpreted as a local stress. So eq. (3.16) gets a form that is very similar to the expression of Heemann.

$$\dot{\varepsilon}_{ij}^{DC} = A e^{-\frac{Q}{R^{gas} T}}\, {}_{Hein}\sigma_{local}^{n-1} \left(h_1\, p \frac{\delta_{ij}}{3} + h_2\, q_{ij} \right) \qquad (3.19)$$

Two variants exist for the calculation of the functions h_1 and h_2. The original version of Hein is given by

$$h_1 = \frac{1 - c_1\, e^{c_2 \eta}}{\left(\frac{c_3}{c_4} \left(\left(\frac{1-\eta}{1-\eta_0} \right)^{c_4} - 1 + \Delta \right) \right)^2},$$
$$h_2 = c_5 + c_6\, h_1 . \qquad (3.20)$$

$c_{1\ldots6}$ are material parameters, Δ is a small value inserted to avoid singularity in the function h_1 for initial porosity.

Eq. (3.20) is based on theoretical reasoning but the analysis of the function shows a physically implausible behaviour so that Korthaus modified this formulation /KOR 96/.

$$h_1 = \frac{a}{\left(\eta^{-c} - \eta_0^{-c} + \Delta\right)^m},$$
$$h_2 = 1 + b\,h_1 .$$
(3.21)

Model CODE_BRIGHT

In CODE_BRIGHT an approach has been defined which is very similar to that of Hein from a continuum mechanical point of view

$$\dot{\varepsilon}_{ij}^{DC} = \frac{1}{\mu_{dev}^{DC}} \langle \Phi(F) \rangle \frac{\partial G}{\partial \sigma'}$$
(3.22)

with the further functions

$$G = F = \sqrt{q^2 + \left(\frac{-p'}{\alpha_p}\right)^2} \qquad \Phi(F) = F^n$$
$$\frac{1}{\mu_{vol}^{DC}} = A(T)\, g_{vol}^{DC}(e) \qquad \frac{1}{\mu_{dev}^{DC}} = A(T)\, g_{dev}^{DC}(e)$$
$$g_{vol}^{DC}(e) = 3(g-1)^n\, f \qquad g_{dev}^{DC}(e) = \left(\sqrt{\frac{1+g+g^2}{3}}\right)^{n-1} \left(\frac{2\cdot g+1}{3}\right) f + \frac{1}{\sqrt{g}}$$
$$A(T) = A_A \exp\left(\frac{-Q_A}{R^{gas}\, T}\right) \qquad \alpha_p = \left(\frac{\mu_{vol}^{DC}}{\mu_{dev}^{DC}}\right)^{1/(n+1)}$$
$$g = \frac{1}{(1-f)^2} \qquad f = \sqrt{\frac{2e}{3\left(1-e^{3/2}\right)(1+e)}}$$
(3.23)

The expression F for the stress potential can formally be modified to

$$F = \mu_{dev}^{DC1/(n+1)} \sqrt{\frac{q^2}{\mu_{dev}^{DC2/(n+1)}} + \frac{p'^2}{\mu_{vol}^{DC2/(n+1)}}}$$
$$= \mu_{dev}^{DC1/(n+1)}{}_{GRS}\, \sigma_{local}$$
(3.24)

so that also a counterpart to the expression of Heemann appears. But it is very hard to compare the given functions from an analytical point of view. Combining all equations of (3.22) and (3.23) for CODE_BRIGHT a final expression results with

$$\dot{\varepsilon}_{ij}^{DC} = \frac{1}{\mu_{dev}^{DC}} F^n \frac{\partial G}{\partial \sigma'} = \frac{1}{\mu_{dev}^{DC}} \sqrt{q^2 + \left(\frac{-p'}{\alpha_p}\right)^2}^{n-1} \left(\frac{p'}{\alpha_p^2}\frac{\delta_{ij}}{3} + \frac{3}{2} q_{ij}\right)$$
$$= A_A \exp\left(\frac{-Q_A}{R^{gas} T}\right) g_{dev}^{DC}(e)\, {}_{GRS}\sigma_{local}^{n-1} \left(\frac{p'}{\alpha_p^2}\frac{\delta_{ij}}{3} + \frac{3}{2} q_{ij}\right). \qquad (3.25)$$

The parameters correspond to the data set in eq. (3.11).

$$A_A = 2.08E-6\, s^{-1} MPa^{-5} \cong 0.18\, d^{-1} MPa^{-5}$$
$$Q_A = 54\, kJ/mol \qquad n = 5 \qquad (3.26)$$

3.3.3 Grain rearrangement due to fracturing

Model Heemann

Fracturing occurs when the local stress in the contact zone exceeds a given limit $\sigma^{\#}$.

$$\sigma^{\#} = \sigma_o^{\#} \sqrt{\frac{10\, mm}{D_i}} \qquad (3.27)$$

In eq. (3.27) it has been taken into account that this limit of stress has experimentally proven to be inverse proportional to the root of grain diameter. For a diameter of about $1cm$ the parameter $\sigma_o^{\#}$ should be about that of fracture stress for compact rock salt. As a reference value for the grain diameter the fraction with the lowest grain diameter has to be taken.

So deformation due to fracture and grain rearrangement will happen as soon as the function

$$G^{\#}(\sigma_{\text{local}}) = \langle \sigma_{\text{local}} - \sigma_{\#} \rangle \qquad (3.28)$$

is getting positive. The local effect due to fracturing must have a similar geometry dependency as that of eq. (3.7) so that

$$\dot{\varepsilon}_{ij}^{\#} = B^{\#}\, G^{\#}\left(\sigma_{local}\right)\cot\left(\alpha\right)\sqrt{U}\, e\,\frac{k^{-1}+e}{1+e}\,\frac{\partial G^{\#}\left(\sigma_{local}\right)}{\partial \sigma_{local,ij}} \qquad (3.29)$$

results. Fracture deformation does not show any temperature dependency. The derivation of the potential $G^{\#}\left(\sigma_{local}\right)$ to the local stresses is given by

$$\frac{\partial G^{\#}\left(\sigma_{local}\right)}{\partial \sigma_{local,ij}} = \frac{1}{\sigma_{local}}\left(\frac{p}{U'}\frac{\delta_{ij}}{3}+\frac{3}{2}\sqrt{b}\,\frac{q_{ij}}{U'^{\beta}}\right). \qquad (3.30)$$

The parameters are the same as those of eq. (3.8). It is essential for the understanding of the process of grain rearrangement that not only the void ratio e is affected but also the value of e_0 which had been understood as the initial void ratio so far. The basic idea is that this shift in void ratio is similar to the change of void ratio in case of shaking of a loose pile.

$$\begin{aligned}\Delta e &= \left(\dot{\varepsilon}_{vol}^{creep}+\dot{\varepsilon}_{vol}^{\#}\right)\left(1+e\right)\Delta t\\ \Delta e_o &= \dot{\varepsilon}_{vol}^{\#}\left(1+e\right)\Delta t\end{aligned} \qquad (3.31)$$

Describing fracture deformation in the form of a creep law has been chosen to adjust it to the other mechanisms of creep. But fracture deformation still is restricted to certain values and cannot get arbitrarily big. For growing compaction it is getting more and more difficult to achieve fracturing. Though fracturing itself is temperature independent, in case of creep at high temperatures the necessary stresses might be reached for a loose material only while for low temperature there will be low creep so that high stresses may be reached favouring fracturing and thus quasi brittle behaviour in agreement with expectation.

The combined deviatoric deformation of creep and fracture is given by

$$\Delta\varepsilon_{dev} = \left(\dot{\varepsilon}_{dev}^{creep}+\dot{\varepsilon}_{dev}^{\#}\right)\Delta t. \qquad (3.32)$$

The interim value of the parameter $B^{\#}$ has been set to $B^{\#} \approx 10$ so far.

It is important from a theoretical point of view that a shift of the initial void ratio due to fracturing will have an impact on the parameters of creep as well and thus on the behaviour at low void ratios.

For a complete derivation of the model see Appendix A.

Model Hein

The model of Hein also involves a part of deformation that is related to grain rearrangement. It follows the attempt given in eq. (3.16). It is characterized by a porosity dependency of the function Γ and a linear dependency in stress. But it has not been implemented yet.

Model CODE_BRIGHT

Grain rearrangement as a consequence of fracturing has been implemented in CODE_BRIGHT by means of a visco-plastic behaviour via a classical continuum mechanical attempt.

$$\dot{\varepsilon}_{ij}^{VP} = \Gamma < \Phi(F) > \frac{\partial G}{\partial \sigma} \qquad (3.33)$$

with

$$\Gamma = \Gamma_0 \exp\left(\frac{-Q}{R^{gas}\,T}\right) \qquad G = F = q^2 - \delta^2\left(p_0\, p' - p'^2\right)$$
$$\Phi(F) = F^m \qquad p_0 = D\,\varepsilon_V^l \qquad (3.34)$$

as a function of volumetric deformation ε_V. The parameters are given by

$$\delta = 10.0 \qquad p_0 = 0.1 MPa$$
$$\Gamma_0 = 7.0E-4\, s^{-1} \qquad Q = 54 kJ / mol$$
$$D = 1.0E5\, MPa \qquad l = 4$$
$$m = 3 \qquad (3.35)$$

3.3.4 Humidity creep

Model Heemann

The modelling of humidity creep is based on the assumption that it is due to the diffusion of salt ions under the driving force of a pressure gradient on the contact areas between the grains of the crushed salt. Right from the principles of stochastical physics a macroscopic creep rate could be derived

$$\dot{\varepsilon}_{vol}^{diff} = -\frac{D^{diff}}{R\, D_i \left(1+\cot(\alpha)\right)^{1/3}} \frac{(1+k\,e)^{2/3}}{k(1+e)} \exp\left(\frac{-Q^{diff}}{R^{gas}\, T}\right) \sinh\left(\frac{\overline{\sigma}_n\, 3\kappa'}{T\, R}\right) \qquad (3.36)$$

as a function of the mean stress $\overline{\sigma}_n$ on the contact area. Here the same idealized geometry of the grains has been used. The radius R results from a radial symmetric capture of the contact area.

$$R = \varsigma \frac{s'}{2} = \varsigma \frac{3}{4} \frac{D_i\left(1+\cot(\alpha)\right)}{\cot(\alpha)} \left(1 - \left(\frac{1+k\,e}{1+k\,e_o}\right)^{\frac{1}{3}}\right) \qquad (3.37)$$

The generalized creep rate including deviatoric components has been found by making further use of the conventional attempt in continuum mechanics.

$$\dot{\varepsilon}_{ij}^{diff} = \frac{D^{diff}}{R\, D_i \left(1+\cot(\alpha)\right)^{1/3}} \frac{(1+k\,e)^{2/3}}{k(1+e)} \exp\left(\frac{-Q^{diff}}{R^{gas}\, T}\right) \sinh\left(\frac{\sigma_{local}\, 3\kappa'}{T\, R}\right) \cdot \left(-\frac{p}{\sigma_{local}} \frac{\delta_{ij}}{3} + c_d \frac{3}{2} \frac{q_{ij}}{\sigma_{local}}\right), \qquad (3.38)$$

Here $\bar{\sigma}_n$ has been replaced by σ_{local} which has been defined already in eq. (3.8). The activation energy has been estimated by $Q^{diff} = 25 kJ / mol$ what is in very good agreement with the value of eq (3.45)). Both parameters D^{diff} and κ' up to now only could be defined via the product $D^{diff}\,\kappa'$. In first calculations they have been fixed by $\kappa' \sim 4.6E-9\, K\,m / MPa$ and $D^{diff} \sim 9.2E-5\, m^2$.

For a complete derivation of the model on humidity creep see Appendix A.

Model Hein

Humidity creep is yet not incorporated in the model of Hein.

Model CODE_BRIGHT

Humidity creep (in CODE_BRIGHT called Fluid-Assisted-Diffusional-Transport, FADT) follows a linear stress dependency similar to what Spiers had found experimentally

$$\dot{\varepsilon}_{ij}^{FADT} = \frac{1}{2\,\mu_{dev}^{FADT}} q_{ij} + \frac{1}{3\,\mu_{vol}^{FADT}} p'\,\delta_{ij} \qquad (3.39)$$

with

$$\frac{1}{\mu_{vol}^{FADT}} = \frac{16\,B(T)\sqrt{S_l}}{d_0^3}\, g_{vol}^{FADT}(e) \qquad (3.40)$$

and

$$\frac{1}{2\,\mu_{dev}^{FADT}} = \frac{16\,B(T)\sqrt{S_l}}{d_0^3}\, g_{dev}^{FADT}(e) \,. \qquad (3.41)$$

The property S_l describes the water saturation of the pores. The thermal dependency is defined by an Arrhenius term.

$$B(T) = \frac{A_B}{R^{gas} T} \cdot \exp\left(\frac{-Q_B}{R^{gas} T} \right) \qquad (3.42)$$

The dependency on void ratio e has been captured by

$$g_{vol}^{FADT}(e) = \frac{3g^2 e^{3/2}}{1+e} \qquad (3.43)$$

and

$$g_{dev}^{FADT}(e) = \frac{g^2}{1+e} \qquad (3.44)$$

The function g is defined by eq. (3.24). The parameters are given by

$$\begin{aligned} &A_B = 1.0E-14\, s^{-1} MPa^{-1} m^3 = 8.64E-10\, d^{-1} MPa^{-1} m^3 \\ &Q_B = 24.53 kJ / mol \qquad\qquad d_0 = 1.5E-4 \end{aligned} \qquad (3.45)$$

3.3.5 Comparison of creep rates

Despite the obvious similarity in the three attempts on creep a direct comparison of the expressions $U' \leftrightarrow 1/h_1$ and $U'^{\beta}/\sqrt{b} \leftrightarrow 1/h_2$ or $U' \leftrightarrow \mu_{dev}^{DC\,2/(n+1)}$ and $U'^{\beta}/b \leftrightarrow \mu_{vol}^{DC\,2/(n+1)}$ could only provide a limited understanding because especially the attempts of Heemann and CODE_ BRIGHT involve further geometrically or continuums mechanical terms influencing the creep rate as a function of porosity.

More insight can be got by means of a graphical comparison of the creep rates found in numerical calculations for a given hydrostatic pressure (for instance $p = 1MPa$) and a set of different deviatoric stresses (e. g. $q = 0\,MPa, 0.1MPa, 1MPa, 10\,MPa$). In the following the influence of initial porosity has been captured by two values ($e_0 = 0.45$ and $e_0 = 0.55$). Temperature has been fixed to one value ($T = 300°K$). Due to the same exponent of stress and the same activation energy for all three models the above given set of stress and temperature conditions can be taken as covering all differences and agreements that can be transferred to other stresses and temperatures.

The model of Heemann has been calculated for two variants one of them corresponding to the standard grain size distribution (see Fig. 3.3 to Fig. 3.7, red line, $k = 6$) and the other one representing a crushed salt with unit grain size (see Fig. 3.3 to Fig. 3.7, green line, $k = 1$). The creep rates for the unit grain size material turned out to be less by about one or two orders of magnitude for loose material.

Regarding deviatoric creep rate it has to be expected that in case of full compaction (zero porosity) it should match creep rate of rock salt. Except for the original model of Hein (see Fig. 3.3 and Fig. 3.4, blue line) all models meet that requirement. The deviatoric creep rate is rising with growing hydrostatic stress (Fig. 3.3 and Fig. 3.4) for all models. But it has to be regarded that even in case of logarithmic scaling the differences in creep rate cannot be overseen, ranging from one to four orders of magnitude between the different models. The deviation of the CODE_BRIGHT model (e.g. Fig. 3.3 and Fig. 3.4, orange line) from the other models suggests that due to functional relations without any influence of initial porosity a close fit to data is not possible for loose material. But in case of high porosity there will be only very low stresses in situ without any relevance for the geomechanical process. The influence of the initial porosity ($e_0 = 0.45$ and $e_0 = 0.55$) is not very high when the axis of porosity is scaled to the same length. The differing creep rates very close to initial porosity may be due to the influence of the same amount of precompaction and are of no significance. The CODE_BRIGHT model is principally not influenced by the value of the initial porosity.

In case of volumetric creep rates (see Fig. 3.5 and Fig. 3.6) the original Hein-model approaches a positive value for zero porosity thus principally allowing to get negative values of porosity. This unreasonable state is prohibited by algorithmic limitation. The model of Heemann provides a linear dependency of creep rate on porosity as a consequence of physical modelling (see Fig. 3.6). In case of the CODE_BRIGHT model and the Hein model modified by Korthaus (Hein_K) /KOR 96/ the steepness of the curves for low porosity is depending on the amount of hydrostatic pressure.

For the models of Heemann and modified Hein model (Hein_K) a change in the initial porosity mainly leads to a compression or stretching of the porosity axis (see Fig. 3.5 and Fig. 3.7). For void ratios below $e \leq 0.2$ about the influence of initial void ratio can be neglected. In the original Hein model a smaller initial void ratio leads to a rising of creep rate for all void ratios.

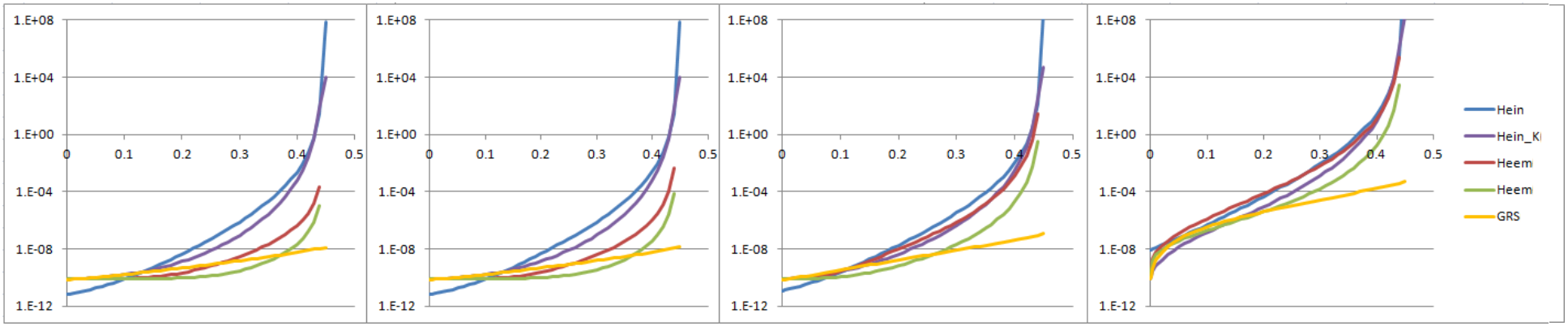

Fig. 3.3 Deviatoric creep rate for the models of Hein (blue), Hein in the version of Korthaus (violet), Heemann for k=6 (standard grain size distribution, red) as well as k=1 (unit grain size, green) and CODE_BRIGHT (GRS, orange) for a deviatoric load of $\sigma^{dev} = 1MPa$, with growing hydrostatic pressure (from left to right) of $|\sigma^{hyd}| = 0\,MPa, 0.1MPa, 1MPa, 10\,MPa$. Initial void ratio $e_0 = 0.45$.

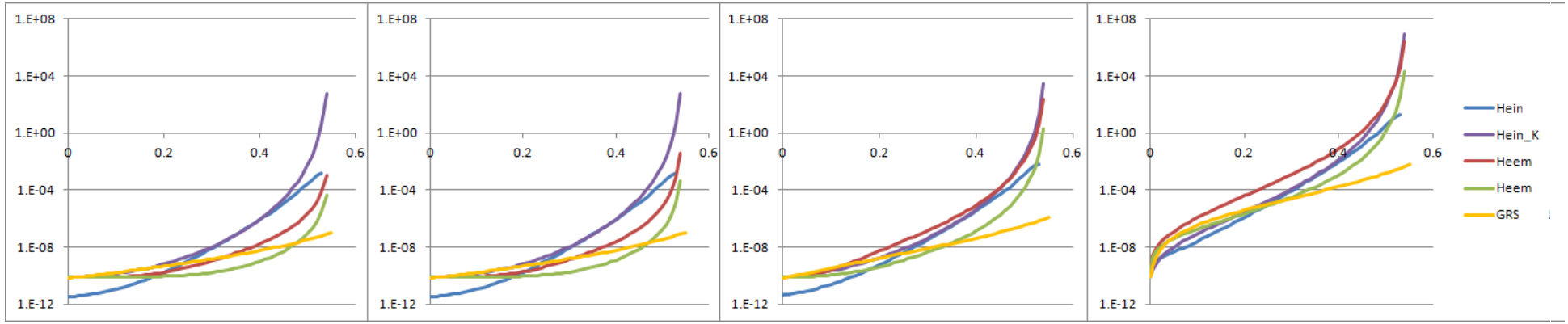

Fig. 3.4 Deviatoric creep rate for the models of Hein (blue), Hein in the version of Korthaus (violet), Heemann for k=6 (standard grain size distribution, red) as well as k=1 (unit grain size, green) and CODE_BRIGHT (GRS, orange) for a deviatoric load of $\sigma^{dev} = 1MPa$, with growing hydrostatic pressure (from left to right) of $|\sigma^{hyd}| = 0\,MPa, 0.1MPa, 1MPa, 10\,MPa$. Initial void ratio $e_0 = 0.55$.

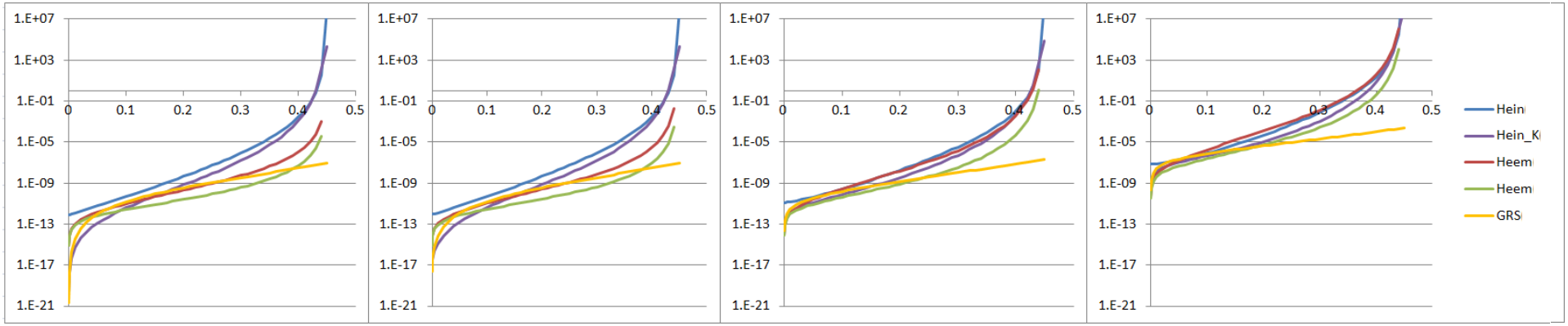

Fig. 3.5 Volumetric creep rate for the models of Hein (blue), Hein in the version of Korthaus (violet), Heemann for k=6 (standard grain size distribution, red) as well as k=1 (unit grain size, green) and CODE_BRIGHT (GRS, orange) for a hydrostatic load of $\sigma^{hyd} = 1MPa$, with growing deviatoric stress (from left to right) of $\sigma^{dev} = 0\,MPa, 0.1MPa, 1MPa, 10\,MPa$. Initial void ratio $e_0 = 0.45$.

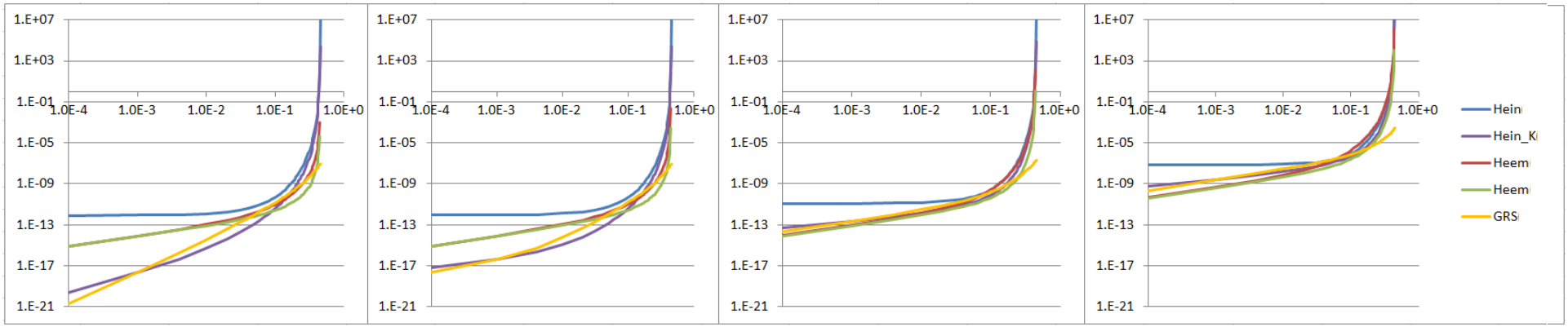

Fig. 3.6 Volumetric creep rate in double logarithmic presentation for the models of Hein (blue), Hein in the version of Korthaus (violet), Heemann for k=6 (standard grain size distribution, red) as well as k=1 (unit grain size, green) and CODE_BRIGHT (GRS, orange) for a hydrostatic load of $\sigma^{hyd} = 1MPa$, with growing deviatoric stress (from left to right) of $\sigma^{dev} = 0\,MPa, 0.1MPa, 1MPa, 10\,MPa$. Initial void ratio $e_0 = 0.45$.

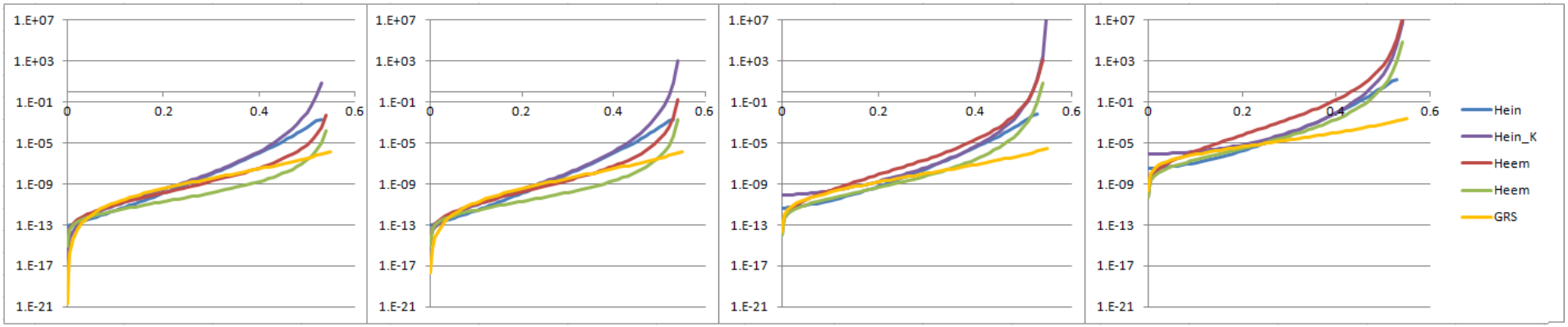

Fig. 3.7 Volumetric creep rate for the models of Hein (blue), Hein in the version of Korthaus (violet), Heemann for k=6 (standard grain size distribution, red) as well as k=1 (unit grain size, green) and CODE_BRIGHT (GRS, orange) for a hydrostatic load of $\sigma^{hyd} = 1MPa$, with growing deviatoric stress (from left to right) of $\sigma^{dev} = 0\,MPa, 0.1MPa, 1MPa, 10\,MPa$. Initial void ratio $e_0 = 0.55$.

3.3.6 Further considerations on behaviour of crushed salt and the material laws

In the model of Heemann additionally the influence of inner crystalline hardening has been taken into account. In case of steadily growing pressure this does not lead to appreciable differences in creep behaviour because the contact zones of the grains always receive a strongly hardened structure comparable to the state of stationary creep. In case of Hein and CODE_BRIGHT this indirectly has been implied already by the choice of the creep parameters of rock salt for stationary creep. Sudden stress reduction or raising common to laboratory tests is to be expected in situ only under exceptional circumstances. Thus, the explicit consideration of hardening seems to be of little relevance for at least most parts of compaction.

However, a fundamental role of the hardening model can be seen in a new attempt to better understand and compare the experimental results of Korthaus and Stührenberg. Due to the high exponents of stress that seemed to appear in the experiments of Stührenberg a model representation of all results of both experimenters with a consistent set of parameters could not be done. But by means of a new evaluation on basis of the hardening model these differences could be overcome. So about the same parameters for hardening could be derived for crushed salt as they are known for rock salt. Especially in an evaluation of stress reduction tests in Stührenberg's test series, taking regard of hardening effects, the exponent of stress was found to be given with $n \approx 5$ as it is known from many experiments on rock salt.

In recent evaluations Hampel found out that an exponent of $m = 7$ would better describe the stress dependency of rock salt for stationary creep (/HAM 10/). Theoretical considerations of Heemann on the mechanisms of creep and hardening lead to the finding that in case of sudden stress changes the corresponding exponent of stress to describe the change in creep rate is lower by 2 compared to the exponent of stress for stationary creep what can be captured by $m = n + 2$. So both results in crushed salt and rock salt perfectly match the theoretical results. Of course, if the exponent of stress has to be changed from 5 to 7, also the activation energy will have to be changed. According to Hampel, the new value will be $Q \simeq 110\,kJ/mol$.

The enhanced evaluation of the laboratory data gives a reliable prognosis of stationary creep in a stress regime typically between $15\,MPa$ and $30\,MPa$. For higher temperatures at $\sim 250°C$ the stress spans $2\,MPa$ to $20\,MPa$. In the mostly rather little contact zones of the crushed salt grains there are rather high local stresses even in case of moderate compaction rates. It is a general finding that the creep rate shows an increasing steepness with growing stress. So, basing on that, the exponent of stress in crushed salt will be given by $m = 7$ at least or even higher.

An evaluation based on this set of changed parameters for the creep of rock salt which are fundamental for all models could not be performed within the REPOPERM-project because it would have made necessary to redetermine all other parameters as well. So the quantitative comparison of the models will have to be regarded as preliminary.

In CODE_BRIGHT as well as in the model of Heemann the effects of grain rearrangement and humidity creep are incorporated. Unfortunately in case of the model of Heemann due to some delay in the implementation of these effects into the FEM-program JIFE no numerical calculations to compare the results could be done. Nevertheless some similarities as well as discrepancies can be identified.

In both models on grain fracturing and rearrangement this process is captured by time dependent creep processes. CODE_BRIGHT explicitly includes a temperature dependency while in the model of Heemann fracturing and rearrangement is triggered by the exceeding of a fracture stress $\sigma^{\#}$ which is grain size dependent. If there is any temperature dependency it should be possible to see it by means of a very careful evaluation of experimental data to be gathered for this purpose. For the model of Heemann the probably most important effect might be that in the wake of the quantitative analysis of this deformation process also the parameters on creep compaction will have to be redetermined thus enhancing the quality of the calculations for low porosity.

In the model of CODE_BRIGHT on humidity creep (fluid assisted diffusional transport, FADT) there is a linear relation on the hydrostatic and deviatoric stress components.

$$\dot{\varepsilon}_{ij} = \frac{A}{T\,D_i^3} \exp\left(\frac{-Q}{R^{gas}\,T}\right)\left(f_1(e)\,q_{ij} - f_2(e)\,p\,\delta_{ij}\right) \qquad (3.46)$$

In case of the model of Heemann there is a hyperbolic dependency on the quadratically combined stress σ_{local} as it is used for all deformation processes. For low or moderate stresses the hyperbolic relation gets linear as well and thus formally can be described in the same way as in eq. (3.46). The function $f_1(e)$ and $f_2(e)$ only differ by a little factor near 1. Up to now in the code of the FEM-program JIFE it has not been taken into account that for small void ratios there will be a certain change in the geometry dependence of creep that must be allowed for as it has been done for dry crushed salt. On the other hand in case of humidity it is not clear up to now at which void ratio the voids are getting impermeable so that the fluid pressure inside will prevent any further compaction.

At the present state of knowledge it is not clear whether the non-linear part of the hyperbolic stress function already reflects the nonlinear stress dependence in the experimental results of Spiers /SPI 93/ or whether this experimental non-linearity results from an overlap with ordinary creep effects. Also, the consistency of the postulated porosity dependency of the model with the experimental data has not yet been verified.

3.3.7 Summary

Overall, the three models yield similar results. The conditions under which the calculations gave rather big deviations practically are of little importance under in situ conditions, especially for a high porosity. Nevertheless, in view of the discrepancies of two orders of magnitude at best these deficiencies cannot be ignored. In case of compaction rates that are ruled by the converging host rock these differences will be less by a factor of 5 about, but for medium porosities already there will be a growing interaction of host rock and backfill. The creep rates may differ by orders of magnitude in case of low porosity what might affect long term safety assessment.

The model variant of Korthaus however seems to lead to more plausible results than the original Hein model. The Korthaus variant is also in better agreement with the geometrically-physically motivated model of Heemann. It is to be expected that for the Heemann model an increase in quality will be reached if the description of grain rearrangement will give satisfying results thus also enabling a better quality for creep calculations at low porosity. A verification is still pending.

The analytical approach of Heemann has the advantage of making use of relations which largely correspond to the physical demands. This reduces the number of parameters and also makes it possible to better analyse deviations between model and laboratory or in-situ results and, if necessary, remediate the reason for that. In this comparison, however, numerical models are compared with one another so that a clear statement about the quality of the calculations is not possible since it is not always clear which of the curve trajectories is closest to the phenomena occurring in real crushed salt.

Regarding the technical implementation of the crushed salt in situ, a separation of the grains of different size is to be expected. For low or medium compaction the model of Heemann yields differences of up to two orders of magnitude. For low porosities the difference vanishes.

The model of Heemann on grain rearrangement and humidity creep still is a very young implementation in the JIFE program and so the parameters could not be finally determined so far. Thus a comparison with the modelling in CODE_BRIGHT was not possible yet.

Despite the advantages of an analytical derivation of the physical behaviour of crushed salt it cannot be ignored that the model of Heemann ultimately also is based on phenomenological fitting to experimental results, albeit to a small extent. On the one hand, this should allow to better take account of details of the phenomena which could not be captured exactly, but on the other hand uncertainties in process understanding are again introduced to a certain amount. These uncertainties, however, have very narrow limits with regard to the given analytical relationships.

With regard to the elastic properties of the crushed salt, it can be stated that these are of little importance since the elastic strains are much smaller than the inelastic ones and thus only are of minor quantitative relevance for numerical modelling.

3.4 Benchmark calculations and parameter improvement

3.4.1 Calculation of experimental bounds on oedometric compaction test results

In order to compare the capabilities of the different models to reproduce experimental data several experimental curves on oedometric compaction test with constant rate of $d\varepsilon/dt = 7 \cdot 10^{-7}\ s^{-1}$ had been compiled to find experimental bounds for given temperatures /STÜ 95/. At first it was tried to reproduce this data based on parameters found in the BAMBUS project by /BEH 99/ called parameter set A (resp. GRS-254[8]) further on. This exercise, however, did not prove to be successful.

The partners had then been allowed to optimize their parameters for this special crushed salt of identical origin and fabric resulting in a parameter set B (resp. GRS-254 modified). The curves of BGR meet the experimental range quite well as shown in Fig.3.8 (left). The results of GRS (symbols) meet the experimental range in a moderate extent (lines) in Fig.3.8 (right).

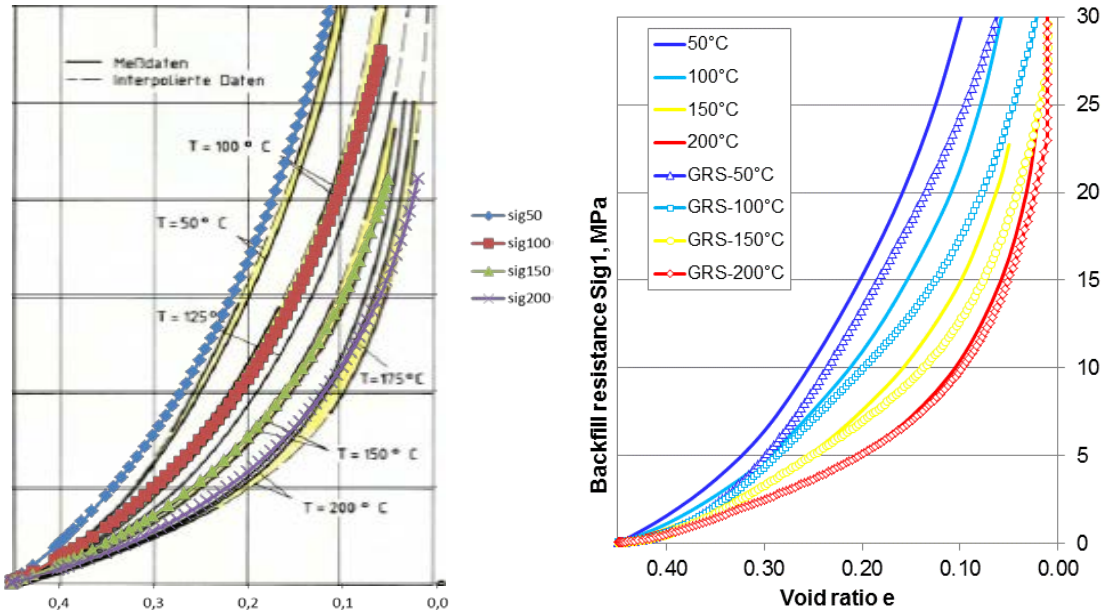

Fig. 3.8 Numerical results of BGR (left) and GRS (right) for stress as a function of compaction strain for different temperatures

[8] Report GRS-254 is identical with /KRÖ 09/

It has to be noted that the strain-rate controlled BGR tests represented a mixture of various overlapping processes as considered in the GRS-model, e.g. non-time-depending and time-depending processes. Therefore, separation of the various processes with respect to calibration of the employed models proved to be problematic. Nevertheless, parameter set B seemed to be adequate for describing the experimental results obtained so far.

3.4.2 Back calculation of the long-term compaction test

In the next step the parameter set B was used for simulating the long-term stress-controlled compaction tests of GRS (c.f. section 2.4.2).

The modelling results of GRS and BGR are compared in with the experimental data for dry crushed salt referring to sample no. 1. The comparison shows clearly that the compaction behaviour of GRS tests could not be reproduced with parameter set B. The results from numerical simulation highly overestimate the time-dependent compaction.

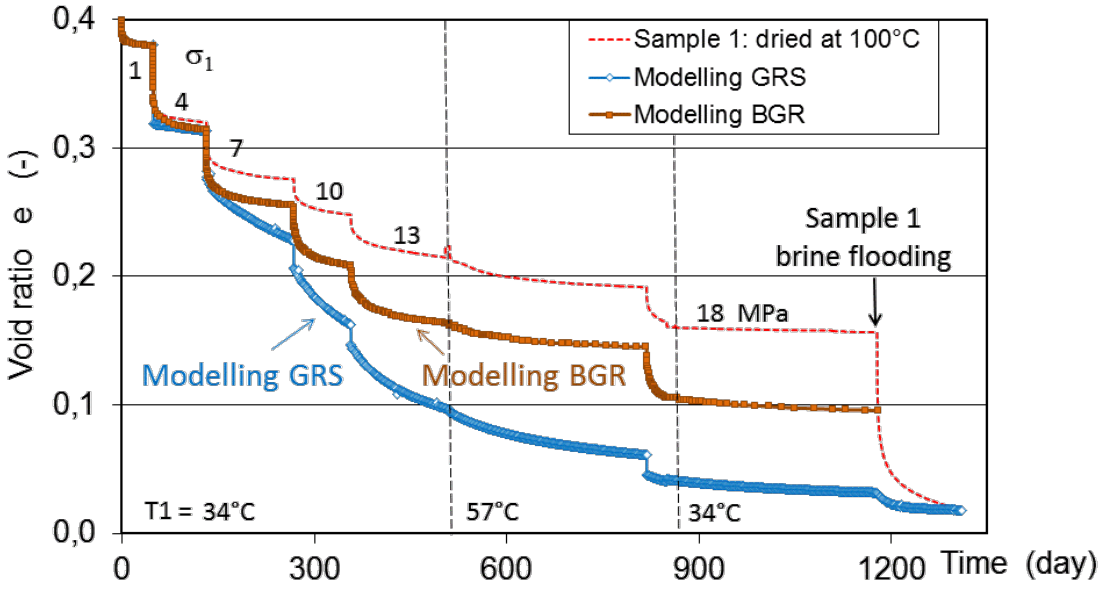

Fig. 3.9 Numerical results of BGR and GRS for creep compaction of dry crushed salt loaded at multi-step increased stresses and elevated temperatures

Note that modelling based on parameter set A also failed to reproduce the measurements of GRS. All in all different and independent compaction tests result in three different parameter sets for the material model.

3.4.3 Parameter improvement for dry and wet compaction of crushed salt

3.4.3.1 Objectives and scope

In order to investigate whether the material models for crushed salt implemented in CODE_BRIGHT are in principle applicable for simulating the long-term compaction behaviour in lab, a simplified model was developed, and several model variants, following the execution of the stress-controlled long-term compaction test (see chapter 2.4.2 and Appendix E) under dry conditions at ambient and elevated temperature, and with brine inflow were simulated.

The objective of these simulations was to test the capabilities of the implemented models, especially with coupling of mechanical, hydraulic and thermal effects, in a simple system. The material parameters that were used for back-calculation of the experiment are referenced to the individual GRS report numbers:

- GRS-254: initial parameters from Repoperm project phase 1,

- GRS-288[9]: a further developed data set used for the Preliminary Safety Analysis of the Gorleben site (VSG)

The calculation results were compared to the experimental findings and selective material parameter were fitted if necessary. The adapted material parameters are shown in the figures, renamed by GRS (2016).

[9] Report GRS-288 is identical with /MÜL 12/

3.4.3.2 Model description

Geometrical model

For the simulation of the crushed salt sample an axial-symmetric model of 110 mm height and 120 mm diameter was used. In addition, the steel piston is h_0 = 340 mm in height and in diameter equal to the sample size. The axial load is applied on top of the steel piston (Fig. 3.10).

The initial temperature of both, the steel cylinder and the crushed salt sample is about 29 °C. The initial porosity of the steel piston is 0.1 % and the porosity of the crushed salt is 27.536 %. The initial stress σ_y is about 1 MPa.

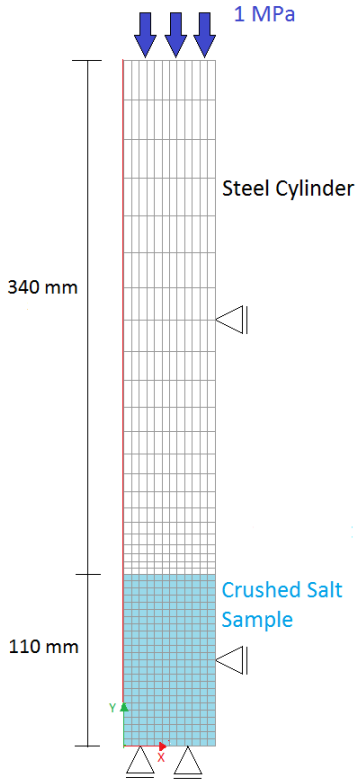

Fig. 3.10 Overview of the model geometry

Physical model and material data

The GRS-model for mechanical behaviour of the crushed salt includes the following mechanisms:

– elastic deformation
– dislocation creep
– viscoplasticity for granular material representing grain reorganisation and breaking
– fluid assisted diffusional transfer
– thermal expansion (for non-isothermal simulations)

The various contributions are combined by adding the individual deformation rates. A description of the formulations is given in Appendix K.

Heat transfer is restricted to conductive flux of heat in the non-isothermal simulation. For thermal-mechanical coupling linear thermal expansion of solid and liquid phases is considered. All material parameters are compiled in Appendix K.

The parameter set for the BGR-model after Heemann have been found by inverse modelling for a fixed power of stress of $n = 5$ and an activation energy of $Q = 54\,kJ/mol$ making use of the experimental data displayed in Fig. 3.8. Unfortunately the data are not suitable to extract parameters for the model on grain fracture and rearrangement processes. They have been determined by setting the fracture stress to a plausible value of $\sigma^{\#} = 20\,MPa$ while the effective (= relevant) grain diameter has been set to $D_i = 0.4\,mm$. Then the remaining parameter which determines the velocity of the fracture process has been chosen as a pure fitting parameter to $B^{\#} = 0.005$ thus making it able to give a rather good agreement with the experimental finding of the GRS-test (see Fig. Fig. 3.9). The total parameter set is shown in Tab. 3.1.

The parameters for wet creep have been taken such that they fit the data of the experiment during strong decrease of stress and will have to be checked in further calculations on experimental curves. The flat experimental curve branch for the wet creep cannot be modelled correctly. The reason is found in the fact that the model is based on the idea that the compaction stress will be dominated by the hydrostatic pressure of the fluid due to the rapidly decreasing permeability of the crushed salt. A valid model for the development of the permeability in case of wet creep could not been established so far and thus could not be implemented into the code. This is the reason for reaching negative void ratios what in case of dry creep never would appear.

Tab. 3.1 Parameter for the creep model of Heemann for dry and wet creep including grain fracture and rearrangement.

parameters for dry creep	parameters for fracture	parameters for wet creep
$A_{creep} = 0.02 / d$	$B^{\#} = 0.005$	$D_{diff} = 5 \cdot 10^{4}$
$Q_{creep} = 54 kJ / mol$	$D_i = 0.4 mm$	$Q_{diff} = 10 kJ / mol$
$R = 8.314 \cdot 10^{-3} kJ / (mol\, K)$	$\sigma^{\#} = 20 MPa$	$\kappa' = 1.39 \cdot 10^{-6}$
$n = 5$	$\gamma = 0.65$	
$b = 3$	$c = 0.85$	
$\kappa = 1$	$k = 6$	
	$m_{\varepsilon} = 0.3$	
	$\kappa_{RN} = 100$	
	$z = 0.65$	

Simulation variants, schedule, and boundary conditions

First, a model for dry compaction was calibrated. The resulting material parameters were then used as input for a numerical simulation of a compaction test with wet material. This allowed for the first time to estimate the parameters for the fluid assisted diffusional transfer (FADT) on the basis of a real test. This is significant as the FADT is believed to describe the impact of water or brine on compaction.

Though it is a thermal-hydraulic-mechanical (THM) problem, the modelling was graduated into three phases.

- The first phase from interval 1 to interval 8 is the mechanical phase. Here the stress is increased stepwise.
- The second phase from interval 9 to interval 14 is the thermal-mechanical phase. The temperature first increases up to 55 °C. Then, after some days the temperature decreases again to 34 °C while the stress level is kept constant.
- The last phase is the thermal-hydraulic-mechanical phase. In interval 15, when the experiment is flooded with brine, the fluid assisted diffusional transfer (FADT) model is active.

The time interval representing the calculation time of CODE_BRIGHT, starting at 0 days, though the laboratory experiment is still running since 50 days. Due to the fact, that the

model is not capable to simulate the man made pre-consolidation process, the stress level after 50 days is taken as initial condition for the calculation process. Hence t = 0 days in modelling is equal to t =50 days in the laboratory experiment. An illustration of the conditions can be found in Appendix K.

3.4.3.3 Results from the GRS-model

In this section, the evolution of porosity in the sample centre as obtained in the calculations using different data sets is compared to experimental findings, Fig. 3.11. The sample-specific features that have been observed in lab (see chapter 2.4.2.5 and Appendix E) are met by the calculation results using parameter data set GRS (2016):

– The temperature increase to 60 °C causes a similar reaction in sample 1 as each stress increase, Fig. 3.13.
– The creep accelerating effect of the load increase to 18 MPa is cancelled at 850 days by reducing the temperature from 60 °C to 34 °C, Fig. 3.13.
– Flooding accelerated compaction in terms of the initial drop of porosity more than any other load change, Fig. 3.14.

More detailed results of the individual parameter fitting process can be found in Appendix K.

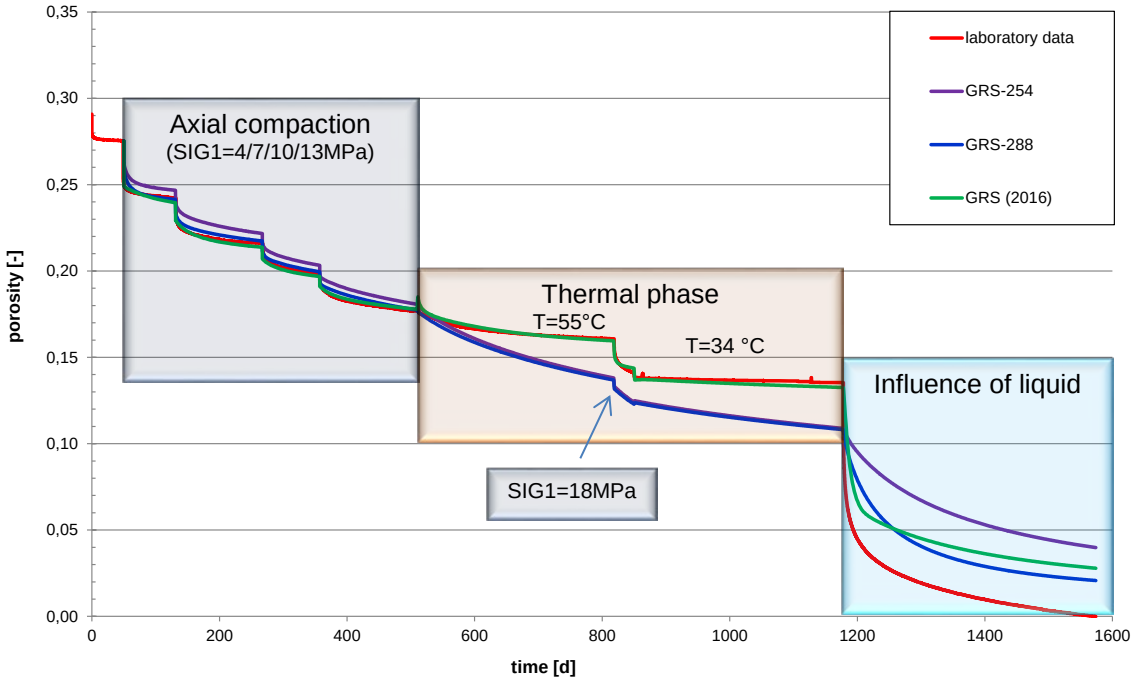

Fig. 3.11 Porosity evolution in the sample centre – comparison of different data sets

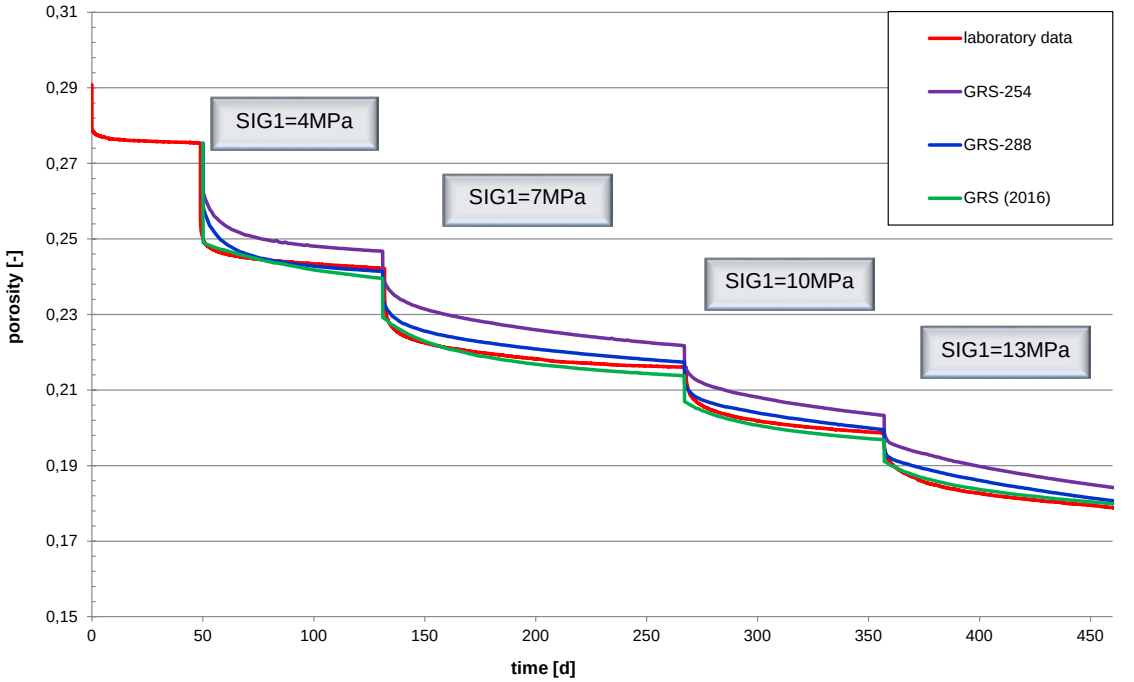

Fig. 3.12 Porosity evolution during the mechanical compaction phase – comparison of different data sets

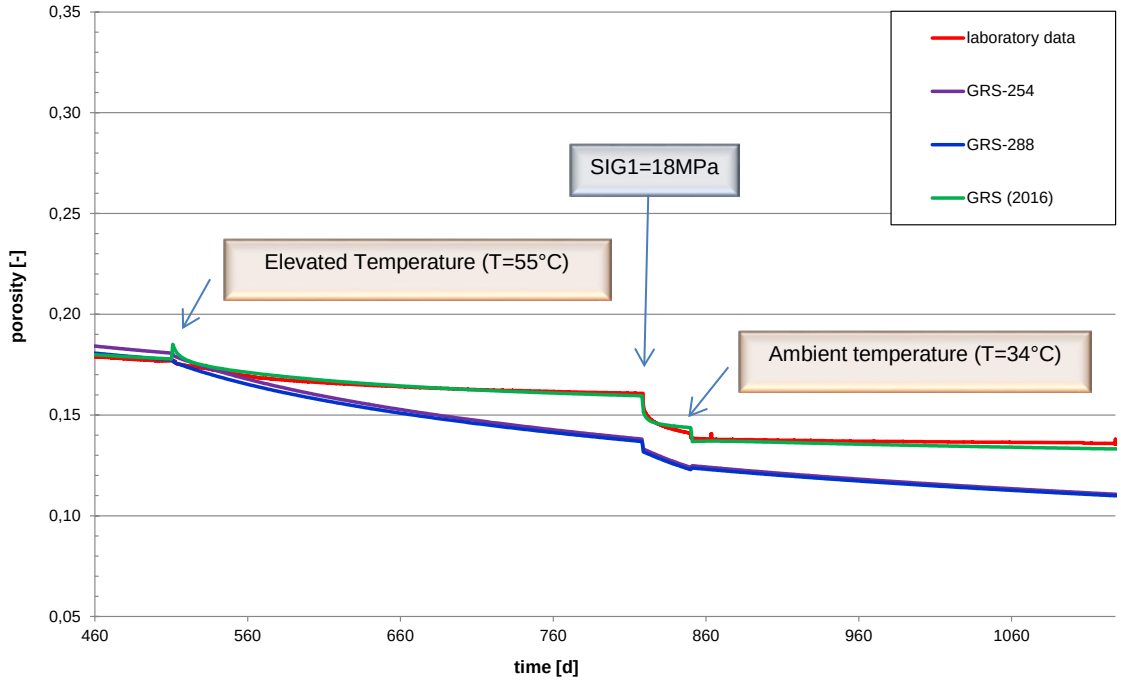

Fig. 3.13 Porosity evolution during the thermal phase – comparison of different data sets

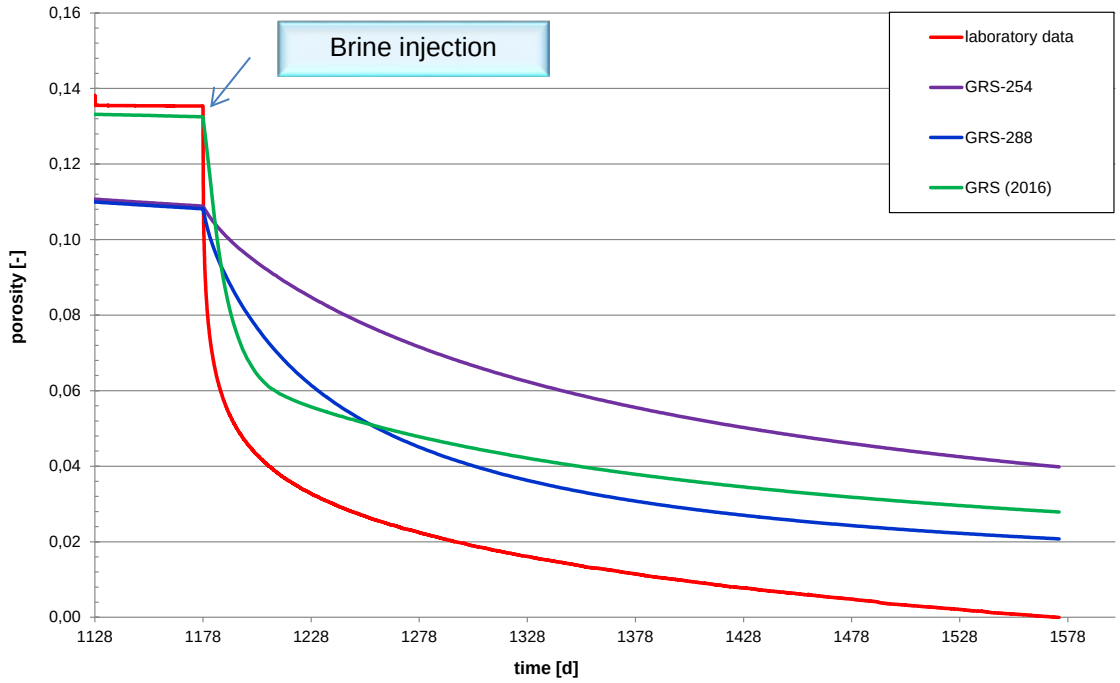

Fig. 3.14 Porosity evolution due to brine injection – comparison of different data sets

3.4.3.4 Results from BGR-model with improved parameter set

The calculations on the long term creep test by means of the Heemann model gave a reasonably good agreement with the experimental data (see Fig. 3.15). But, as far as fracture processes are concerned, there have not been any independent experimental data to use for parameter determination. So the parameters chosen are quite preliminary and may also influence the parameters for creep necessary to regain “good” curves. So up to now the calculations show that fracture seems to work quite well, but the fixing of valid parameters is quite difficult yet due to lack of data.

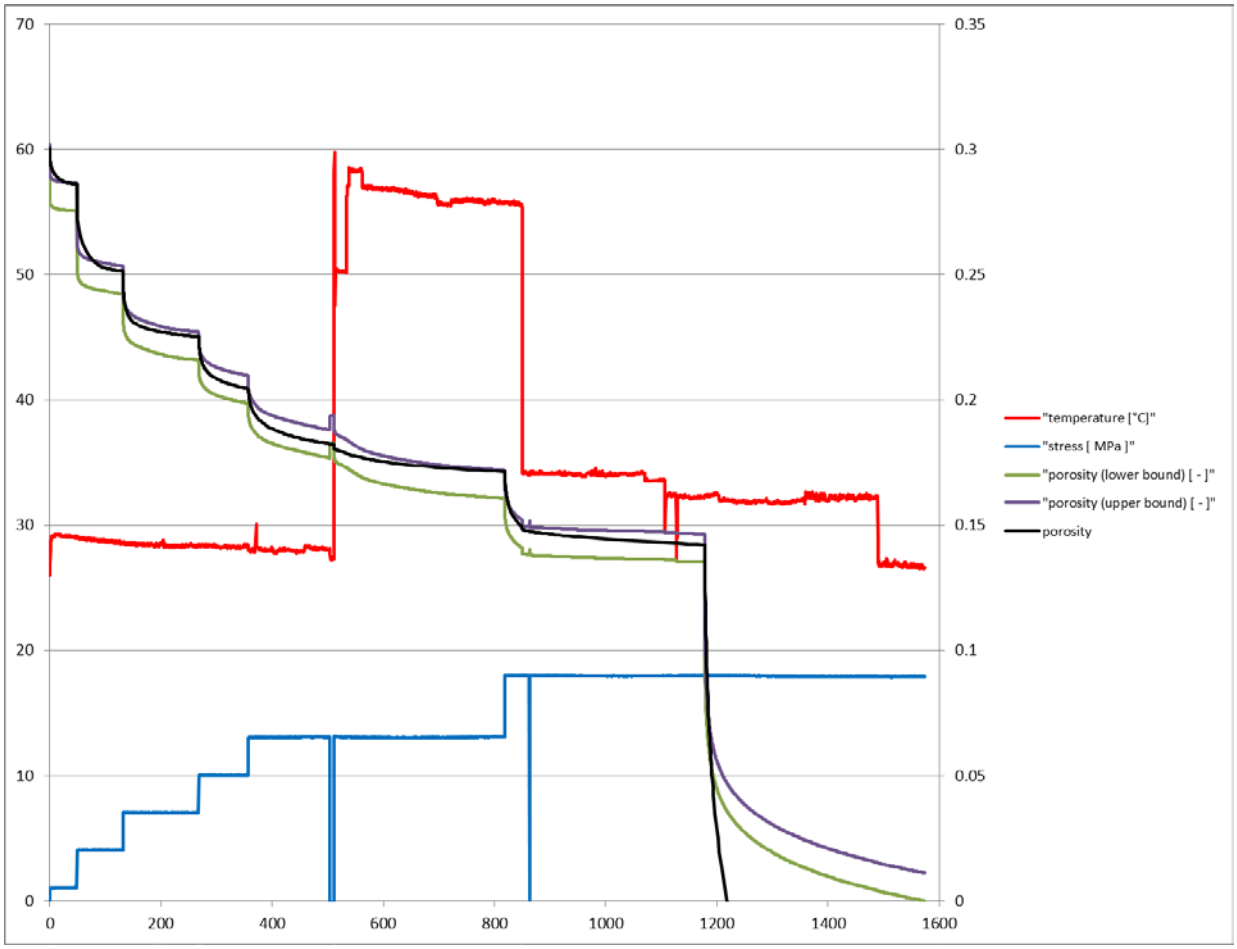

Fig. 3.15 Development of porosity for dry and wet creep over time. See text for further explanation.

Making use of the wet creep model as well, only for the phase of very steep decrease of stress an acceptable agreement could be reached while the model could not deliver the

flat branch of the creep curve. It has already been mentioned that this deficiency is due to the fact that a reliable physical model for the evolution of permeability for wet creep could not be developed so far. Thus the necessary hydro-mechanical interaction leading to an increase of the pressure of the fluid inside the pores thus hindering a fast compaction could not be modelled yet. In consequence of this missing limiting effect the compaction of crushed salt is going on also if zero porosity is reached. This has not to be judged as a consequence of a wrong model. In fact, it is supposed that the physical model of wet creep is physically very reliable down to rather low porosity. So the difference may be taken as a strong indication that indeed the hydro-mechanical interaction is the governing physical mechanism to explain the creep curve of wet creep for low porosity.

3.4.4 Conclusions

Different tests concerning dry compaction formed the basis for checking on the validity of the presently available material models. The idea behind this exercise was that a valid material model should correctly describe any of the compaction tests. However, this was not the case. None of the calibrated parameter sets could be transferred to another test with satisfying results. Using sets of intermediate parameter values led to the same result.

The simulations have shown that the application of the available material models on the long-term compaction tests leads to plausible and coherent results. Compaction of crushed backfill can in principle be modelled, both for the dry case and for a brine inflow, at constant or variable temperature.

While the numerical tools might be able to describe crushed salt compaction in principle, the understanding of the compaction tests in general and/or of the material models in particular is not sufficient to allow for reliable predictions at the time.

3.5 Scaling-rules for capillary pressure

3.5.1 Motivation

Flow of brine into the salt backfill under repository-relevant conditions can only be described either as two-phase flow or as unsaturated flow. In either case knowledge is required about the constitutive relations (CRs) namely the capillary-pressure saturation relation (CPS) and the relative-permeability saturation relation (RPS).

As the backfill will be compacting over time the pore space will be reduced accordingly. The tightening of the flow channels means a reduction of the mean pore radius and therefore an increase of capillary pressure at the water-air interface and a decrease of the absolute permeability[10]. CPS and RPS will thus change during compaction and depend among other things on the degree of compaction. The degree of compaction can be quantified by the actual porosity.

The porosity of a crushed salt backfill covers a wide range during compaction. The initial value immediately after installation it is estimated to amount to approx. 35 % (e.g. /KRÖ 09/). The final value, though, is presently rather obscure. However, it is expected to lie somewhere in the range between approx. 0.1 % for rock salt and 1 %. According to this rather wide range of possible porosity values large changes are expected also for the CRs.

Determination of the CRs from measurements is already effortful and time-consuming for one sample especially for low-permeable materials. A series of such measurements is required in case of compacting crushed salt as changes with the degree of compaction are expected. This huge effort could be reduced considerably if the changes of the CRs could be predicted by means of theoretical considerations or, more precisely, by means

[10] However, in a real system the degree of saturation – defined as the ratio of fluid volume to the total pore volume – increases during compaction without sufficient advective flow of the liquid phase. The pore volume decreases but as long as the gas phase is connected throughout the pore space only gas is pressed out by compaction while the liquid phase remains in place. This phenomenon increases the local degree of saturation until the residual saturation of the gas phase is reached. Only then will further compaction squeeze out brine as well.

of scaling-rules such as the classic J-function proposed by Leverett /LEV 41/. However, there is presently not sufficient data for compacted crushed salt /KRÖ 09/.

The oil and gas producing industry faces a similar question. Caused by capillary forces between oil or gas and groundwater there is a transition zone between the two phases. The extent of this zone is of high interest regarding the economic efficiency of an oil or gas production. To optimize the yield the water saturation over depth must be known as precisely as possible. While probing boreholes and determination of the water saturation profile in the laboratory would provide the most realistic information, this cost-intensive method is often replaced by estimations based on scaling-rules.

Knowledge concerning theory and application of scaling-rules from the oil industry are therefore compiled in the following and evaluated with regard to the applicability of these rules to compacting crushed salt.

3.5.2 Introduction

An important driving force for the migration of brine in the unsaturated crushed salt is the saturation-dependent capillary pressure. Here, the CPS is directly of interest. To estimate the capacity of an oil deposit a saturation-height function (SH) is often sought. In this case the water saturation is described as a function of height above the free water surface where the height can be interpreted as a capillary pressure. The SH is therefore equivalent to the CPS.

Several techniques are applied in the oil industry to correlate the CPS for different types of rock, porosities and permeabilities /HAR 01/. The oldest method is based on a theoretical approach by Leverett /LEV 41/ and is still used today. Apart from that several newer empirical approaches are also known.

3.5.3 Scaling-rule after Leverett

A fundamental scaling-rule was derived by Leverett /LEV 41/. Theoretical considerations for a medium consisting of sphere-like particles were confirmed by experiments with water and air in six different unconsolidated sands. The hydraulic conductivity of the sam-

ples varied between 0.7 and 17.2 Darcy[11] and the porosity between 39 % and 49 %. The measurements were performed under saturating as well as de-saturating conditions.

All CPS could be more or less well aligned after multiplying the capillary pressure by the factor

$$\frac{1}{\sigma}\sqrt{\frac{k}{\Phi}} \qquad (3.47)$$

σ - surface tension at the phase interface [N/m]
k - permeability [m²]
Φ - porosity [-]

and thus making the product dimensionless[12]. Leverett concluded that a unique, characteristic, and dimensionless function exists that represents a variety of different sands. This function was later called “J-function”:

$$J(S_w) = \frac{p_c}{\sigma}\sqrt{\frac{k}{\Phi}} \qquad (3.48)$$

$J(S_w)$ - characteristic and dimensionless function (J-function) [-]
S_w - saturation oft he wetting phase [-]
p_c - capillary pressure [Pa]

For a specific J-function it must be known which two fluids are present in the pore space in order to quantify the surface tension σ. Additionally, as many data defining the relation between saturation, capillary pressure, permeability and porosity as possible are required. From these data an approach for the saturation-dependent J-function can be formulated that inserted into (3.48) results in a scaling-rule for a specific material. An approach that is easy to fit to the data has been found in form of a power law /HAR 01/ (q.v. /IBR 92/):

[11] 1 Darcy ≙ 0,987 10^{-12} m²

[12] The analysis showed also clearly a hysteresis between saturation and de-saturation.

$$J(S_w) = a\frac{1}{S_w^b} \qquad (3.49)$$

a, b - constants [-]

Later, also the contact angle θ between the interface and the solid phase was introduced in (3.48) to incorporate the influence of the surface structure of the solid phase on the wetting behaviour /ROS 49/:

$$J(S_w) = \frac{p_c}{\sigma \cos\theta}\sqrt{\frac{k}{\Phi}} \qquad (3.50)$$

θ - contact angle between the interface and the solid phase [-]

Including surface tension and contact angle allows to use other fluids in the laboratory for the measurement of the capillary pressure than those that are present in the field. By changing the fluids involved the measurements can be accelerated or the accuracy can be increased. While the surface tension can be measured rather easily in the laboratory the value might be a bit different in the field /HAR 81/. An even higher uncertainty is related to the contact angle. Typical data for conversion of the capillary pressure for different combinations of fluids are compiled in Tab. 3.2.

Tab. 3.2 Surface tension and contact angle for interfaces between brine, mercury, and gas; from /COR 82/ (cited in /HAR 01/)

wetting phase	non-wetting phase	measured in	contact angle θ [°]	surface tension σ [mN/m]
brine	oil	laboratory	30	30
brine	oil	reservoir	30	48
brine	gas	laboratory	0	72
brine	gas	reservoir	0	50
gas	mercury	laboratory	140	480

The applicability of the J-function meaning scaling a known CPS-relation from one rock type to another type of rock is theoretically restricted to rocks with comparable pore space geometry /HAR 01/. Initially, this had not been considered but with increasing examples of applications it was found that the prognosis of capillary forces became much better if a J-function was established for each rock type of a formation /BRO 51/. It was

nevertheless common practice for quite some time still to work with just one J-function for a whole reservoir /CUD 93/. Further experience brought to light that this approach works satisfyingly only within a permeability range of two to three orders of magnitude /HAR 01/.

3.5.4 Comparison of scaling-rules

Compilation of CPS-relations from the literature

The CPS-relations that were found in the literature and included the necessary parameter values as well did generally not allow a direct comparison as they are based on different fluid combinations and different variables. An analysis of these relations aiming at a common formulation can be found in Appendix H. In order to make the resulting curves comparable they were scaled with Leverett's J-function (3.48) to a water-gas system where necessary. The results are compiled in Tab. 3.3 and depicted in Fig. 3.16. Where data for permeability or porosity were missing the values according to /CIN 06/ were inserted. Also plotted in Fig. 3.16 are the CPS-relations after /CIN 06/ for crushed salt fitted by the approaches of Brooks and Corey /BRC 64/ as well as by the approach of van Genuchten /GEN 80/ (cf. /KRÖ 09/).

The CPS-relation after /SWA 81/ differs considerably from all others on account of two points. Firstly, it is the only one to describe the dependency of the capillary pressure on saturation as a linear function while the other formulations result in an exponential decrease. Secondly, the capillary pressure at full water saturation is equal to zero. Most other relations[13] show a value greater than zero which can be interpreted as a gas entry pressure. However, the calculated gas entry pressures are rather low, less than 0.7 MPa, except for the CPS-curve after /HES 74/ which yields a value slightly in excess of 0.27 MPa.

[13] The approach of van Genuchten used by /CIN 06/ does also not show a gas entry pressure explicitly even if the course of the curve indicates one.

Tab. 3.3 Basic data for the scaling-rules

source	measuring fluids	factor[14]	capillary pressure	permeability	porosity	Scaling-rule
/THO 60/	Hg – Gas	0,136		1 – 2000 mD		$p_c = p_e \cdot 10^{-\frac{G}{\log(1-S_{nw})}}$
/HES 74/	Hg – Gas	0,136	50 – 1000 psia		2 % – 24 %	$p_c = 10^{\left\{\frac{1}{2f}\left(-g+\sqrt{g^2-4fh}\right)\right\}}$
/SWA 81/	Hg – Gas	0,136	up to ~600 psia	1 – 10000 mD		$p_c = \left(\frac{a}{k}\right)^{\frac{1}{b}} \Phi\, S_{nw}$
/JOH 87/	Hg – Gas	0,136	1 psi and 180 psi	1 – 10000 mD	15 % – 29 %	$p_c = \left[\frac{1}{c}\log\left(\frac{k^{\bar{a}}}{S_w}\right)\right]^{\frac{1}{d}}$
/PRI 89/	H_2O – Öl H_2O – Gas	1,92 1		k_{min} < 1 mD; k_{max} =3785 mD	Φ_{max} = 19,9 – 39 %	$p_c = \left[\left(a\frac{1-S_w}{S_w-S_{wr}}\right)^{\frac{1}{c}}+b\right]\frac{\sigma\cos\theta}{0{,}217}\sqrt{\frac{\Phi}{k}}$
/IBR 92/	H_2O – Gas	1		0,05 – 0,3 mD	7,9 – 12,5 %	$p_c = \frac{\alpha}{S_w^{\beta}}\sigma\cos\theta\sqrt{\frac{\Phi}{k}}$
/CUD 93/	H_2O – Gas	1		0,1 – 10 mD	5 % – 20 %	$p_c = \frac{\alpha}{S_w^{\beta}}\sigma\cos\theta\sqrt{\frac{\Phi}{k}}$
/SKE 95/	H_2O – Öl ?	1,92	< 180 psi			$p_c = -\frac{b}{\left[-\ln\left(S_{nw\,eff}\right)\right]^{\frac{1}{c}}} - p_e$
/DIN 03/	H_2O – Gas ?					$p_c = a\ e^{b\,S_w}\sigma\cos\theta\sqrt{\frac{\Phi}{k}}$

[14] for the transformation into a H_2O-gas system

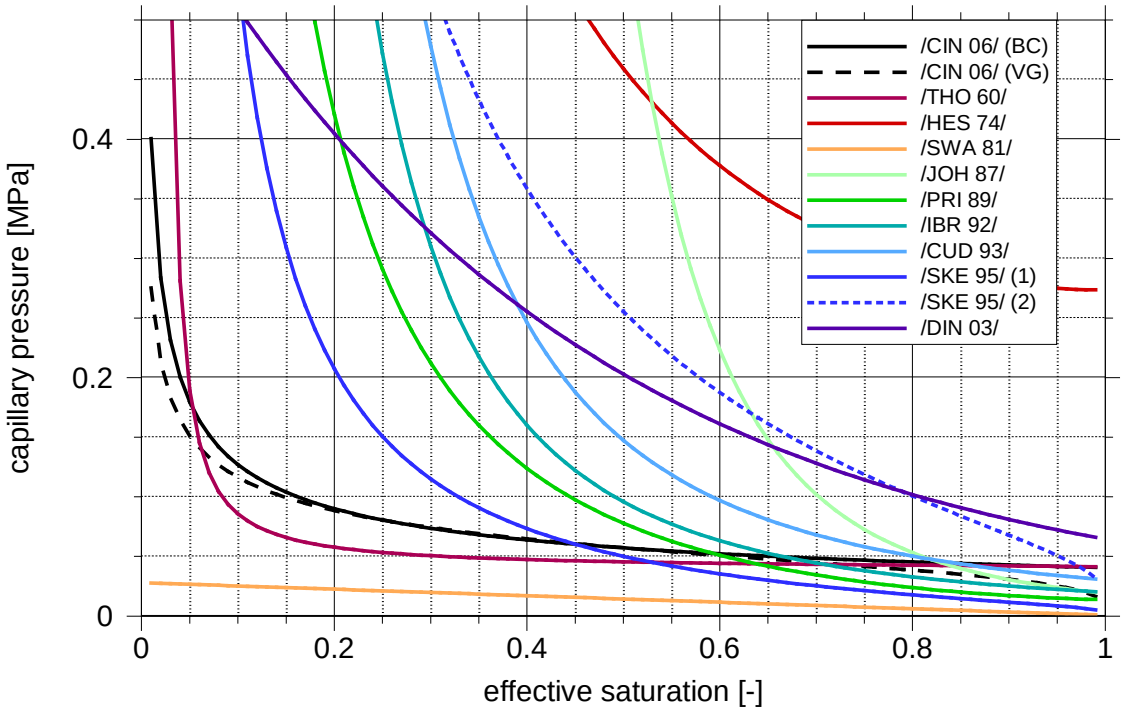

Fig. 3.16 CPS-relations from the literature based on a water-gas system

The CPS-curves for crushed salt according to /CIN 06/ as well as the relation after /THO 60/ attract attention by the fact, that there is little variation in the capillary pressure above a saturation of 0.3. Only below a saturation of 0.2 the exponential character of these curves becomes apparent. This sort of curve shape is typical for a certain uniformity of the pore space. This may be the result of a grain size distribution with a singular dominant grain size which has actually been used as sample material for the compaction tests of /CIN 06/. Something along these lines can also be suspected for the material that formed the basis of the CPS-curve after /THO 60/. For crushed salt with varying grain sizes like the material used in the DEBORA-project /ROT 99/ the steep branch in the CPS-curve should be shifted to the right and thus be lying closer to the curves for the reservoir rocks.

Formal comparison

The discussed scaling-rules are based on measurements of reservoir rocks containing oil or gas. The compilation of data in Tab. 3.3 shows that the range of measured permeabilities and porosities encompasses values in the range from 10^{-16} m² to 10^{-11} m² and

from 5 % to 30 %, respectively. These bandwidths cover the measurements of /CIN 06/ for material with a dominant single grain size which were performed at a permeability of 10^{-15} m² and a porosity of 5 %.

The quite varying hydraulic properties of the different reservoir rocks lead obviously to formally very different CPS-relations. The compilation of the related equations in Tab. 3.3 shows, however, that several of these curves are scaled according to Leverett's J-function. This applies to the approaches after /PRI 89/, /IBR 92/, /CUD 93/ and /DIN 03/. A deeper insight into scaling-rules concerning varying permeabilities or porosities beyond the classic approach after /LEV 41/ can thus not be expected from these four approaches.

Scaling the capillary pressure according to /SWA 81/ is very similar to a scaling after Leverett's approach so that this scaling-rule can also be sorted out. In contrast to the J-function the dependency on the porosity is linear in the approach of /SWA 81/ and not with the square root. This means that a change in the porosity by a factor of a, say due to compaction, leads to difference between the calculated capillary pressures of $\sqrt{a}$ confirming the formal similarity between the approaches after /SWA 81/ and /LEV 41/. This leads to the curious conclusion that a scaling with the approach of /SWA 81/ leads to similar results as using Leverett's J-function while the linear shape of the curve is quite unique in the ensemble of curves.

Exemplary comparison: variation of the degree of compaction

The behaviour of the CPS-curves due to changes in the permeability and the porosity as they are expected for compacting crushed salt, is investigated in the following. It is thus assumed that the relations are also valid for compacting crushed salt. In order to allow a meaningful comparison all relations are fitted to the results of /CIN 06/ for a permeability of 10^{-15} m² and a porosity of 5 % which represents a reference state for the subsequent parameter variations.

In some cases the parameters for the CPS-relations from the literature had to be strongly changed in order to fit the curves to the reference case. This applies to the curves after /SWA 81/, /JOH 87/, /IBR 92/ and /CUD 93/. As shown in Fig. 3.17 a good fit could

be achieved for most of these relations. Only the curves after /SWA 81/ and /DIN 03/ are different in that the capillary pressure remains finite at residual water saturation.

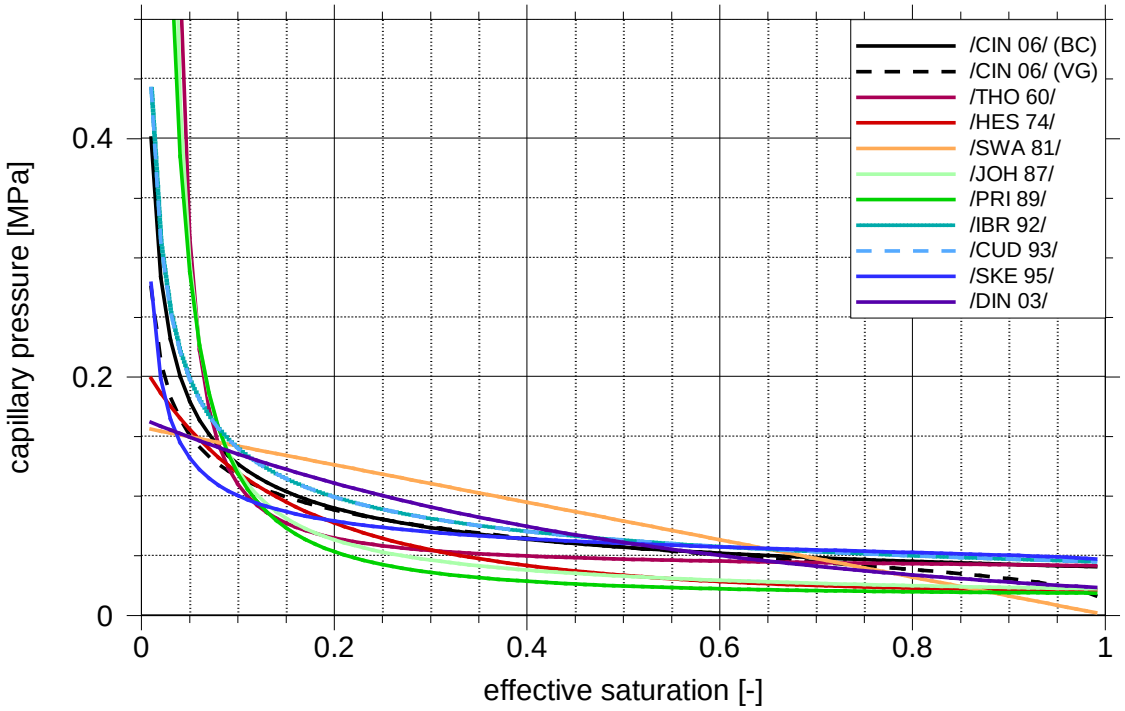

Fig. 3.17 Reference case (k = 10^{-15} m²) for the CPS-relations from the literature

Having established the reference case the degree of compaction was varied in terms of permeability. As variations of the reference state the permeability was increased and decreased by two orders of magnitude. According to the porosity-permeability relation derived in /KRÖ 09/ the related porosity values are 10 % and 2 %.

Performing these two parameter variations calls for some comments:

– Scaling the CPS-curves from /CIN 06/ is done using the classic J-function after /LEV 41/. For this purpose the new permeability values as well as the new porosities are required.
– Only the porosity enters the scaling-rule after /HES 74/.
– In the scaling-rule after /JOH 87/ only the permeability can be varied.
– The scaling-rule after /SKE 95/ contains neither the porosity nor the permeability explicitely but only the gas entry pressure which is chosen according to the findings of /CIN 06/.

– The geometry factor containing the porosity as well as the gas entry pressure are considered in the scaling-rule after /THO 60/. The gas entry pressure was again chosen after /CIN 06/.

Because of the formal similarity to the J-function the relations after /PRI 89/, /IBR 92/, /CUD 93/ and /DIN 03/ are not considered in the following anymore. The approaches after /LEV41/ – based on the measurements of /CIN06/ –, /THO 60/, /HES 74/, /SWA 81/, /JOH 87/ and /SKE 95/ thus remain to be discussed. The referring CPS-curves for the reference case are put together in Fig. 3.18.

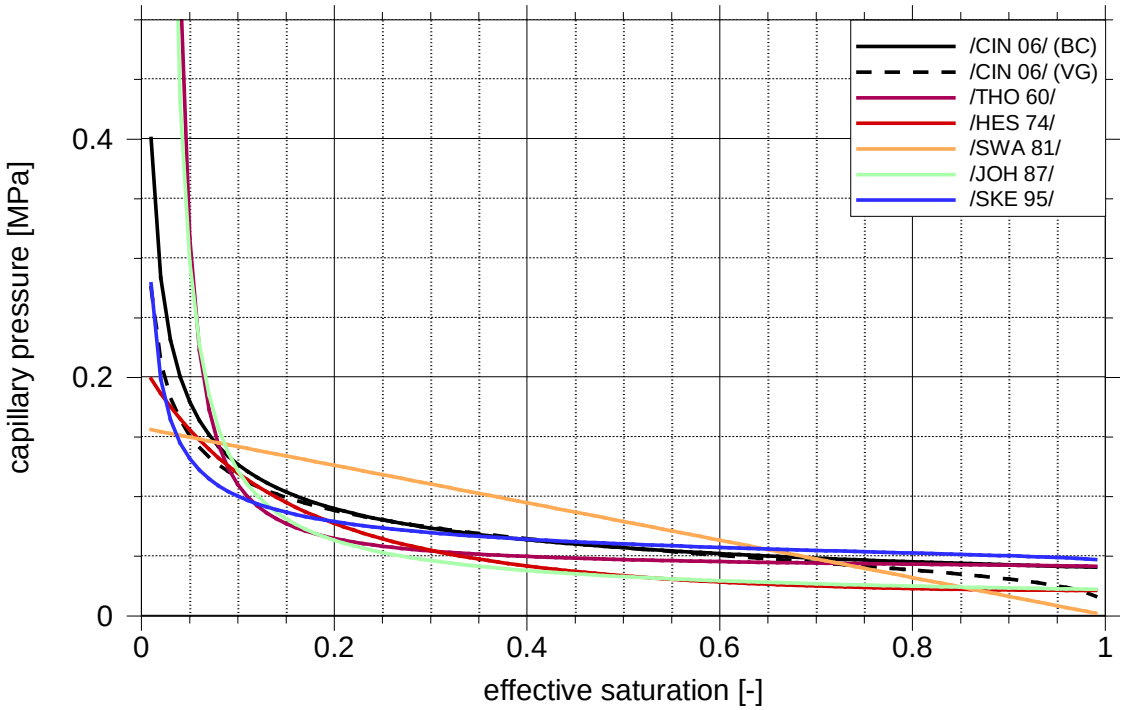

Fig. 3.18 Reference case (k = 10^{-15} m²) for selected CPS-relations

Taking the curves that are scaled after /LEV41/ as a reference, since they represent the most widely known and accepted scaling-rule, each of the following five figures (Fig. 3.19) depict a comparison with one of the other five approaches.

Generally, the CPS-curves show a curve shape similar to the approach of Brooks and Corey /BRC 64/ except for the curve after /SWA 81/ which looks more like a van-Genuchten-type of curve as it reaches a capillary pressure of zero at full water saturation. However, in all cases they react quite diversely to the parameter changes that are

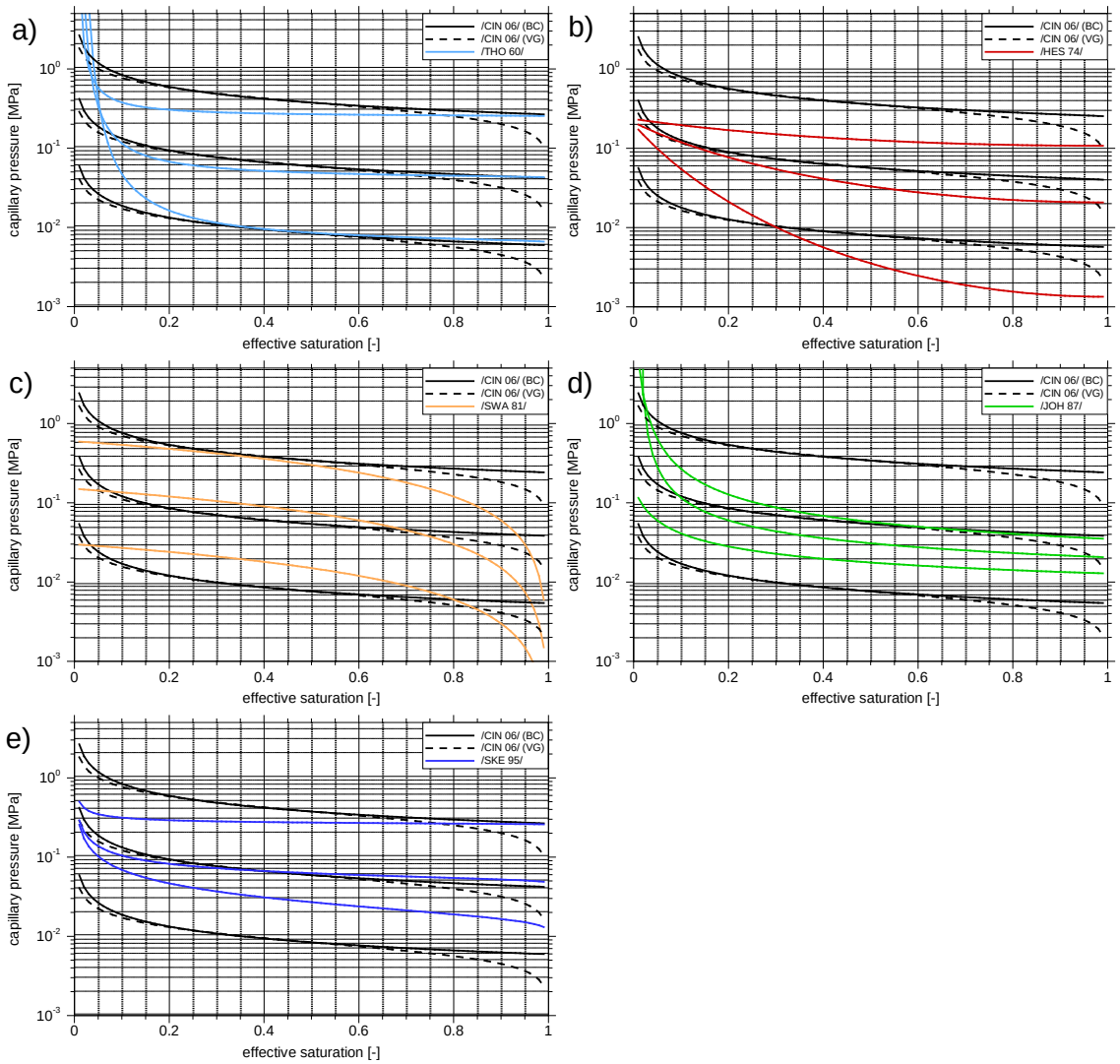

Fig. 3.19 CPS-relations after /CIN06/ for k = 10^{-13}/10^{-15}/10^{-17} m² compared to relations after a) /THO 60/, b) /HES 74/, c) /SWA 81/, d) /JOH 87/, e) /SKE 95/

expected to occur with compaction. Three characteristic properties of a CPS-curve form the basis of the following qualitative comparison of the scale-rules: the gas entry pressure, the curve shape in the range of medium saturations and the curve shape at low water saturation.

Gas entry pressure: According to the classic scaling-rule after /LEV 41/ the gas entry pressure is inverse proportional to the permeability and thus to the degree of compaction. The same trend can be observed in the curves after /JOH 87/ and after /HES 74/ but the absolute values change much less after /JOH 87/ while the increase of the gas

entry pressure according to /HES 74/ appears to be dependent on the degree of compaction as it becomes less with a decreasing permeability.

The formulation after /THO 60/ contains a “geometry factor” that should change with the porosity. But since it is not directly related to physically interpretable quantities (c.f. Appendix H) the CPS-curves for the variants cannot be calculated. In case of the approach of /SKE 95/ there is no dependency of the capillary pressure on permeability or on porosity at all. To enable the graphical comparison in Fig. 3.19 the gas entry pressure was varied according to /LEV 41/. Since in the formulation after /THO 60/ the gas entry pressure is a factor this leads formally to the same gas entry pressures as the fit after /BRC 64/ in /CIN 06/. In contrast the gas entry pressure in the approach after /SKE 95/ is a summand resulting in a good fit for the advanced degree of compaction but also in quite a deviation for the less compacted state.

Curve shape in the range of medium saturations: In the half-logarithmic scale of the plots in Fig. 3.19 a) to e) the scaling after /LEV 41/ leads simply to a vertical shift of the curves. This means that the ratio of capillary pressures for two states of compaction is constant for any given saturation. The same applies also to the scaling after /SWA 81/ and by approximation also to the approach after /JOH 87/. The change of capillary pressure with the degree of compaction is highest after /LEV 41/, a little less after /SWA 81/ and even less after /JOH 87/. In contrast the curves after /THO60/, /HES 74/ and /SKE 95/ become increasingly flat with compaction which is least pronounced in the curves after /THO 60/ and highest in the curves after /HES 74/.

Curve shape at low water saturation: Most formulations converge to infinity for a saturation converging to zero. The referring steep gradients in the case investigated here can be observed in the range of 5 to 10 % saturation. Only the approaches of /HES 74/ and /SWA 81/ lead to a finite capillary pressure at residual saturation. While the capillary pressure $p_c\left(S_{weff} = 0\right)$ increases considerably with compaction according to the formulation after /SWA 81/ the approach of /HES 74/ does not result in a significant change.

All in all the six approaches appear to react rather differently to changes of the degree of compaction. This is confirmed by Fig. 3.20 where the results from all six approaches for the three degrees of compaction are compiled in such a way that the curves for each compaction level have the same colour: green for the reference case ($k = 10^{-15}$ m²), blue

for the lower degree of compaction (k = 10^{-13} m²) and red for the higher degree of compaction (k = 10^{-17} m²). It shows clearly that scaling with the different formulations leads already to a considerable spreading of CPS-curves if the permeability changes only by two orders of magnitude. Despite the fact that these formulations have been derived for the rather specific case of storage formations there is apparently no theoretical basis for choosing a representative approach for either the CPS-relation as such or the scaling-rule.

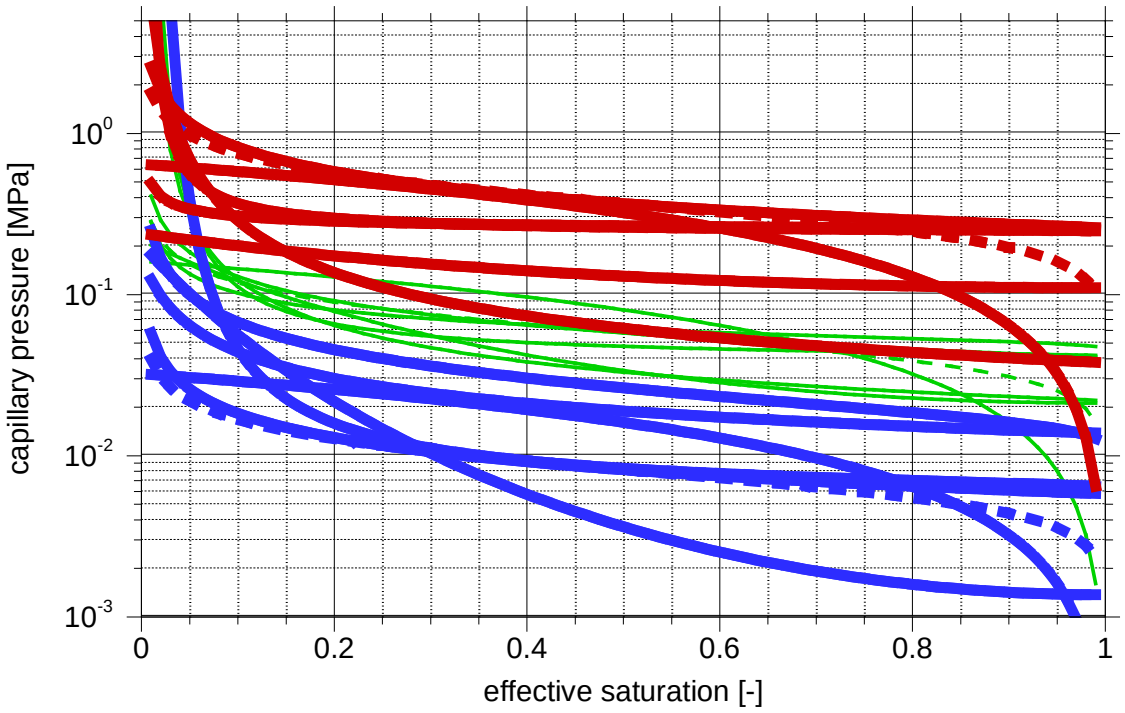

Fig. 3.20 All investigated CPS-relations for k = 10^{-13} (blue)/10^{-15} (green)/ 10^{-17} (red) m²

3.5.5 Summary and conclusions

CPS-relations are of great importance for the oil industry. Scaling-rules that describe the changes of the capillary pressure with permeability and/or porosity theoretically without the considerable effort of measurements are therefore in great demand. Already in the first half of the last century Leverett developed the ground-breaking J-function for that purpose /LEV 41/. However, the reliability of predictions based on the J-function was apparently not entirely satisfying as there were a number of attempts until today to improve this function or to derive superior approaches.

The field of applications for the CPS-functions and scaling-rules as seen with a view to oil and gas production is limited to typical storage formations, especially sand- and limestone. Comparatively recently also dolomite was included in the investigations, for instance in /PRI 89/. Therefore a range of parameters was covered that lies in case of permeability between 10^{-16} m² and 10^{-11} m² and in case of porosity between 5 % and 30 %. These ranges relate to a low to medium degree of compaction in crushed salt.

Considering the fact that only few, very specific formations were investigated the derived formulations for the CPS-relations and scaling-rules are quite different. The approaches of /LEV 41/, /JOH 89/, /CUD 93/ and /SKE 95/ were thus exemplarily applied on the basis of existing data for a gas and for an oil field /HAR 01/. The results, however, were rather ambiguous as no method produced a prediction that was clearly superior to the others.

Due to the wide variety of CPS-relations and scaling-rules it is impossible to select representative formulations for storage formations. It is therefore also not possible to draw conclusions from this investigation about scaling-rules for compacting crushed salt. While it is interesting to note that different authors from the oil industry returned in recent times to Leverett's J-function or certain variations of it /PRI 89/, /IBR 92/, CUD 93/, and /DIN 03/, the fact remains that Leverett's scaling-rule is not without serious competition so that uncritical application appears to be inadvisable.

Transferring the results for storage formations to crushed salt as backfill material would have been questionable anyway. There is for instance the duration of the compaction which requires in case of natural rocks periods of time on a geological time scale. Storage formations are thus porous media that have properties of a rigid solid matrix while the compaction of crushed salt can be considered to be quite dynamic by comparison. Another difference between storage formations and a crushed salt backfill is the fact that the grains in rocks are usually bonded by binding materials like quartz or calcite while pure salt grains are expected to be used in a backfill. These differences let a direct investigation of two-phase flow parameters appear to be necessary, too.

Moreover, practical experience with scaling using Leverett's J-function indicates rather tight limits in its application. In /HAR 01/ it is reported that scaling after /LEV 41/ yields satisfying results only for a permeability range of 2 to 3 orders of magnitude. Crushed

salt by comparison undergoes a permeability change over 8 to 9 orders of magnitude according to the permeability-porosity relation after /KRÖ 09/. The proposal in /CIN 06/ to use their measurements for the retention curve at a permeability of 10^{-15} m² and apply the J-function in case of advanced degrees of compaction thus appears to be rather ambitious.

This applies even more considering the fact that the CPS-relation after /CIN 06/ is based on single-grain salt rather than the crushed salt that is envisioned for a real repository. For this purpose it is intended to use a material that comes from the excavation and has thus a certain “natural” grain size distribution. If used as borehole backfill, larger grain-fractions are sorted out as in the DEBORA-project /ROT 99/ where grain sizes between 0.06 and 8 mm established the backfill material. Such a material shows a higher curvature in the medium range of saturations which explains the difference of the retention curves after /CIN 06/ to most of the curves for storage formations in Fig. 3.16. It is thus that the retention curves after /CIN 06/ represented on the one hand the state of science and technology but were on the other hand unsuitable as a basis for reliable calculations of two-phase flow in compacting crushed salt barriers.

The following final conclusions can thus be drawn:

– It is not possible to derive retention curves and/or scaling-rules for compacting crushed salt by means of analogies with the extensively investigated storage formations for gas and oil. Direct measurements of the constitutive relations (CRs) for two-phase flow or unsaturated flow are thus imperative.
– As the physical laws controlling the changes of the CRs during compaction are unknown the CRs must be determined for different degrees of compaction. The quality of the resulting scaling-rule depends on the number of degrees of compaction that are investigated and on the reproducibility of the measurements.

For technical reasons it is not possible, though, to collect data for the complete compaction path. Measurements below a certain permeability that may lie in the order of 10^{-18} m² are not feasible because of the extremely little quantities of fluid that are involved. A scaling-rule for compacting crushed salt is therefore nevertheless of vital importance for advanced degrees of compaction.

3.6 Application of Discrete Element Codes

Numerical simulations for crushed rock salt are usually based on continuum mechanical approaches. In such simulations the relevant deformation processes are simply homogenized over the volume by using appropriate constitutive models. As long as the considered dimension is a few orders of magnitude above the grain size, this idealization is valid /HEI 91/. The material behavior is therefore largely considered at the macroscopic level and the explicit representation of local deformation processes (e.g. rearrangement, deformation or cracking of grains) is only feasible to a limited extend. However, the discrete element method (DEM) is able to simulate a discontinuous distribution of grains at the microscopic level. So far, there are no systematic studies that deal with the compaction of granular rock salt at grain scale using the discrete element method. To test their suitability for modeling the compaction of granular rock salt the DEM was used as an exploratory analysis.

The DEM seems to be an appropriate tool for analyzing the fracture and damage behavior of rocks. The basic approach of the DEM is an assemblage of blocks/ particles and contacts among them establishing the domain of interest /JIN 03/. The approach allows an arbitrary displacement and rotation of the individual discrete elements, a separation of particles along their contacts as well as a detection of new contacts. Two different approaches, the PFC3D and the 3DEC code from Itasca, were investigated. PFC3D represents a specific DEM method at which the basic elements are represented by non-deformable spheres. A deformability of the model is realized solely by contact laws between the spherical elements. However, the representation of granular geomaterials by spherical structures is often inadequate due to lack of angularity, as interlocking effects between the grains cannot be realized /KAZ 10/. Thus, an optimization of the particle shape was done by a grouping of individual particles to so called clusters. A cluster is a complex of several spherical elements, which build a new, arbitrary shaped particle (Fig. 3.21a). Since the particles of a cluster are connected by contact laws, deformability or even a fraction of the cluster is possible. A 3DEC model consists of discrete elements (in 3DEC called blocks) that can be arbitrarily shaped (Fig. 3.21b). Unlike PFC3D, mechanical load acting on a discrete element can result in translation as well as deformation. A deformation is arranged by continuum mechanical approaches in which the blocks are discretized in tetrahedral elements (finite difference zones). A translation of a block is transferred to adjacent blocks over contacts by a stress-strain relationship.

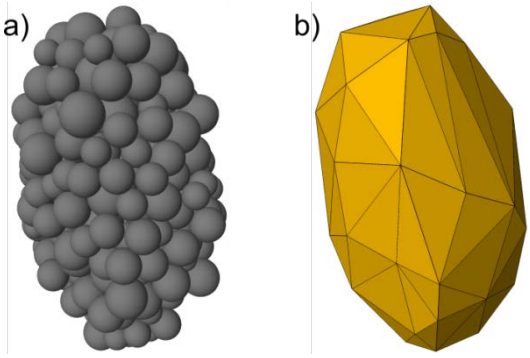

Fig. 3.21 PFC3D (a) and 3DEC (b) rock salt grains

The key point of the DEM is the representation of the controlling deformation processes taking place at grain scale level. Dry crushed rock salt has an initial porosity between 25 to 45 % that can be further compacted by the converging rock mass and the resulting stress load. The porosity decrease over time can be characterized by different deformation mechanisms. At low confining pressure the compaction is mainly denoted by rearrangement of grains. With increasing stress grain crushing can be observed in addition. These time-independent deformation processes are active in restraints up to 30 MPa and lead to residual porosities of about 10 % /POP 12/. For a further compaction of the pore space time-dependent processes will become increasingly important due to intracrystalline dislocation mechanisms (dislocation creep or in combination with small amounts of water as moisture creep). A further amount of strain can be realized by pressure solution mechanisms, but the amount of strain on the proportion of the total quantity is not insignificant especially for small restraints and in the presence of moisture in the pores /SPI 93/. In summary, it can be concluded that the resulting salt backfill deformation mechanisms are qualitatively the same as with natural rock salt. However, in salt backfill volume compaction prevails over intracrystalline dislocation glide mechanisms /POP 12/.

Since the DEM describes a discontinuous distribution of grains at the microscopic level, the accurate construction of a representative microstructure is very important for grain scale modelling. In order to derive relevant input parameters for microstructure reconstruction, the DEOBORA/REPOPERM grain-size distribution was used /KRÖ 09/. In addition, photo-optical computer-aided investigations (computerized particle analyzer, CPA) were carried out on excavated rock salt from the Asse salt mine to characterize the particle shape /JOB 15/. For the two applied discrete element codes PFC3D and 3DEC developed by Itasca (/ITA 03/ and /ITA 13/) the particle shapes were formed based on

the grain size distribution and the CPA analysis. The objective was to generate an unconsolidated sample, which can be used for oedometer simulation tests. The generation of PFC rock salt grains was performed using the internal programming language FISH. In doing so, adequate shaped shells were transferred to a pre-generated polydisperse sphere packing and the corresponding spheres whose centers lie within the peripheral shell were readout in order to generate PFC-Clusters. As a first approximation, the shape of an ellipse was used. Different sized clusters were integrated as a function of the grain size distribution, while the maximum width is adjusted by the distribution of the length-to-width ratio coming from the CP analyzer. To compare the abilities of both simulation codes, the generation of identical 3DEC particle samples was necessary. A corresponding comparability was achieved by building a convex hull of the individual particle clusters. The convex polyhedra generated this way are composed of triangular surfaces (Fig. 3.21).

As already described, granular rock salt shows a variety of deformation processes that need to be described by means of appropriate constitutive laws and its related parameters. A significant drawback of the DEM method is that material parameters used in the constitutive models are difficult to obtain. The DEM considers the mechanical behavior an order of magnitude below the model dimension. Therefore, relevant micro-parameters are generally difficult to determine from classical investigations. The identification of relevant material parameters is oftentimes conducted by back-calculation of laboratory experiments. However, it turned out that this kind of calibration procedure with samples containing many particles is too time consuming. This applies in particular to the use of PFC3D. Therefore, an attempt was made to calibrate the individual PFC3D cluster particles so that their mechanical behavior corresponds to a salt grain. Since laboratory tests on single crushed salt particles are not available, the assumption was made that the mechanical behavior of a single salt crystal is the same as a consolidated rock salt sample. Furthermore the assumption was made that all clusters have the same strength values because size-dependent or shape-dependent values are not available.

Beyond that, further restrictions were necessary with regard to the material models used. The impact of time-dependent creep on the mechanical behavior was not incorporated in this simulation. PFC3D supplies built-in constitutive models for simulating creep (simple viscoelastic model, Burger's model). However these models are not suitable for modelling the compaction of granular rock salt since creep inside clusters does not work. More

advanced constitutive models for PFC3D are under development. 3DEC, however, is based on continuum mechanical approaches where appropriate models for simulating the deformation of rock salt exist. Due to numerical problems with regard to contact detection and the extreme long calculation times only rigid blocks could have been analyzed though. It should be noted, that 3DEC was initially developed for simulating the mechanical behavior of larger jointed rock masses rather than simulating granular flow.

Despite the problems mentioned above, simulations of compaction tests were carried out in order to verify the suitability of the PFC3D and 3DEC models for studying the consolidation of granular rock salt. Compaction tests, especially oedometer tests are designed to measure the consolidation properties (e.g. the stress-stress relationship or porosity change) of a granular media. These tests are usually performed by applying loads to an unconsolidated sample and measuring the deformation response under fixed lateral expansion. First DEM models were built using the usual laboratory sample geometry with a diameter of d = 300 mm.

Although significant simplifications were applied with respect to the particle shape (ellipsoidal particles) and the constitutive models used (no time-dependent deformation), the computation times for the compaction simulations were – again – beyond practical application. Thus, the simulation of the compaction tests had to be carried out on model samples with significantly reduced diameter. Therefore, it was assumed that a validation of the numerical calculations against results of laboratory tests does not make sense. The objective of simulating the compaction process under these simplified conditions were to evaluate the advantages and disadvantages of the two different codes when applied to this kind of compaction simulation and to identify future code improvements which may lead to sufficient results.

PFC-particles were generated in a cylindrical specimen with a diameter of 25 mm and a length of 70 mm using the method described. After the generation process gravitational settling had to be calculated by which the particles fall down to the bottom of the vessel because the particles do not touch each other after their generation. The gravitational settling leads to a sample with a height of 15 mm which serves as a basis for the compaction test. The sample consists of 250 clusters and 57415 spheres. After the settling of the particles the upper loading plate was generated and provided with a velocity bounda-

ry condition in order to compact the sample. Subsequently, the sample was loaded to 10 MPa axial stress (Fig. 3.22).

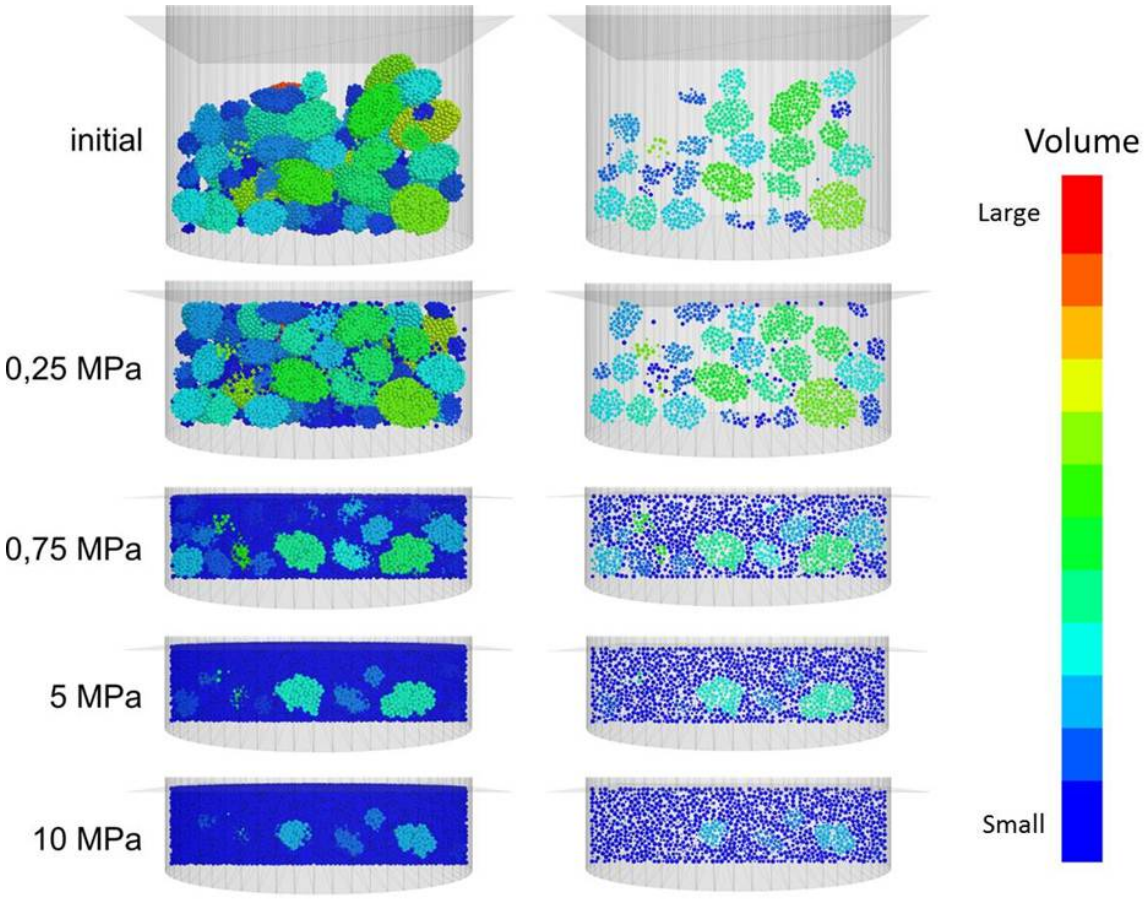

Fig. 3.22 Compaction of the clusters for different stress levels. A vertical cutting plane was used in order to show in a) a half-cylinder and in b) a thin-section

At certain intervals additional data was recorded using the internal program language FISH. The axial stress was calculated as the sum of reaction forces at the loading plate divided by the sample area. Another important parameter to be determined is the porosity which is defined as the ratio of the volume of void-space (pore volume) to the total volume of the specimen. The total volume of the cylindrical specimen was calculated by using the diameter and measuring the current sample height. The pore volume is calculated by determining the sum of all particle volumes and subtracting this from the total cylinder volume. By monitoring the volume of each particle during the course of the simulation, also information can be supplied about the evolution of cluster volumes relative to the initial state due to grain crushing. This was done by summing the volume of all spheres of a cluster. Since each cluster itself has a certain void-space between its peb-

bles, this results in a total volume of the grains which is smaller than it really is. That means that the calculated porosity is much too high.

When loading starts, the compaction is mainly characterized by a rearrangement of grains. However, plastic deformation in terms of grain crushing starts relatively early at stress levels of 0.5 MPa. Grain crushing was mostly observed for single spheres at the outer shell of a cluster. Due to fewer contacts to the cluster, these spheres can be disconnected more easily. The separation of single spheres leads to the fact that larger particles became progressively smaller with increasing stress. At an applied stress of 0.75 MPa for example the sample still consists of clusters but they are surrounded by an increased amount of single spheres. The rearrangement of clusters leads to a large reduction in porosity. The porosity reveals an axial strain accumulation of over 70 % and a reduction in porosity to 45 % at 1 MPa loading stress for the cluster model. With increasing axial stress, the strain rate is decreased and the porosity is reduced only slightly to a value of 42 %.

In order to generate a very similar particle sample for 3DEC, the PFC3D particle model (after settling) was converted to a corresponding 3DEC volume elements model using the methods already described. Since the surfaces of the volumes are based on the convex hull algorithm that uses the center coordinates of the spheres, the method leads to slightly smaller volumes in case they do not touch each other. Therefore, some calculation runs must be performed first to make sure that the particles are in mechanical equilibrium. The following procedure is the same as for the PFC3D Model. However, due to numerical problems with regard to contact detection and in contrast to the initial intention only 3DEC models with non-deformable polyhedral elements could be investigated.

Fig. 3.23 shows the 3DEC model at different compaction levels. After start of the mechanical loading, the compaction is characterized by a rearrangement of grains (blocks). Since the polyhedral elements represent rigid bodies, interlocking effects arise very quickly. As a consequence, the compaction to axial stresses of about 10 MPa is achieved without visually significant rearrangement of grains. Mechanically the interaction between two contacting polyhedral elements is described by stiffness springs in the normal and shear direction. Depending on the contact stiffness, this includes a certain amount of contact overlap. Therefore, with increasing stress a considerable part of the

strain is mainly caused by interpenetration of adjacent blocks. The porosity of the model is reduced from 61 % to 41 % which corresponds to a reduction of about 34 %.

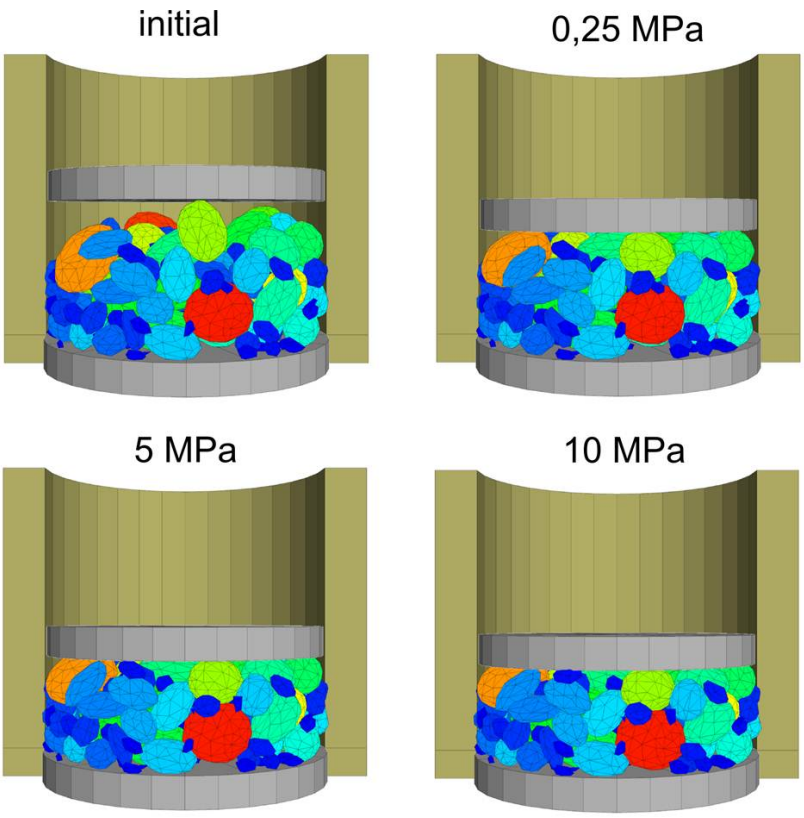

Fig. 3.23 Compaction status of the polyhedral elements at different stress levels

One disadvantage of the DEM method appears when modelling the oedometer tests. Due to long numerical calculation times when using the usual laboratory sample geometry, the compaction tests had to be carried out on samples with significantly reduced diameter. Using the REV concept, this leads to a sample dimension that is far below the smallest volume that is necessary for measurements. Generally, the diameter of the sample should be ten times the largest grain size in the sample. Since the particles are rather large in relation to the cylindrical container, interlocking effects arise relatively quickly between the larger particles when loading starts. A further rearrangement of grains is suppressed and peak stresses are generated leading to an unrealistic fracture behavior of the clusters by losing more and more single spheres at the outer shell of a cluster. At the time being, necessary calculation times for the compaction of particle arrangements representing real oedometer conditions is far beyond practical application.

4 THM-coupled model calculations

4.1 Relevant scenarios and boundary conditions

4.1.1 Introductory remark

A definition of initial and boundary conditions as well as the characterisation of the materials involved has obviously to precede model calculations and were thus discussed at an early stage of the project. Later, the Preliminary Safety Analysis Gorleben (Vorläufige Sicherheitsanalyse für den Standort Gorleben, VSG) /FIS 13/ was performed specifying the safety relevant aspects of a possible repository at this particular site. These considerations have partly outdated the earlier results which are nevertheless outlined in Appendix B for completeness.

However, in the framework of VSG it became apparent that flow of brine in a back-filled drift cannot be predicted without considering unsaturated flow or even two-phase flow /LAR 13/. This draws attention to the backfill in the vicinity of a drift seal which will be in the focus of the THM-models presented later on. This will also be the first THM-model for compaction of crushed salt that uses calibrated data for the changing compaction behaviour under the influence of a changing moisture content.

4.1.2 Components of a generic repository

Before inflow scenarios for the subsequent THM-modelling can be defined, the relevant components of a repository in a salt dome are identified. The repository investigated here is orientated at preliminary plans but nevertheless sufficiently abstract to gain an insight from the modelling that is also relevant for a concrete application at a later time.

Basically, the components of the assumed repository are

– shafts,
– infrastructure area,
– development drifts,
– crosscuts,
– access drifts, and
– deposition boreholes.

Between the infrastructure area and the field of deposition boreholes a vertical anhydrite layer is assumed. The whole set-up is depicted in Fig. 4.1. A typical cross-section of a drift is shown in Fig. 4.2. The geotechnical openings are filled by geomaterials constituting backfill or seals. The assignments of sealing or backfill materials to the repository components are compiled in Tab. 4.1.

In the following the materials involved are roughly characterised. Note that concrete specifications may be outdated by the time of printing. As no credit is taken from these data no effort was undertaken to update them.

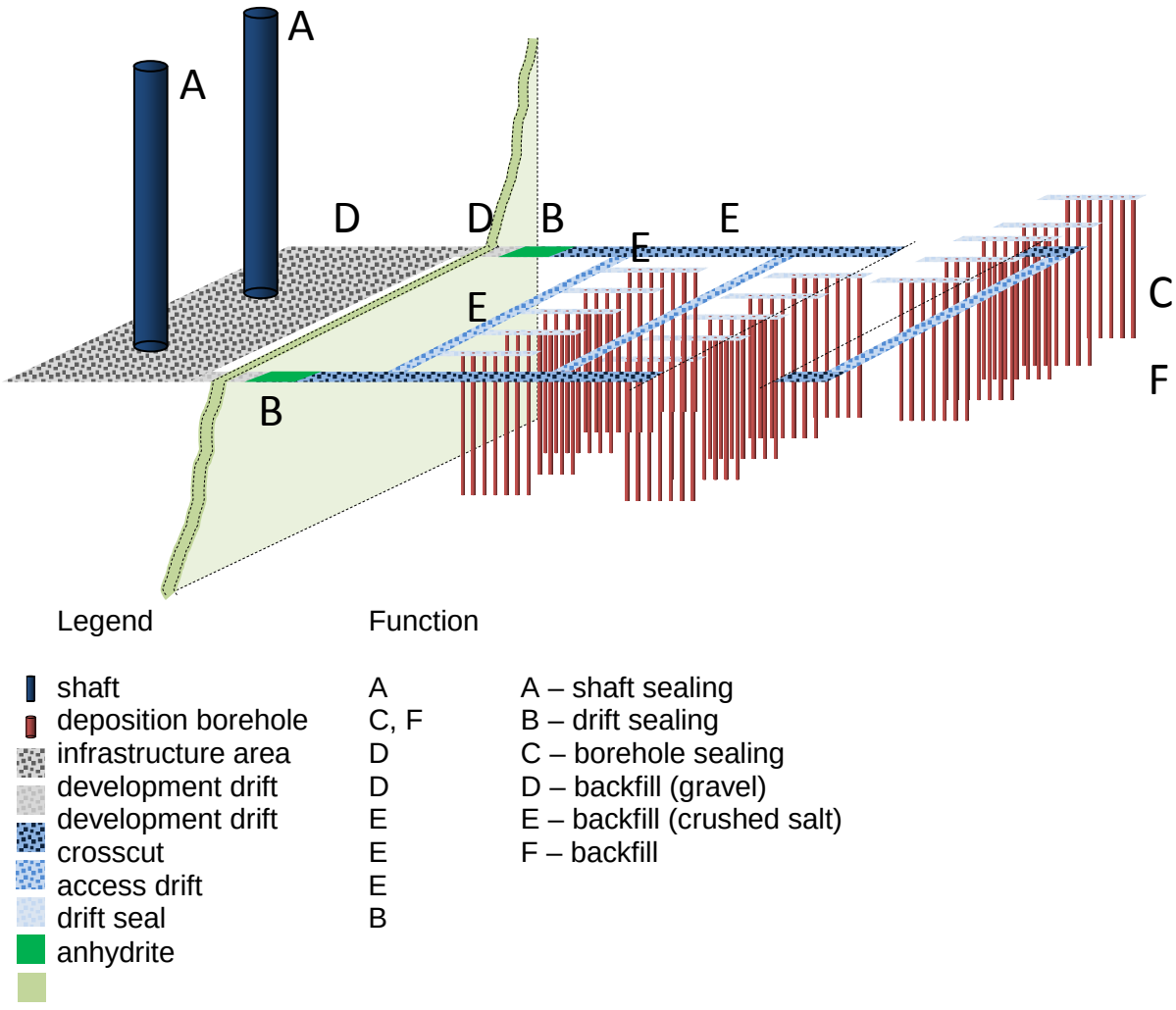

Fig. 4.1 Components of a generic repository in salt rock

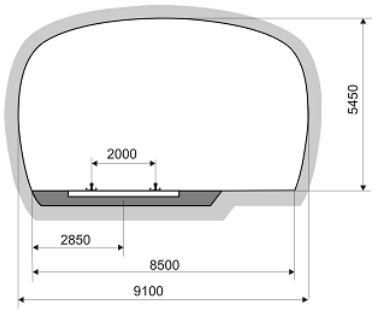

Fig. 4.2 Sketch of a typical cross-section of a drift

Tab. 4.1 Assignment of materials to the repository components

Component	Function	Material
shafts	A - shaft sealing	various
Infrastructure area	D - backfill (gravel)	gravel
development drifts	D - backfill (gravel)	gravel
	B - drift sealing	sorel-concrete and abutment
	E - backfill	crushed salt
crosscuts	E - backfill	crushed salt
access drifts	E - backfill	crushed salt
deposition boreholes	F - backfill	crushed salt
	C - borehole sealing	solid core and crushed salt

4.1.3 Conceptual considerations for brine inflow at a drift seal

In case of brine passing the drift seal and entering a previously dry backfill two radically different paths of development can be conceived depending on the flow rate. Crucial for distinction is the ratio r of the brine inflow rate q_i and the rate q_e at which water evaporates at the water-air interface in the pore space. If the inflow rate is in the range of the evaporation rate or lower ($r \leq 1$), the pathway for brine is expected to become clogged by the precipitating salt that remains after evaporation of brine. But if brine inflow is faster than evaporation ($r > 1$), the pores should become brine-filled fast enough to prevent serious precipitation. The latter issue is addressed further on.

As the previous basic considerations are based on a view at pore size level, a distinction of effects can only be done on a local scale. It is therefore necessary to take not only the total inflow rate into account but also the distribution of flow over the backfill boundary.

Localized flow via the EDZ, for instance, can meet the criterion $r > 1$ at a much lower total flow rate than an equally distributed inflow over the whole face of the drift seal.

Hydraulics (H)

A sufficiently high inflow leads initially to a volume of brine in the pore space of the backfill at the drift-backfill contact whose evolution is basically controlled by gravity and capillary forces. A plume-like increase of this volume prevails as long as the hydrostatic pressure is lower than the capillary pressure (see Fig. 4.3 a)). When the weight of the brine exceeds the capillary pressure, though, it starts moving downwards essentially forming a pool of brine at the bottom of the drift with an unsaturated fringe on top of the free brine surface (Fig. 4.3 b)). This pool tends to spread due to the capillary forces at the front and due to pressure differences according to a decreasing height of the free surface. There are thus three possible driving forces for brine migration in the backfill: capillary forces, gravity and hydraulic pressure differences.

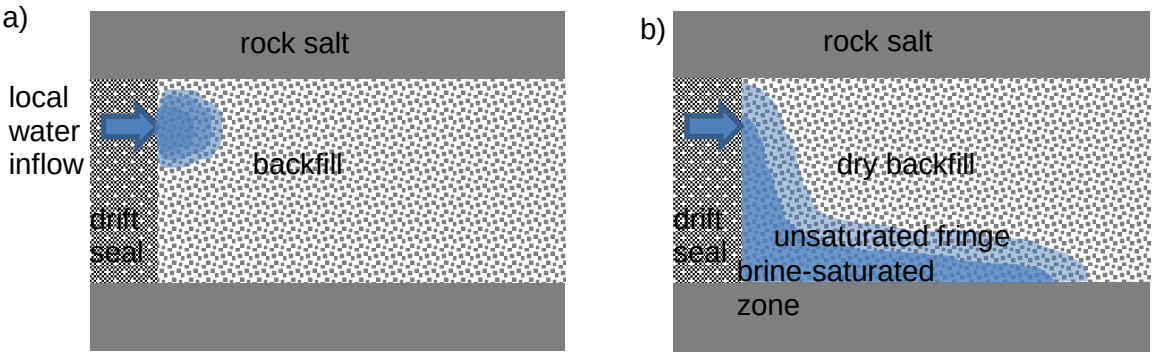

Fig. 4.3 Modes of water migration in the backfill;
a) by capillary forces only, b) capillary forces plus influence of gravity

Mechanics (M)

An isotropic stress distribution prevails in the undisturbed rock salt. This state becomes disturbed by excavations, initiating creep of the rock salt towards the geotechnical openings. Convergence of drifts and boreholes can thus be observed right after excavation.

With the continuing displacement of the drift contour after installation of the crushed salt backfill, the compaction of the backfill commences. Compaction, in turn, activates the

mechanical resistance of the backfill to further convergence thus beginning to counteract the drift convergence.

It is highly likely that a gap at the ceiling of the drift will remain for procedural reasons. In case of pre-wetted crushed salt, the weight of the backfill itself can additionally lead to a collapse of the backfill. In the beginning, convergence will therefore be most pronounced in the vicinity of the gap at the ceiling as long as no resistance to creep is experienced by the host rock (Fig. 4.4 a)). With further progress of rock salt creep, the backfill resistance increases, thereby building-up normal stresses at the drift contour as well as slowing down the compaction process (Fig. 4.4 b)). Displacement of the drift contour and thus compaction of the backfill come to an end when the deviatoric stresses in the rock salt reach a minimum (Fig. 4.4 c)).

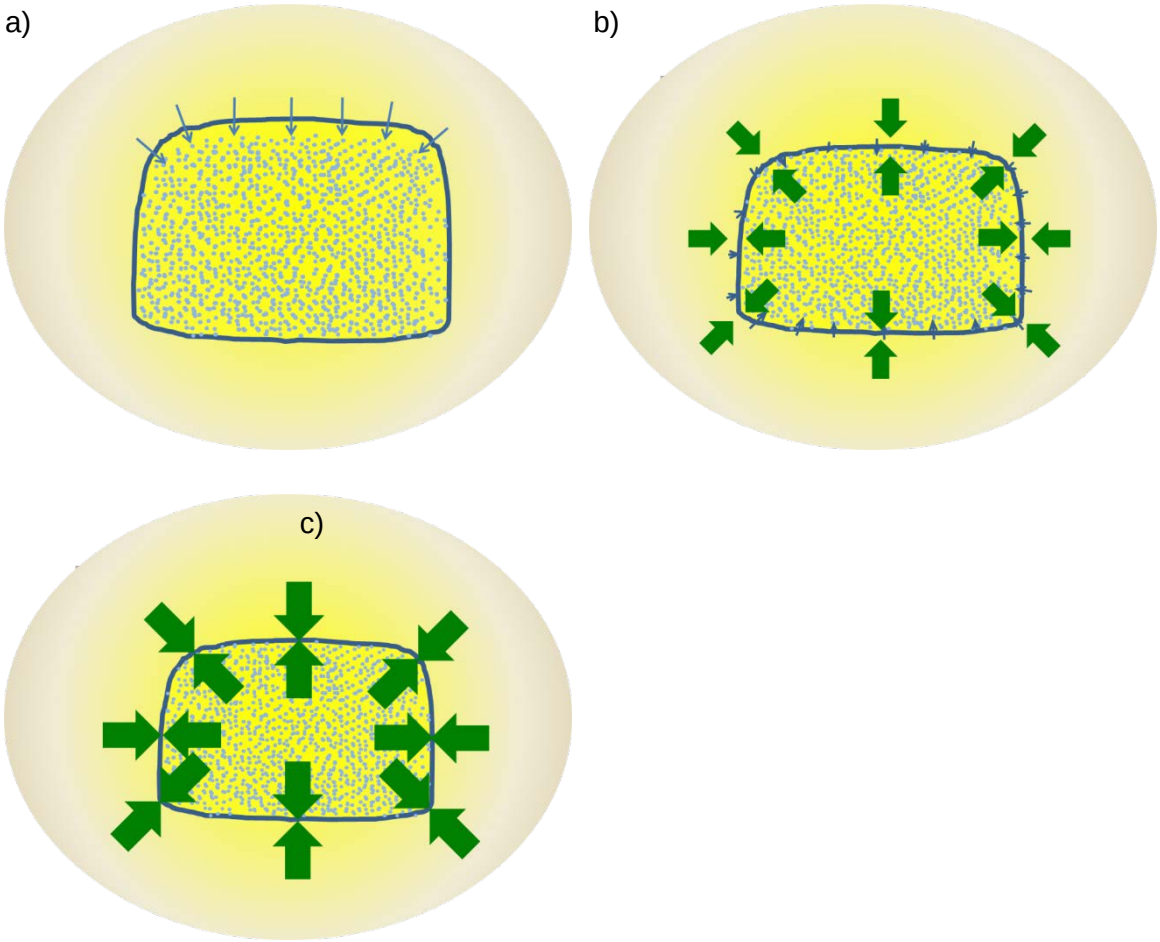

Fig. 4.4 Characteristic phases of backfill compaction

Heat flow (T)

Hydraulic as well as mechanical processes can be influenced by the heat produced by the radioactive waste. This concerns a variety of parameters and processes such as the hydraulic conductivity of fluids, creep, and thermal expansion. Even heat flow itself is influenced by temperature via the thermal conductivity and the specific heat capacity. Generally speaking, increasing temperature accelerates other processes.

THM-coupling

Each of the previously described processes influences, at least theoretically, each other process. Increased temperature accelerates compaction as well as brine flow via temperature-dependent hydraulic and mechanical parameters.

A comparatively little moisture content in the crushed salt can reduce backfill resistance to mechanical stresses considerably thus accelerating compaction. Flow distributing brine in the pore space of the backfill can thus change the compaction behaviour considerably. By filling the pores with brine the effective heat conductivity as well as the effective specific heat is increased, accelerating heat flow even if not necessarily accelerating the spreading of temperature changes. It has to be conceded, though, that this effect becomes less and less significant during compaction because of the decreasing porosity.

Since the compressibility of a single grain in the crushed salt backfill can be considered to be negligible in the context of backfill compaction, this process means basically a reduction of pore space and a constriction of flow channels. Compaction thus also throttles brine flow. With a view to flow driven by capillary pressure, this is expected to slow down further spreading. Visualising flow channels as a bundle of capillary tubes, compaction reduces the tube diameter, but the resulting increase of the capillary pressure cannot compensate the decrease of permeability. A final consequence of compaction is that heat flow is increased due to the rather high thermal conductivity of rock salt.

It is thus that inflow of brine into the drift backfill poses a thermo-hydro-mechanically (THM) coupled problem where

– heat flow,
– unsaturated brine flow including phase changes and solution/precipitation of salt,
– elastic deformation,
– creep, and
– FADT

need to be addressed simultaneously as indicated by Fig. 4.5. The dashed arrows in the sketch on the left hand side imply that the coupling of brine flow to heat flow as well as of compaction to heat flow is comparatively weak. As phase changes and solution/precipitation of salt are not considered in the following investigation for the sake of simplicity, they are also not included in the sketch on the right hand side in Fig. 4.5.

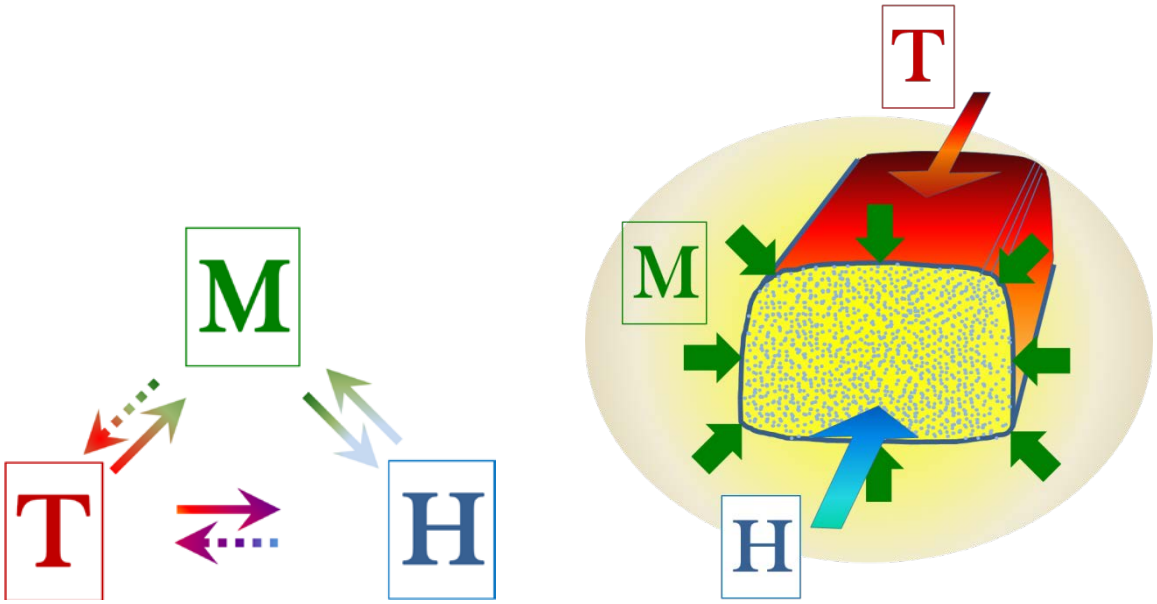

Fig. 4.5 Process coupling during compaction of crushed salt

4.2 Inflow into the drift backfill at the drift seal

4.2.1 Objectives and scope

In order to investigate whether the constitutive models for crushed salt implemented in CODE_BRIGHT are in principle applicable for simulating the in-situ behaviour of a backfilled drift, a simplified drift model was developed, and several model variants involving the backfill evolution under dry conditions and with brine inflow, at ambient and elevated temperature, were simulated.

The objective of these simulations was to test the capabilities of the implemented models, especially with coupling of mechanical, hydraulic and thermal effects, in a system involving the crushed salt backfill and the surrounding rock salt. To perform a reliable prediction of the backfill evolution in a realistic repository system was not the aim. Therefore, several simplifications regarding geometry and boundary conditions introduced and explained further down were considered acceptable.

4.2.2 Model description

Geometrical model

For the simulations an axial-symmetric model of 80 m length and 100 m radius was used, with the axis in the direction of the drift (Fig. 4.6). Consequently, the drift has a circular cross section, the drift radius amounts to 2.9 m. The surrounding rock salt is divided into rock mass, near field and excavation-damaged zone (EDZ). These are modelled essentially in the same way, although the EDZ features a somewhat higher porosity (see next section). 65 m of drift length (left hand side in Fig. 4.6) are backfilled with crushed salt, while a concrete plug is installed drift in the right 15 m of the model. The EDZ has been removed in the plug region.

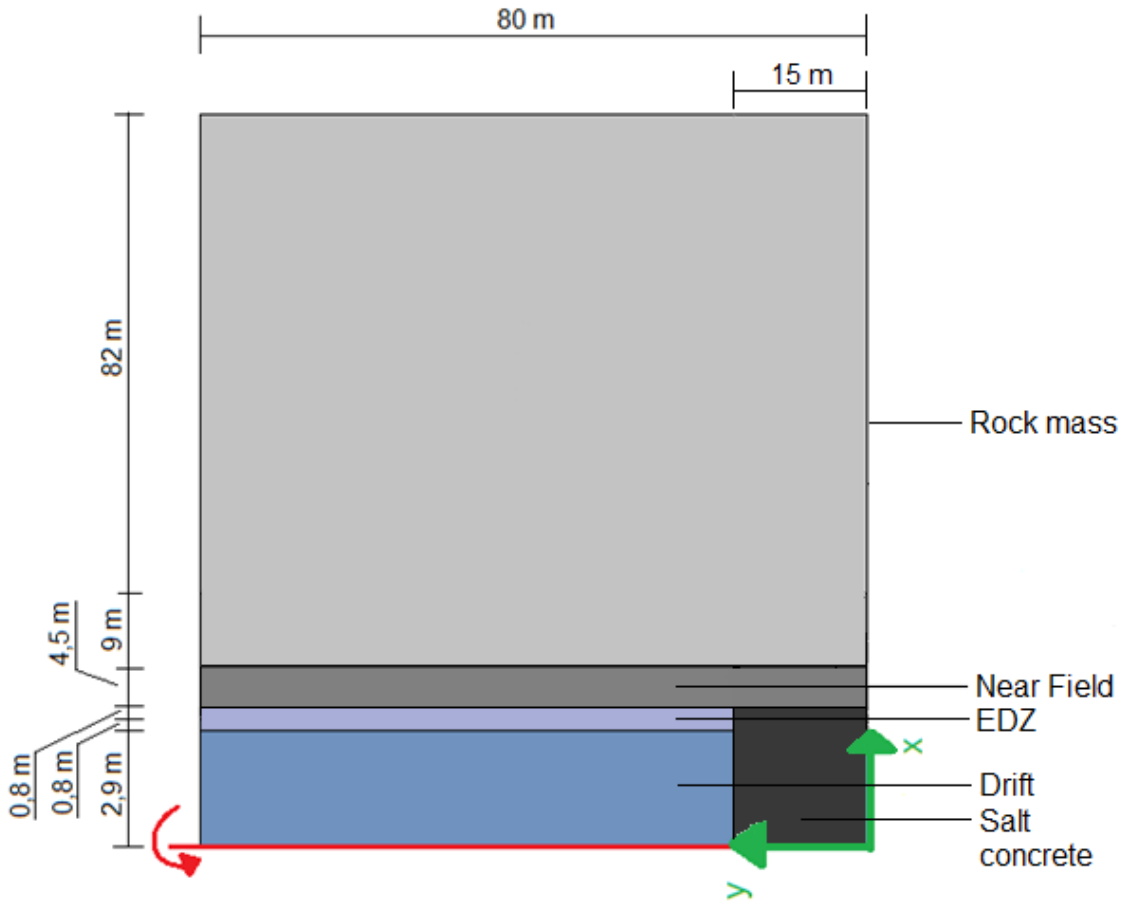

Fig. 4.6 Overview of the model geometry

Physical model and material data

The model for mechanical behaviour of the crushed salt includes the following mechanisms:

– elastic deformation
– dislocation creep
– viscoplasticity for granular material representing grain reorganisation and breaking
– fluid assisted diffusional transfer
– thermal expansion (for non-isothermal simulations)

The various contributions are combined by adding the individual deformation rates. A description of the formulations is given in Appendix J.

For rock salt, only elasticity, dislocation creep and thermal expansion are considered. The EDZ is modelled with the same parameters as the undisturbed rock, except for an increased porosity (3 % instead of 1 %). The idea is to slightly moderate the sharp porosity contrast to the backfill (initially 29.77 %). Dilatancy evolution of the EDZ is not considered, because the work is focused on backfill performance (although a respective approach is available in CODE_BRIGHT). Like rock salt, salt concrete is modelled with elasticity, dislocation creep and thermal expansion, but with different parameters.

The hydraulic behaviour of the materials is described by their intrinsic permeabilities, van Genuchten type retention curve and relative permeabilities, and diffusive fluxes of vapour and dissolved salt. The simulations consider partially saturated systems and run at most until full saturation of the backfill, therefore positive pore pressures do not occur.

Heat transfer is restricted to conductive flux of heat in the non-isothermal simulation. For thermal-mechanical coupling linear thermal expansion of solid and liquid phases is considered.

All material parameters are compiled in Appendix J.

Simulation variants, schedule, and boundary conditions

Three simulation variants were performed and analysed:

– A coupled hydro-mechanical (HM) simulation at ambient temperature (38.67 °C), relevant for backfilled drifts far from waste disposal areas
– A coupled HM simulation at elevated temperature (60 °C), more relevant for drifts closer to disposal areas
– A coupled thermal-hydro-mechanical (THM) simulation with an axial temperature gradient

All variants featured a period of 100 years of drift convergence and backfill compaction under dry conditions and a subsequent brine inflow from the open drift side (left hand in Fig. 4.6), resulting in an accelerated backfill compaction. Each simulation was continued until a residual backfill porosity of 1 % was reached.

In the following, the initial and boundary conditions of the simulation cases are discussed. An illustration of the conditions can be found in the Appendix J.

In all simulation variants, the drift axis is the rotation axis, at the left and right hand sides of the model (Fig. 4.6) horizontal displacement is prevented, and a radial load of 18.67 MPa is applied circumferentially. Because of the axial symmetry, gravity has to be neglected in the model. Initial mechanical stress is 18.67 MPa isotropic which is considered representative for the 850-m level of a repository. An initial suction of -10 MPa is applied in the entire model, corresponding to a saturation of 2.7 % of the rock.

At simulation start-up, the drift is excavated and the stress inside is set to -0.1 MPa (air pressure). Additionally, the EDZ is created and the salt concrete plug is emplaced. The drift is kept open for one year, afterwards it is backfilled instantly with crushed salt, again with a saturation of 2.7 % (-10 MPa suction). The initial porosities of the materials are 0.01 (rock salt), 0.03 (EDZ), 0.06 (plug), and 0.2977 (backfill). In Tab. 4.2, these data are summarised.

Tab. 4.2 Conditions of the simulation at ambient temperature after backfilling of the drift

	Drift	EDZ	Near field and rock	Salt concrete
Porosity	0.2977	0.03	0.01	0.06
Stress	-0.1 MPa	-18.67 MPa		
Liquid Pressure	-10.0 MPa			
Temperature	38.67 °C			

After 100 years of convergence at dry conditions, the suction condition at the open drift side (Fig. 4.6, right hand) is changed to -0.01 MPa, which corresponds to a backfill saturation of 25 %. This is done in order to simulate a re-saturation of the crushed salt from the left side. At the same time, the mechanism of fluid-assisted diffusional transfer is activated in the backfill, and a seepage condition is applied to the right end of the salt concrete plug.

In the following simulation, the backfill is saturated from the left side of the model. Moreover, saturation additionally increases by the accelerated re-compaction of the backfill. The simulation runs until a residual porosity of 1 % in the backfill is reached.

The three simulation variants differ with regard to the temperature field. For the isothermal HM simulations at 38.67 °C and 60 °C, temperature is kept constant over the whole simulation.

In the THM simulation, directly after emplacement of the backfill (one year simulation time) another interval of one year is inserted during which the temperature condition at the right hand model side is raised to 60 °C. This temperature gradient is then kept over the rest of the simulation. After another 100 years of simulation at dry conditions the hydraulic boundary conditions are changed in the same way as for the isothermal simulations. Saturation is increased to 25 % at the left side of the backfill, and a seepage condition is applied at the right end of the salt concrete plug.

4.2.3 Results

In this section, the evolution of porosity, saturation, and stress in the drift centre as obtained in the different simulations are compared. More detailed results of the individual simulations including longitudinal sections can be found in the Appendix J.

Fig. 4.7 shows the evolution of porosity. From year 1 until year 101 the porosity decreases as a consequence of the mechanical compaction process due to drift convergence. After year 101, the curve slopes increase significantly because of the softening effect of the brine, enabling fluid assisted deformation. An increased temperature accelerates compaction both in the dry and wet phase, as can be seen when comparing the curves for ambient temperature and 60 °C. The THM simulation with temperature gradient results in a porosity curve running between the other two. This can be expected, because the temperature in the drift centre amounts to 49 °C in this simulation. Depending on the simulation variant, the minimum porosity of 1 % is reached between 120 and 182 years.

Saturation evolution is compared in Fig. 4.8. Over the first 101 years there is no change in saturation because of the boundary condition. When brine enters the drift as a consequence of the increased saturation condition there is a rapid increase of saturation degree in all simulations, due to the high hydraulic conductivity of the backfill. Then, the saturation degree increases with time to a maximum of 100 % which is reached with the residual porosity of 1 %.

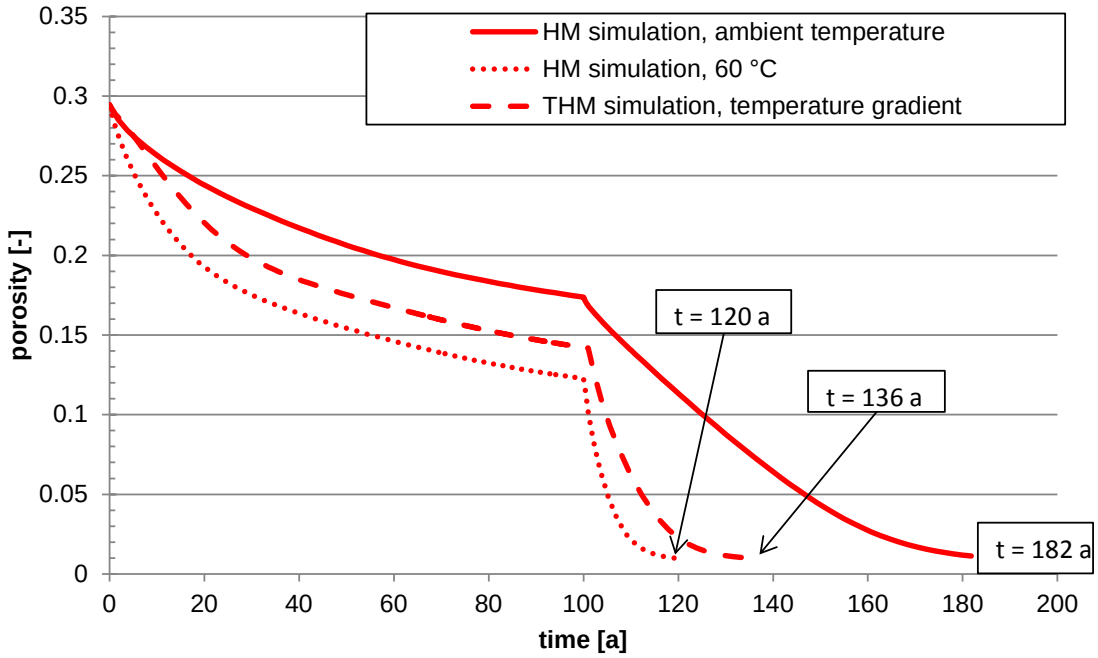

Fig. 4.7 Porosity evolution in the drift centre – comparison of different simulations

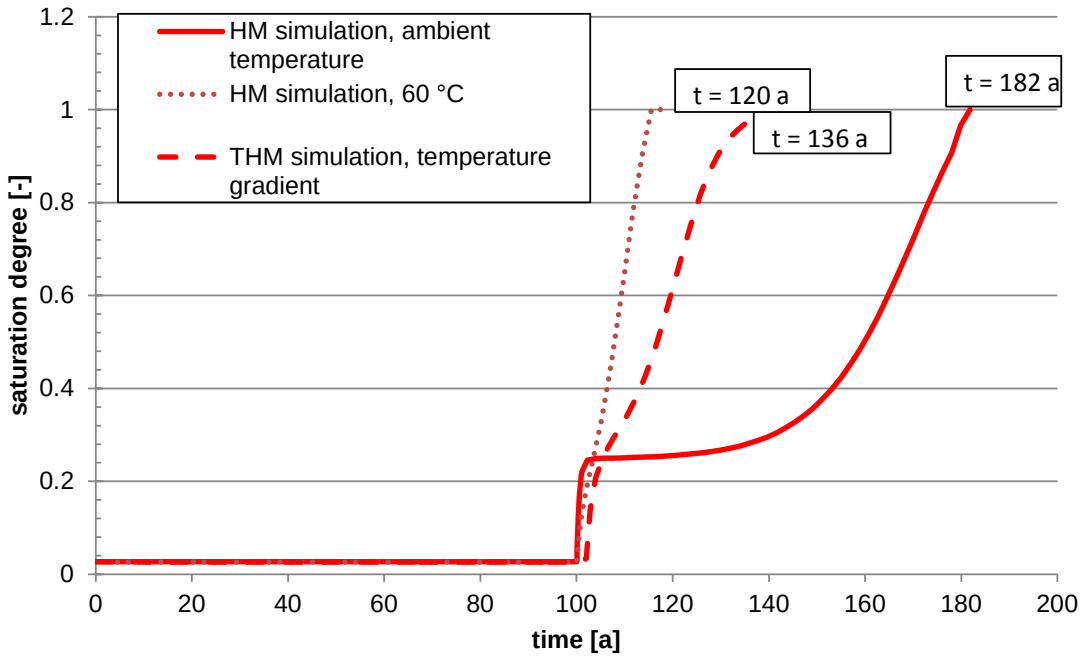

Fig. 4.8 Saturation evolution in the drift centre – comparison of different simulations

In the very early re-saturation phase, saturation in the ambient temperature simulation increases faster than for those with increased temperature. This can be explained by the higher porosity and related higher permeability of the backfill at the time of brine entry.

Shortly afterwards, however, saturation in the warmer backfill rises much faster because of the accelerated porosity decrease.

Both higher temperature and presence of brine result in a softening of the affected materials. While temperature affects both the backfill and the surrounding rock salt, mainly because of increased creep rates, the moisture effect is restricted to the crushed salt. Accelerated compaction is the result of a difference in stress-strain behaviour. This is illustrated by Fig. 4.9 which shows the evolution of minimum principal stress in the three simulations.

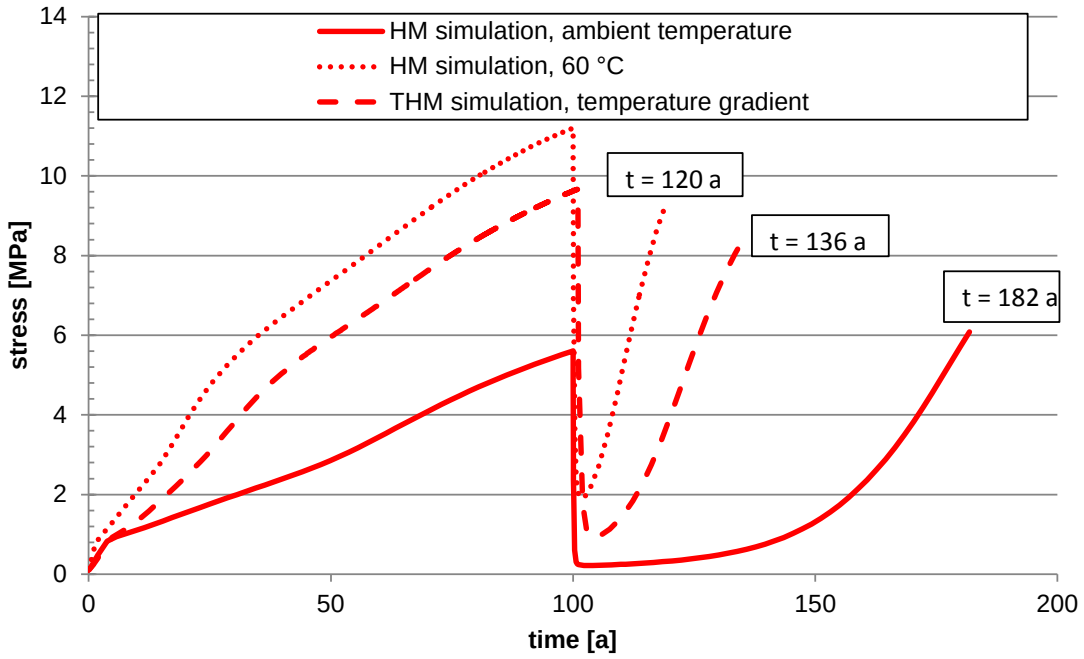

Fig. 4.9 Evolution of minimum principal stress in the drift centre – comparison of different simulations

In the dry phase, minimum stress rises with time to nearly 6 MPa at ambient temperature, but to 11 MPa for the 60 °C case. This is explained by the fact that in the 60 °C case a significantly lower porosity is reached in the dry phase. The dry-phase end porosity of the ambient temperature case of 17.4 % is reached already after 31 years at 60 °C. This is a result of higher creep rates of the surrounding rock, so that a lower porosity is reached after 100 years.

Brine entry results in an instant softening of the backfill, visible by the sudden drop in all stress curves. With further compaction, stress in the backfill increases again with time. This happens faster again at higher temperature because of higher creep rates and faster compaction.

4.2.4 Conclusions

The simulations have shown that the application of the available constitutive models on a system of a backfilled drift leads to plausible and coherent results. Compaction of crushed backfill in a repository drift can in principle be modelled, both for the dry case and for a brine inflow, at constant or variable temperature. If it is possible to validate and calibrate the parameters for the constitutive models for crushed salt implemented in CODE_BRIGHT, it has a high potential for the prediction of the THM behaviour of a repository in rock salt.

5 Summary

5.1 Scope of the project

The REPOPERM-project started out to answer the question about hydraulic properties of crushed salt at low porosities (< 3 %) and in particular about a possible percolation threshold where the permeability would be reduced to 0 at a finite porosity. However, in phase 1 of the project it had become clear that it is extremely difficult to reach such states in an acceptable amount of time while keeping to repository-relevant conditions for example doing without exceedingly high compaction pressures. Inherent problems with the determination of low porosities caused by the natural variation of the mineralogical composure had been revealed.

In REPOPERM phase 2 the initial question was thus rephrased: to what degree is it necessary to know these properties at all? To answer this question of prerequisites must be fulfilled:

– Provide a reliable set of parameters for the constitutive models in use for as low porosities as can be measured with reasonable accuracy.
  - Calibrate the parameters of the constitutive models against different compaction tests with dry crushed salt.
  - Provide a data base for compaction with wet material.
  - Calibrate the parameters of the constitutive models against compaction tests with wet crushed salt.
– Apply the constitutive models for the range of very low porosities, vary the parameters within reasonable boundaries and do a sensitivity analysis of the consequences for a brine intrusion scenario.

Phase 2 of the REPOPERM-project has therefore essentially been devoted to the first prerequisite. The compaction behaviour of crushed salt has been extensively investigated by means of experimental as well as theoretical work. Compaction tests were performed under repository-relevant conditions. These tests were supplemented by laboratory work aiming at specific aspects of compaction such as impact of an increased humidity in the pore atmosphere or two-phase flow characteristics in compacting crushed salt. Additionally, the microstructure of compacted crushed salt samples was investigated.

Comparison of mathematical models describing compaction-relevant processes as well as benchmark calculations based on three different compaction tests aimed at checking the validity of the established numerical tools. In parallel new theories and constitutive models were developed based on the experimental results. This includes an investigation of a possible application of the Discrete Element Method to describe crushed salt compaction.

A discussion of repository-relevant scenarios formed the basis for a realistic but generic numerical model of brine inflow into a converging back-filled drift. This exercise demonstrates the feasibility of modelling crushed salt compaction as a fully coupled thermo-hydraulic-mechanical process including two-phase flow effects.

5.2 Results of experimental investigations

Compaction of crushed salt can be accelerated by increasing the confining stress, temperature, and/or the moisture content. The impact of stress and temperature on compaction is already well investigated for dry material at a rather high degree of compaction ($e > 3$ %). It is also well-known that moisture can have the same effect and theoretical development of a constitutive model for wet compaction has been developed. This refers either to brine inflow into the backfill, or to an artificially increased initial moisture content, or to vapour flow. Comparatively little has been done in the past, though, to establish the related parameters for a quantitative description of compaction under increasing moisture content due. Even less was known about the potential impact of humid pore air on compaction.

Flow processes in compacting crushed salt were basically envisaged as single-phase flow of brine or gas. Migration of vaporous water together with adsorption on the salt grain surfaces as well as unsaturated or even two-phase flow have generally not been considered yet to the point where comprehensive data were collected to quantify a constitutive model.

While both, hydraulic and mechanical phenomena refer to wet(ted) crushed salt material the description for dry material must be ensured as well to distinguish between effects from dry and from wet compaction. The experimental work in this project thus covers both types of compaction.

The key results in detail:

– *Examining the porosity in relevant, past experiments*
  The effect of the uncertainty in the grain density on the void ratio of the oedometer tests used are in the range $\Delta e \approx 0.0045 – 0.0065$.

– *Influence of the grain size distribution on compaction behaviour*
  As shown in the framework of REPOPERM phase 1, the backfill resistance of DEBORA material (maximum grain size of 8 mm) at 150 °C behaves similar to the backfill resistance of reference material for drift backfilling, even though the latter has a much larger maximum grain size (d = 31.5 mm) than the DEBORA material. The result from project REPOPERM I was confirmed for a temperature of 50 °C.

– *Triaxial compaction test with dry material at low porosities*
  A triaxial compaction test was performed with respect to the residual porosity range where compaction stress (formation pressure) is not expected to rise any further in-situ, with the result that creep compaction dominates in the test specimen. A comparison with an earlier oedometer test showed that the results appear to disagree increasingly towards small porosities.

– *Influence of humidity on compaction*
  - Strain-rate controlled oedometer tests
    The backfill resistance for 1 % added brine at 33 °C (test 105) compared well with the curve for 0.6 % added brine at 50 °C (test 106). Compaction under the influence of injected humid air of 85 % relative humidity was faster than with a comparable dry sample but not as fast as in tests 105 and 106 with added brine. It has to be mentioned, though, that the moisture content of the sample had increased by more than 0.1 % by weight during the treatment with moistened air.
  - Stress-controlled uniaxial long-term compaction
    An initial moisture content in the order of 0.1 % does not significantly influence compaction in comparison to initially oven-dry conditions. Compaction of the sample with initially 1 % moisture content was much faster under much less load than compaction of the initially dryer samples. A temperature increase of about 30 °C had a similar effect as a mechanical load increase in the range of 3 to 5 MPa. Temperature decrease at maintained mechanical load results in a “hardening” of the material as the subsequent strain rate dropped considerably. The

effect of flooding under high stresses can result in a loss of porosity in the order of 8 to 13 % within a year. A qualitatively similar behaviour is expected for low stresses.

All in all, the gained data forms a comprehensive basis for testing constitutive models for crushed salt.

- Triaxial compaction in an autoclave

  The test indicates that the transition from dry compaction to wet compaction occurs between 0.3 % and 0.6 % initial moisture content.

- Compaction in a humid atmosphere

  In general the development of the porosity under increased humidity compares quite well in terms of shape with the measured porosity in the oven-dry sample of the long-term test. An influence of high relative humidity in the pore air can therefore not be confirmed.

  The results from flooding of the samples in the first test as well as from flooding in the long-term compaction test look rather similar considering that the porosity as well as the mechanical load were quite different at the time of flooding.

- Adsorption of water to salt in a humid atmosphere

  The amount of water drawn by crushed salt from a moist atmosphere is either rather low or it takes time in the order of years to reach a significant mass of adsorbed water. It can thus not be expected that sorption exerts a significant effect either on retardation of vapour flow in the pore space of a crushed salt backfill or on the backfill resistance.

– *Permeability associated with low porosity*

- Permeameter test with brine

  The new D-A-025 test confirms and supplements the permeability-porosity relation for wet crushed salt derived in /KRÖ 09/ particularly for low porosity values down to 2 %.

- Permeability tests with gas (nitrogen)

  Even with the already highly compacted cores from oedometer test 099 in the range e = 1 %, it has not been possible to verify complete barrier effectivity under natural (“dry”) moisture conditions.

  The spontaneous treatment of the highly compacted crushed salt samples with moist air gave rise to a clear change in compaction and permeability behaviour. The reduced backfill resistance in the “wet“ state led to a much higher compac-

tion under triaxial load than in the “dry“ state. These findings, however, must be verified by other tests and quantitatively expanded.

– *Constitutive equations for two-phase flow*

  Measurement of two-phase flow properties of crushed salt with a repository-relevant grain size distribution is possible down to a brine permeability of 10^{-15} m² is possible.

  The theory of Brooks and Corey fails for compacting crushed salt. It is apparently not possible to derive the Relative Permeability-Saturation relation from parameters for the Capillary Pressure-Saturation relation as the work of Brooks and Corey implies.

  Concrete predictions based on the presented results (present knowledge) are therefore not advisable.

  A much higher range of data scatter is to be expected from the uncertainties caused by the backfill preparation under in-situ conditions in an operational repository. Related model predictions might have considerable difficulties in covering all possible consequences on the dynamics of brine inflow, particularly under the varying THM-conditions during compaction.

– *Microstructural Investigations*

  It was also found that penetration took place along grain boundaries and in cracks that run through larger halite grains.

  The addition of 1.2 % brine during compaction obviously had the effect that the small grains in the fine grained section “bonded’’ leading to new crystalline structures so that the amount of fine pores in this section was reduced significantly. By contrast, the addition of moist air during compaction did not lead to such bonding.

  Flushing with brine after dry compaction led to the formation of a “vessel system” in the crushed salt that could be permeated by the resin. This indicates that early brine inflow into the crushed salt backfill of a repository could lead to the formation of an unwanted system of larger pores which might remain for a certain period of time until it is compacted by the convergence.

  Analyses with XCT and FIB-nt reveal that the pore space must be considered as isotropic in its connectivity and percolation threshold.

  An approach, which combines local porosity theory and percolation theory, applied to reconstructed pore structures, leads to the result that, while a fully connected and thus percolating pore network must be taken into consideration for porosities ex-

ceeding 5 %, a very poorly or maybe even not connected pore network can be assumed for porosities of 1% or less.

5.3 Results of theoretical investigations

With respect to theoretical considerations the work presented here aims at the evaluation of numerical modelling capabilities for the prediction of the long-term behaviour of crushed salt backfill. Several constitutive models are available, and different aspects of material behaviour can be modelled separately. Presently, not all of the constitutive equations are shown to be valid over the whole range of primary unknowns (stress, temperature, porosity etc.), though.

Three constitutive models were compared in detail. Overall, the three models yield similar results. The conditions under which the calculations gave rather big deviations practically are of little importance under in situ conditions, especially for a high porosity. Nevertheless, in view of the discrepancies of two orders of magnitude at best these deficiencies cannot be ignored. In case of compaction rates that are ruled by the converging host rock these differences will be less by a factor of 5 about, but for medium porosities already there will be a growing interaction of host rock and backfill. The creep rates may differ by orders of magnitude in case of low porosity what might affect long term safety assessment.

Especially in the case of wet compaction the description of the physical phenomenon leaves no doubt that it correlates with the inverse third power of the grain size (or its contact zone) making clear that it is the small grain that vitally dominates the compaction behaviour. The dominance of the small grains is even also true in case of dry crushed salt.

The consideration of hardening of the salt grains (physically not in doubt) could deliver a much better agreement with experimental data in case of stress reduction for a low exponent in the power-law of stress, but other experiments seem to prove that a higher exponent has to be used what could explain the data for stress reduction as well. As an alternative to the widely used power-law approach a hyperbolic stress dependency is suggested which might reconcile the seemingly contradicting results of low exponents for rock salt and high exponents for crushed salt.

In case of very loose crushed salt fracturing at the – mostly very small – contact zones between the grains may influence the mechanical behaviour. This may be less important from an engineering point of view in case of the low macroscopic stresses but is supposed to have an important influence on the parameters governing the creep for higher states of compression.

To avoid costly laboratory experiments concerning two-phase flow parameters in crushed salt at different degrees of compaction the potential of scaling-rules – extensively used by the oil industry – was investigated. However, the use of scaling-rules even of the most established J-function of Leverett has proved to be quite limited as validity was attested only for a permeability range of 2 to 3 orders of magnitude.

So far, there are no systematic studies that deal with the simulation of the compaction of granular rock salt at grain scale using the discrete element method (DEM). To test their suitability for modeling the compaction of granular rock salt the DEM was used as an exploratory analysis. Two different computer codes have been used for this analysis, the PFC3D and the 3DEC code. During the application analysis a couple of problems occurred with both of the codes which are, amongst others, related to porosity determination and most of all related to necessary calculation times that are far beyond practical application. Further development is needed with respect to the constitutive models used, particularly in PFC3D. The impact of time-dependent creep on the mechanical behavior could not be incorporated in the simulations. 3DEC, however, is based on continuum mechanical approaches where appropriate models for simulating the deformation of rock salt exist. But significant numerical problems occurred mainly with regard to particle contact detection. Finally, it has to be stated that both codes need significant improvements prior to an application to simulate compaction processes.

5.4 Results of model calculations

The long-term compaction tests were accompanied by model calculations. First, a model for dry compaction was calibrated. The resulting material parameters were then used as input for a numerical simulation of a compaction test with wet material. This allowed for the first time to estimate the parameters for the fluid assisted diffusional transfer (FADT) on the basis of a real test. This is significant as the FADT is believed to describe the impact of water or brine on compaction.

Three rather different tests concerning dry compaction – two of which were performed in the framework of the REPOPERM-project – formed the basis for checking on the validity of the presently available constitutive models. The idea behind this exercise was that a valid constitutive model should correctly describe any of the three compaction tests. However, this was not the case. None of the calibrated parameter sets could be used for another test with satisfying results. Using sets of intermediate parameter values led to the same result. While the numerical tools might be able to describe crushed salt compaction in principle, the understanding of the compaction tests in general and/or of the constitutive models in particular is not sufficient to allow for reliable predictions at the time.

The simulation of backfill compaction in a drift under a thermal gradient including brine inflow at a certain point in time using repository-relevant material parameters led to plausible and coherent results. Compaction of crushed backfill in a repository drift can in principle be modelled, both for the dry case and for a brine inflow, at constant or variable temperature. If it is possible to validate and calibrate the constitutive models for crushed salt implemented in CODE_BRIGHT, it has a high potential for the prediction of the THM behaviour of a repository in rock salt.

6 Conclusions and recommendations

The ultimate goal of the investigations presented here is a reliable prediction of crushed salt behaviour under repository conditions. This project has contributed considerably to this goal particularly by the following results:

– The first data base for compaction of wet crushed salt has been established.
– It could be shown that compaction is not significantly controlled by the largest grains of a crushed salt mixture.
– Feasibility of two-phase flow measurements on compacted crushed salt with a gas permeability of 10^{-15} m² and with a repository-relevant grain size distribution could be demonstrated.

The experimental data as well as theoretical considerations have shown, though, that that the hydro-mechanical behaviour of compacting crushed salt is not yet completely characterized, sufficiently understood and thus cannot precisely predicted.

Several constitutive models have been formulated in the past and not all components, even the fundamental law of creep of salt, are entirely validated. Related parameters are in some cases only used out of habit being not yet precisely determined. It is thus imperative to enhance the predictive capability of the models for the compaction behaviour of crushed salt backfill over the whole range of possible THM conditions hence ensuring reliable numerical predictions of the long-term performance of the repository. Material parameters must not be allowed to be test dependent. Subsequently, a catalogue should be prepared containing all constitutive equations including the supporting experimental evidence for validity and the conclusions concerning the range of validity.

Compaction of crushed salt is usually investigated by means of uniaxial or triaxial tests. The results of such tests appear to be similar but to reconcile them quantitatively remains to be another important task. A detailed knowledge about all phenomena involved in these tests, qualitatively as well as quantitatively, is required for this purpose. This includes effects like friction between crushed salt and the cell wall as well as the usually unknown lateral stress variation during oedometer compaction tests, which are not of direct concern to in-situ compaction but are a prerequisite to derive compaction parameters from the tests.

Evaluation of previous creep compaction tests on crushed salt showed that the data often are not of that precision that would be needed to get that information that allows a satisfactory description of compaction at low porosity. This has to be attributed to high requirements for the experimental devices and methods. But in order to overcome these unfortunate circumstances (from a theoretical point of view) new methods have to be developed that allow a better insight into the phenomena and a deep understanding which can provide a data basis for a verifiable theory.

With somewhat less effort it could be tried to investigate the consequences of the remaining uncertainties theoretically by means of sensitivity analyses. This might indicate a level of compaction at which the difference between very little flow and complete cut-off does not matter anymore with a view to the safety of a repository and possibly make more sophisticated (and expensive) laboratory investigations obsolete.

A big impact on the crushed salt compaction has moisture. A moisture content of less than 1 % achieved by adding a small amount of brine is sufficient to exert a considerable influence on the compaction and the hydraulic properties of crushed salt. The presented compilation of compaction tests allowed for estimating the model parameters for wet compaction which has been done exemplarily in the framework of this project. Also covered is the hardening of the material with decreasing temperature which is not relevant for actual backfill in a repository but might be of interest for the understanding of the material behaviour and interpretation of test results. The range over which the compaction behaviour changes from being typical for dry material to typical for wet material could not be exactly determined even if it is suspected to be in the range of 0,3 % to 0,6 %. What remains to be investigated are therefore the exact location and range of this transition on the one hand and a quantitative description in terms of moisture dependent compaction parameters on the other hand.

The influence of an increased humidity in the pore atmosphere on compaction could not be quantified unequivocally. Adsorption of water from the humid air appears to be minimal and the impact on compaction of crushed salt at a porosity of about 30 % and at a comparatively low mechanical stress (1 MPa) was negligible on the one hand. This would mean that an increased vapour content in the pore atmosphere could spread out over the whole repository and reach the waste canisters virtually unimpeded possibly enhancing corrosion. Flow of air with 85 % humidity in highly stressed samples (up to

~30 MPa) on the other hand reduced the backfill resistance considerably. If these somewhat contradictive results are a consequence of the difficulties with avoiding condensation at a high relative humidity or if a more sophisticated explanation is still to be sought, needs to be clarified in the future.

The classic two-phase flow theory fails to describe the constitutive equations for two-phase flow mathematically. In the light of this finding the robustness of the safety case regarding the compaction of crushed salt must be strengthened. This can be done either by further and much deeper investigation of two-phase flow properties of compacting crushed salt or by doing without quantitative two-phase flow effects.

Most of the compaction tests reported here have been performed using material from the Asse mine. The grain size distribution has been chosen to comply with the so-called “DEBORA-material” (cp. Appendix G) and all samples have been prepared to show a maximum of homogeneity in the material. But the impact of deviations from this specification is not at all clear. In the framework of this project only the effect of a larger maximum grain size, as envisaged for the backfill of drifts, was shown to be of little importance. Other deviations are still to be investigated. To transfer the results to other locations the effect of origin meaning basically the mineralogy of the crushed salt material on the compaction behaviour requires some further insight.

Possibly even more important is the impact of inhomogeneity in the grain size distribution on the hydraulic overall performance of a drift backfill. Demixing of grain sizes due to technical procedures during emplacement can easily counteract any conclusions about material parameters, compaction behaviour, porosity and permeability, two-phase flow, model predictability, and a possible percolation threshold. It can also change the constitutive relations for two-phase flow considerably which makes the consequences extremely hard to predict because of the high non-linearity of this flow process.

References

/BEC 00/ Becker, D.-A., Bremer, N.-M., Richter, K.-J., Schneider, L., Storck, R.: Experimentelle und theoretische Untersuchung physikalisch-chemischer Vorgänge beim Laugenzutritt in Einlagerungsstrecken. FKZ 02 E 8956 and 02 E 8966 (BMWi), Report GRS-164, GRS Braunschweig, 2000.

/BEH 99/ Bechthold et al.: Backfilling and Sealing of Underground Repositories for Radioactive Waste in Salt (BAMBUS Project). Final Report. - European Commission, nuclear science and technology, EUR 19124 EN, Luxembourg, 1999.

/BEH 03/ Bechthold, W., Smailos, E., Heusermann, S., Bollingerfehr, W., Bazargan Sabet, B., Rothfuchs, T., Kamlot, P., Grupa, J., Olivella, S., Hansen, F. D.: Backfilling and Sealing of Underground Repositories for Radioactive Waste in Salt (BAMBUS-II Project), European Commission, Nuclear Science and Technology, EUR 20621, EN, 2004.

/BEH 04/ Bechthold et al.: Backfilling and sealing of underground Repositories for radioactive waste in salt (BAMBUS II Project). Final report. - European Commission, nuclear science and technology, EUR 20621 EN, Luxembourg, 2004.

/BRO 51/ Brown, H.: Capillary Pressure Investigations. AIME Petroleum Transactions, Vol. 192, pp. 67-74, 1951.

/BRC 64/ Brooks, R.H., Corey, A.T.: Hydraulic Properties of Porous Media. In Hydrol. Pap., volume 3, Colorado State University, Fort Collins, 1964.

/BUN 95/ Bunde, A., Havlin, S.: Percolation I, Fractals and Disordered Systems. (A. Bunde, & S. Havlin, Hrsg.) Berlin: Springer,1995.

/CAD 88/ Cadek, J.: Creep in Metallic Materials. Elsevier, Amsterdam, 1988.

/CAJ 59/ Carslaw, H.S. and Jaeger, J.C.: Conduction of Heat in Solids, Oxford 1959.

/CAR 48/ Carman, P.C.: Some physical aspects of water flow in porous media. Discussions Farady Soc. (1948) Nr. 3, p. 72.

/CIN 06/ Cinar, Y., Pusch, G., Reitenbach, V.: Petrophysical and Capillary Properties of Compacted Salt, Transport in Porous Media (2006) 64: 199-228, Springer, 2006.

/COD 10/ CODE-BRIGHT User's Guide, Departament d'Enginyeria del Terreny, Cartogràfica i Geofisica, Universitat Politècnica de Catalunya (UPC), 2010.

/COR 82/ Core Laboratories: Special core analysis. Dallas, 1982.

/CUD 93/ Cuddy, S., Allinson, G., Steele, R.: A simple, convincing model for calculating water saturations in southern North Sea gas fields. SPWLA 34th Annual Logging Symposium, 1993.

/DIN 03/ Ding, S., Pham, T., Yang, A.: The Use of An Integrated Approach in Estimation of Water Saturation and Free Water Level in Tight Gas Reservoirs: Case Studies. Proceedings - SPE Annual Technical Conference and Exhibition, 2003, p 2929-2937, Society of Petroleum Engineers (SPE), 2003.

/FIS 13/ Klaus Fischer-Appelt, K., Baltes, B., Buhmann, D., Larue, J., Mönig, J.: Sythesebericht für die VSG - Bericht zum Arbeitspaket 13. FKZ UM10A03200 (BMU), Gesellschaft für Anlagen- und Reaktorsicherheit (GRS) mbH, GRS-290, Köln, 2013.

/FRÖ 95/ Fröhlich, H., Förster, S., Hohenthanner, C.R.: Bestimmung des Diffusions- und Permeabilitätsverhaltens von Wasserstoff in Steinsalz und kompaktiertem Salzgruz. Abschlußbericht. Batelle Ingenieurtechnik, Eschborn, 1995.

/GEN 80/ van Genuchten, M.T.: A Closed-Form Equation for predicting the hydraulic Conductivity of Unsaturated Soils. - Soil Sci. Soc. Am. J., 44: 892-898, 1980.

/HAM 10/ Hampel, A.: Vergleich aktueller Stoffgesetze und Vorgehensweisen anhand von 3D-Modellberechnungen zum mechanischen Langzeitverhalten eines

realen Untertagebauwerks im Steinsalz, – Ergebnisbericht zu Teilvorhaben 1, BMBF-Verbundprojekt, 2010.

/HAR 01/ Harrison, B., Jing, X.D.: Saturation Height Methods and Their Impact on Volumetric Hydrocarboni n Place. Proceedings - SPE Annual Technical Conference and Exhibition, 2001, Society of Petroleum Engineers (SPE), 2001.

/HEE 91/ Heemann, U. and Stein, E.: Transient Creep in Rock Salt Structure, in Życzkowski, M. (ed.): Creep in Structures, International Union of Theoretical and Applied Mechanics, Proceedings of the 4th IUTAM Symposium, Cracow, Poland, September 10–14,1990, Springer, 1991.

/HEE 04/ Heemann, U., Sarfeld, W., Faust, B.: JIFE – ein neues FE-Programm zur Simulation von THMC-Prozessen. Proceedings of the 5th workshop on Porous Media, Blaubeuren, 2004.

/HEI 91/ Hein, H. J.: Ein Stoffgesetz zur Beschreibung des thermo-mechanischen Verhaltens von Steinsalzgranulat, Dissertation, RWTH Aachen, 1991.

/HES 74/ Heseldine, G.M.: A method of averaging capillary pressure curves. The log analyst, 15th Annual Symposium, 1974. SPWLA 33rd Annual Logging Symposium, 1992.

/HIL 00/ Hilfer, R.: Local porosity theory and stochastic reconstruction for porous media. In: LNP 554, Eds.: K.R. Mecke and D. Stoyan, pp. 203-241, 2000, Springer-Verlag Berlin Heidelberg.

/HIR 08/ Hirasaki, G.J.: Chapter 3 Hydrostatic Fluid Distribution. In: lecture notes, Rice University, http://www.owlnet.rice.edu/~ceng671/notes.htm, 2008.

/HU 04/ Hu, J. & Stroeven, P.: Local porosity analysis of pore structure in cement paste. Cement and Concrete Research 35, pp. 233-242, 2004, Elsevier, (doi:10.1016/j.cemconres.2004.06.018).

/IBR 92/ Ibrahim, A., Bassiouni, Z., Desbrandes, R.: Determination of relative permeability curves in tight gas sands using log data.

/ITA 03/ Itasca: PFC3D Manual – Theory and Background, 2003.

/ITA 13/ Itasca: 3DEC - 3 Dimensional Distinct Element Code Users's Guide, 2013.

/JIN 03/ Jing, L.: A review of techniques, advances and outstanding issues in numerical modelling for rock mechanics and rock engineering. International Journal of Rock Mechanics and Mining Sciences, 40(3), 283-353, 2003.

/JOB 15/ Jobmann, M., Müller, C., Schirmer, S: Remaining porosity and permeability of compacted crushed rock salt backfill in a HLW repository, Final Report, DBE TECHNOLOGY contribution, Peine, 2015.

/JOH 87/ Johnson, A.: Permeability averaged capillary data: a supplement to log analysis in field studies. SPWLA 28th Annual Logging Symposium, 1987.

/KAZ 10/ Kazerani, T., Zhao, J.: Micromechanical parameters in bonded particle method for modelling of brittle material failure. International journal for numerical and analytical methods in geomechanics, 34(18), 1877-1895,2010.

/KEL 13/ Keller, L., Holzer, L., Schuetz, P., & Gasser, P.: Pore space relevant for gas permeability in Opalinus clay: Statistical analysis of homogeneity, percolation, and representative volume element. Journal of Geophysical Research: Solid Earth, 118(doi: 10.1002/jgrb.50228), 1-14,2013.

/KOR 96/ Korthaus, E.: "Consolidation and deviatoric deformation behaviour of dry crushed salt at temperatures up to 150 °C", 4th Conference on the Mechanical Behaviour of Salt, Montreal, p. 365-377, 1996

/KOZ 27/ Kozeny, J.: Über kapillare Leitung des Wassers im Boden. Wien. Akad. Wiss. Sitzgsber. A Bd. 136 (1927), S. 271.

/KRÖ 09/ Kröhn, K.-P., Stührenberg, D., Herklotz, M., Heemann, U., Lerch, C., Xie, M.: Restporosität und -permeabilität von kompaktierendem Salzgrus-Versatz; Projekt REPOPERM - Phase 1. Abschlussbericht, FKZ 02 E 10477 (BMWi), Gesellschaft für Anlagen- und Reaktorsicherheit (GRS) mbH, GRS-254, Köln, 2009.

/KRÖ 12/ Kröhn, K.-P., Zhang, C.L., Wolf, J., Stührenberg, D., Jobmann, M., of Borstel, L., Lerch, C. (2012): The compaction behavior of salt backfill at low porosities. Mechanical Behavior of Salt VII –, In: Bérest/Ghoreychi/Hadi-Hassen/Tijani (eds.), Proceedings of 7th conference on the mechanical behavior of salt, Paris, France, April 2012: p. 161– 168. CRC Press, Taylor & Francis Group

/LAR 13/ Larue, J., Baltes, B., Fischer, H., Frieling, G., Kock, I., Navarro, M., Seher, H.: Radiologische Konsequenzenanalyse - Bericht zum Arbeitspaket 10 - Vorläufige Sicherheitsanalyse für den Standort Gorleben. FKZ UM10A03200 (BMU), Gesellschaft für Anlagen- und Reaktorsicherheit (GRS) mbH, Bericht GRS-289, Köln, 2013.

/MLY 99/ Müller-Lyda, I., Birthler, H., Fein, E.: Ableitung von Permeabilitäts-Porositätsrelationen für Salzgrus. Bericht GRS-148, GRS Braunschweig, 1999.

/MÜL 12/ Müller-Hoeppe, N., Breustedt, M., Wolf, J., Czaikowski, O., Wieczorek, K.: VSG: Integrität geotechnischer Barrieren - Teil 2 Vertiefte Nachweisführung (AP 9.2) **Vertiefte** Nachweisführung. FKZ UM10R03200, (BMU), Bericht GRS-288, GRS Braunschweig, 2012.

/MÜN 08/ Münch, B., Holzer, L.: Contradicting geometrical concepts in pore size analysis attained with electron microscopy and mercury intrusion. J. Am. Ceram. Soc., 91, 4059-4067, 2008.

/LEV 41/ Leverett, M. C.; Capillary behavior in porous solids; Petroleum Transactions of AIME (1941); 142; 152-169, 1941.

/OLI 93/ Olivella, S., Gens, A., Carrera, J., Alonso, E.: Behaviour of porous salt aggregates – Constitutive and field equations for a coupled deformation, brine, gas and heat transport model, the 6th Inter. Conference on Mechanical Behavior of Salt, Palaiseau, France, Sep. 1993.

/OLI 02/ Olivella, S., Gens, A.: A constitutive model for crushed salt, Int. J. Numer. Anal. Meth. Geomech.; 26; 719-746, 2002.

/PEN 12/ Peng, S., Hu, Q., Dultz, S., Zhang, M.: Using X-ray computed tomography in pore structure characterization for a Berea sandstone: Resolution effect. J. of Hydrology, 472-473, 254-261, 2012.

/POP 12/ Popp, T., Salzer, K., Schulze, O., Stührenberg, D.: Diskussionsbeitrag zum Kompaktionsverhalten und den hydraulischen Eigenschaften von Salzgrusversatz. unpubl., 2012.

/PRI 89/ Prickett, H.D., Bremer, R.E.: Improved initial water saturation distribution for a three-dimensional model. Society of Petroleum Engineers SPE, SPE 17958, 1989.

/PRI 09/ Pringle, D., Miner, J., Eicken, H., Golden, K.: Pore space percolation in sea ice single crystals. Journal of Geophysical Research, 114, C12017, 2009.

/REN 07/ Renard, F., Bernard, D., Thibault, X., Boller, E.: Synchrotron 3D microtomography of halite aggregates during experimental pressure solution creep and evolution of permeability. Geophys. Res. Lett., 31(L07607), 2007.

/ROS 49/ Rose, W., Bruce, W.A.: Evaluation of Capillary Character in Petroleum Reservoir Rock. Petroleum Transactions of AIME 186: 127 – 142, 1949. (zitiert in /IBR 92/)

/ROT 99/ Rothfuchs, T.; Feddersen, H.-K.; Kröhn, K.-P.; Miehe, R.; Wieczorek, K.: The DEBORA-Project: Development of Borehole Seals for High-Level Radioactive Waste - Phase II. Final report, FZK02E8715, Gesellschaft für Anlagen- und Reaktorsicherheit (GRS) mbH, Bericht GRS-161, GRS Köln, 1999.

/SCH 07/ Schulze, O.: Thermomechanisches und hydraulisches Verhalten von Salzgestein. BGR-Ergebnisbericht zum AP 9Y 3214 0800 00, Hannover, 2007.

/SCH 14/ Schulze, O.: Untersuchungen zur Feuchte-Wirkung auf das Deformationsverhalten. BGR-Ergebnisbericht zum AP 9Y 3214 0800 00: Ermittlung des thermomechanischen und hydraulischen Verhaltens von Salzgestein. Hannover, 2014

/SKE 95/ Skelt, C., Harrison, B.: An integrated approach to saturation height analysis. SPWLA 36th Annual Logging Symposium, 1995.

/SPI 89/ Spiers, C. J., Peach, C. J., Brzesowsky, R., H., Schutjens, P., M., T., M., Liezenberg, J. L., Zwart, H., J.: Long-term rheological and transport properties of dry and wet salt rocks, Commission of the European Communities, EUR 11848 EN, 1989.

/SPI 90/ Spiers, C.J. et al. : Experimental determination of constitutive parameters governing creep of rock salt by pressure solution, Geological Society special Publication No 54. pp. 215-227, 1990.

/SPI 93/ Spiers, C.J.: Densification behaviour of wet granular salt: Theory versus experiment, Seventh Symp. on Salt, eds.:H. Kakihana, H.R.Jr. Hardy, T. Hoshi, K. Toyokura, Vol. 1, p. 83-92, 1993.

/SPI 05/ Spiers, C.J., Grupa, J., Salzer, K., Popp, T., Stührenberg, D. (2005): Buffer / backfill in salt, presentation in NFPRO second training course and workshop, Cardiff, Wales, UK, 19-20 Oct. 2005.

/STA 95/ Stauffer, D., Aharony, A.: Perkolationstheorie: Eine Einfuehrung. VCH, Weinheim, New York, Basel, Cambridge, Tokyo, 1995.

/STE 85/ Stelte, N.: "Analytische Approximation der Konvergenzrate salzgrusversetzter und unter hydraulischem Druck stehender Hohlräume im Salzgestein.", Fachband 15 zum Projekt Sicherheitsstudien Entsorgung: Einzeluntersu-

chungen zur Radionuklidfreisetzung aus einem Modellsalzstock, Abschlußbericht, Berlin, Jan. 1985

/STÜ 95a/ Stührenberg, D.; Zhang, C.-L.: Untersuchungen zum Kompaktionsverhalten von Salzgrus als Versatzmaterial für Endlagerbergwerke im Salz unter besonderer Berücksichtigung der Wechselwirkung zwischen Gebirge und Versatz. BGR-Abschlußbericht zum BMFT-Fv. Förderkennzeichen 02 E 8552 8, Archiv-Nr. 113 259, Hannover, 1995

/STÜ 95b/ Stührenberg, D.; Zhang, C.-L.: Results of Experiments on the Compaction and Permeability Behavior of Crushed Salt. Proc. of the Fifth Intern. Conf. on Radioactive Waste Management and Environmental Remediation, Berlin (ICEM' 95), 1995

/STÜ 09/ Stührenberg, D.: Salzgruskompaktion im Restporositätsbereich. Genauigkeits-analyse anhand des BGR-Oedometerversuchs 099. BGR-Fachbericht März 2009, Tagebuchnummer 10530/09.

/STÜ 12/ Stührenberg, D., Schulze, O.: Porosity and permeability of crushed and damaged salt during compaction. Mechanical Behavior of Salt VII –, In: Bérest/Ghoreychi/Hadi-Hassen/Tijani (eds.), Proceedings of 7th conference on the mechanical behavior of salt, Paris, France, April 2012: p. 275–282. CRC Press, Taylor & Francis Group

/SWA 81/ Swanson, B.G.: A Simple Correlation Between Permeability & Mercury Capillary Pressure. Journal of petroleum technology, 1981.

/THO 60/ Thomeer, J.H.M.: Introduction of a Pore Geometrical Factor Defined by the Capillary Pressure Curve. Journal of petroleum technology, 1960.

/URA 07/ Urai, J., Spiers, C.: The effect of grain boundary water on deformation mechanisms and rheology of rocksalt during long-term deformation. In K. L. M. Wallner (Hrsg.), The Mechanical Behavior of Salt – Understanding of THMC Processes in Salt, Proceedings of the 6th Conference on the Mechanical Behavoir of Salt' 'Saltmech6'. Hannover, May 2007.

/WAT 87/ Watson, E., & Brennan, J.: Fluids in the lithosphere, 1. Experimentally determined wetting characteristics of CO2-H2O fluids and their implications for fluid transport, host rock physical properties, and fluid inclusion formation. Earth Planet. Sci. Lett, 85, 497-515, 1987.

/ZHA 93/ Zhang, C.-L., Heemann, U., Schmidt, M., Staupendahl, G.: Experimental and modelling results for compaction of crushed salt, the 6th Inter. Conference on Mechanical Behavior of Salt, Palaiseau, France, Sep. 1993.

Table of figures

List of tables

Contents of enclosed CD

Appendix A	Physical derivation of the crushed salt model of Heemann
Appendix B	Relevant scenarios and boundary conditions
Appendix C	Report on triaxial test TK-031
Appendix D	Analysis and geochemical interpretation of inflowing and outflowing solutions in the long-term compaction test
Appendix E	Stress-controlled uniaxial long-term compaction test
Appendix F	Constitutive Equations for two-phase flow
Appendix G	Grading curve of backfill material
Appendix H	Scaling-rules from the oil industry
Appendix I	Sorption of vapour on crushed salt
Appendix J	THM-coupled simulation of a compacting backfilled drift
Appendix K	Parameter improvement for dry and wet compaction of crushed salt

Gesellschaft für Anlagen- und Reaktorsicherheit (GRS) gGmbH

Schwertnergasse 1
50667 Köln
Telefon +49 221 2068-0
Telefax +49 221 2068-888

Boltzmannstraße 14
85748 Garching b. München
Telefon +49 89 32004-0
Telefax +49 89 32004-300

Kurfürstendamm 200
10719 Berlin
Telefon +49 30 88589-0
Telefax +49 30 88589-111

Theodor-Heuss-Straße 4
38122 Braunschweig
Telefon +49 531 8012-0
Telefax +49 531 8012-200

www.grs.de

ISBN 978-3-946607-32-8